INFORMATION TO USERS

This material was produced from a microfilm copy of the original document. While the most advanced technological means to photograph and reproduce this document have been used, the quality is heavily dependent upon the quality of the original submitted.

The following explanation of techniques is provided to help you understand markings or patterns which may appear on this reproduction.

1. The sign or "target" for pages apparently lacking from the document photographed is "Missing Page(s)". If it was possible to obtain the missing page(s) or section, they are spliced into the film along with adjacent pages. This may have necessitated cutting thru an image and duplicating adjacent pages to insure you complete continuity.

2. When an image on the film is obliterated with a large round black mark, it is an indication that the photographer suspected that the copy may have moved during exposure and thus cause a blurred image. You will find a good image of the page in the adjacent frame.

3. When a map, drawing or chart, etc., was part of the material being photographed the photographer followed a definite method in "sectioning" the material. It is customary to begin photoing at the upper left hand corner of a large sheet and to continue photoing from left to right in equal sections with a small overlap. If necessary, sectioning is continued again — beginning below the first row and continuing on until complete.

4. The majority of users indicate that the textual content is of greatest value, however, a somewhat higher quality reproduction could be made from "photographs" if essential to the understanding of the dissertation. Silver prints of "photographs" may be ordered at additional charge by writing the Order Department, giving the catalog number, title, author and specific pages you wish reproduced.

5. PLEASE NOTE: Some pages may have indistinct print. Filmed as received.

Xerox University Microfilms
300 North Zeeb Road
Ann Arbor, Michigan 48106

74-25,346

TIMM, Edward Earl, 1945-
AN EXPERIMENTAL PHOTOGRAPHIC INVESTIGATION OF VAPOR BUBBLE COLLAPSE AND LIQUID JET IMPINGEMENT.

The University of Michigan, Ph.D., 1974
Engineering, chemical

University Microfilms, A XEROX Company, Ann Arbor, Michigan

THIS DISSERTATION HAS BEEN MICROFILMED EXACTLY AS RECEIVED.

AN EXPERIMENTAL PHOTOGRAPHIC INVESTIGATION OF VAPOR BUBBLE COLLAPSE AND LIQUID JET IMPINGEMENT

by
Edward Earl Timm

A dissertation submitted in partial fulfillment
of the requirements for the degree of
Doctor of Philosophy
(Chemical Engineering)
in The University of Michigan
1974

Doctoral Committee:

Professor Frederick G. Hammitt, Co-Chairman
Professor G. Brymer Williams, Co-Chairman
Assistant Professor D. E. Briggs
Professor R. L. Curl
Associate Professor J. D. Goddard
Professor H. Merte

DEDICATION

Dedicated to my father, Earl E. Timm. Without him it would not have been possible.

ACKNOWLEDGEMENTS

The author wishes to thank the following individuals and groups for their contributions to this work:

F. G. Hammitt

G. B. Williams

D. E. Briggs

R. L. Curl

J. D. Goddard

H. Merte

C. L. Kling

T. M. Mitchell

J. Varner

Jack Brigham and the Auto Lab shop crew

Ed Rupke and the Instrument shop crew

TABLE OF CONTENTS

DEDICATION ii

ACKNOWLEDGEMENTS iii

LIST OF ILLUSTRATIONS vii

LIST OF TABLES ix

LIST OF SYMBOLS x

CHAPTER ONE: INTRODUCTION 1

1.1 Motivation For Research 1
1.2 A Brief Survey of Research in the Field of Bubble Dynamics 1
1.2a Early Research 2
1.2b Contemporary Research 10
1.3 A Brief Survey of Research in the Field of Liquid Impingement Erosion 18
1.4 Objectives of Research 26

CHAPTER TWO: SCIENTIFIC PHOTOGRAPHY AND HOLOGRAPHY 29

2.1 A Review of Scientific Cinematography 29
2.2 Photographic Systems Utilized in This Study 38
2.2a Beckman and Whitley Dynafax Camera and U-M Custom Light Source 39
2.2b Beckman and Whitley Model 330 Camera and Cordin Model 450 Light Source 42
2.2c Miscellaneous Photographic and Optical Equipment 45
2.3 A Brief Review of Holography 45
2.4 The University of Michigan Radar and Optics Laboratory Holographic Facility 47

CHAPTER THREE: EXPERIMENTAL EQUIPMENT 48

3.1 Experimental Equipment Used in Study of Vapor Bubble Collapse 48
3.1a Vapor Bubble Generator 48
3.1b Static Fluid Chamber 49
3.1c High Speed Water Tunnel 50
3.1d Two-Dimensional Venturi 51
3.1e Two-Optical-Axis Venturi 53
3.2 Experimental Equipment Used in Study of Water Jet Impingement 54
3.2a Water Jet Gun 54
3.2b Target Materials 55

3.3 Miscellaneous Equipment 56
3.3a Photodiode Detector 56
3.3b Photoelectric Velocity Sensor 57
3.3c Stock Equipment 57

CHAPTER FOUR: EXPERIMENTAL INVESTIGATION OF VAPOR BUBBLE COLLAPSE 72

4.1 General Procedure 72
4.2 Experiments In a Static Fluid Environment Utilizing High Speed Cinematography 73
4.2a Bubble Generator Characterization 74
4.2b Bubble Collapse Adjacent to a Rigid Surface 74
4.2c Bubble Collapse Adjacent to a Compliant Surface 75
4.2d Bubble Collapse Adjacent to Another Bubble 75
4.3 Experiment in a Static Fluid Environment Utilizing Holography 75
4.4 Experiments in a Flowing Fluid Environment Contained by the Two-Dimensional Venturi 76
4.4a Two-Dimensional Venturi - Dynafax Camera 77
4.4b Two-Dimensional Venturi - Model 330 Camera 77
4.5 Experiments in a Flowing Fluid Environment Contained by the Two-Optical-Axis Venturi 78

CHAPTER FIVE: RESULTS AND DISCUSSION OF EXPERIMENTAL INVESTIGATION OF VAPOR BUBBLE COLLAPSE .. 124

5.1 Problems in Interpretation of Photographic Records 124
5.2 Presentation of Results 126
5.3 Results and Discussion of Experiments in a Static Fluid Environment Utilizing High Speed Cinematography 128
5.3a Bubble Generator Characterization 128
5.3b Bubble Collapse Adjacent to a Rigid Surface 128
5.3c Bubble Collapse Adjacent to a Compliant Surface 129
5.3d Bubble Collapse Adjacent to Another Bubble 131
5.4 Results and Discussion of Experiment in a Static Fluid Environment Utilizing Holography 132
5.5 Results and Discussion of Experiments in a Flowing Fluid Environment Contained by the Two-Dimensional Venturi 133
5.6 Results and Discussion of Experiments in a Flowing Fluid Environment Contained by the Two-Optical-Axis Venturi 135

5.7 Discussion and Conclusions Concerning Investigation into Vapor Bubble Collapse 141
5.8 Further Directions in Bubble Collapse Research 147

CHAPTER SIX: EXPERIMENTAL INVESTIGATION OF WATER JET IMPINGEMENT 176

6.1 General Procedures 176
6.2 Photographic Investigation of Impact Phenomena 176
6.3 Experimental Investigation of Impact Damage Susceptibility 177

CHAPTER SEVEN: RESULTS AND DISCUSSION OF EXPERIMENTAL INVESTIGATION OF WATER JET IMPINGEMENT .. 187

7.1 Photographic Investigation into Water Jet Impingement 187
7.1a Problems in Interpretation of Photographic Records 187
7.1b Results of Photographic Investigation 189
7.2 Experimental Investigation into Material Damage Resulting from Water Jet Impingement 192
7.2a Problems in Interpretation of Material Damage Data 192
7.2b Results of Investigation into Material Damage 194
7.3 Discussion and Conclusions Concerning Investigation into Water Jet Impingement 199

BIBLIOGRAPHY 210

APPENDIX: LIQUID RELAXATION PHENOMENA IN LIQUID-SOLID IMPACT 217

A.1 Introduction 217
A.2 Experimental Approach 219
A.3 Discussion of Results 221
A.4 Appendix Bibliography 242

LIST OF ILLUSTRATIONS

FIGURE	FIGURE NAME	PAGE
1.1	Asymmetric Collapse Mechanism	6
3.1	Schematic of Bubble Generator	59
3.2	Bubble Generator	59
3.3	Static Spark Chamber	60
3.4	Electrode Assemblies	60
3.5	Schematic of High Speed Water Tunnel	61
3.6	Schematic of Two-Dimensional Venturi	62
3.7	Two-Dimensional Venturi	63
3.8	Schematic of Two-Optical-Axis Venturi	64
3.9	Two-Optical-Axis Venturi, Assembled	65
3.10	Two-Optical-Axis Venturi, Disassembled	65
3.11	Pressure Tap Location, Two-Optical-Axis Venturi	66
3.12	Schematic of Jet Gun	67
3.13	Jet Gun, Automated Configuration	68
3.14	Jet Gun, Single Shot Configuration	69
3.15	Photodiode Detector	70
3.16	Schematic of Photodiode Detector	70
3.17	Photoelectric Velocity Sensor	71
4.1	Static Spark Chamber w/Dynafax Camera	81
4.2	Single Bubble Measurement Diagram	82
4.3	Rigid Wall Measurement Diagram	82
4.4	Prints, Run 1099-DSB-3	83
4.5	Prints, Run 1120-DSB-1	84
4.6	Prints, Run 10300-DSB-1	88
4.7	Prints, Run 10210-DSB-2	92
4.8	Double Bubble Measurement Diagram	96
4.9	Schematic of Holographic Facility	97
4.10	Photograph of Hologram, Run 1229-HSB-5	98
4.11	Prints, Run 1191-DFB-1	99
4.12	Two-Dimensional Venturi Measurement Diagram	101
4.13	Two-Dimensional Venturi w/ Model 330 Camera	102
4.14	Prints, Run 1252-BW-FB-2	103
4.15	Schematic of Two-Optical Venturi Setup	107
4.16	Two-Optical-Axis Venturi w/ Model 330 Camera	108
4.17	Interpretation of Two-Optical-Axis Prints	109
4.18	Two-Optical-Axis Measurement Diagram	109
4.19	Prints, Run 7102-BW-2D-4	110
4.20	Prints, Run 842-BW-2D-5	113
4.21	Prints, Run 852-BW-2D-3	115
4.22	Prints, Run 7312-BW-2D-1	118
4.23	Partially Compliant Window, Disassembled	121
4.24	Prints, Run 842-BW-2D-2	122
5.1	Illustration of Apparent Wall Position	151
5.2	Wall Position, Run 1099-DSB-3	152
5.3	Wall Position, Run 1120-DSB-1	153
5.4	Wall Position, Run 10300-DSB-1	154
5.5	Wall Position, Run 10210-DSB-1	155

FIGURE	FIGURE NAME	PAGE
5.6	Wall Position, Run 1191-DFB-1 and Run 1252-BW-FB-2	156
5.7	Wall Position, Run 1252-BW-FB-2	157
5.8	Wall Velocity, Run 1252-BW-FB-2	158
5.9	Eccentricity, Run 1252-BW-FB-2	159
5.10	Wall Position, Run 7312-BW-FB-2	160
5.11	Wall Position, Run 852-BW-2D-3	161
5.12	Wall Velocity, Run 7312-BW-2D-1	162
5.13	Wall Velocity, Run 852-BW-2D-3	163
5.14	Eccentricity, Run 7312-BW-2D-1	164
5.15	Eccentricity, Run 852-BW-2D-3	164
5.16	Wall Position, Run 7102-BW-2D-4	165
5.17	Wall Position, Run 842-BW-2D-5	166
5.18	Wall Position, Run 842-BW-2D-2	167
5.19	Wall Velocity, Run 7102-BW-2D-1	168
5.20	Wall Velocity, Run 842-BW-2D-5	169
5.21	Wall Velocity, Run 842-BW-2D-2	170
5.22	Eccentricity, Run 7102-BW-2D-1	171
5.23	Eccentricity, Run 842-BW-2D-5	171
5.24	Eccentricity, Run 842-BW-2D-2	171
5.25	Centroid Position	172
5.26	Centroid Position Comparison	173
5.27	Wall Velocities From Chapman	174
5,28	Wall Velocity Comparison	175
6.1	Jet Gun w/ Model 330 Camera	179
6.2	Jet Impact Measurement Diagram	180
6.3	Prints, Run 892-BW-I-1	181
6.4	Prints, Run 4290-BW-I-1	182
6.5	Prints, Run 4300-BW-I-1	183
6.6	Prints, Run 4300-BW-I-2	184
6.7	Prints, Run 510-BW-I-4	185
6.8	Prints, Run 892-BW-I-3	186
7.1	Liquid Impact Radial Splash Velocity	206
7.2	Liquid Impact Specimens Volume Loss	207
7.3	Liquid Impact Specimens	208
7.4	Schematic of Proposed Fluidic Cutoff for Jet Gun	209
A.1	Prints from Shalnev and Kozirev	224
A.2	Liquid Stream Impact Unit w/ Model 330 Camera	225
A.3	Prints, Run 4192-BW-BF-2	226
A.4	Prints, Run 4192-BW-BF-1	228
A.5	Prints, Run 4202-BW-BF-2	230
A.6	Prints, Run 4192-BW-BF-3	232
A.7	Prints, Run 4192-BW-BF-4	234
A.8	Prints, Run 522-BW-BF-1	236
A.9	Prints, Run 522-BW-BF-2	238

LIST OF TABLES

TABLE	DESCRIPTION	PAGE
3.1	Impact Target Specimens	58
5.1	Bubble Characteristics	150
7.1	Incubation Period Data	195
7.2	Damage Rankings of Materials	197
A.1	Impact Photographic Sequences	221

LIST OF SYMBOLS

SYMBOL	DESCRIPTION
A	Area
B	Florschuetz-Chao Parameter
B_L	Blur
b^L	Bubble Centroid Distance
C	Shock Propagation Velocity
Co	Sonic Velocity
C_{fc}	Florschuetz-Chao Parameter
D^{fc}	Diameter of Circle of Confusion
D^c	Clear Diameter of Objective Lens
D^L	Apparent Diameter along X Axis
D^x	Apparent Diameter along Y Axis
D^y	Apparent Diameter along Z Axis
d^z	Centroid Distance From Surface
F	Force
f	Relative Aperture
F_L	Focal Length
Jā	Jakob Number
M	Mass
m	Magnification
N	Number of Frames per Sequence
P	Pressure
Pc	Internal Pressure in Bubble
P_∞	Far Field Pressure
Pwh	Water Hammer Pressure
ΔP	$\Delta P = P_\infty - Pc$
R	Bubble Wall Radius
$\dot{R}$	Bubble Wall Velocity
r	Radius
S	Framing rate
T	Effective Aperture
T_L	Liquid Temperature
t^L	Time from start of event
t_{BR}	Besant-Rayleigh Collapse Time
te	Exposure Time
tp	Pulse Duration Time
tr	Relaxation Time
Δt	Time Interval
U	Depth of Field
u	Solidified Liquid Length
V	Velocity
Vob	Object Velocity
W	Writing Time

SUBSCRIPTS

o	Initial (Maximum) Value
x	Referring to X Axis
y	Referring to Y Axis
z	Referring to Z Axis

GREEK

α	Evaporation coefficient
ϵ	Eccentricity
θ_{OB}	Object Velocity - Optical Axis Angle
η	Luminous Efficiency
ρ_L	Liquid Density
σ	Gibson Parameter

CHAPTER 1

INTRODUCTION

1.1 MOTIVATION FOR RESEARCH

Multiphase flow has always presented engineers with a number of practical problems. This is particularly true in hydraulic machinery where multiphase flow often leads to failure due to erosion of critical parts. Depending on the flow situation involved, this erosion may be classified as either cavitation erosion, due to the presence of vapor bubbles in a flowing liquid stream, or impact erosion, due to the presence of liquid drops in a flowing gas stream. Typical examples of cavitation erosion can be found in damage to pump impellers or ship propellers, while typical examples of impact erosion can be found in damage to low pressure steam turbine blades or aircraft which fly in rainstorms.

The mechanisms by which erosion damage occurs in these cases is not well understood, and may be closely related. As technology progresses and machinery is developed which operates ever closer to the failure limits of practical materials, more understanding of the mechanisms of erosion damage is clearly necessary. The research reported in this dissertation was motivated by this need and represents a further attempt to shed light on the mechanisms of erosion damage through an experimental approach.

1.2 A BRIEF SURVEY OF RESEARCH IN THE FIELD OF BUBBLE DYNAMICS

For the purposes of this survey, research in the field of Bubble Dynamics has been divided into two periods. Early

research in this field has a well established chronology, and its development is best categorized chronologically. Contemporary research is best categorized by subject. The arbitrary division between these periods has been chosen to be 1960, although this division is not strictly followed where inappropriate.

1.2a EARLY RESEARCH

As with most kinds of scientific research, research into vapor bubble collapse was first motivated by practical problems encountered in the development of technology. The earliest mention of cavitation occurs in a treatise on Hydraulic Turbines[1] written by Euler in 1754. In 1859 Besant[2] developed a mathematical model for the collapse of a single spherical bubble collapsing in an ideal, incompressible liquid. A similar model was developed by Rayleigh[3] and solved to show that a bubble with no gas or vapor present inside collapses with ever increasing wall velocity as the radius of the bubble decreases. As the radius of the collapsing bubble approaches zero the wall collapse velocity approaches infinity and very high pressures are built up in the fluid adjacent to the bubble wall. Rayleigh also mentioned the enormous impulse which would be delivered to any solid object interrupting the flow of the imploding liquid. Early experimental work in the field of cavitation was conducted in 1894 by Reynolds[4], who wrote about boiling at ordinary temperatures and reduced pressure; and postulated the reduction of a liquid's pressure below its vapor pressure was the cause of this boiling. Reynolds also

reported acoustic "hissing", and concluded the source of this noise was the collapse of the bubbles formed by boiling.

Cavitation research acquired importance when Parsons[5] in 1897 developed the steam turbine for shipboard use. The consequent increase in shaft horsepower and speed showed design flaws in early screw propellors which resulted in cavitation with a corresponding loss in efficiency and damage to the propellors. In subsequent work Parsons, Barnaby[7] and many others conducted experimental cavitation studies leading to the perfection of the marine screw propellor. About this time, interest in cavitation research waned and did not pick up again until WW II provided additional impetus. Subsequent research was primarily directed into three areas. These are: extention of mathematical models to include real fluid properties, extention of mathematical models to include deviations from spherical symmetry during collapse, and further experimental studies in the area of vapor bubble collapse utilizing modern instrumental techniques.

Beeching[8], in 1942, made the first attempt to extend the Besant-Rayleigh Spherical Collapse Model to include real fluid properties. Beeching included forces due to surface tension in his model and concluded for a pure vapor bubble in water that the effect of surface tension is negligible unless the bubble is very small, or the liquid pressure is of the same magnitude as the liquid's vapor pressure. He also observed that bubbles with an appreciable internal gas

content should have a lesser capability to damage nearby surfaces than bubbles containing only vapor, because the internal gas cushions the cavity's collapse. This observation assumes the internal gas does not have time to dissolve in the surrounding liquid during collapse.

In a wartime investigation of underwater explosions Herring[9] made two important contributions to the mathematical modeling of single bubble collapse. Herring introduced liquid compressibility into the model and found an appreciable portion of the energy available to the collapse is utilized to compress the liquid, leaving only a fraction available for compressing the gaseous contents of the bubble. This resulted in the conclusion that for a bubble containing appreciable gas, such as the bubble formed by an underwater explosion, about 70% of the collapse energy is radiated away in the form of acoustic energy during the collapse cycle. This conclusion was experimentally verified by studying the ratios of successive maximum radii of explosion produced bubbles which contain sufficient internal gas to rebound after collapsing to some minimum size.

Herring also showed, both analytically and experimentally, a collapsing bubble migrates toward a solid surface and away from a free surface. In the solid surface case collapse is retarded relative to the infinite liquid case, while for the free surface case it is accelerated.

If, during the collapse of a bubble, the internal vapor cannot condense fast enough to avoid a rise in internal pressure; the collapse will be retarded. This is a

thermodynamic effect on collapse, and the first attempt to incorporate thermodynamic effects into the Besant-Rayleigh Spherical Collapse Model was made by Silver[10] in 1942. Utilizing several simplistic assumptions concerning the vapor condensation rate and subsequent latent heat transfer rates Silver predicted lower peak pressures than Rayleigh or Besant, but concluded the pressures generated were still sufficient to damage nearby surfaces.

In 1944 Kornfeld and Suvorov[11] suggested that asymmetries arising in the later stages of the collapse of an initially spherical bubble play an important role in cavitation damage. Reasoning from the great similarity found between material damage resulting from cavitation and damage produced by the impingement of high velocity liquid jets on a surface Kornfeld and Suvorov hypothesized that during the final stages of collapse adjacent to a surface the bubble takes on an involute shape resulting in the formation of a high velocity liquid jet which strikes the surface. This is the first mention of the importance of asymmetrical collapse in cavitation damage. This collapse mechanism is depicted in Fig. 1.1.

Underwater Explosions was the subject of a book by Cole[12] (1948) in which is presented compressible and incompressible fluid flow equations modeling underwater explosion bubbles. Of primary importance in this work is Cole's use of the method of images to derive differential equations modeling the effect of a nearby solid or free surface on a rebounding spherical bubble. Cole also developed approximations for the magnitude

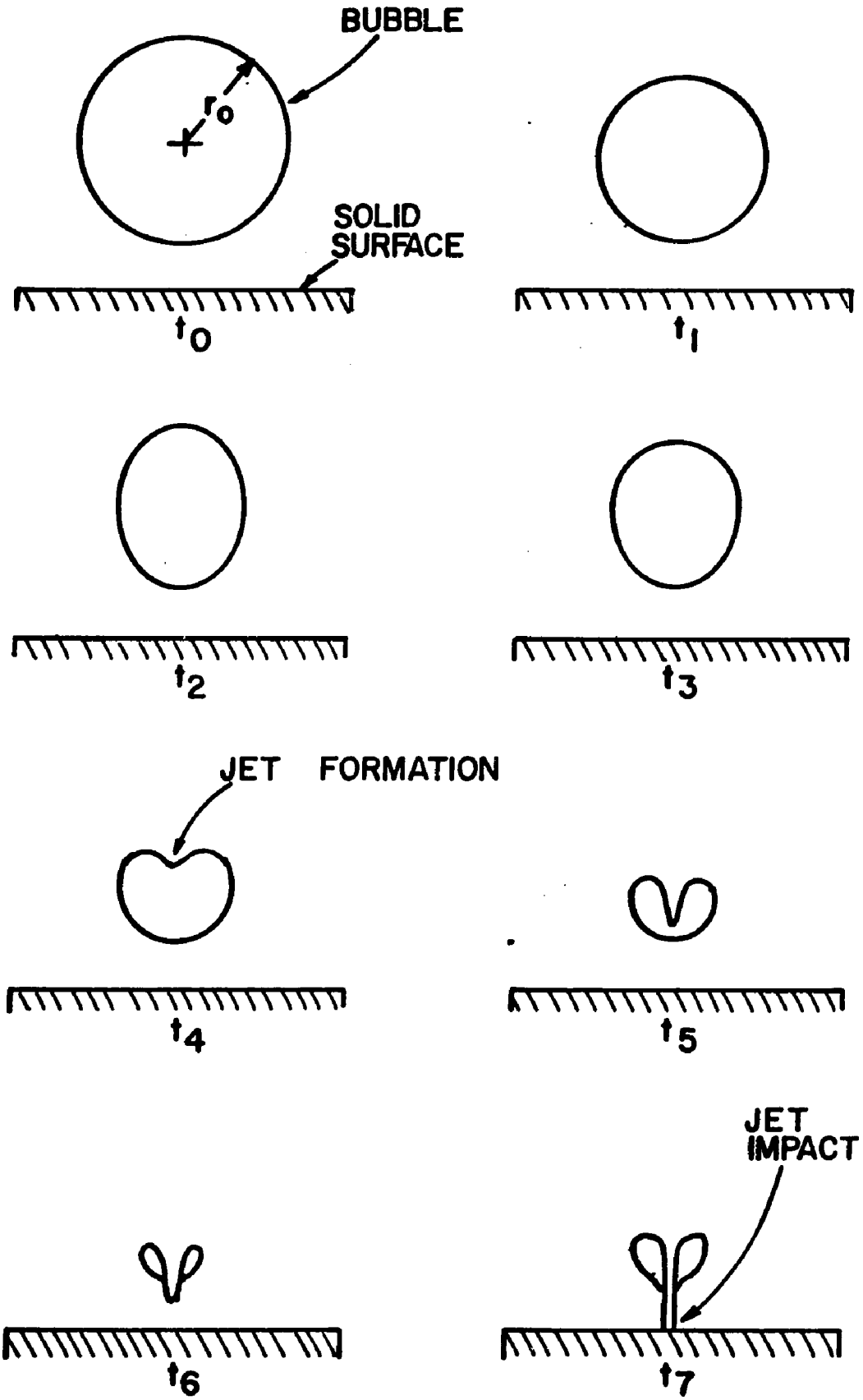


Figure 1.1 Asymmetric Bubble Collapse Mechanism

of the shock wave emitted by an underwater explosion discussed tehniques for experimentally investigating underwater explosions, and concluded that underwater explosion produced bubbles are well modeled by incompressible flow theory during most of their lifetime.

Plesset[13], in a spherical bubble collapse model including thermodynamic parameters, postulated, for bubble wall velocities below a certain critical value, condensation occurs rapidly enough to avoid internal pressure rise due to heat transfer limitations. At bubble wall collapse velocities greater than this condensation velocity, internal pressure rise cushions the collapse, reducing pressure peaks in the surrounding fluid.

Eisenberg[14] (1950) considered the asymmetrical bubble collapse-jet impingement mechanism of cavitation danage, and further discussed the water hammer pressure as an estimate of the peak pressure produced by this mechanism. The classical water hammer pressure is calculated from Eq. 1.1.

$$Pwh = \rho_L CoV \qquad 1.1$$

Pwh = Water Hammer Pressure
ρ_L = Liquid Density
Co = Sonic Velocity in Liquid
V = Impact Velocity

The advent of high speed digital computers made it possible to solve some complex differential equations through the application of numerical methods. Early efforts to apply this technique to models of bubble collapse without the assumption of spherical symmetry were made by Rattray[15] and Plesset and Mitchell[16]. Utilizing perturbation methods to obtain a system of coupled ordinary differential

equations modelling the collapse, Plesset and Mitchell established that perturbations in the shape of a collapsing spherical bubble are unstable and tend to grow as the collapse proceeds. Rattray analyzed the cases of initially spherical bubbles collapsing both adjacent to a solid surface, and in a free liquid stream with a slip velocity. For the solid wall case, Rattray found the bubble first elongates along the axis normal to the surface, then becomes involuted on the side opposite the surface. For the slip velocity case, analysis showed involution on the trailing side of the bubble. However, due to the perturbation methods Rattray employed, these mathematical analyses became unreliable as soon as collapse progressed to the point where the asymmetries became sizeable.

Poritsky[17] (1952) added viscous effects to the classical spherical collapse model and found for sufficiently high viscosities the collapse is severely retarded. Utilizing simplifying assumptions and a model including both surface tension and viscosity, Shu[18] found the collapse time to be finite regardless of viscosity; but that both viscosity and surface tension have only a small effect unless the bubble is very small, or the difference between the internal pressure in the bubble and the liquid pressure is small. Concurrently, Gilmore[20, 21] extended Herring's extension of the Besant-Rayleigh analysis to include compressibility effects in a more rigorous manner and found the bubble wall velocity, $(\dot{R})$, to vary in proportion to $R^{-1/2}$, in the later stages of collapse. This is in contrast to the incompressible

model, which has $\dot{R}$ varying as $R^{-3/2}$ throughout collapse.

Utilizing the then developing techniques of high speed cinematography, and a water tunnel, Ellis[21] (1952) made the first good experimental study of cavitation bubbles collapsing in a pressure gradient. Ellis' work tended to support the conclusions of Rattray and others regarding the asymmetric collapse mechanism.

Zwick and Plesset[22] and Benjamin[23], in 1955, published a further thermodynamic effect extension of the Besant-Rayleigh model, and concluded, for a typical cavitation bubble in water (Ro=2.5 mm, P_∞ =0.54 atm, T_L =22°C), that thermodynamic effects are negligible. In a study of cavitation in centrifugal pumps, Stahl and Stephanoff[24] helped quantify the conditions under which thermodynamic effects on bubble collapse play an important role. Flynn[25] logically concluded that thermodynamic effects are most important in the later stages of collapse, with the initial phases of collapse being essentially isothermal and the later stages becoming increasingly adiabatic.

In the 1930's the observation was made that bubbles collapsing under some conditions emitted light. This phenomena was termed sonoluminescence, and hypotheses for its cause included electrical discharge, chemiluminescence, shock wave formation, and high temperature emission. Early experiments by Prudhomme and Guilmart[26] (1957) demonstrated sonoluminescence to be most intense for pure gas bubbles. The peak temperatures of the gas compressed in the bubbles was thought to be as high as 10,000°K. Additional

experimental work by Jarmain[27] supported the theory of the thermal origin of sonoluminescence, and therefore the importance of thermodynamic effects in bubble collapse.

Hickling[28] and later Hickling and Plesset[29] constructed models for the collapse of a gas filled cavity, solved them through numerical techniques, and came to two important conclusions. First, bubble collapse is an isothermal process during the early part of the collapse. As the collapse proceeds and the collapse velocity increases, heat transfer is reduced and the collapse becomes an adiabatic process. Small bubble diameter and high internal heat transfer rates tend to prolong the isothermal phase of collapse, which results in a more violent collapse, giving of higher peak pressures and greater damage capability. The second conclusion from this model was that the shock wave given off during the collapse of a gas filled bubble attenuates by an approximate factor of 1/r as it propogates through the liquid, and might be sufficiently intense to damage nearby solids.

1.2b CONTEMPORARY RESEARCH

Contemporary research in the field of bubble dynamics has been a logical extension of previous work. By bits and pieces, both mathematical models and experimental knowledge have come to be more realistic. However, no author has been able to conclusively define the mechanism by which damage occurs to nearby solid surfaces during bubble collapse. Neither the jet impact mechanism, nor the high pressure shock mechanism, has been demonstrated to be dominant. It may well be that neither of these mechanisms is dominant,

as each has been shown capable of causing damage under some circumstances. In this section the literature has been divided into two groups by subject. The first area considered is research into thermodynamic effects; the second considers research into the effects of real fluid properties, pressure gradients, and nearby surfaces.

In 1965 Florschuetz and Chao[30] developed a quantitative distinction between heat transfer controlled collapse and inertia controlled collapse. This distinction was based upon a parameter, $B = Ja^2 / C_{fc}$. Ja is the Jakob Number; and C_{fc} is a function of the liquid density, bubble size, liquid thermal diffusivity, and pressure difference between the bulk of the liquid and the interior of the bubble. They concluded that heat transfer controls collapse when $B < 0.05$, and inertia controls collapse when $B > 10$. Both phenomena are important in the intermediate region. Wittke and Chao[31] continued this work, and concluded that under conditions where heat transfer is important, bubbles with a slip velocity relative to the liquid collapse more rapidly than similar ones without a slip velocity.

This effect is due to increased heat transfer rates. Obviously, this conclusion applies only to bubbles where heat transfer is a factor in the collapse.

A different approach to modelling heat transfer controlled collapse was taken by Canavelis[32] and Theofanous, et. al.[33] These authors introduced an evaporation or condensation coefficient, α, into their models, and found it to be very important in predicting bubble behavior. The

evaporation coefficient eliminates the assumption of saturation conditions in the bubble; consequently the Theofanous model agrees very well with experiments over a wide range of conditions.

The most recent study of thermodynamic effects on bubble collapse was made by Mitchell[34] in this laboratory. In a spherical collapse model, Mitchell included the effects of non-condensable gas; liquid and vapor thermal conductivities; and evaporation or condensation coefficient. His model, realistically, allows for the development of temperature profiles both inside and outside the bubble. From this analysis, as well as one further detailed below, Mitchell concluded three things. First, the collapse of a typical cavitation bubble (Ro=1.27mm, P_∞ = 1 atm, T_L=22°C) is an essentially adiabatic process so long as the bubble retains something like spherical symmetry. Second, if a bubble collapses to a minimum diameter and rebounds, a pressure wave, which may steepen into a shock wave, is propagated outwards. The strength of this shock wave, and therefore its capability for damaging nearby materials, is a strong function of initial vapor and gas content, evaporation coefficient, vapor and gas thermal conductivities, initial bubble size, liquid temperature, and liquid pressure. Consequently, the strength of this shock is not easily predicted. And finally, if assymmetries develop with $R/Ro > 0.25$, it is a safe assumption that the internal gas and vapor content have no substantial effect on jet formation.

By 1965 the classical Besant-Rayleigh Spherical Collapse analysis had been extended by Ivany,[35] Ivany and Hammitt,[36] and Hickling and Plesset[37] to include the effects of viscosity, surface tension, compressibility, and non-condensable gas. Compressibility was found to have the greatest effect on collapse, and the shock wave emitted on rebound was concluded to be sufficiently intense to damage weak materials but not strong ones.

Recent analyses by Khoroshev,[38] Khorovkin and Levkovskik[39], Green[40] and Shima[41] have modelled the collapse of a spherical or nearly spherical bubble adjacent to a solid surface. Three of these analyses have allowed for migration of the bubble centroid, and have shown the collapsing bubble migrates towards and strikes the wall if the initial bubble centroid-wall distance is small enough. However, as originally shown by Plesset and Mitchell[16], it is likely that asymmetric effects become substantial under these conditions, and these analyses become increasingly invalid as the collapse proceeds.

The problem of a nearly spherical bubble collapsing in a moving fluid has been further modelled by Yeh[41] and Yeh and Yang,[42] and the problem of a spherical bubble collapsing in a pressure gradient has been further investigated by Gibson[43]. Gibson defined a parameter, σ, and concluded for $|\sigma| < 10^{-2}$ the collapse is essentially spherical.

$$\sigma = R_o \frac{dP}{dZ} (P_\infty - P_{co})^{-1} \qquad 1.2$$

$\frac{dP}{dZ}$ = Pressure Gradient
P_{co} = Initial Internal Pressure
P_∞ = Far Field Pressure

It has become obvious that asymmetric effects dominate the final stages of bubble collapse near a solid surface or in pressure or velocity gradients. Naude and Ellis[44] in 1962 studied the collapse of a nonhemispherical bubble attached to a solid surface. By both a perturbation theory model and experiments utilizing spark produced bubbles, they demonstrated clearly, for the first time, the production of a high velocity liquid jet which strikes the solid surface during collapse. Naude and Ellis found small pits in the solid surface approximately where the jet impacted, and hypothesized that these pits, which were much smaller than the bubble, were due to the jet impact. They also hypothesized that, in addition to the velocity of the jet, some other factor, possibly the shape of the tip of the jet, played an important role in causing damage. A similar study of nonhemispherical attached bubbles was made by Shutler and Mesler[45] in 1964. This study concurred with Naude and Ellis concerning the shape of the collapsing bubble and jet formation, but disagreed on the damage mechanism. Shutler concluded, on the basis of an observed lack of damage in the area where the jet impinged and on the basis of the nature and disposition of damage, that damage was due to a pressure pulse emitted when the bubble collapsed to minimum

volume and rebounded. Additional conclusions were: at minimum volume the bubble assumes the shape of a torus; the bubble produced by rebound may have more capability for damage than the parent bubble; and spark produced bubbles behave similarly to bubbles produced by hydrodynamic forces. In another experimental study, Kozirev[46] took photographs which indicated that bubbles collapsing next to a surface only contracted by a factor of 1.5-3 when jet formation occurred, and the resulting jet had insufficient energy to cause damage. Kozirev hypothesized that a bubble collapses and rebounds many times in its life, and in such a series of collapses forms a cumulative jet with sufficient energy to cause damage. Gibson[43] experimentally demonstrated that the effect of a nearby compliant surface on a collapsing bubble was to cause the bubble to collapse asymmetrically, and form a jet striking away from the compliant surface.

A recent survey article by Benjamin and Ellis[47] summarized the arguments developed to support both the jet impact and shock wave mechanisms of cavitation damage. This article described additional experimental work on bubbles collapsing in a pressure gradient, and concludes the jet impact damage mechanism is predominant in cavitation damage. Subsequently, three major studies have been made and are reported below.

Mitchell,[34] in addition to his study of thermodynamic effects, constructed two dimensional incompressible viscous models for bubbles collapsing in pressure gradients, with slip velocities, and near solid surfaces. Mitchell's

model allows asymmetric behavior and, since it utilizes the marker and cell numerical technique for solution, is valid through most of the collapse. This analysis shows asymmetric collapse with jet formation in all cases and, in the case of a bubble collapsing at a distance of 1.5Ro from a solid surface, comes to the following conclusions: (1) The collapsing bubble first elongates along an axis perpendicular to the surface and then, as the segment of the bubble's wall furthest from the surface accelerates faster than other segments, involution and jet formation occur; (2) There is no buildup of pressure in the liquid between the bubble and the solid surface during the collapse, precluding this buildup (originally postulated by Rayleigh[3]) as the cause of damage. However, the bubble may give off a shock wave upon rebound.

Chapman[48] at the California Institute of Technology constructed a two dimensional, incompressible, inviscid model for bubbles collapsing both contiguous with, and 1.5 Ro from a solid surface, and solved it with a numerical technique developed by Plesset and Chapman. Additional studies were made of attached bubbles, and the following conclusions were supported: (1) The solid wall influences the bubble early in the collapse by reducing the upward motion of the segment of the bubble adjacent to the surface, and consequently the bubble becomes elongated along an axis normal to the wall. (2) As the collapse progresses the bubble acquires kinetic energy and this energy is concentrated in the segment of the wall furthest from the surface forming a jet.

(3) Once the jet is formed its velocity is fairly constant. (4) The effect of a distorted initial shape is, typically, to decrease the velocity of the resulting jet.

Kling[49] recently completed the first experimental study using ultra-high-speed cinematography of spark generated bubbles collapsing adjacent to a solid surface in a flowing liquid stream. Utilizing high speed cinematography to observe and reconstruct the bubbles, coupled with microscopic examination of the resultant damage, Kling came to the following conclusions: (1) The effect of the solid boundary is to change the collapse mechanism from a spherically symmetric to an asymmetric one. (2) Damage produced by spark generated bubble collapse is sometimes grossly asymmetric. (3) Damage produced by liquid jet impingement is symmetric only when the jet strikes normal to the surface, while damage produced by shock waves is always symmetrical. (4) A collapsing bubble has maximum potential for damage only when it does not form a jet until minimum volume is reached, and when the bubble has migrated close enough to the surface so the jet strikes it without having to penetrate a thick film of water. (5) Maximum damage potential is achieved when a bubble has an initial centroid distance in the range of 1.1 to 1.4 times the maximum bubble radius. A non-dimensionalized parameter for initial centroid distance is bo.

$$bo = \frac{do}{Ro} \qquad 1.3$$

Ro = Initial (Maximum) bubble radius

do = Corresponding centroid distance from surface.

1.3 A BRIEF SURVEY OF RESEARCH IN THE FIELD OF LIQUID IMPINGEMENT AND EROSION

As in the field of vapor bubble collapse, research into liquid impingement erosion was initially motivated by practical problems encountered in the development of technology. Erosion of turbine wheels caused by liquid drop impingement became a severe problem as Pelton Hydraulic Turbines and steam turbines driven by wet steam were developed. The first investigation of liquid impingement erosion was conducted by Worthington[50] in 1894. Other early research concerning erosion in turbines was undertaken by Honeggar[51] and Cook[52], who concluded that liquid impingement erosion was caused by local pressure pulses resulting from rapid acceleration of the liquid drops upon impact with the solid surface of the turbine blades. These pressure pulses were thought to attain a magnitude predicted by the water hammer equation (1.1). However, the use of better alloys and higher quality steam in turbines brought the impingement erosion problem under control, and research in this area was largely discontinued, until recently, when extremely large turbines with correspondingly high blade tip velocities have developed severe erosion problems in the low pressure blading. Very recently, a similar problem has

developed in the high pressure blading of turbines in nuclear plants due to the low quality steam conditions.

Research into liquid impingement erosion was reawakened in the early '50's when severe erosion was experienced on aircraft flying through rainstorms. One of the first researchers to put liquid impingement erosion on a firm scientific footing was Engel,[53,54,e.g.] who published several papers on this subject. Engel's work includes chemical mapping of the radial flow of an impacting water drop, high speed cinematography of the impact between a drop and a solid surface, and schlieren photography of an impacting drop, all to study further the radial flow occurring after impact. Additionally, Engel was the first to suggest that cavitation might occur within the body of an impacting drop as a result of reflection of the impact pressure wave as a rarefaction wave from the trailing free surface of the drop. At about the same time, Savic and Boult[55] developed a mathematical model of the flow of a low velocity drop as it impacts on a solid surface, utilizing incompressible flow theory. From this work, and work of her own, Engel[56] proposed that radial flow from the body of an impacting drop begins immediately following the impact.

In 1961 Bowden and Brunton[57] developed an apparatus for producing cylindrical liquid jets 1-2mm in diameter with velocities on the order of 700 m/s. Utilizing this apparatus in conjunction with high speed cinematography to study the impact of liquid jets on various solid surfaces, and the resultant damage, Bowden and Brunton came to several

conclusions. For impact velocities above 500 m/s a liquid mass was found to behave in a compressible manner. As a result of this a short intense compression pulse moves into the solid from the region of impact. This compression pulse produces most of the deformation found in the target with the remainder produced by shear forces generated by the radial outflow of the liquid from the point of impact. Radial outflow was thought to begin only after the impact pressure wave moved ahead of the locus of contact between the tip of the jet and the solid surface. The peak pressure generated on impact was found to closely approach the water hammer pressure, and the decay time for this peak pressure was found to be on the order of 2 μs for a liquid jet with a diameter of 3mm. The radial outflow velocity of the liquid following impact was thought to be about the same as the impact velocity for normal incidence. Several mechanisms of damage to the solid surface were outlined with the one predominant dependent on the type of surface and its finish.

The description and analysis of the damage produced by liquid impingement erosion has been the subject of many papers. Christie and Hayward[58], Caldwell[59], Smith[60], and many others have studied damage to low pressure blading in turbines, while Fyall[61], Schmitt[62], and Wahl[63], among many others, have studied damage to leading surfaces on aircraft. The main thrust of this work has been to typify the kinds of damage found in various materials and to deduce from this the mechanisms by which this damage was produced. Another area, which has been the subject of much

research, consists of attempts to predict erosion rates of prototype structures from various laboratory scale simulation devices, and to correlate the erosion rates found in simulation devices with material properties. The laboratory scale simulation devices used in these studies include: rotating arm or disc devices, which rotate a sample through falling liquid drops or jets; jet impact devices, which repeatedly impinge a high velocity liquid jet against a solid surface; and acoustic cavitation devices, which place a sample in proximity to a cavitation field in a liquid. Authors active in these areas include Thiruvengadam[64, e.g.], Hobbs[65, e.g.], Plesset[66, e.g.], Hammitt[67, e.g.], Canavelis[68, e.g.], and many others. The erosion history of a test specimen on these devices may be divided into four periods. The incubation period during which the surface may be slightly roughened but is not significantly damaged; the acceleration period during which the specimen loses mass at an accelerating rate; the steady period during which the specimen loses mass at an approximately constant rate; and the deceleration period during which the specimen loses mass at a decelerating rate. Several exceptions to this general chronology have been found, although most authors accept and use this four stage erosion model. Erosion rates over the four periods may vary by a factor of a hundred. No general correlation applicable to all materials has been found which will predict erosion rate in any of the periods from material properties. However, within homogenous groups of materials, useful correlations have been found which predict the steady erosion rate as a function of hardness, strength,

ultimate resilience, strain energy, etc.

Due to their extensive use in aircraft radomes, composite materials have been the subject of much liquid impingement erosion research. Hancox and Brunton[69] demonstrated that under repeated impacts the heterogeneous crystalline structure of metals tends to result in irregular surface deformation. Once this irregular deformation occurs, rapid erosion follows immediately. This behavior was not found in polymeric materials that have no distinct microstructure. On the basis of these results, Hancox and Brunton suggested erosion resistance of a material can be increased by reducing the size of individual elements in the material's microstructure. Composite materials have two or more discrete phases and consequently have a relatively low liquid impingement erosion resistance. Both Mok[70] and Field, Camus, and Gorham[71] have concluded the sharp stress peak caused by the compressible behavior of liquids on impact results in interlaminar failure of composite materials. Once an interlaminar failure has occurred the fracture acts as a free surface and reflects subsequent stress waves. This results in spall type fractures at the delamination and, as the cracks produced link up, severe erosion damage occurs. The erosion rate also accelerates as liquid flows between the delaminated layers. One possible means of reducing the erosion damage to composite materials is through selecting a dispersed phase which attenuates the stress waves produced on impact through a process of multiple reflection. As has been pointed out by Schmitt[72] and others, another means of

increasing the erosion resistance of composite materials is through the use of protective coatings. Field, Camus, and Gorham[71] demonstrated that, provided a protective coating is thicker than a certain critical value and the substrate-coating bond is sufficiently strong, cushioning of impact stresses occurs. The critical value of coating thickness required for protection was estimated to lie between ½ Ctp and Ctp; where C is the dilational stress wave velocity in the coating, and tp is the duration of the impact pressure pulse. A coating provides no protection if it is ruptured and removed by an impact, and this was found to occur most often at an impact angle of approximately 30^{o} from perpendicular. Brunton[73] and Wenzel and Wang[74] have discussed the cushioning effect of a stagnant water film on the impact pressures produced by liquid impingement and the consequent effect on erosion. A recent survey article by Heymann[75] discusses the relationship between impact parameters and erosion rate more completely, and a paper by Conn[76] discusses the importance of using dynamic material properties in impingement erosion rate correlations.

The most recent experimental photographic study of liquid impingement was conducted by Fyall[77]. Using a high speed cine camera to study the collision between a suspended spherical droplet and a solid protectile, Fyall concluded for a typical case that the radial outflow velocity is about three times the impingement velocity, and the duration of the first pressure pulse produced on impact is about 1.5 μ s. In another experimental photographic study, Brunton and Camus[78]

confirmed Engel's suggestion that cavitation may occur in an impacting drop as a result of reflection of the impact pressure wave from the trailing surface of the drop.

Heymann[79] developed a microscopic model of liquid impingement erosion which assumed that the eroding material was composed of layers of cells. These cells were described by a statistical distribution and the dependence of the erosion rate on the lifetime of a layer of cells was discussed. Further work in this area has been done by Engel[80], and this work has resulted in a microscopic model which is developed in terms of a typical cell. The eroded material is considered to be made up of layers which are assemblies of cells, and the lifetimes of the individual cells in each assembly are treated statistically. This model predicts the shape of the curve of volume loss, as a function of number of impacts, quite well and, with some adjustment, has been made to fit erosion data for various metals. Engel's model has shown the accumulated volume loss of a material as a function of time to be relatively independent of drop size; in an appendix, she concludes that water may be ionized appreciably during high velocity impacts.

Recently, Huang[81] in this laboratory has developed a two dimensional mathematical model of the unsteady flow resulting from the impact of a liquid drop on a non-deforming solid surface. Assuming the solid surface to be rigid, compressibility effects in the liquid predominate. The fluid is assumed to have no surface tension or viscosity, and axial symmetry is applied. Huang's model investigates the effect

of drop geometry and impact velocity on the pressures produced by impact, and the flow patterns during impact. Utilizing a compressible cell-and-marker solution technique with water as the impacting fluid, Huang came to the following conclusions: (1) The one dimensional water hammer pressure corrected with the actual shock wave velocity represents the maximum pressure generated by the normal impact of a water droplet on a rigid plane surface. (2) For the impact of a two dimensional liquid drop bounded by a free surface, the radial outflow begins essentially immediately following impact and consequently the pressure buildup is affected from the first instant of contact. (3) A spherical drop generates a lower maximum impact pressure than a right cylindrical drop impacting at the same velocity. (4) For the impact of a right cylindrical drop, the larger the drop diameter, compared to its length, the closer its impact pressure comes to the corrected water hammer pressure. The critical diameter (beyond which the effect is small) is about four times the drop's length. (5) For a given drop shape and boundary condition, the lower the impact velocity, the higher the ratio of radial outflow velocity to impact velocity. (6) Cavitation can occur in the body of a drop as a result of reflection of the impact pressure wave from the trailing surface of the drop. (7) A central cavitation bubble on the solid-liquid interface can occur when the radial outflow velocity exceeds the impact velocity and the liquid next to the interface axis is subjected to sufficient tension to form a cavity. (8) For a 2 mm. diameter spherical water drop

impacting at 300 m/s, the impact pressure reaches a maximum at 0.25 μ s after impact, and the duration of the most severe first pressure pulse is about 1.5 μs. (9) The radial pressure gradients on the impacted surface are most severe near the contacting edge of the drop and, as the impact continues, the strong radial pressure gradients remain in the vicinity of the contacting edge of the drop. The radial pressure gradients reach a peak value when the angle between the impacting spherical drop's face and the solid surface is about 12^{o}.

1.4 OBJECTIVES OF RESEARCH

It has long been hypothesized that the mechanism through which vapor bubbles generated by cavitation cause damage to a nearby rigid surface involves the impact of liquid jets, formed from collapsing bubbles, on the rigid surface. Consequently, research directed at determining the mechanism of cavitation damage includes research in the area of liquid-solid impact damage because, on the microscale, these research areas overlap. The Cavitation and Multiphase Flow Laboratory at the University of Michigan has, under the direction of Professor F. G. Hammitt, been extensively involved in both theoretical and experimental investigations of cavitation and liquid-solid impact phenomena. It was proposed to utilize the technique of photography, high speed cinematography, and holography, in conjunction with this Laboratory's facilities for producing vapor bubbles and high velocity liquid jets, in order to investigate experimentally the basic mechanisms of vapor bubble collapse, liquid-solid impact, and the

erosive damage to surfaces caused by these phenomena. Through an understanding of these mechanisms, the properties necessary for a material to resist cavitation and liquid impingement attack should become more understandable.

A series of increasingly complex experiments was designed to pursue this goal. The main thrust of these experiments was to investigate, through optical techniques, the collapse mechanism of spark generated vapor bubbles. Supporting experiments in the area of liquid-solid impact were also to be conducted. In order to train the author in the optical techniques to be used in these experiments, repetition of the work of earlier experimenters was desirable. Following is a list of experiments conducted for this purpose which overlap with previous experimental work:

(1) Cinematographic study of spark generated bubble collapse in still water;

(2) Cinematographic study of spark generated bubble collapse adjacent to a rigid surface in still water;

(3) Cinematographic study of spark generated bubble collapse adjacent to a compliant surface in both still and flowing water;

(4) Cinematographic study of spark generated bubble collapse adjacent to a rigid surface in flowing water.

The experience gained through these experiments led to the design of the following new experiments:

(5) Holographic study of spark generated bubble

collapse in still water;

(6) Cinematographic study of spark generated bubble collapse adjacent to another spark generated bubble in still water;

(7) Simultaneous two-axis cinematographic study of spark generated bubble collapse adjacent to a rigid surface in flowing water.

In order to further investigate the collision between a high velocity liquid jet and a solid surface and to quantify the susceptibility of various materials to liquid impingement damage, the following experiments were conducted:

(8) Cinematographic study of the impact of high velocity liquid jets on various target materials;

(9) Quantitative study of the susceptibility of these target materials to damage by multiple liquid impacts.

One of the main objectives of this work was to obtain data that could be compared to mathematical models of the phenomena under study and gain insight into how these models can be improved.

CHAPTER 2

SCIENTIFIC PHOTOGRAPHY AND HOLOGRAPHY

2.1 A REVIEW OF SCIENTIFIC CINEMATOGRAPHY

The need for scientific photography arises when an event being studied exceeds the temporal or spatial resolution capabilities of the human eye. A photographic record of an event may take the form of a single exposure or of a sequence of exposures, commonly called frames, separated by discrete time intervals. Sequential photography is often called cinematography and, due to the phenomenon of persistence of vision, when a cinematographic record is projected at greater than sixteen frames per second, the eye perceives continuous motion rather than a flickering series of images.

A photographic system consists of an optical system, which forms an image of the event being studied and controls exposure, and a photosensitive material which makes a record of the image. Cine cameras can be classified by the type of optical system they utilize and the type of photosensitive material employed. A streak camera utilizes an optical system which makes a one dimensional record of an event. That is, its photosensitive material looks at the event through a narrow slit with a continuously open shutter. This type of camera is usually used to follow the progress of a discontinuity, typically a shock wave, along a line. As opposed to a streak camera, a cine or framing camera utilizes an optical system that produces a sequence of two dimensional images separated in time. The optical

system required to do this consists of an element or series of elements to produce the images, and a light control or shuttering mechanism to separate the images temporally. A further distinction involves the type of photosensitive material used to record the image. This material may be either a photosensitive emulsion or a photo cathode. Cameras employing various types of photo cathodes are less well known and are usually called electronic image conversion cameras.

Some definitive parameters of a cine camera system are:

1. The framing rate, which is the temporal interval between frames, usually given in units of frames per second;
2. The exposure time, which is the amount of time the shutter is open while exposing a single frame, usually given in units of seconds;
3. The magnification, which is the dimensionless ratio of the size of the primary image in the camera to the size of the object;
4. The resolution, which is the smallest object that will form a record on the recording medium. Resolution is conventionally defined by the number of dark lines separated by equal width light spaces per millimeter that can be clearly distinguished on the recording medium, i.e. lines per millimeter;
5. The depth of field, which is the distance over which there is no significant loss of resolution for a given magnification;

6. The total number of frames the system is capable of exposing.

Unfortunately, for a real cine camera system, these parameters are not totally independent and there are several things that must be considered when deciding whether an available camera system is suitable for recording a given event.

The writing time, W, of a cine camera is the time interval the camera can record at a given framing rate and is given as:

$$W = SN \qquad 2.1$$

S = Framing rate, (fr/sec)

N = Number of frames/sequence

Since it is the purpose of high speed cine photography to examine a segment of time too small to be resolved by the human eye, the minimum framing rate required to capture an event is fixed by the time scale of the event. This gives rise to one of the most bothersome realities of high speed photography, insufficient writing time to capture the whole of an event at a framing rate sufficient to capture its critical period. One way out of this dilemma with a repeatable event is to study the whole of the event with a low framing rate and then zero in on the critical phase(s) with a much higher framing rate. Often this procedure requires two camera systems as most high speed cine camera systems operate over a relatively narrow range of framing rate.

In most high speed cine camera systems the exposure time is fixed within narrow limits by the selection of a framing rate. Blur, due to object motion during

the exposure period, is given as:

$$B_1 = te\ m\ Vo_B \sin \Theta_{oB} \qquad 2.2$$

B_1 = Blur, (mm)

te = Exposure time, (sec)

m = Magnification

Vo_B = Object velocity, (mm/sec)

ΘoB = Angle between velocity vector and optical system axis.

In order to utilize a camera system to its fullest extent the amount of blur should be less than or equal to the reciprocal of the resolution. For optimum results, it is obviously desirable to set up the camera system so that the smallest critical dimension of the event being studied is several times the resolution of the camera system. This consideration fixes the required magnification of the system and thus, for a given camera system, there are no independent variables in Eq. 2.2. Blur considerations often determine the suitability of a camera system for recording an event.

Since the photosensitive material in a camera system requires a certain minimum exposure to produce a satisfactory record and exposure is the product of light intensity and exposure time, once the exposure time for a camera-event system has been determined the problems associated with lighting must be considered. The light intensity at the film plane in a camera system is a function of the following three parameters:

1. The light economy of the camera's optical system,
2. The light economy of the illumination system,

3. The intensity of the light source.

Light economy may be qualitatively defined as the amount of light transmitted by the system for the desired purpose compared to the amount of light entering the system.

For a camera system the light economy is fixed by the optical design and is quantitatively defined as the effective aperture, T, where:

$$T = \left(\frac{\text{Object brightness}}{\text{Image brightness}}\right)^{\frac{1}{2}} \qquad 2.3$$

The effective aperture is a function of the luminous efficiency of the camera's internal design and the relative aperture, f, defined as:

$$f = \frac{F_L}{D_L} \qquad 2.4$$

F_L = Objective lens focal length, (mm)

D_L = Objective lens clear aperture diameter, (mm).

The relationship between effective aperture and relative aperture is:

$$T = f\eta$$

η = Camera's internal luminous efficiency.

In most cameras the relative aperture is a variable and, although for maximum light economy it should be minimized, its minimum value is dictated by depth of field considerations. It is desirable to have sufficient depth of field to insure maximum resolution across the important part(s) of the object being photographically examined. The depth of field, U, of a camera's optical system for objects close to the objective lens is:

$$U = \frac{2(m+1)f\ DC}{m^2} \qquad 2.6$$

Dc = Diameter of the circle of confusion, (mm).

To utilize a camera system to its maximum spatial resolution it is necessary to set the circle of confusion equal to the reciprocal of the resolution. Often with marginally sufficient lighting and very short exposure times a trade off between relative aperture and depth of field must be made to insure adequate exposure.

Photographic lighting systems may be classified as front lighting systems, where the light source is on the same side of the object as the camera, and back lighting systems, where the light source is on the opposite side of the object from the camera. Further classification may be made on the basis of whether the light source is diffuse, with light emerging from the source in all directions, or collimated, with light emerging from the source as a beam with more or less parallel rays. When studying non-luminous events with a photographic system the lighting system economy of a front lighting system depends upon the reflectivity of the object and background, with highly reflective objects and backgrounds of suitable contrast giving acceptable efficiencies. On the other hand, a back lighting system depends on the transmittance of the object and background, with highly transparent backgrounds and objects of suitable contrast giving acceptable efficiencies. In this study the objects (vapor bubbles, water jets, etc.) are only slightly reflective so

in order to achieve acceptable lighting system efficiencies a back lighting system had to be used. With sources of equal light output a collimated back light system is more economical with light than a diffuse back light system since the collimated beam is uniformly directed into the camera's optical system while only a small portion of the light from a diffuse system reaches it. However, these two lighting systems produce different records and, consequently, one may be favored for the study of a given event. With collimated back light anything that interrupts a ray of light or diffracts a ray out of the ray bundle will not expose the recording medium. Therefore, the majority of translucent objects that can be photographically examined appear as silhouettes on the record. Additionally, density gradients oblique to the optical axis of the system will, if they are of sufficient magnitude and the light source is well collimated, diffract portions of the ray bundle and leave a record. For obvious reasons a photographic recording system utilizing well collimated back lighting is called a shadowgraph system and it will record the passage of density gradients produced by strong shocks or other phenomena as well as physical objects. Diffuse backlight, on the other hand, illuminates the object with rays in all forward directions from a large planar source. The resulting photographic record is largely a result of the object's opacity with translucent objects showing a great deal of surface, and some internal, detail.

High speed cine photography, even with the most economical lighting and optical systems, requires a light source which has a duration at least as long as the writing time of the camera and which has extreme intensity due to the short exposure time available. Most high intensity light sources that fulfill these requirements are of the arc discharge type with high potential electrical energy stored in a capacitor bank or delay line and then discharged in the form of an arc. As the state of the art progressed it was found that an arc in an enclosed tube through xenon gas produced light of wavelengths more suitable for exposing modern photographic emulsions and produced it more efficiently. This type of light source, with appropriate associated electronic circuitry, provides in theory precise control over the initiation, intensity, and duration of the output light pulse necessary for high speed cinematography.

The film utilized in high speed cinematographic systems is common photographic film, although some cameras require film with a special, high tensile strength base. All film consists of a base material coated with an emulsion made up of silver bromide and sensitizers. When light strikes this emulsion the silver bromide dissociates, and with proper development a negative record is made with opaque metallic silver left on the base to indicate the presence of light. The film is sensitized so that the image optical density is directly proportional to a constant plus the logarithm of the exposure. This is how the human eye responds to light, with a certain minimum light intensity necessary to see at all,

and perceived brightness proportional to the logarithm of the intensity. The exposure necessary to produce a usable image is a measure of a film's sensitivity or speed, while the slope of a plot of image density versus the logarithm of exposure is the contrast index of the film. A film requiring little light for proper exposure is a "fast" film, while the difference between the exposure required for maximum usable density and the exposure required for minimum usable density is the latitude of the film. A doubling or halving of exposure is called an exposure difference of one stop. Films as well as cameras have a maximum achievable resolution and for optimum results this should obviously be equal to or greater than the resolution of the camera system in which it is used. Film speed, contrast index, latitude, and resolution may all be affected by the choice of development process. However, a process that has a favorable effect on film speed, i.e. one that increases it, always has an unfavorable effect on film resolution. Since the resolution of some high speed cine camera systems approaches that of modern high speed photographic emulsions, great care must be exercised in selecting a film/developing process combination. Additionally, this combination must have a contrast index appropriate to the contrast range of the object being studied in combination with the lighting system utilized. Finally, film is subject to dimensional changes during processing and to minimize the effect of this on measurements made of the object from the film, strict adherence to manufacturers' processing conditions is necessary. The inclusion of a measurement standard in the

object field minimizes this problem as true magnification can be determined directly. Measurements of the object can be made either from a projected image of the photographic negative or from positive prints made from the negative.

2.2 PHOTOGRAPHIC SYSTEMS UTILIZED IN THIS STUDY

Ideally, it would have been desirable to utilize a high speed cine camera system capable of taking a thousand frames per sequence at a rate of a million frames per second in this study. Additionally, this ideal camera system should have continuous access in time. A continuous access camera system is one which is available for recording at any time and which doesn't require synchronization of the event with the camera. No camera system exists which meets the first of these requirements. Since the events to be recorded in this study were thought to be largely repeatable, it was decided to adopt the technique of utilizing a camera with a relatively low framing rate to conduct preliminary studies and then, utilizing the results from these preliminary studies, to conduct studies of the critical phase(s) of these events with an available high speed camera system. Many of the events to be recorded, however, necessitated that the requirement of continuous access be realized.

Of the many high speed camera systems available at the University of Michigan it was decided to pick the two that, while fulfilling the requirements mentioned in the previous paragraph, possessed the highest spatial resolution. The following is a discussion of the high speed cine camera systems utilized in this study along with a discussion of

other photorecording equipment used.

2.2a: BECKMAN AND WHITLEY DYNAFAX CAMERA AND U-M CUSTOM LIGHT SOURCE

The Beckman and Whitely Dynafax Camera is one of the workhorses of the high speed cinematographer. First developed in 1950, it has gone through many model changes and is still produced. *

The Dynafax Model utilized in this study produces a maximum of 224 sixteen-millimeter standard format frames at a maximum rate of 26,000 frames/sec. The camera uses a short strip of 35 mm. film with the frames arranged in two staggered rows; temporally adjacent frames go into alternate rows. The film is held inside a rotating drum, of approximately 300 mm. inside diameter, with image transport and shuttering provided by an arrangement of diamond shaped stops and relay mirrors coupled with a rotating prism differentially geared to the drum. Exposure time is a function of framing rate and stop size with variations available over a range of four. Decreased stop size, which results in decreased exposure time, also results in significant loss of resolution. Exposure times on the order of one microsecond are available with the smallest stops installed at near maximum framing rates. The objective lens of this camera is a standard 16 mm., C-mount type with extension tubes used to decrease object-primary image plane distance below the minimum the focusing mount of the lens can achieve. Due to

*In 1971 the Beckman and Whitley Co. was sold by its parent company, Technical Operations, to The Cordin Co., Salt Lake City, Utah.

the shuttering arrangement of the Dynafax Camera it has very poor internal light efficiency. Consequently, it requires a very intense light source with a nearly square wave output of precisely controlled duration to photograph non-luminous events. This is because the capping shutter of the camera is quite slow and the light source must turn off after the writing time to prevent multiple exposure of the film. Electronics shop technicians at the Michigan Memorial Phoenix Project have constructed a light source specifically for operation with this camera. It is of the xenon arc type utilizing a Kemlite type MW-5 flash tube with a maximum energy input of 1000 joules at 800 volts. Energy is stored in a capacitor-inductor pulse forming network and flash duration is controlled by dumping the remaining stored energy through a shunt after a flash duration adjutable between 0.8 and 12 milliseconds. The light output of this device approaches a square wave and, at maximum framing rate, about 200 of the possible 224 frames in the Dynafax Camera are usable without serious under or double exposure. Additionally, this device puts out enough light to photograph at a magnification of approximately 0.1 utilizing a 135 mm., f/2.8 camera objective; Kodak Tri-X film normally processed to a film speed of ASA 400; and either collimated or diffuse back light. This combination resulted in a resolution of 20-30 lines/mm on the film.

Operation of this Dynafax Camera System is quite simple. The camera is set up and focused on the object by means of a reflex viewer. The nature of the event to be

recorded determines the hookup of the light source but it must be arranged so the following sequence occurs. First, the capping shutter of the camera must open, which may be done either manually or by means of a solenoid arrangement built into the camera. Under normal ambient light the capping shutter may be left open for several seconds without seriously fogging the film. Second, when the event to be recorded starts the light source must be turned on. And, finally, after an interval corresponding to the writing time of the camera, the light source must turn itself off and the capping shutter must close. The framing rate of the Dynafax System is adjusted by means of a variable autoformer built into the camera. It is monitored by either a tachometer built into the camera or, more accurately, by means of an external electronic counter hooked to the camera. Prior to exposure the film must be loaded into the camera and, after exposure, the film must be unloaded and processed. Loading and unloading are accomplished by means of an ingenious light tight casette which, when locked in the camera, is supposed to load film into the camera's revolving drum or retrieve it at the turn of a crank. Emperical experience, however, demonstrated this system functions only sporadically unless the unperforated 35 mm. film used has reverse curl put on it. 35 mm. unperforated film is normally supplied in 100 ft. lengths wound on standard #10 spools with the emulsion side of the film facing the center of the spool. This is called inside wind and puts a set or curl in the film. Winding the film onto another spool with the emulsion side

out, so called outside wind, and storing it for several days, puts a reverse curl on the film. The film may then be cut into lengths and loaded into Dynafax casettes with confidence that valuable experimental time won't be spent cleaning shredded film from the camera's interior. Little more needs be said about the light source utilized in this camera system due to its prototype nature. However, such devices have enormous potential for electrocution and, even when designed by the most qualified engineers, often seem to operate in a contrarational manner.

2.2b BECKMAN AND WHITLEY MODEL 330 CAMERA AND CORDIN MODEL 450 LIGHT SOURCE

At the time of writing this combination represented the state of the art in high speed cinematography system design. The camera is a high speed continuous access type capable of exposing 80 frames at a maximum rate of 2×10^6 frames/sec., while simultaneously making a streak record of a chosen portion of the event on a separate strip of film. This streak capability was not thought desirable for this study and, to prevent loss of a strip of the framing image to the streak section of the camera, it was disabled by replacing the optical element in the camera, that functioned to split off the streak image, with a similar optical element that functioned to reflect a whole image to the framing section. The Model 330 Camera operates with the film held stationary and image transport provided by means of a rotating mirror. The image formed by the camera's objective lens is transported by a complex primary optical

system to the rotating mirror which in turn sweeps it across a secondary optical system. This secondary optical system consists of a bank of spherically figured rectangular mirrors with each mirror used to form the image for one frame. The geometry of this arrangement causes a series of 80-16 mm. by 24 mm. images to form on a strip of 35 mm. film held in a circular track of about one meter in diameter. The internal optical arrangement of the camera also magnifies the image formed by the objective lens by a factor of two. Exposure time is a function of framing rate and stop size with the basic exposure time approximately equal to the reciprocal of the framing rate. This basic exposure time can be decreased by factors of 1/2 or 1/4 by changing the stops in the optical system; decreased exposure time is gained at the cost of lost resolution. The Model 330 Camera is loaded with a 100 ft. #10 spool of inside wound perforated 35 mm. film. This is sufficient for 12-15 camera runs with exposed film being removed from the camera in small casettes.

The Cordin Model 450 Light Source is designed for operation with the Beckman and Whitley Model 330 Camera. It is of the xenon arc type and operates on the same principle as the light source previously described. The light output pulse of this unit approximates a square wave and has a duration adjustable between 40 and 600 microseconds. Light output is sufficient to photograph at an overall magnification of 0.1, utilizing diffuse back light, 175 mm., f/2.8 camera objective, and Kodak Tri-X film normally processed to

a film speed of ASA 400. This combination resulted in a resolution of 15-20 lines/mm. on the film.

Operation of this camera system closely parallels that of the Dynafax System. The principal difference is that the Model 330 Camera's framing rate is set by fixing the rotation rate of the camera's rotating mirror. The rotating mirror is coupled to a gas driven turbine. The gas used to drive the turbine is compressed nitrogen for framing rates up to 10^6 frames/second and compressed helium for framing rates up to the maximum of 2×10^6 frames/second. At the maximum framing rate the turbine mirror combination rotates at 8,333 revolutions/second and the rotational speed is controlled through control of the inlet pressure of the turbine's drive gas. This system does not permit precise control of the camera's framing rate but the exact framing rate of any sequence is known by means of an electronic counter built into the camera's electro-pneumatic control unit.

The Model 330 Camera in the possession of the University of Michigan is one of the first built by Beckman and Whitley. Unfortunately, it has a major design flaw; the mirror mounts for the eighty secondary mirrors in the camera don't hold the mirrors with sufficient rigidity. Every time the camera is moved some of the mirrors have to be realigned. Hopefully, this flaw has been corrected in later versions of this camera. The Model 450 Light Source also proved disappointingly unreliable and required a great deal of maintenance.

2.2c: MISCELLANEOUS PHOTOGRAPHIC AND OPTICAL EQUIPMENT

Many types of photographic and optical equipment of a familiar nature were utilized in this study. Primary among these were:

1. A 35 mm. Pentax Camera System consisting of camera bodies, numerous lenses, a macrophotographic bellows, a microscope adaptor, and many other accessories. The extreme versatility of this system made it useful wherever single exposures were required.
2. A 4 in. by 5 in. view camera equipped with both polaroid and sheet film backs.
3. A Polaroid Oscilloscope Camera.
4. A Bausch and Lomb Metallograph. This was used for minute examination of small objects.
5. A Unitron Metallurgical Microscope.
6. A Spectra-Physics Model 132 Ne-He Laser. This was used many times both as a light source and as an optical alignment tool and often simplified complex alignment problems.

2.3 A BRIEF REVIEW OF HOLOGRAPHY

Holography is an image reconstruction technique operating on an entirely different principle than photography. A photographic plate responds only to the intensity of incident light. In holography the object is illuminated with light from a mode locked laser producing coherent light. Coherent light has all the light emitted from the source at any instant in time, in phase. Coherent illumination makes

it possible to record both intensity and phase shift in the light incident on the plate from the image in a holographic set-up. This is done by splitting the output pulse from the laser into two beams, one of which strikes the plate directly and is called the reference beam and the other which illuminates the object before striking the plate and is called the object beam. When the combination of the reference and object beams is recorded in the extremely thin emulsion on the holographic plate the record is a diffraction pattern resulting from the constructive and destructive interference of the two beams. When this diffraction pattern is illuminated with coherent light incident at the same angle as the original reference beam, an exact image of the original scene is formed. The result is as if the original scene were being viewed through a window the size of the hologram at the instant of time when exposure occurred. This has many advantages over photography, three of which are: unlimited depth of field; preservation of all three dimensions of the object; and extremely short exposure time. The image reconstructed from a hologram may be photographed, with the result being a two dimensional slice through the image. In theory, cine holography should be possible using only one plate and varying the incidence angle of the reference beam between exposures. However, the state of the art has not progressed this far.

2.4 THE UNIVERSITY OF MICHIGAN RADAR AND OPTICS LABORATORY HOLOGRAPHIC FACILITY

The Radar and Optics Laboratory at the University of Michigan under the direction of Dr. Emmet Leith, one of the pioneers of modern holography, has numerous facilities for holographic experimentation. Of these, one was thought useful for a feasibility study in the area of holographic investigation of vapor bubble collapse. This facility consisted of a large optical bench, a pulsed ruby laser, a low power continuous output alignment laser, and all the optical paraphernalia necessary to make holograms. The pulsed laser had output sufficient to expose 4 in. by 5 in. holographic plates with an exposure time on the order of 100 nanoseconds. Only a single exposure was possible on each plate and diffuse back lighting of the object was used. Further details of this investigation are contained in sections 4.3 and 5.4.

CHAPTER 3

EXPERIMENTAL EQUIPMENT

3.1 EXPERIMENTAL EQUIPMENT USED IN STUDY OF VAPOR BUBBLE COLLAPSE

Photographic studies of the collapse of vapor bubbles in water require a means of maintaining the fluid environment in the appropriate condition and a means of generating the vapor bubbles in a location where they may be photographed. The University of Michigan Cavitation and Multiphase Flow Laboratory is equipped specifically for studies in the field of vapor bubble birth, growth, and collapse. Section 3.1 is devoted to discussion of the various items of equipment, other than photographic, used in this study of vapor bubble collapse.

3.1a VAPOR BUBBLE GENERATOR

An electric arc used for the underwater generation of vapor bubbles should have precisely controllable initiation and discharge times. It was decided to use electronic circuitry similar to that used by Kling[49] to form the high voltage pulse which produces the arc. Figure 3.1 is a schematic drawing of the bubble generator circuitry and the assembled unit is shown in Figure 3.2. A high voltage power supply is used to charge a capacitor, and the charged capacitor is then switched across the bubble forming arc electrodes by means of a switching arc. The switching arc consists of a pair of electrodes sufficiently far apart to hold off the applied voltage and another electrode mounted coaxially inside one of the switching electrodes. When a low energy, high

voltage pulse is applied to the coaxial electrode, the air in the vicinity of the electrode is sufficiently ionized to cause the switching electrodes to arc over and thus act as a switch. The low energy pulse is provided by discharging a capacitor charged to a moderate voltage across the primary of a step up transformer by means of a switching thyristor. The switching thyristor and consequently the bubble forming arc is triggered by a low voltage control pulse. To insure that the bubble forming arc is of brief duration, a damping resistor is incorporated in series with it so that the arc circuit discharges in the first half cycle. The main problem associated with this type of circuit is an uncertainty, or "jitter", in the time period between the application of the control pulse and the initiation of the switching arc. This uncertainty is a function of the condition of the atmosphere around the switching electrodes and the time required to produce the initiation pulse. By careful design and selection of components the jitter time was reduced to the order of a microsecond, an acceptable amount for the purpose intended. Section 5.3 discusses the results of a study undertaken to characterize the performance of this bubble generator.

3.1b STATIC FLUID CHAMBER

The principle design parameters for a containment vessel to be used in a photographic study of spark initiated vapor bubble collapse are: sufficient volume to minimize unwanted surface effects; transparent and distortion free viewing ports which are sufficiently large and so oriented as to give the required clear aperture; a means of precisely

positioning the arc electrodes; watertight integrity and sufficient strength if it is to be used as a pressure vessel; and convenient access to its interior. The decision was made to conduct all the static bubble studies under ambient atmospheric conditions since this greatly simplified vessel design and there was no clear reason to do otherwise. Chamber size was set at 150 mm. width, 150 mm. length, with a fluid depth of 200 mm. The resulting minimum bubble chamber cross sectional dimension to maximum bubble radius ratio was approximately ten for all the bubbles studied in this chamber. This was believed more than sufficient to eliminate unwanted bubble-surface interactions. Figure 3.3 is a photograph of the static fluid vessel. Construction is of glued plexiglas with cemented in glass windows. A top fits on the vessel and supports the electrode holding structure. Two electrode holders were fabricated, one with a single spark gap and one with two spark gaps connected in series and in close proximity to each other. These electrode holders are pictured in Figure 3.4. The electrodes used were constructed of stainless steel music wire ground with one end conically pointed and the other end hemispherical. These electrodes had a useful life of about 100 arc cycles before they had to be repointed.

3.1c HIGH SPEED WATER TUNNEL

The high speed water tunnel, designed and housed in the Cavitation and Multiphase Flow Laboratory of the University of Michigan, has been described in research reports (49,82). This facility was used to provide fluid flow through the

experimental section where the bubbles were generated. The high speed water tunnel is a closed loop system consisting, in essence, of a variable speed centrifugal pump, a high pressure receiver, an extremely versatile fluid distribution and support framing system, an experimental section, a closed low pressure sump, and a surge tank. The loop may be pressurized by applying gas pressure to the partially filled surge tank. Heat exchangers are incorporated to remove pump work, thus controlling fluid temperature, and a bypass loop feeding through a vacuum deaerator is incorporated to control fluid air content. The loop is well instrumented and, by manipulation of pump speed, surge tank pressure, bypass flow, etc., the fluid environment in the test section can be stabilized at the desired condition. Fluid flow rate is monitored by measuring the pressure differential across a calibrated orifice plate; pressures are measured with pressure taps and Heise gauges; and fluid air content is monitored by withdrawing samples and measuring the air content with a modified Van Slyke blood gas apparatus. Figure 3.5 is a schematic drawing of the high speed water tunnel.

3.1d TWO-DIMENSIONAL VENTURI

Since it is desirable to minimize frictional losses in the water tunnel, the piping is much larger in cross sectional area than the flow channel in the experimental section. The removable experimental section, therefore, takes the form of a venturi and must be properly designed if the working part of the venturi is to have a flat fluid velocity profile with no separated flow. The working part of the

venturi must also have sufficient cross sectional area to minimize unwanted bubble-surface interactions, transparent and distortion free viewing ports which are sufficiently large and so oriented as to give the required clear aperture, a means of precisely positioning the electrodes, watertight integrity, and strength sufficient to withstand the operating pressure. Figure 3.6 is a drawing of a venturi utilized by Kling[49] in his study of vapor bubble collapse. This venturi is constructed of bolted aluminum plates and its working section is in the form of a channel with two straight sides and two sides which diverge at an included angle of 7^{o}. This diverging channel is split into two channels by a wedge with a 7^{o} tip angle. The windows over the working section are constructed of clamped-in plexiglass, and the electrodes are inserted into holes drilled in one of the plexiglass plates. The electrodes are fabricated from stainless steel music wire, sealed into position with silicone rubber, and ground to streamlined shape with a hand grinder. Figure 3.7 is a photograph of the complete venturi assembled into the high speed water tunnel.

Kling studied the collapse of bubbles approximately 2.5 mm. in radius flowing in one of the split channels of his venturi. The cross section of this channel is 12.7 mm. wide by 12.7 mm. deep. This results in a minimum cross section dimension to maximum bubble radius ratio of 5.1. Kling also made a study of the axial pressure profile in the working section of his venturi. Under typical working conditions there was an axial pressure gradient of approximately 0.16

Atm/cm in the working channel around the area of bubble collapse. The Reynold's number based on the minimum channel cross section dimension of 12.7 mm. under these conditions is 1.9×10^5.

3.1e TWO-OPTICAL-AXIS VENTURI

To permit photography of a collapsing vapor bubble from two mutually perpendicular axes which define a plane perpendicular to the fluid flow direction, a new venturi test section for the water tunnel was designed and fabricated. Figure 3.8 is a schematic drawing of the two-optical-axis venturi. Figures 3.9 and 3.10 are photographs of the venturi in assembled and disassembled condition. The body of the venturi and the window holders are machined from aluminum bar stock. Windows were fastened to the window holders with silicone rubber. Windows could be easily changed by removing the old window and cementing a new one to the window holder. Windows on the sides of the venturi away from the collapsing bubble were 6 mm. thick optical glass circles; the window on the side of the venturi next to the collapsing bubble was changed to vary the experimental design. The windows used in each experiment are described in Chapter 4. Experience showed that the 76 mm. diameter optical glass windows fractured at a loading of about 10 atmospheres. Electrode holders were fabricated of plexiglass and sealed into the venturi body with silicone rubber. Electrodes were cut from stainless steel music wire and bent to the desired shape; they were then installed in the split venturi and streamlined with a hand grinder. No electrode failures were

experienced. The halves of the venturi assembly were sealed with a thin film of silicone rubber. The window holders were O-ring sealed. No leakage problems were encountered.

Typically, the bubbles studied in the two optical axis venturi had a maximum radius of 3 mm. The cross section of the flow channel was 52 mm. wide by 18 mm. deep. This results in a minimum cross section dimension to maximum bubble radius ratio of 6. Pressure taps are located in the working section of the venturi as illustrated in Figure 3.11. During typical experimental runs the pressure in the vicinity of bubble collapse is estimated to be 2.06 Atm, and the axial pressure gradient is estimated to be 0.8 Atm/m. The Reynolds number in the throat of the venturi, based on the minimum throat cross section dimension of 18 mm., during typical experimental runs was calculated to be 3.2×10^5.

3.2 EXPERIMENTAL EQUIPMENT USED IN STUDY OF WATER JET IMPACT.

Experimental studies of water jet impact require an apparatus for producing the water jets and a target material upon which the jets are impacted. As a Master's Thesis Project the author developed a device which reliably and repeatably projects small diameter jets of water. The author's report on the design, development and testing of this water jet gun is Reference 83. Section 3.2 is devoted to discussion of the apparatus and materials used in this study of jet impact.

3.2a WATER JET GUN

Figure 3.12 is a schematic drawing of the jet gun. A conical chamber formed in a steel plate is backed by a

relatively thick steel diaphragm. In operation, the chamber is partially filled with water and the diaphragm is subsequently struck by a steel bolt propelled by a spring. Upon striking the diaphragm the bolt transfers a portion of its momentum to the diaphragm which, in turn, transfers part of its momentum to the water in the chamber. This causes part of the water to be expelled from the orifice in the form of a slender, high velocity jet. The shape and velocity of the jet are affected by many factors. Primary among these are chamber geometry, bolt geometry, diaphragm material and thickness, bolt velocity, and the position of the fluid meniscus in the chamber. By manipulating these factors the jet gun's performance was optimized to the point where it is now used to test material specimens for repeated water impact erosion resistance[84]. The jet gun has been found to produce jets of reproducible shape with a mean tip velocity variable between 200 and 500 m/s at the discretion of the operator. When set up to produce jets of a particular mean velocity, the distribution of individual velocities around that mean has a standard deviation on the order of 2%. When set up for repeated impact testing the jet gun is used in automated form, as pictured in Figure 3.13. When used as a device to produce water jets for photographic study the jet gun is manually operated with a solenoid trigger arrangement, as pictured in Figure 3.14.

3.2b TARGET MATERIALS

The materials chosen to be used as target materials in this study of water jet impact can be classed into three

groups; rigid, flexible, and compliant coatings. Table 3.1 lists the actual materials and their physical properties. Target samples for the jet gun take the form of squares 32 mm. on a side. The sample holder of the jet gun can be adjusted to compensate for materials of different thickness. The metal and plastic samples were sawn from 6 mm. thick sheet stock. The rubber samples were fabricated by bonding a 0.8 mm. thick sheet of the rubber to a 6 mm. thick stainless steel substrate; the rubber samples can be considered as coatings on a rigid substrate. These materials were chosen to represent typical materials which, in application, are subject to erosion from water jet impact.

3.3 MISCELLANEOUS EQUIPMENT

Several items of equipment were fabricated for the purposes of this study. Two of the most used are discussed in this section along with some items of stock equipment.

3.3a PHOTODIODE DETECTOR

The photodiode detector was designed to monitor a beam of light, typically from the Spectra Physics Laser, and give off an electrical pulse when the beam of light was interrupted. Figure 3.15 is a photograph of the unit with the cover removed and Figure 3.16 is an electronic schematic of it. To detect the incident light beam a E.G.G.* type SGD-100A photodiode was used. This was chosen because of its fast response time, typically less than a microsecond. The photodiode detector survived much abuse and always operated reliably.

*E.G.G. is Edgerton, Gemerhausen and Grier, Inc.

3.3b PHOTOELECTRIC VELOCITY SENSOR

The photoelectric velocity sensor, pictured in Figure 3.17, was designed to provide a convenient means of monitoring the velocity of small objects. It consists of a pair of light sources, lenses which shape the light beams, and an E.G.G. SGD-100A photodiode wired into a circuit like that pictured in Figure 3.16. When connected to an oscilloscope, the device allows measurement of the time interval between interruption of the two light beams by an object. Object velocity is then computed from this time interval and the distance between the two light beams. The photoelectric velocity sensor was used to measure the velocity of solid and semitransparent objects travelling between 10 and 1000 m/s. Accuracy of measurement was limited by inaccuracies in the scope sweep circuits and was estimated to be within $\pm 2\%$ of the true velocity.

3.3c STOCK EQUIPMENT

Following is an annotated list of some items of off-the-shelf equipment used in this study:

1. Beckman & Whitley Model 100 electronic delay generator. This device provides an output pulse a preset time interval after the input pulse and is used to control event sequence.

2. Tektronix Model 551 oscilloscope. Used to monitor functioning of electronic equipment.

Material	Material Group	Tensile Strength (psi)	Elongation (%)	Density (g/cm^3)	Hardness	Hardness Scale
Aluminum	Rigid	13,000	45	2.71	22	Brinell (50 kg) (1/8 Ball)
EPON 828	Flexible			1.60	99.5	Shore A
Plexiglass	Flexible	10,500	4	1.19	99.5	Shore A
Rubber A	Coating	4,200	740	0.976	36	Shore A
Rubber B	Coating	3,000	900	1.215	75-80	Shore A

Table 3.1 Impact Target Specimens

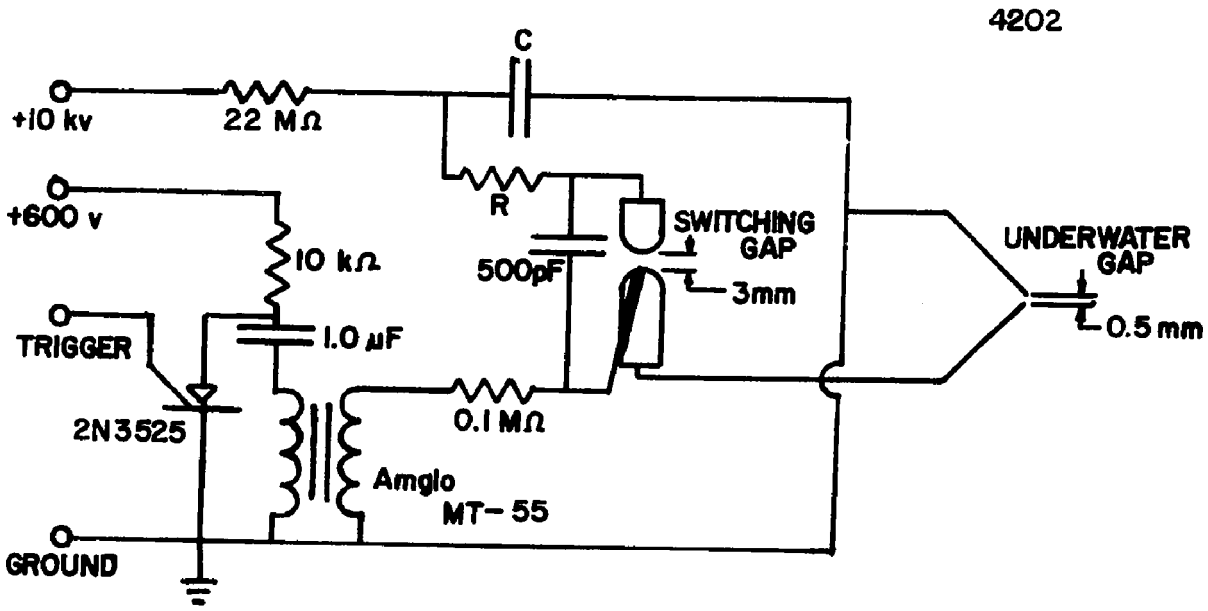


Figure 3.1 Schematic of Bubble Generator

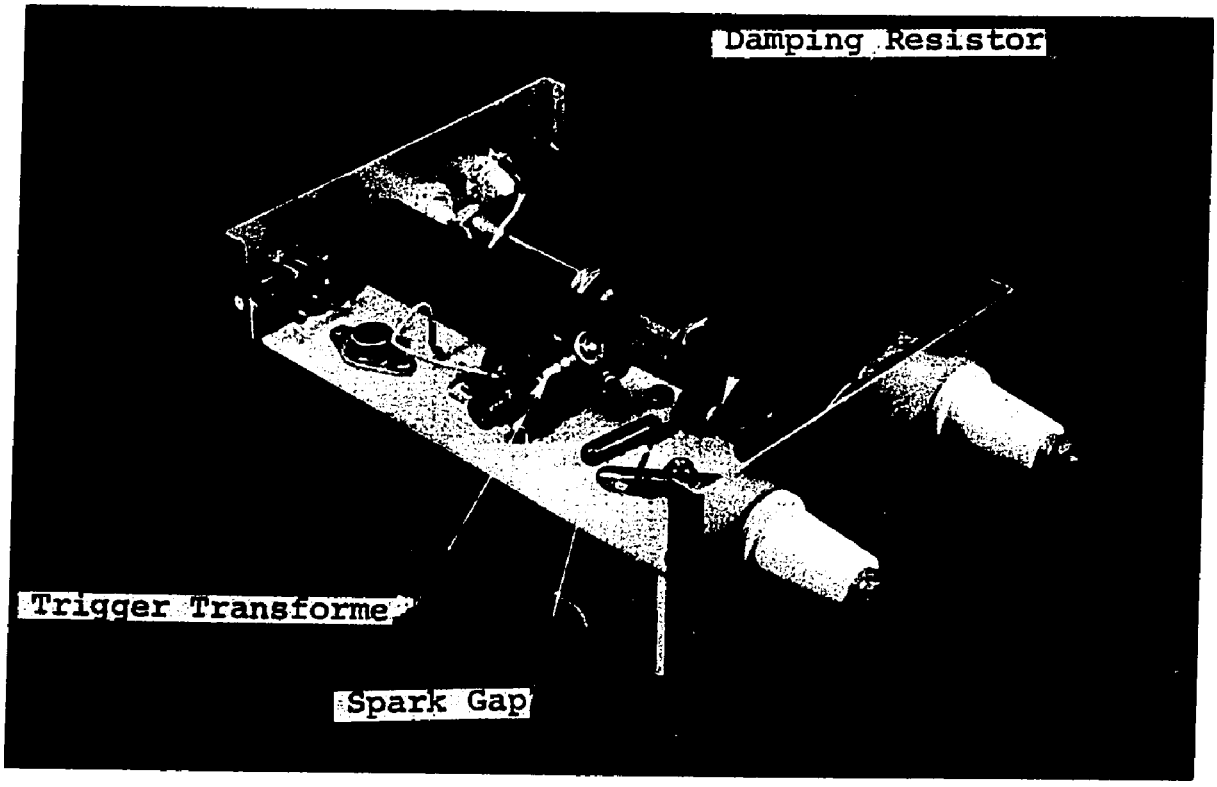
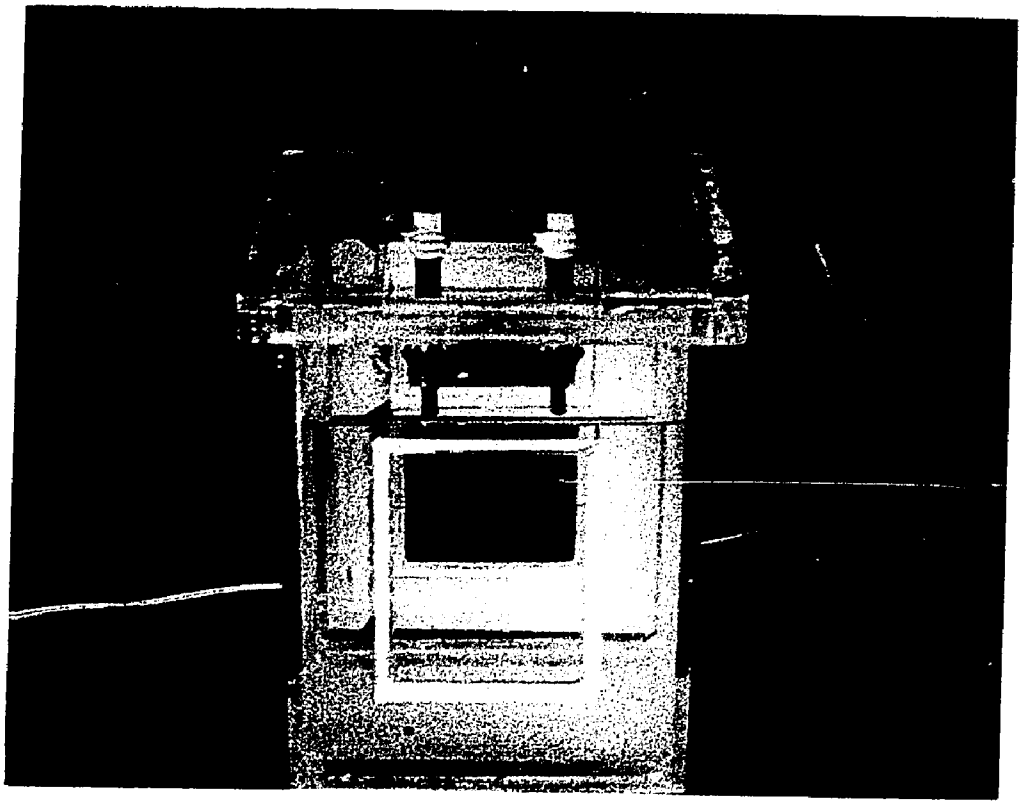
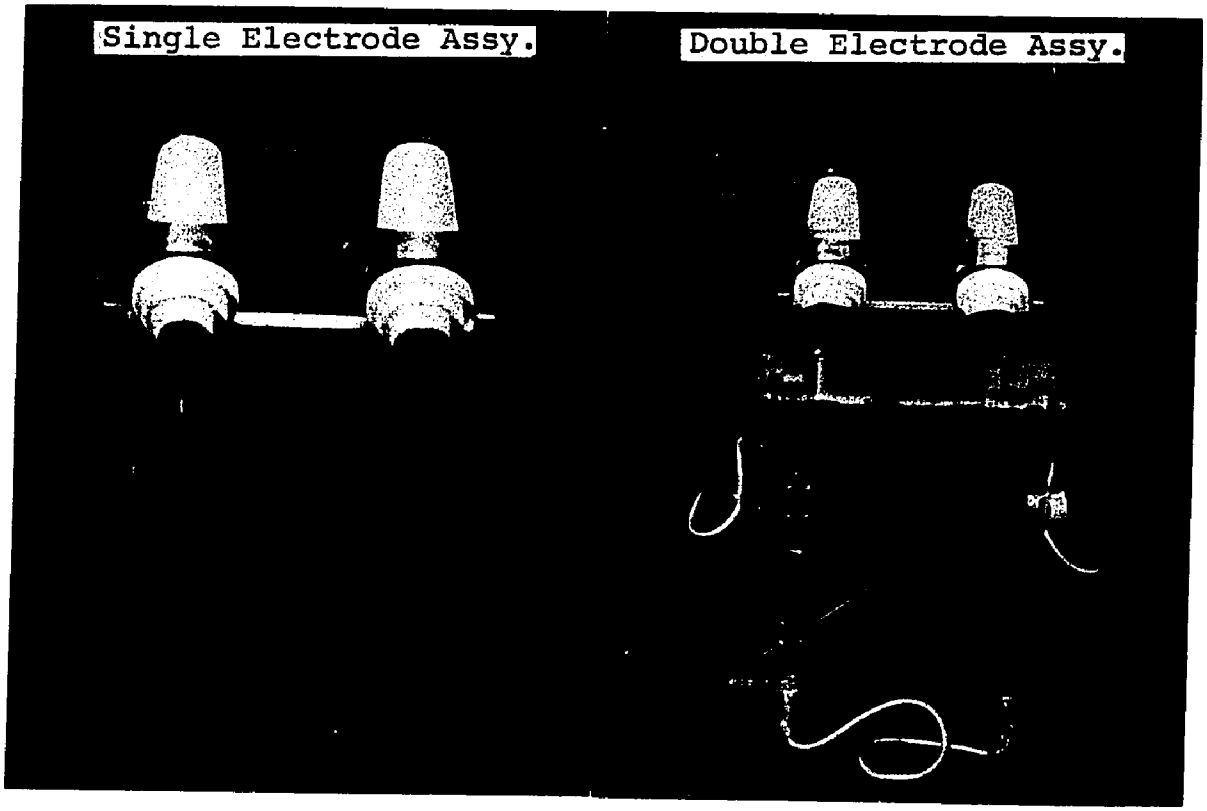


Figure 3.2 Bubble Generator



4204

Figure 3.3 Static Spark Chamber



4205

Figure 3.4 Electrode Assemblies

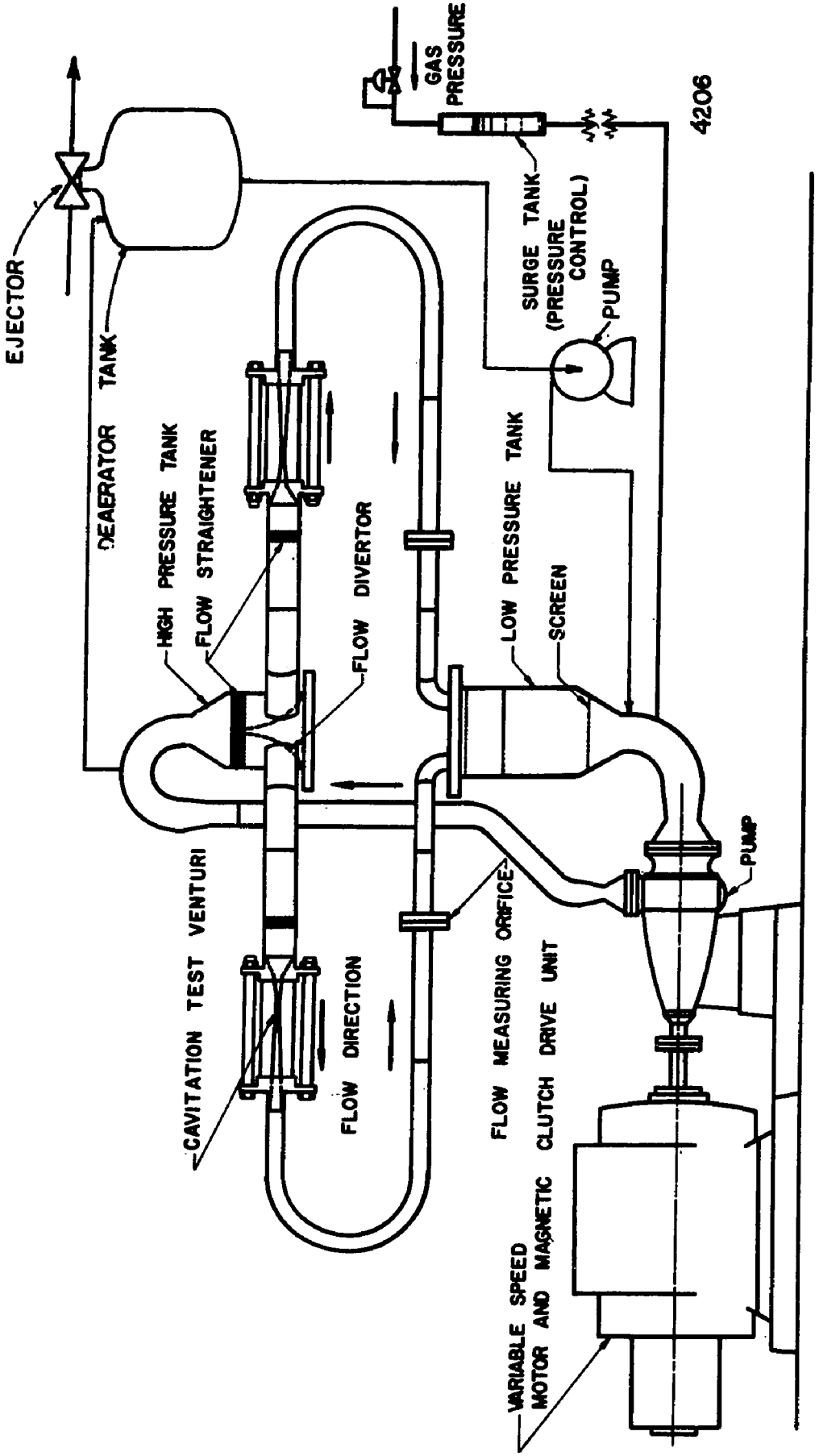


Figure 3.5 Schematic of High Speed Water Tunnel

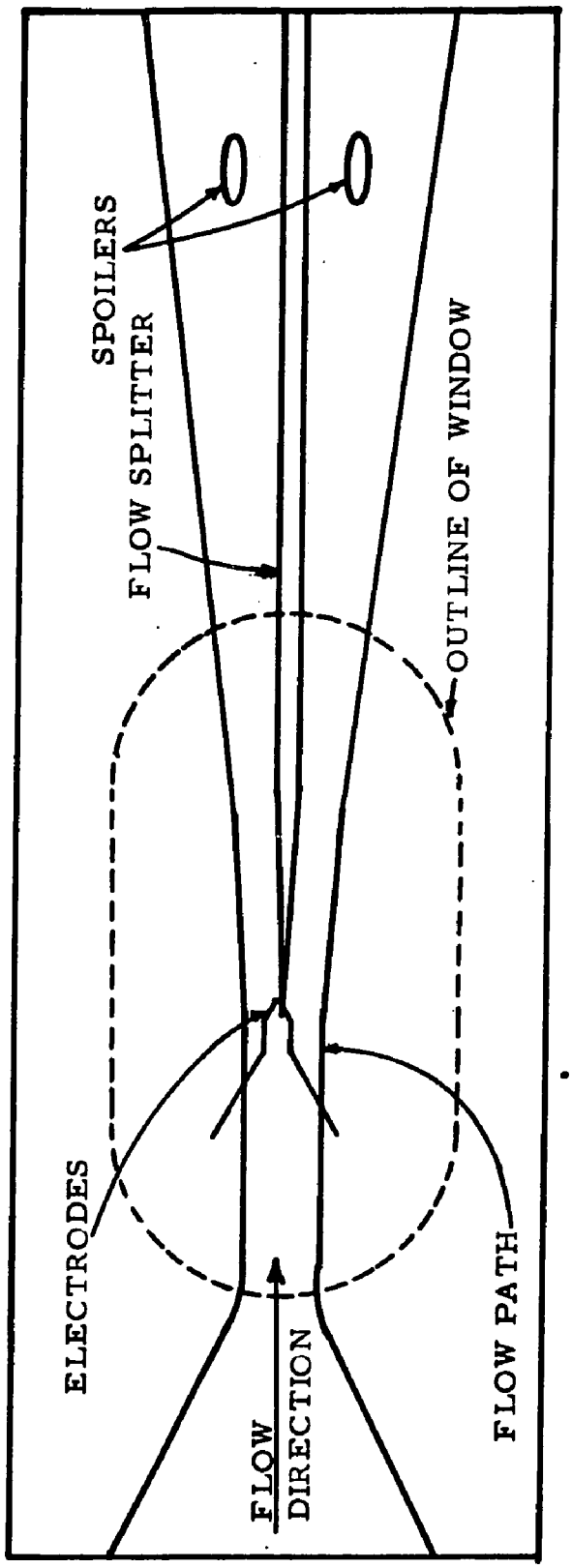


Figure 3.6 Schematic of Two Dimensional Venturi

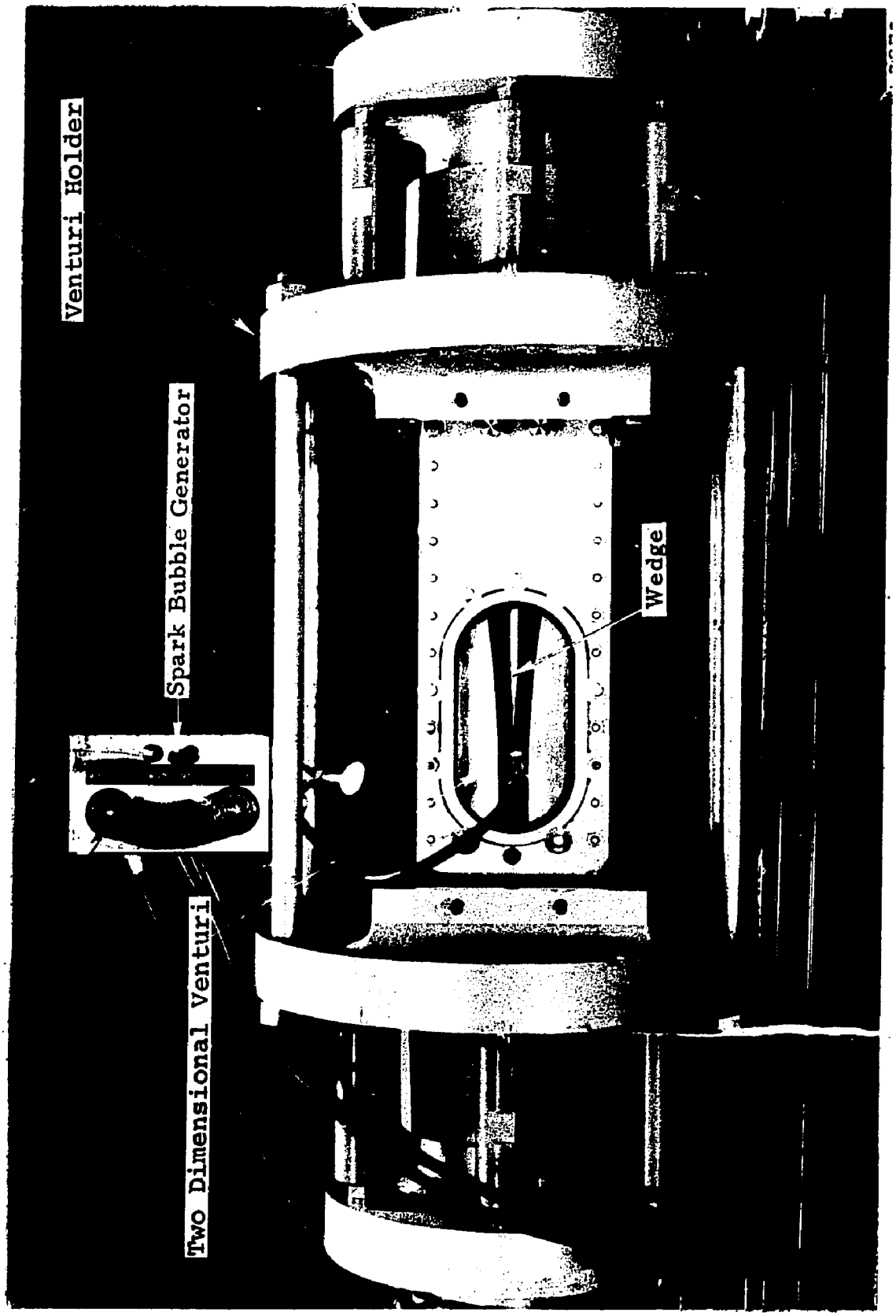


Figure 3.7 Two Dimensional Venturi

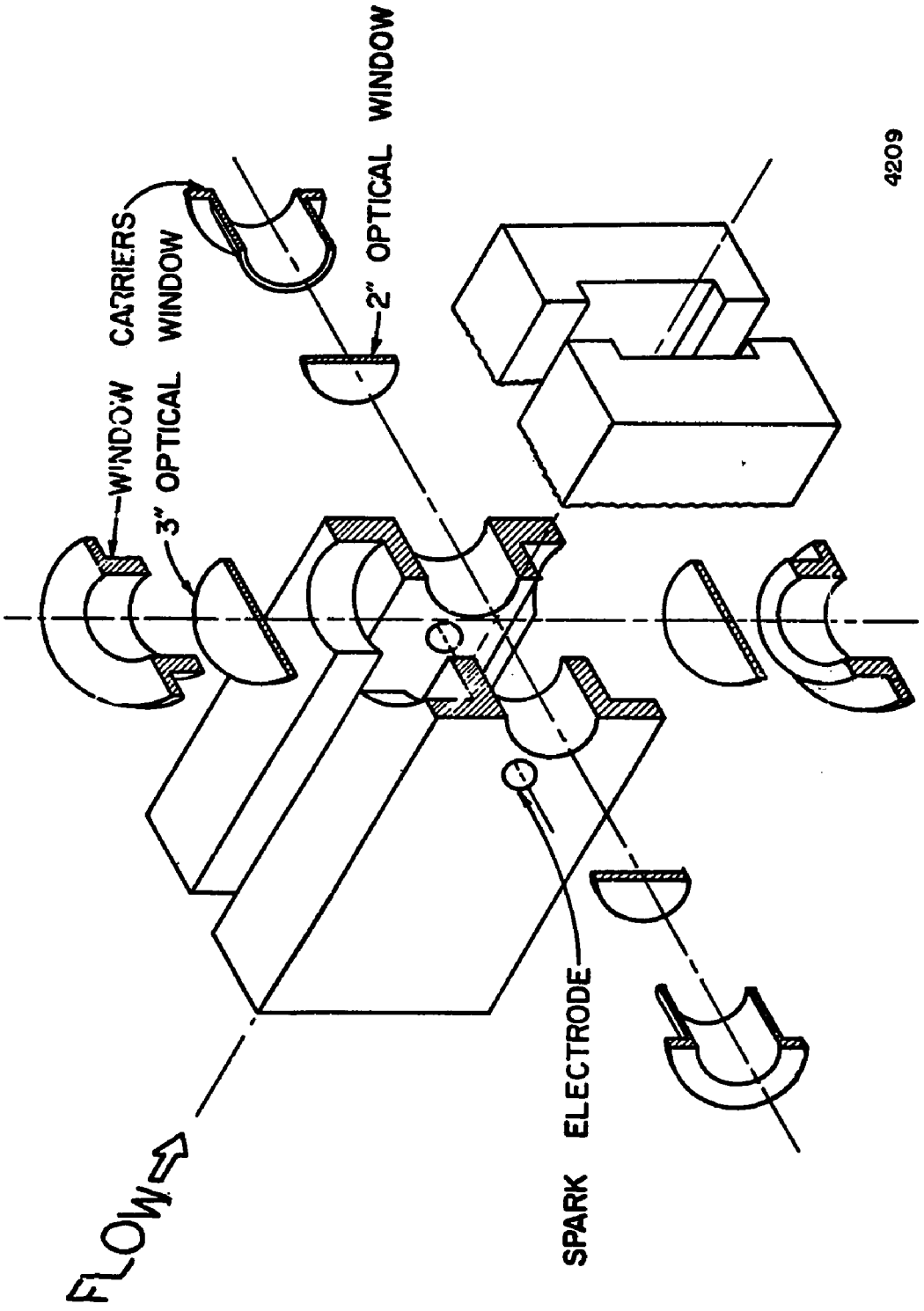
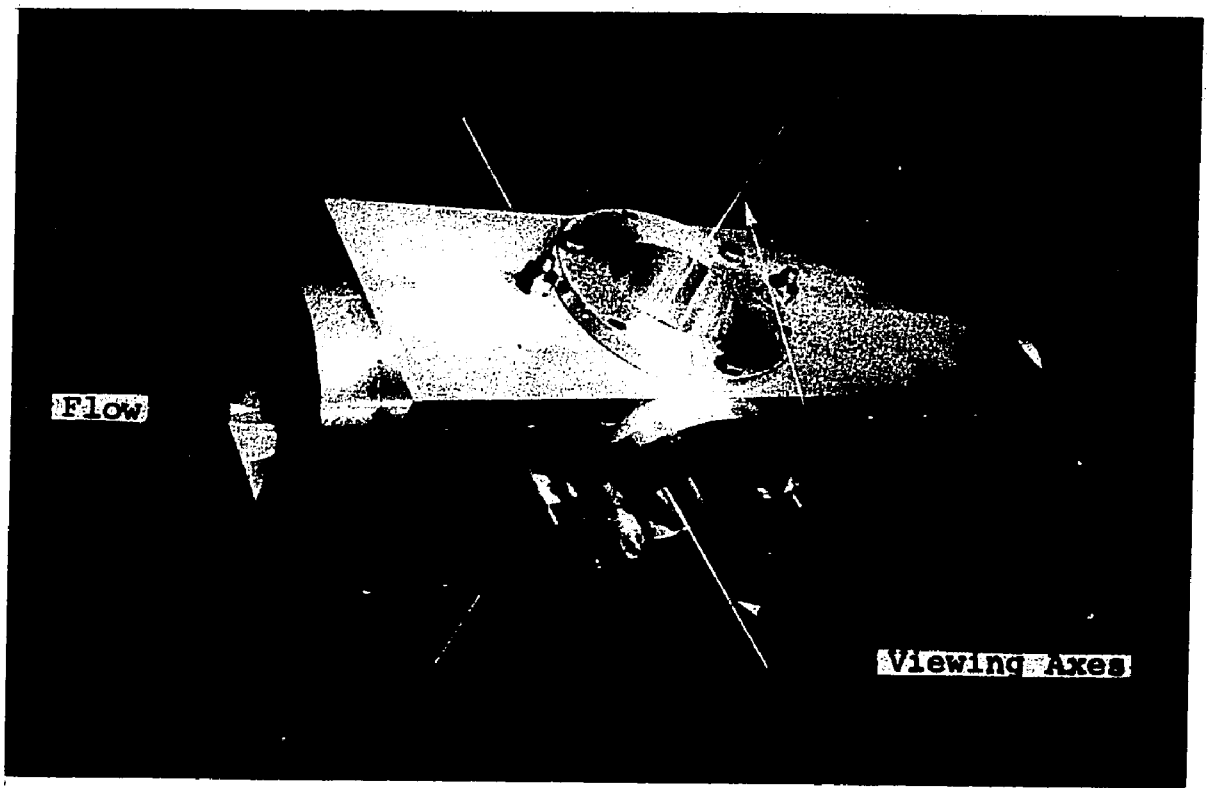
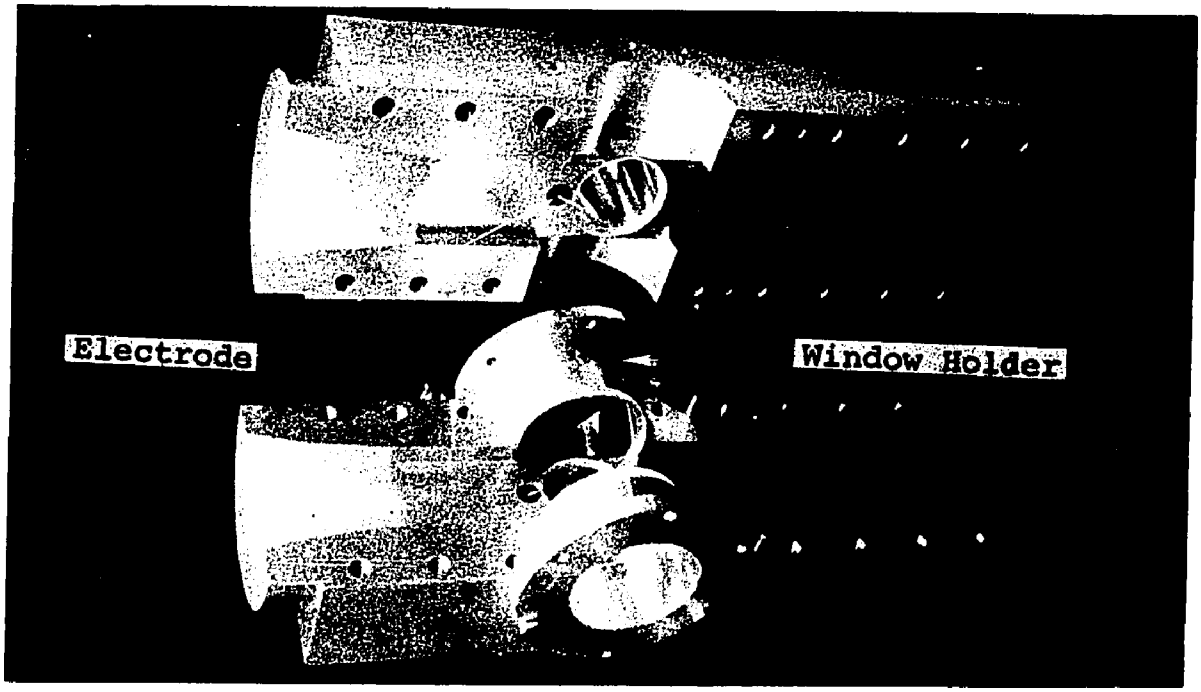


Figure 3.8 Schematic of Two Optical Axis Venturi



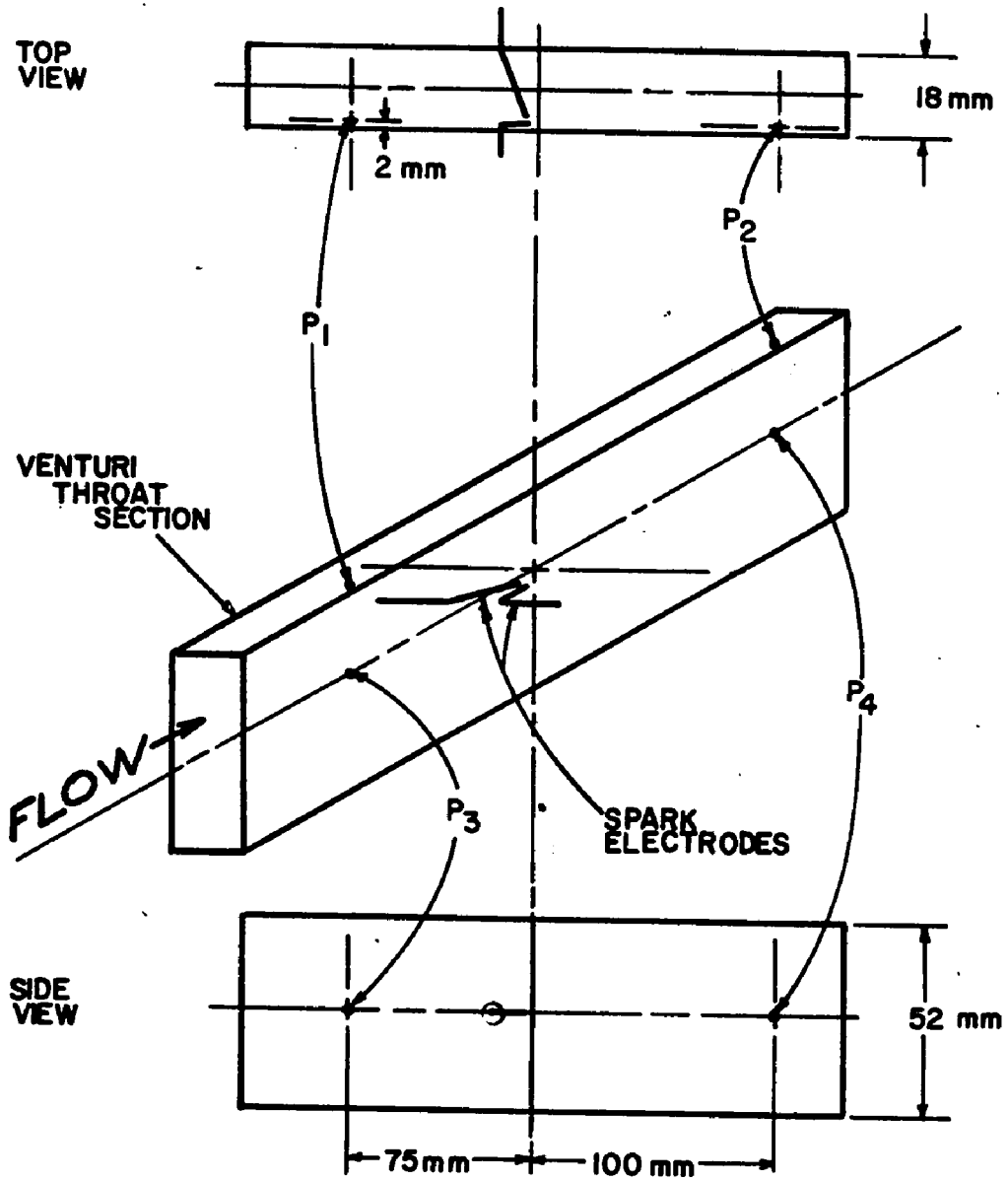
4210

Figure 3.9 Two Optical Axis Venturi, Assembled



4211

Figure 3.10 Two Optical Axis Venturi, Disassembled



TYPICAL RUN CONDITIONS
FLOW VELOCITY = 18 m/s
MAXIMUM BUBBLE RADIUS = 2.5 mm
PRESSURE DATA :
1 = 2.14 ATM ABS.
2 = 2.00
3 = 2.14
4 = 2.00
ESTIMATED PRESSURE IN AREA OF BUBBLE COLLAPSE = 2.06 ATM

ESTIMATED AXIAL PRESSURE GRADIENT = 0.8 ATM/METER

NOT TO SCALE

4212

Figure 3.11 Pressure Tap Location in Two Optical Axis Venturi

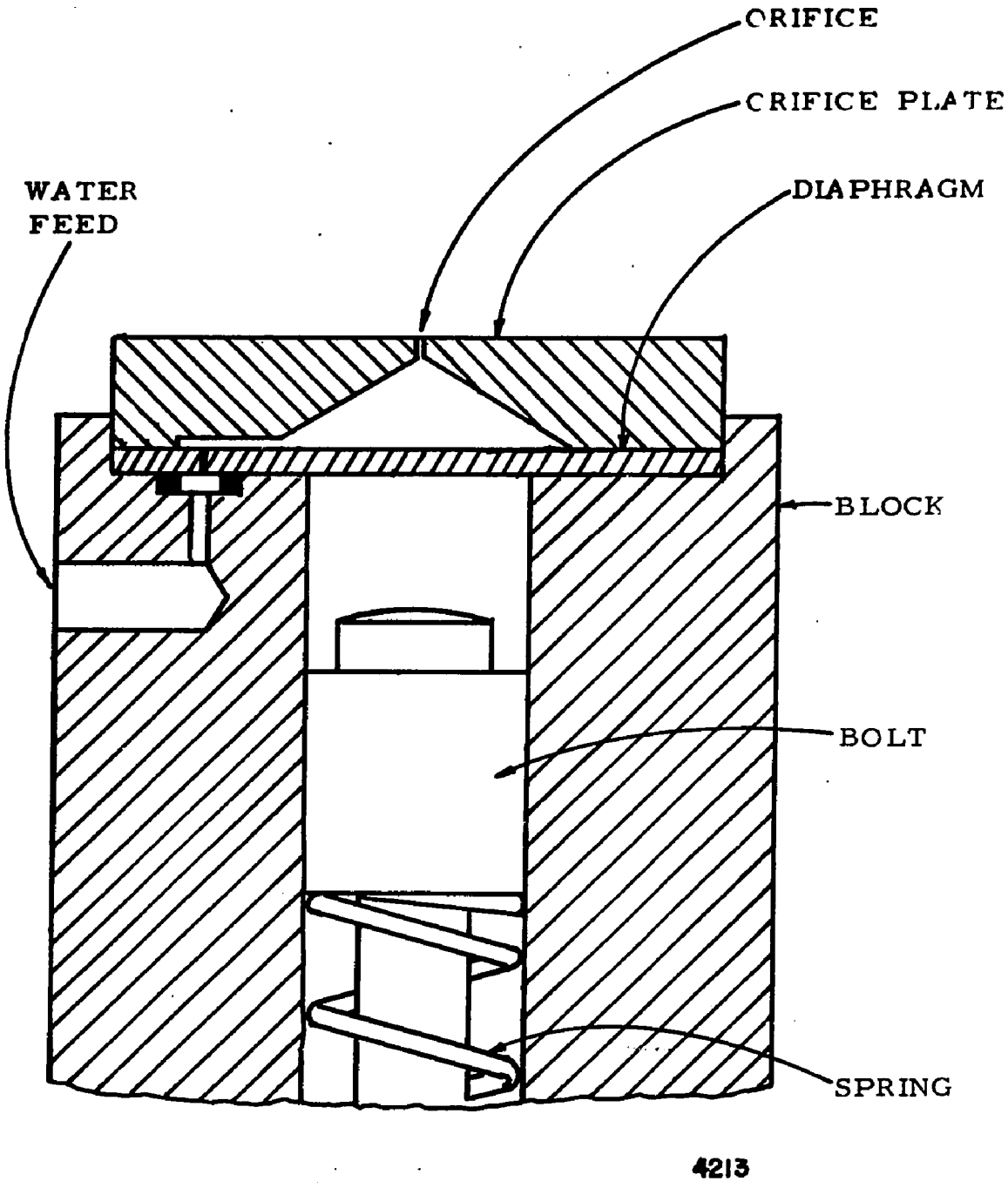
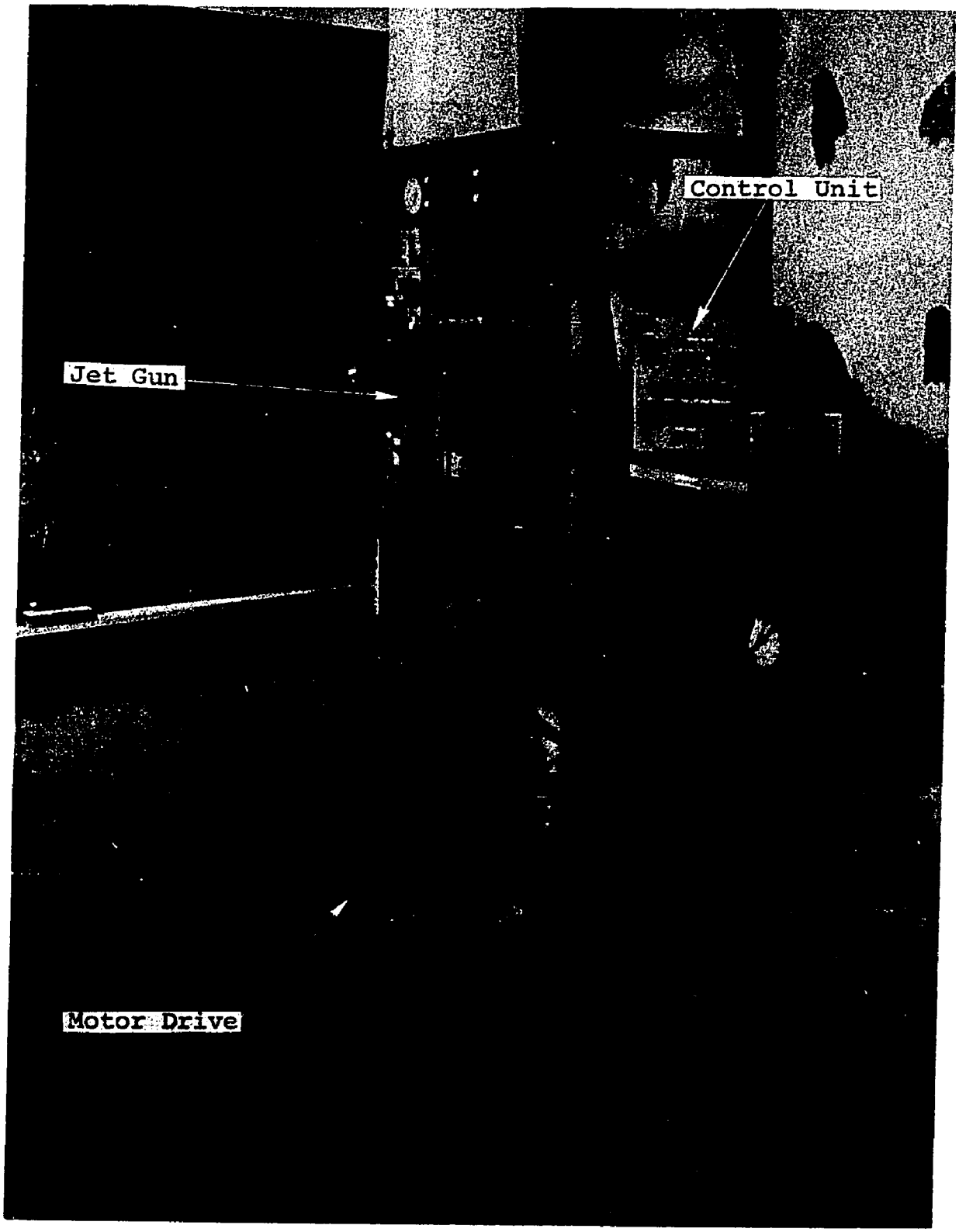
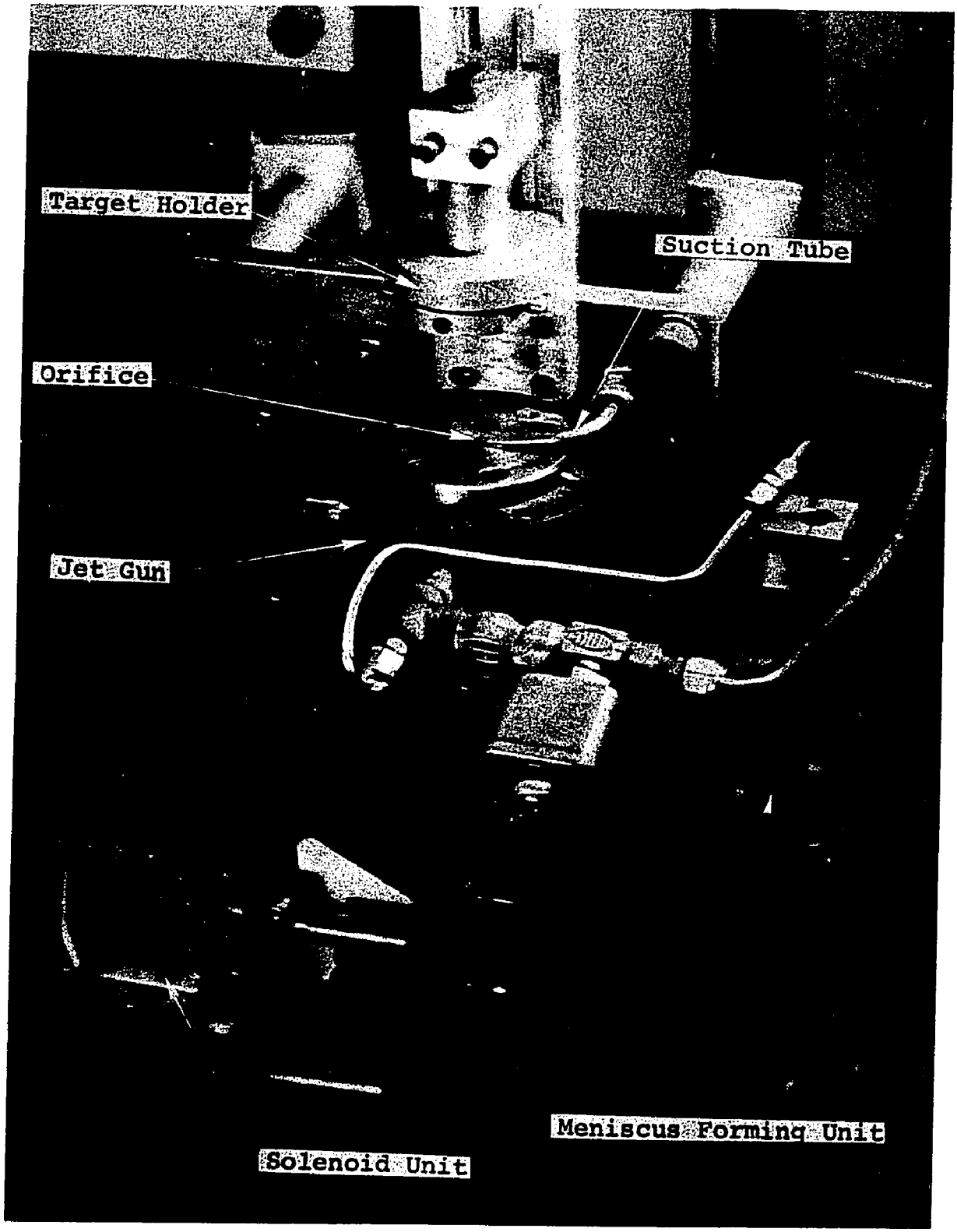


Figure 3.12 Schematic of Jet Gun



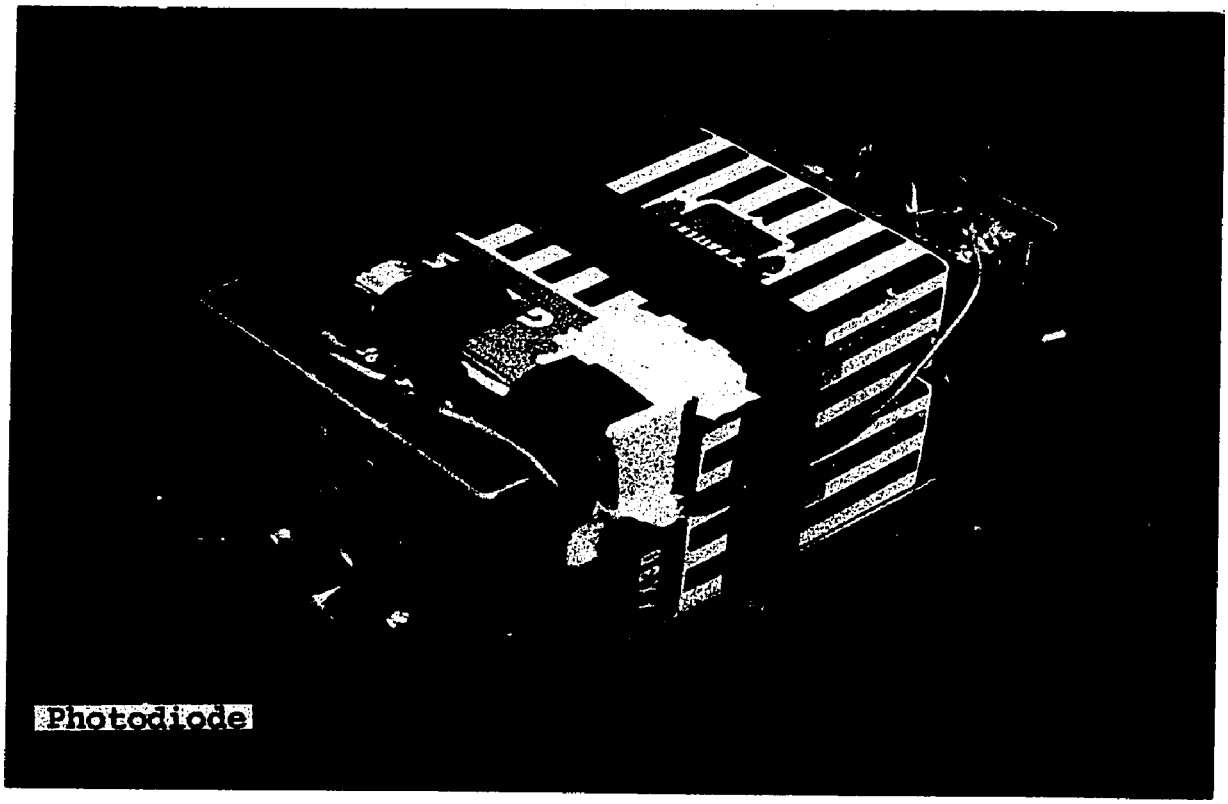
4214

Figure 3.13 Jet Gun, Automated Configuration



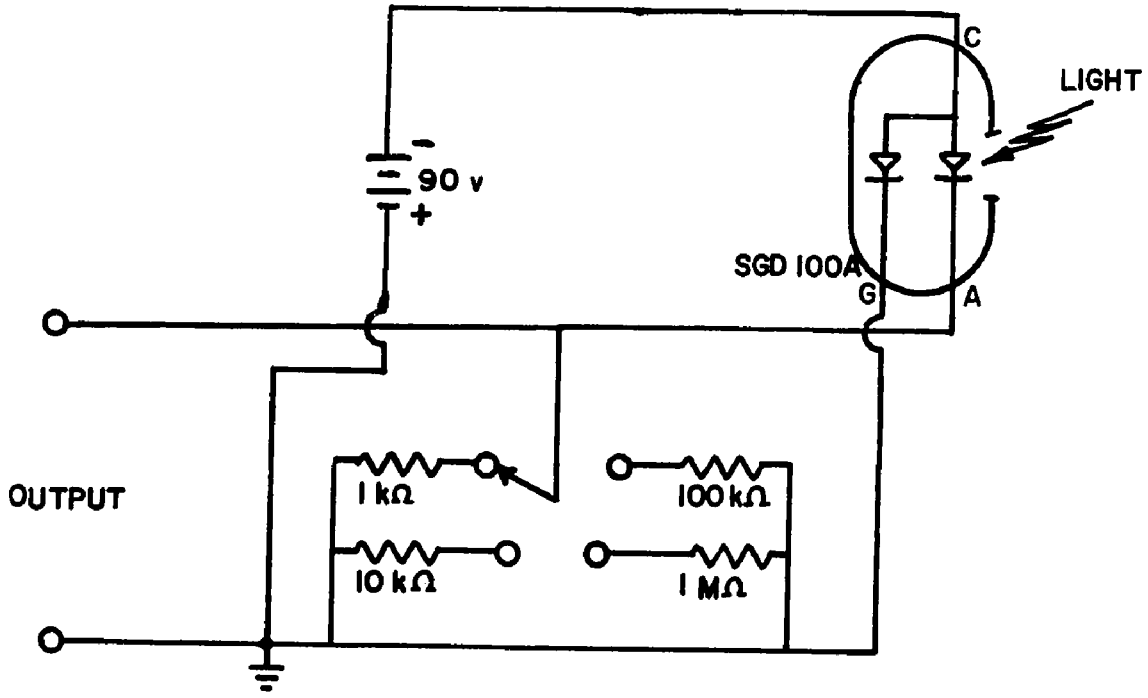
4215

Figure 3.14 Jet Gun, Single Shot Configuration



4216

Figure 3.15 Photodiode Detector



4217

Figure 3.16 Schematic of Photodiode Detector

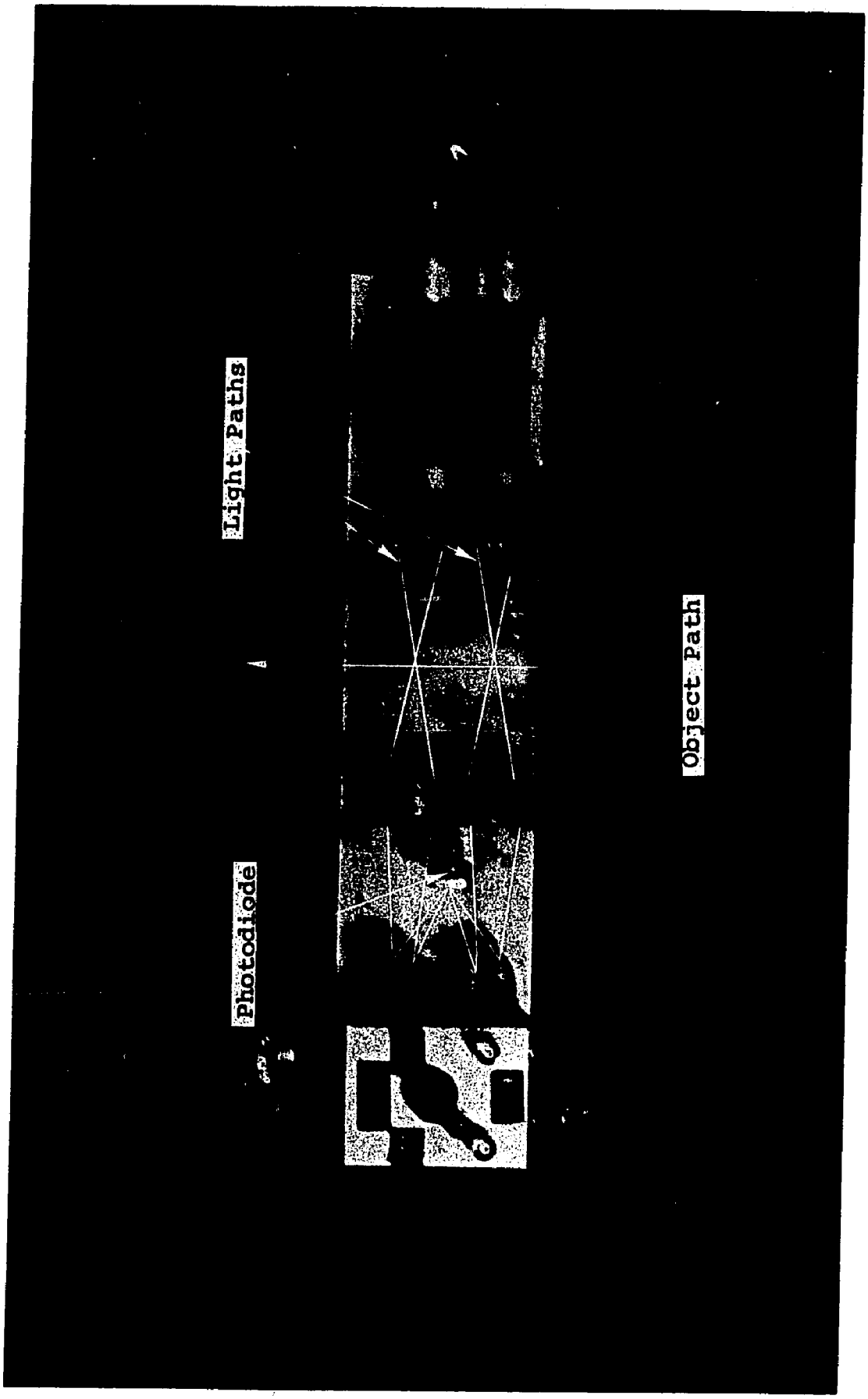


Figure 3.17 Photoelectric Velocity Sensor

CHAPTER 4

EXPERIMENTAL INVESTIGATION OF VAPOR BUBBLE COLLAPSE

4.1 GENERAL PROCEDURE

Photography was utilized to acquire data on the collapse mechanism of vapor bubbles in various aquatic environments. A series of experiments was designed so that equipment and procedures could be perfected in a stepwise manner of increasing complexity. Each experiment was run and evaluated until the equipment operated reliably and high quality photographs of the vapor bubble's collapse were obtained. Experimental conditions were carefully recorded for each camera run and the exposed film was immediately processed in the darkroom facilities of the Cavitation and Multiphase Flow Laboratory. The processed negative(s) were qualitatively analyzed by inspection, and those of high photographic quality were subjected to quantitative analysis. Quantitative analysis was made by manual measurement of significant dimensions, either from projected images of the negatives or from positive prints of the negatives. Magnification was determined by the inclusion of a measurement standard in the camera's field of view. This approach to the determination of magnification, as opposed to a purely mathematical approach, minimizes errors due to dimensional changes of photographic materials upon processing. When quantitative analysis showed that a high quality photographic record of the required phenomena at the required conditions had been produced the experiment was terminated. The following sections of Chapter 4

discuss experiments in the area of spark generated vapor bubble collapse conducted for the purposes of this study.

4.2 EXPERIMENTS IN A STATIC FLUID ENVIRONMENT UTILIZING HIGH SPEED CINEMATOGRAPHY

Experiments were conducted utilizing the Dynafax camera system in conjunction with the static fluid chamber and bubble generator in order to characterize the performance of the bubble generator and evaluate the effect of nearby objects on the collapse mechanism of spark generated vapor bubbles. In all cases presented below the liquid phase in the static fluid chamber was water at $25^{o}C$ and atmospheric pressure. The equipment was arranged as illustrated in Figure 4.1. Diffuse back lighting was demonstrated to produce the most detailed negatives. The flash head of the U-M Custom light source was set up, together with a light pipe made from an aluminum foil lined plastic tube and a ground glass diffuser, to provide diffuse backlight. Kodak Tri-X film processed in Kodak D-76 developer was the recording medium. An exposure rate of 2.5×10^{4} frames/sec. and an exposure time of one microsecond, both representing maximum camera performance in terms of high exposure rate and low exposure time, were used in all static bubble studies. Wiring was arranged so that, once the loaded camera was brought up to speed, the bubble generator and light source were fired by the flash synchronization contacts on the camera's capping shutter. These contacts close when the capping shutter opens fully. The capping shutter was released by means of an electrical pulse applied to the camera's shutter tripping

solenoid. This same pulse also stopped the electronic counter used to monitor framing rate so the exact framing rate at the instant of exposure was known. The true framing rate was always found to be within ½% of the nominal framing rate of 2.5×10^4 frames/sec, and variations were considered so small that they were ignored for the purposes of data reduction.

4.2a BUBBLE GENERATOR CHARACTERIZATION

As a first step in this study it was decided to undertake an experiment to characterize the performance of the bubble generator. The single bubble electrode assembly was installed in the fluid chamber with the electrode gap set at 0.2 mm., and the bubble generator was connected. After the equipment was demonstrated to be operable, thirteen photographic runs were made. Each set of negatives was projected and each frame was measured for the dimensions given in Figure 4.2. (Run 1099-DSB-3 was selected for printing, and these prints appear as Figure 4.4.)

4.2b BUBBLE COLLAPSE ADJACENT TO A RIGID SURFACE

To act as a rigid surface, a brass plate was centered under the single bubble electrode assembly in the static fluid chamber. The plate was 50 mm. square by 6 mm. thick and the vertical distance from the electrode tips to the surface of the plate was set at 4.17 mm. Of the various runs made, run 1120-D-SB-1 was photographically best, and prints therefrom were made for analysis. Each frame was measured for the dimensions shown in Figure 4.3. The prints from this run form Figure 4.5.

4.2c BUBBLE COLLAPSE ADJACENT TO A COMPLIANT SURFACE

A compliant surface was centered under the single bubble electrode assembly in the static fluid chamber. This compliant surface consisted of a thin rubber diaphragm stretched over the end of a piece of plastic tubing. The rubber was 0.4 mm. thick, and the tube was 30 mm. diameter by 60 mm. long. The vertical distance between the electrode tips and the rubber diaphragm was 4.17 mm. The air-filled tube length was 50 mm. below the rubber diaphragm to maximize the compliancy of the surface. Camera run 10300-DSB-1 was printed as Figure 4.6, and was measured for the dimensions shown in Figure 4.3.

4.2d BUBBLE COLLAPSE ADJACENT TO ANOTHER BUBBLE

The double-bubble electrode assembly was installed in the static fluid chamber with the electrode gaps set at 0.1 mm. Experimental runs were made with the bubble-forming arcs separated horizontally by a distance of 8.3 mm. Camera run 10210-DSB-2 was printed, appears as Figure 4.7, and was measured for the dimensions shown in Figure 4.8.

4.3 EXPERIMENT IN A STATIC FLUID ENVIRONMENT UTILIZING HOLOGRAPHY

An experiment was designed to determine whether holography offered any significant advantages over photography as a means of recording single, high-quality images of a spark generated vapor bubble. The static fluid chamber was set up with the single bubble electrode assembly and bubble generator at the Radar and Optics Laboratory Holographic Facility. Figure 4.9 is a schematic drawing of the experimental layout. The pulsed laser used to expose the

holographic plates had the characteristic of not firing until a random delay of from 400 to 600 microseconds had elapsed after the firing pulse was applied. This made accurate timing impossible, so the time interval between the firing of the bubble generator and the firing of the laser was monitored with the photodiode sensor and an oscilloscope. The delay generator was used to delay the firing pulse to the bubble generator, so some control over timing was possible. Exposed plates were processed immediately after exposure and were qualitatively evaluated by visual inspection of the reconstructed image. Run 1229-HSB-5 was selected for further analysis, and photographs of the reconstructed image were taken. Figure 4.10 is a photographic print of run 1229-HSB-5. This holograph was exposed 285 microseconds after firing the bubble generator.

4.4 EXPERIMENTS IN A FLOWING FLUID ENVIRONMENT CONTAINED BY THE TWO-DIMENSIONAL VENTURI

The two dimensional venturi was set up in the High Speed Water Tunnel, and high speed cinematography was used in order to conduct preliminary studies on the collapse mechanism of spark generated vapor bubbles in a flowing fluid environment near a solid wall. The purpose of these studies was twofold: to acquire experience operating the water tunnel and photographing collapsing bubbles, and to acquire knowledge necessary to design further experiments in this area. Two experiments were conducted: one utilizing the Dynafax camera to provide timing information, and one using the Model 330 camera to study the critical phase of the collapse with a high framing rate.

4.4a TWO-DIMENSIONAL VENTURI - DYNAFAX CAMERA

The Dynafax camera was set up so that its field of view included a large area downstream from the spark electrodes in the two dimensional venturi. A ground glass diffuser was attached to the venturi and the flash head of the U-M Custom Light Source was placed in close proximity to the diffuser. This arrangement provided sufficient diffuse backlight to expose Tri-X film with an exposure time of one microsecond at a rate of 2.5×10^4 frames/second. The wiring was arranged as in Section 4.2. Preliminary photographic runs were made to study conditions in the venturi around the bubble and to optimize them so that bubbles of suitable diameter were produced, natural cavitation was suppressed, and the fluid velocity was approximately 20 m/s. Run 1191-DFB-1 was chosen for analysis, printed, and appears as Figure 4.11. Conditions for run 1191-DFB-1 were as follows; fluid velocity = 23 m/s, fluid pressure = 1.14 Atm Abs, fluid temperature = 21^{o}C, and fluid air content = 0.42% (Vol. Gas/Vol. Liq.). Under these conditions the collapse phase of the bubble's life lasted from 300 to 500μs after the spark was initiated. The measurements diagrammed in Figure 4.12 were taken from the prints of this run.

4.4b TWO-DIMENSIONAL VENTURI - MODEL 330 CAMERA

The Model 330 Camera was set up so that its field of view included an area extending 15 mm. downstream from the electrode tips. The Model 450 light source was set up with a ground glass diffuser to provide diffuse back light, as shown in Figure 4.13. The writing time required to capture the

collapse was previously found to be 200μs. With 80 frames available in the Model 330 camera, the required framing rate was 4×10^5 f/s. The delay generator was used to delay the light source firing pulse by 300μs after the bubble generator firing pulse. Exposure time was set at 2.5 s/f. Under these conditions sufficient light was available to produce good records on Tri-X film developed in D-76. Several photographic runs were made and run 1252-BW-FB-2 was selected as the best photographically. This run was printed, appears as Figure 4.14, and the prints were measured for the dimensions shown in Figure 4.10. The fluid conditions in the venturi were the same as those in run 1191-DFB-1 with the exception of air content, which was 1.04%.

4.5 EXPERIMENTS IN A FLOWING FLUID ENVIRONMENT CONTAINED BY THE TWO OPTICAL AXIS VENTURI

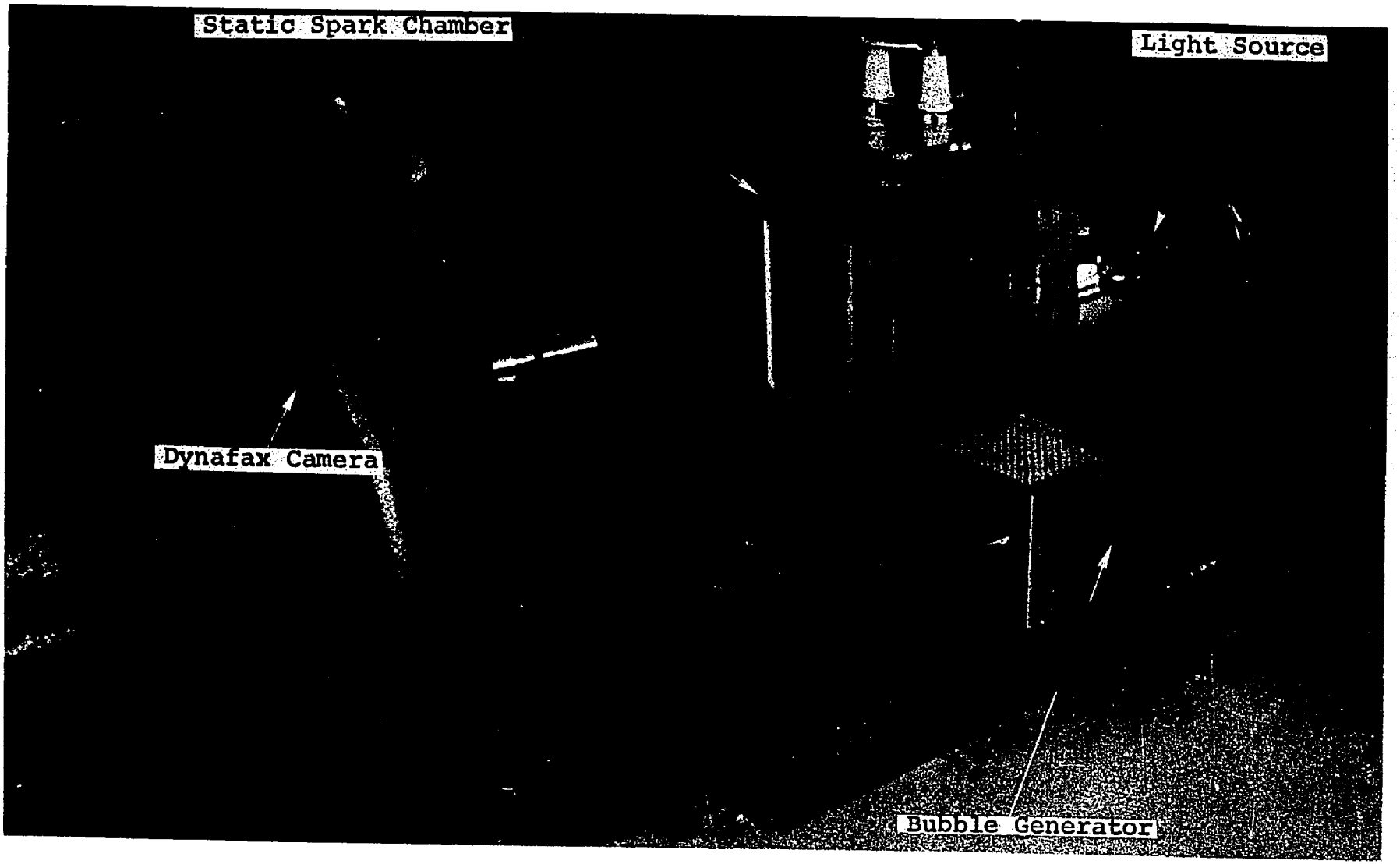
The two optical axis venturi was set up in the High Speed Water Tunnel and high speed cinematography was employed to conduct further studies on the collapse mechanism of spark generated vapor bubbles in a flowing fluid environment near a solid wall. Mirrors were used to fold the light paths so that the Model 330 camera could be used to take split field photographs of the collapsing bubble from two mutually perpendicular directions. Mirrors were also used to split the output of the Model 450 light source and provide diffuse back light to both fields. Figure 4.15 is a schematic drawing and Figure 4.16 is a photograph of this experimental setup. The purpose of this experiment was threefold: to provide further information on the collapse mechanism itself; to provide information about the effect of the collapse on the

nearby surface; and to provide information about the effect of the nearby surface on the collapse mechanism. Initial photographic runs were made to refine the experimental design and establish optimal conditions in the venturi. A glass window, cemented to the window holder adjacent to the collapsing bubble, was used for these initial runs. A camera framing rate of 2×10^5 f/s was chosen to provide a writing time of 400μs, which was sufficient to include all of the collapse. The exposure time was set at approximately 5μs and, under these conditions, adequate exposures were obtained on Tri-X film developed in D-76. The following nominal fluid conditions were chosen for this experiment: fluid velocity = 18 m/s, fluid pressure = 2 Atm Abs, and fluid temperature = 20-25^{o}C. Exact conditions for each run, along with fluid air content information, appear in the figure containing the prints from that run. Figure 4.17 is a diagramatic explanation of what the prints made from each negative show and Figure 4.18 illustrates the dimensions taken off each set of prints. Of the initial runs made, run 7102-BW-2D-4 was printed and appears as Figure 4.19.

After the initial runs were made, the window holder adjacent to the collapsing bubble was removed and fitted with a plexiglass window. This window was marked with a grid so that the area struck by the jet from the collapsing bubble could be located. The window was replaced in the venturi, the water tunnel was brought to the required experimental conditions, and a photographic run was made. The window was then removed and microscopically inspected for signs of

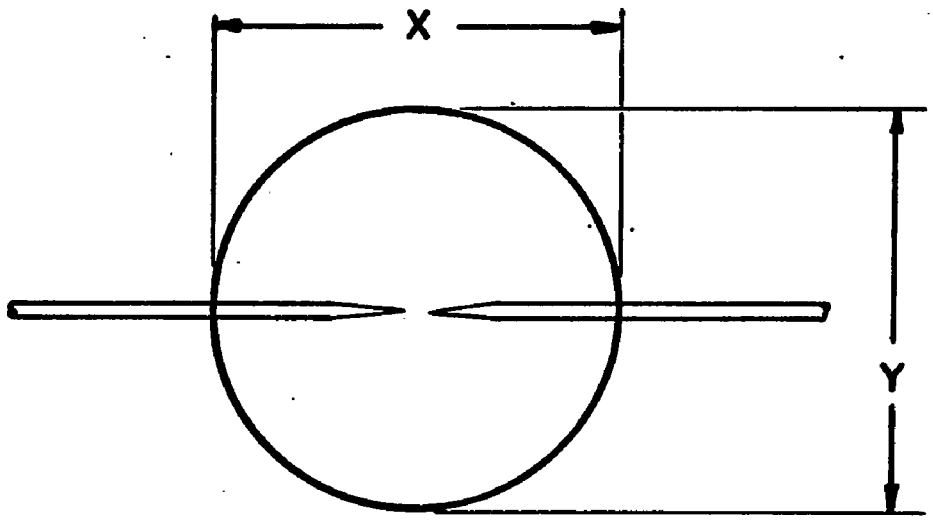
damage. This procedure was then repeated with another window. Figures 4.20 and 4.21 are the prints from these runs, numbered run 842-BW-2D-4 and run 852-BW-2D-3, respectively. A window assembly was also fabricated from plexiglass coated with transparent laquer, and it was subjected to this procedure. This resulted in run 7312-BW-2D-1, the prints from which appear as Figure 4.22. Finally, another plexiglass window was installed, and this window was subjected to attacks from 100 bubbles in the water tunnel without corresponding camera runs.

In order to partially study the effect of the nearby surface on the collapse mechanism the window holder adjacent to the collapsing bubble was modified to act as a partially compliant surface. A rubber diaphragm backed by a ventilated aluminum plate was installed in place of the window. This assembly was not transparent so one view was lost from the photographs. The intention of this experimental design was to provide a compliant rubber surface which was backed by air and free to move to facilitate liquid flow whenever the local pressure in the test section fell below atmospheric. The success of this design was dependent on the adequacy of the ventilation holes in the aluminum backing plate. Figure 4.23 is a photograph of this unit in disassembled condition; and Figure 4.24, which was taken with the partially compliant window assembly in the venturi, consists of the prints from camera run 842-BW-2D-2.



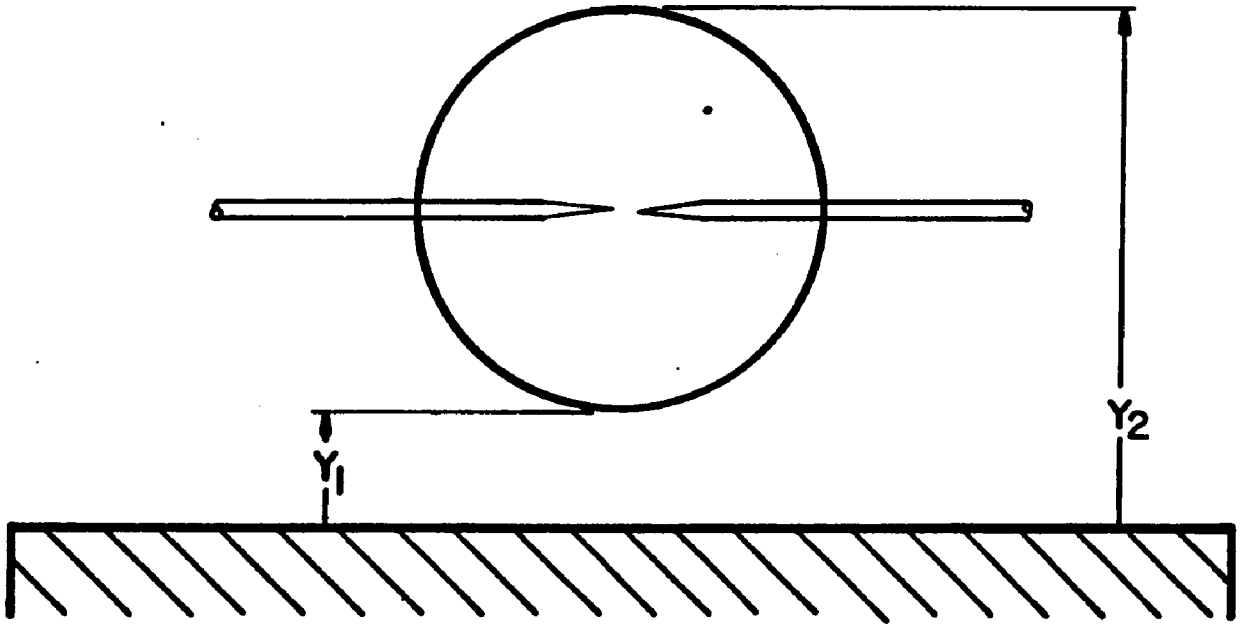
4219

Figure 4.1 Static Spark Chamber w/ Dynafax Camera



4220

Figure 4.2 Single Bubble Measurement Diagram



4221

Figure 4.3 Rigid Wall Measurement Diagram

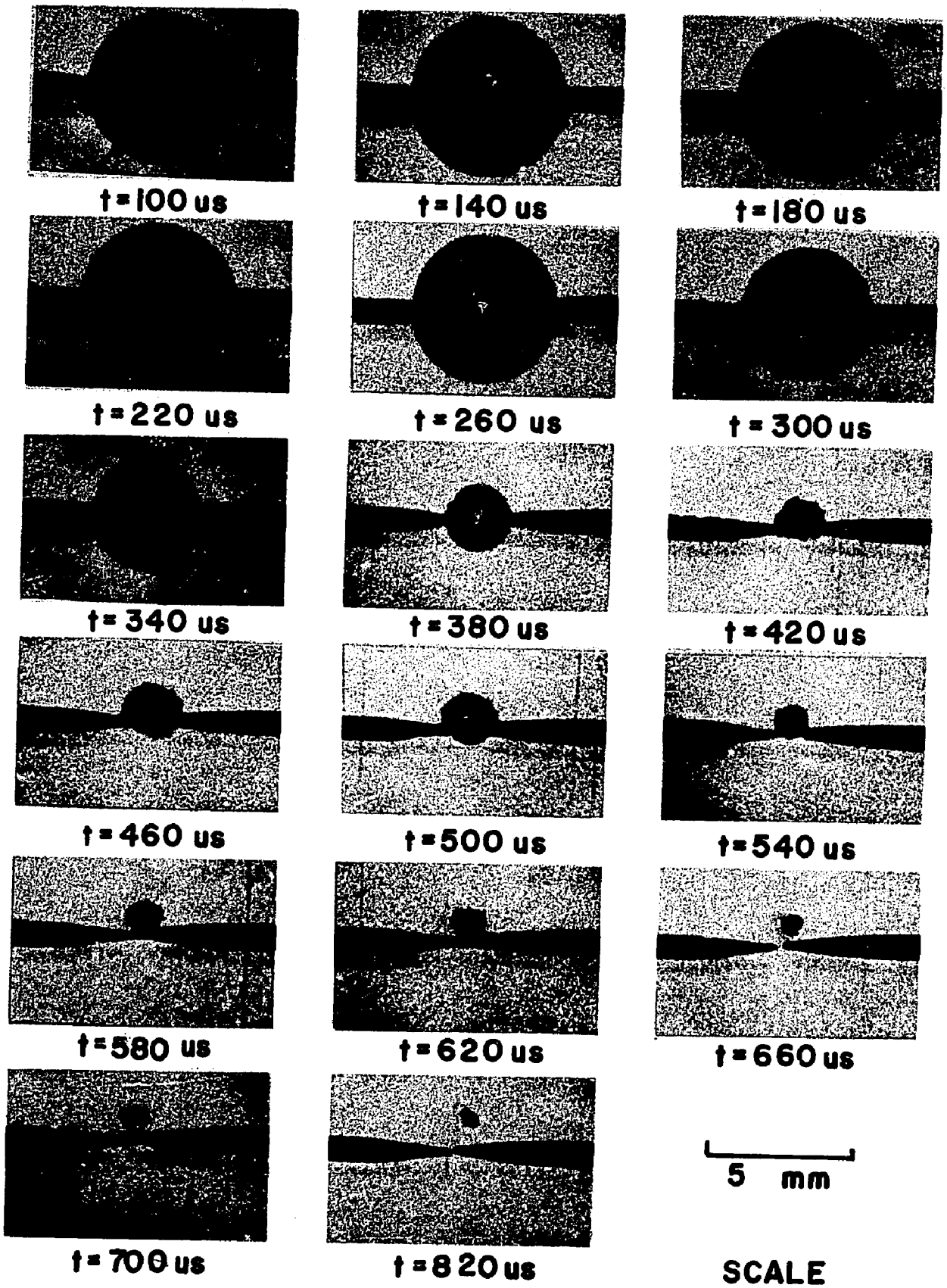


Figure 4.4 Prints, Run 1099-DSB-3

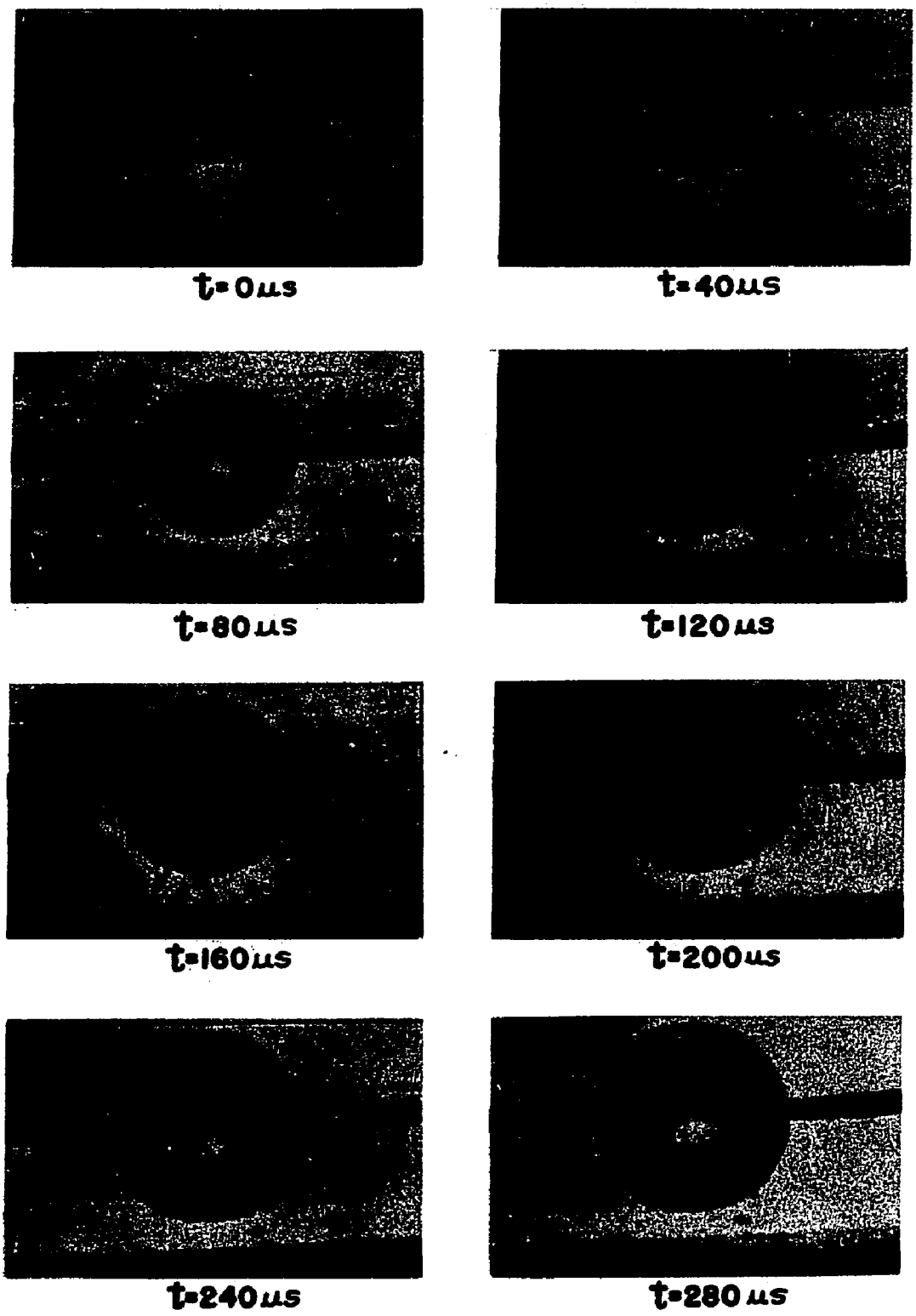


Figure 4.5 Prints, Run 1120-DSB-1, p.1

1120-1 4223

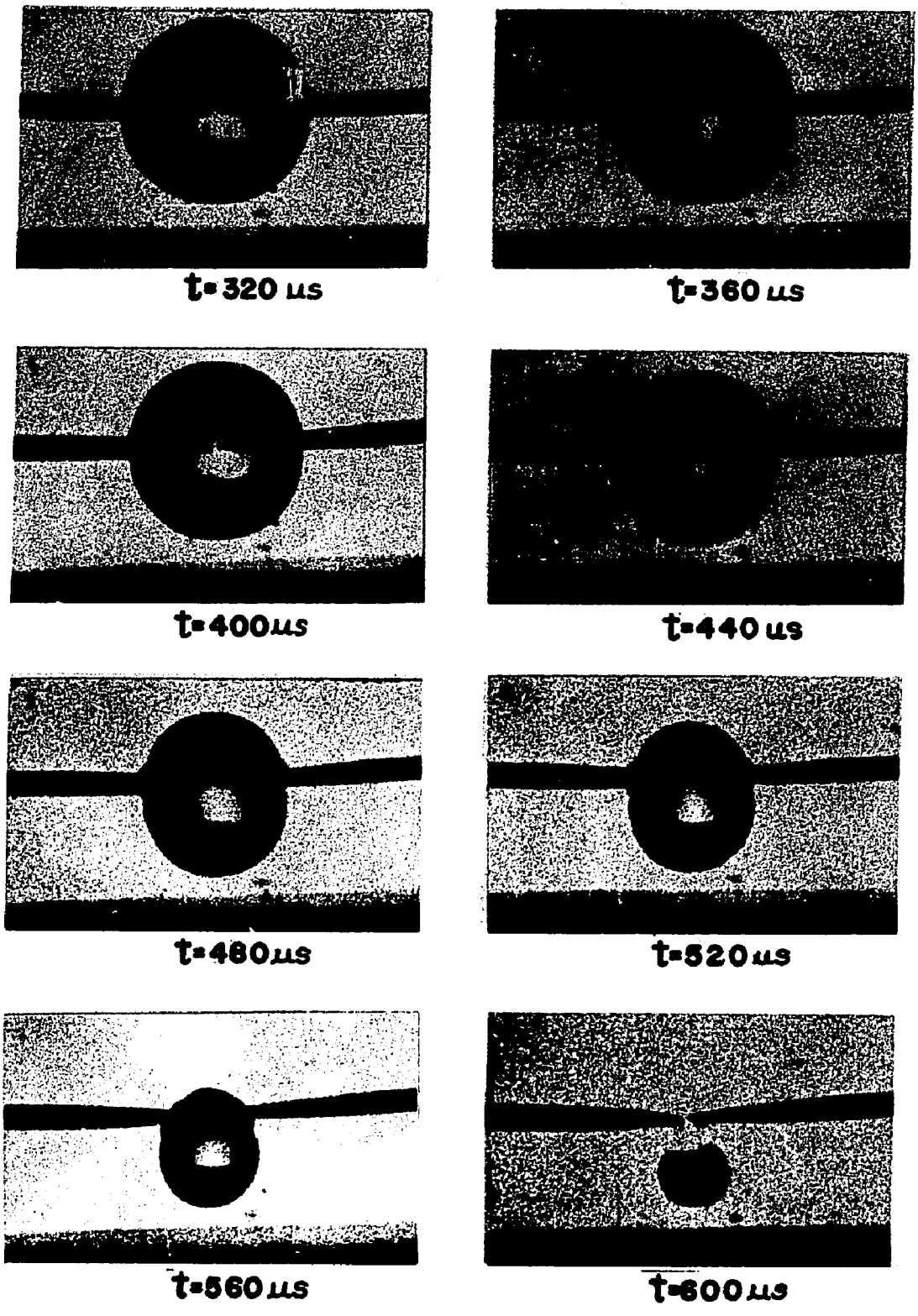


Figure 4.5 Prints, Run 1120-DSB-1, p.2

1120-1 4224

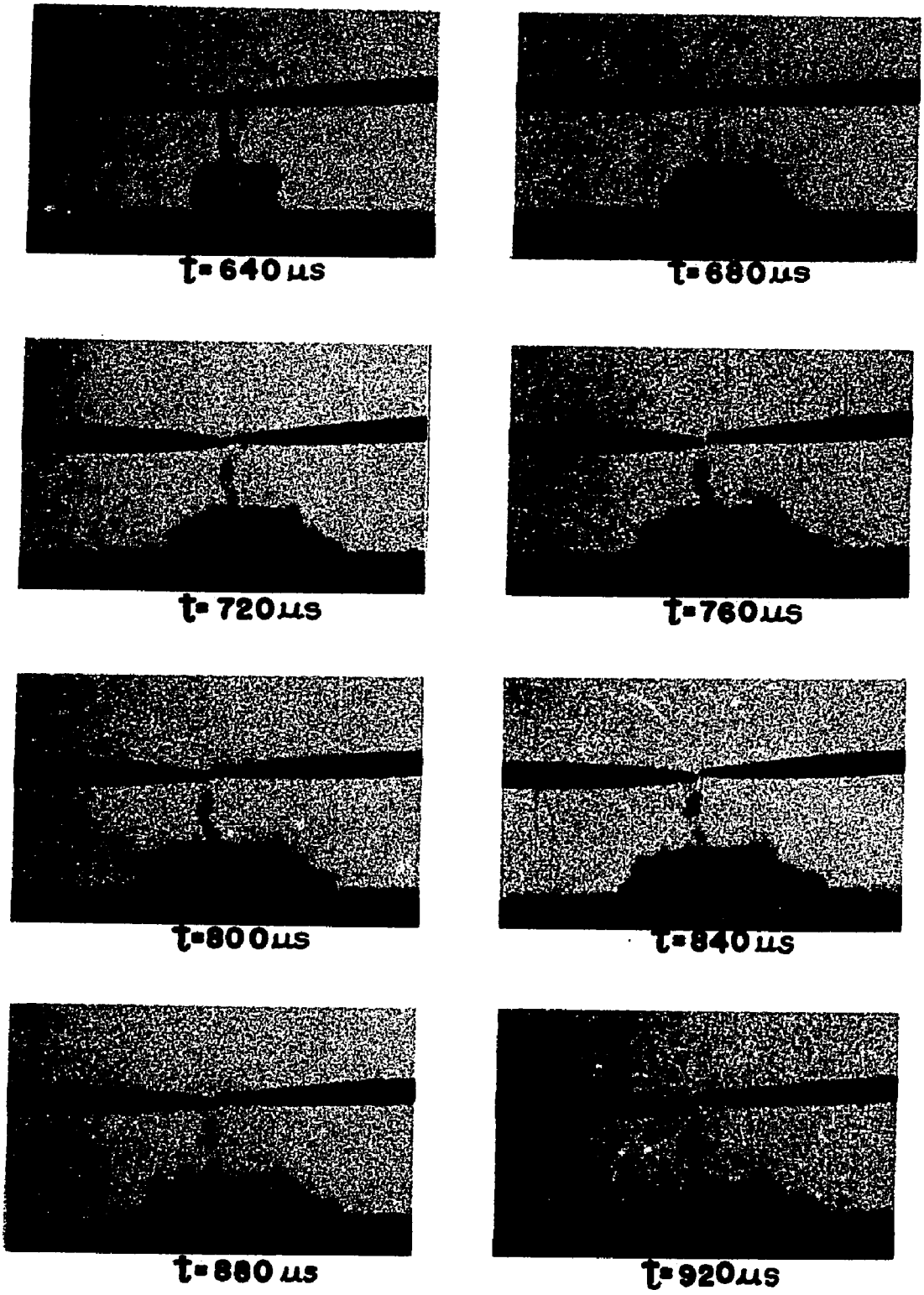


Figure 4.5 Prints, Run 1120-DSB-1, p.3

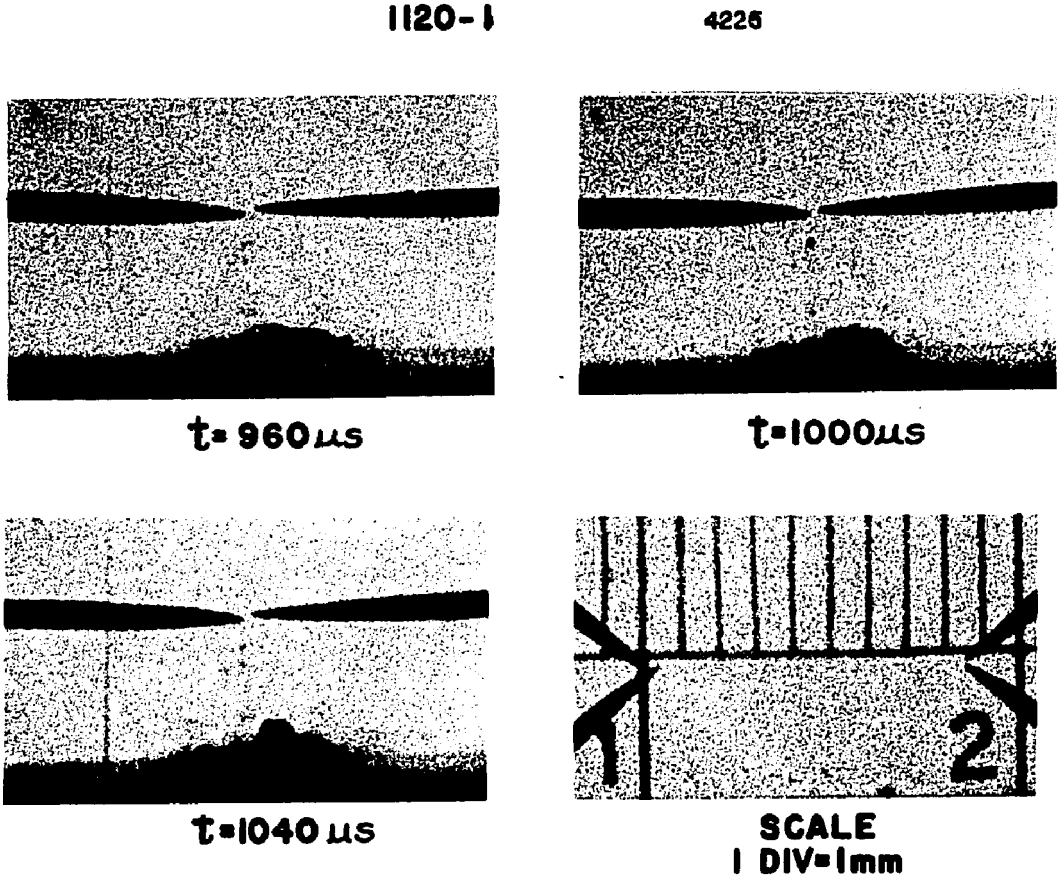


Figure 4.5 Prints, Run 1120-DSB-1, p.4

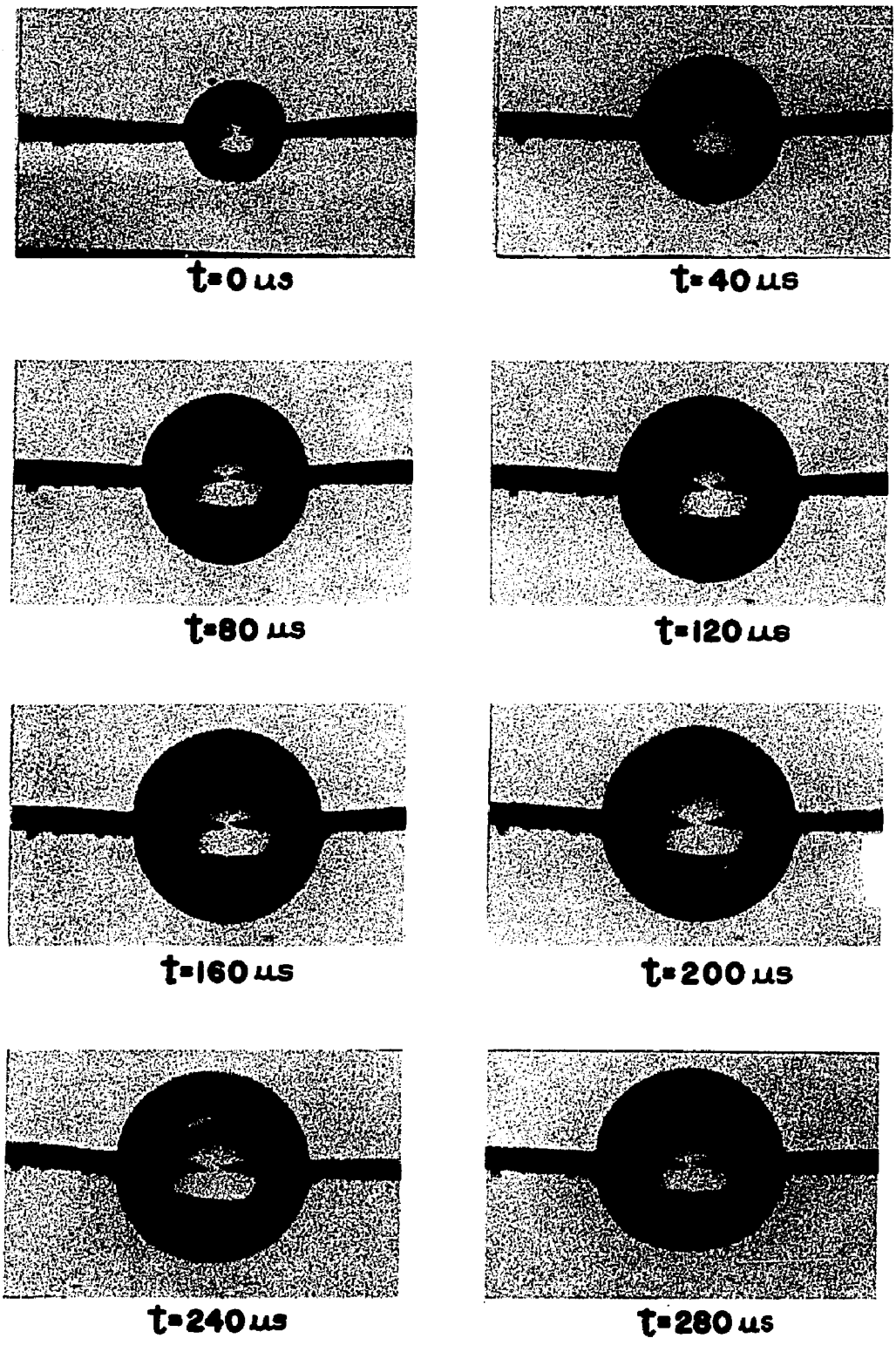


Figure 4.6 Prints, Run 10300-DSB-1, p.1

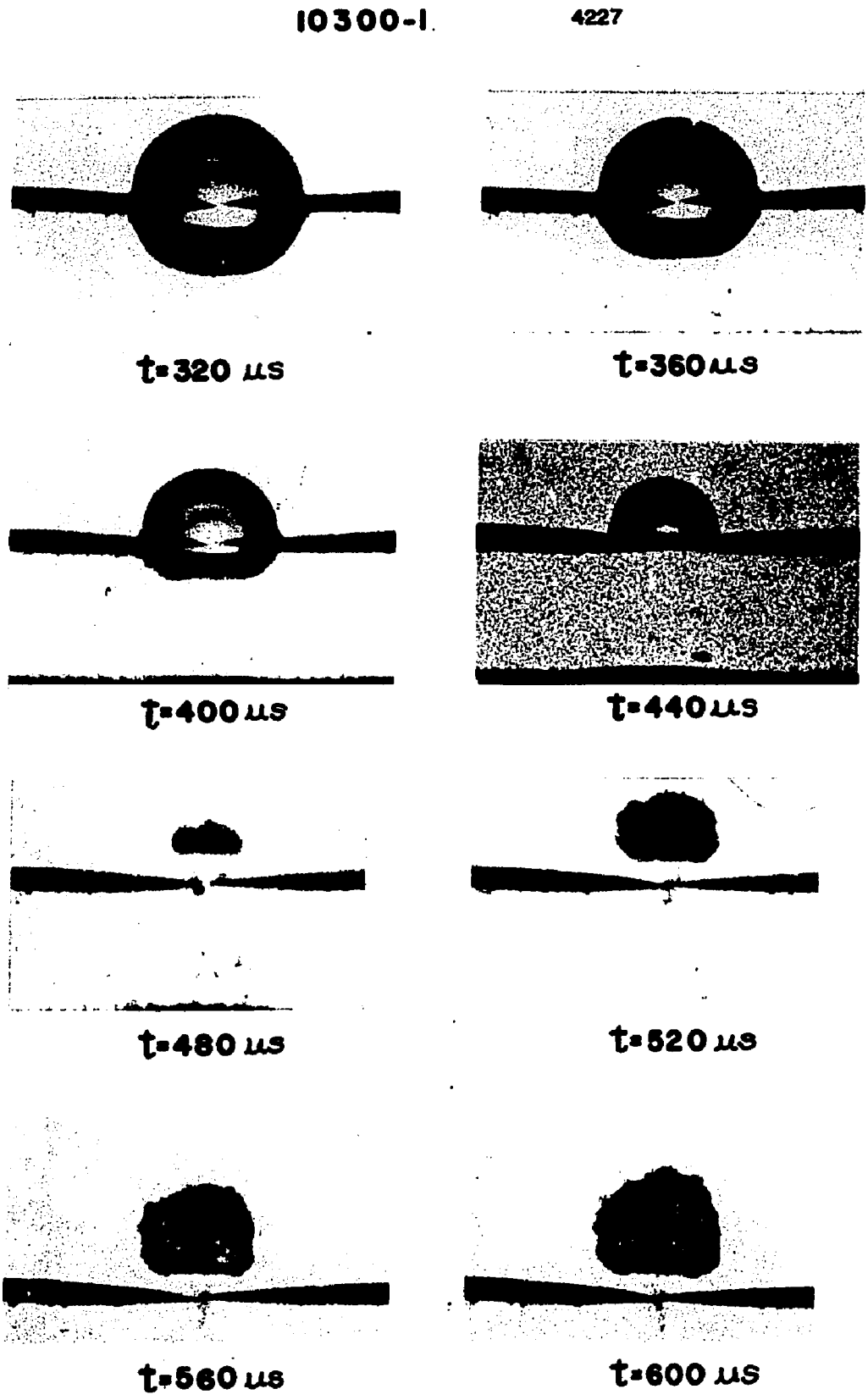


Figure 4.6 Prints, Run 10300-DSB-1, p.2

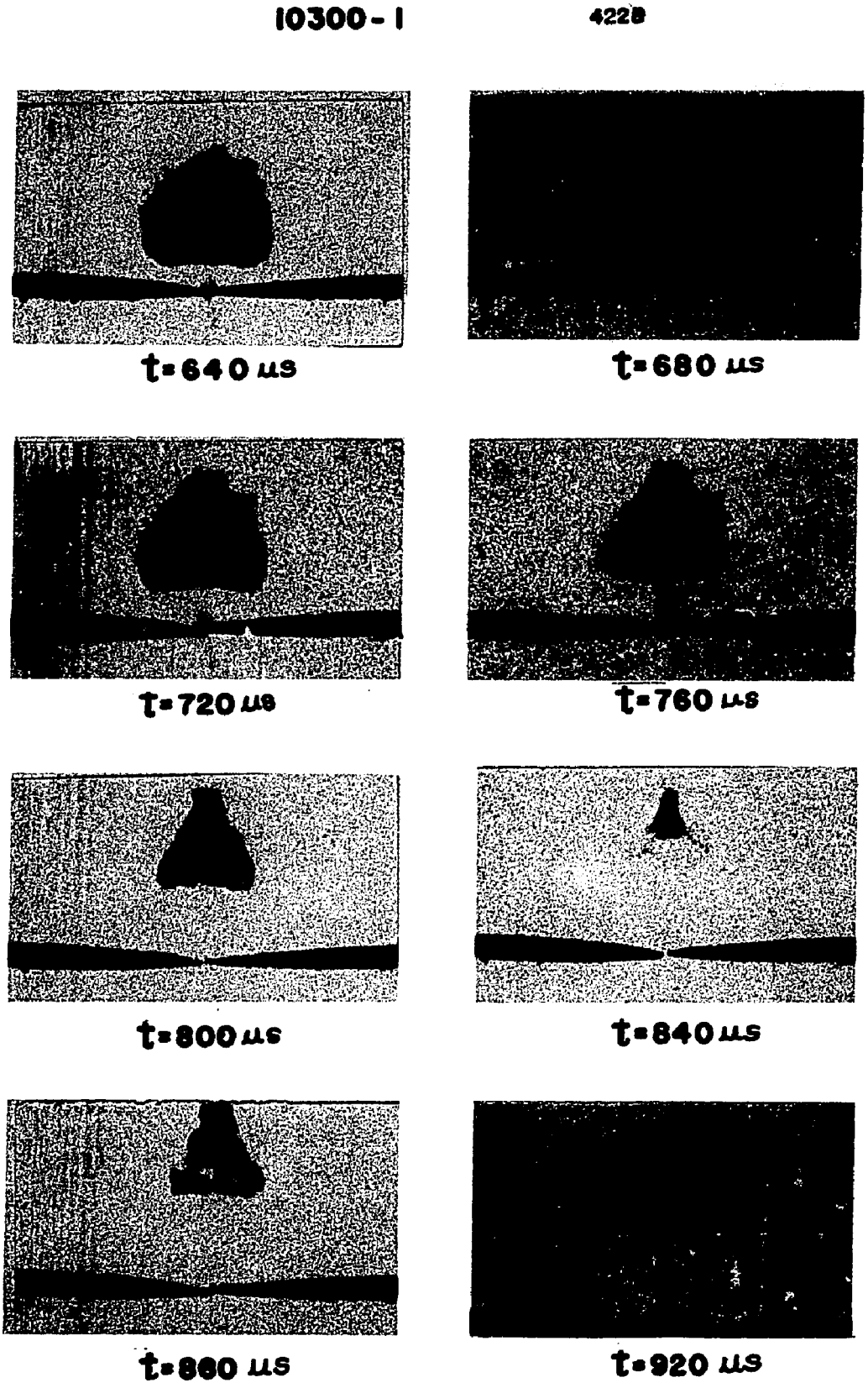


Figure 4.6 Prints, Run 10300-DSB-1, p.3

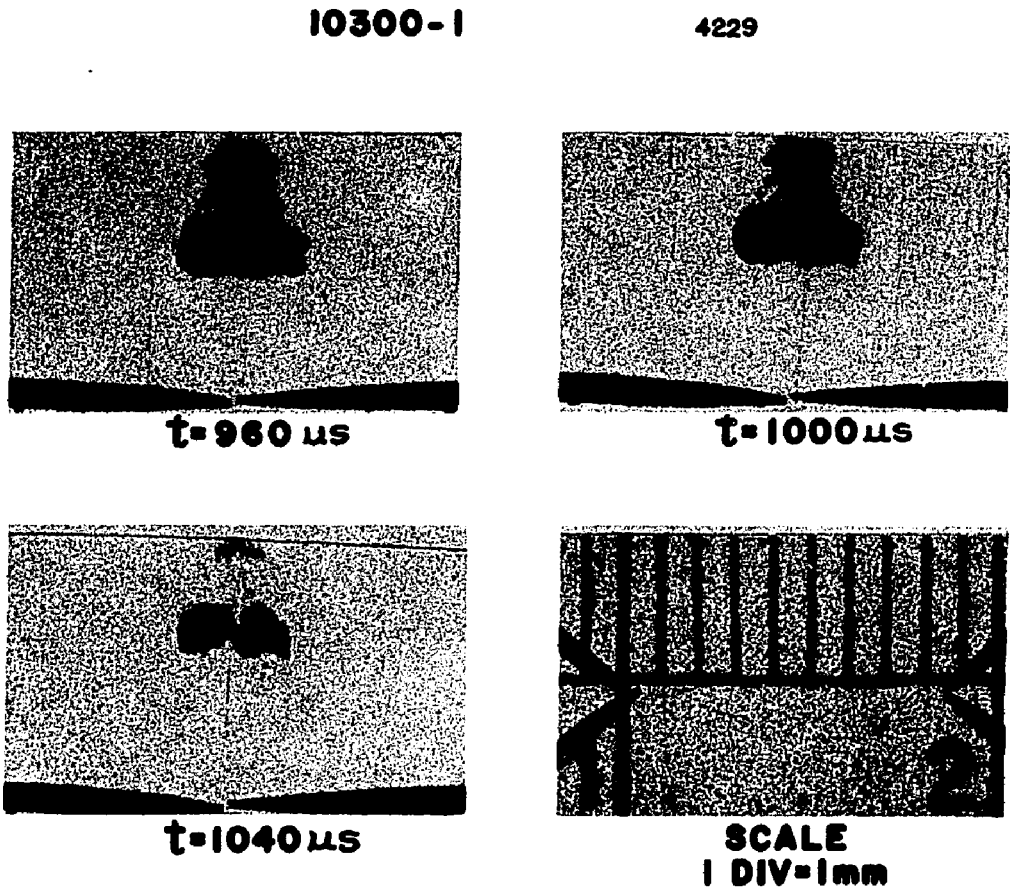


Figure 4.6 Prints, Run 10300-DSB-1, p.4

RUN 10210 – D-SB-2 4230

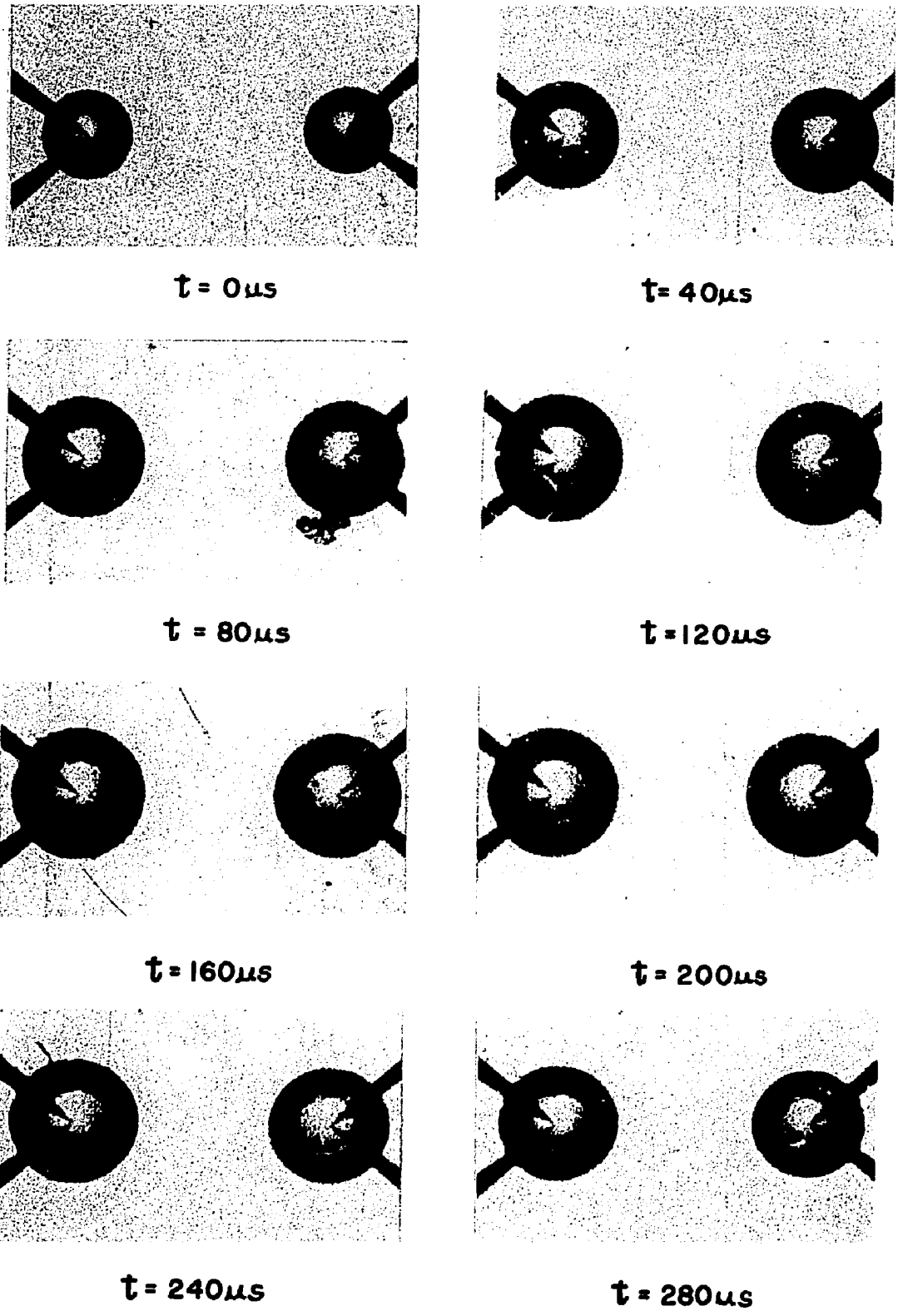


Figure 4.7 Prints, Run 10210-DSB-2, p.1

10210 – 2 4231

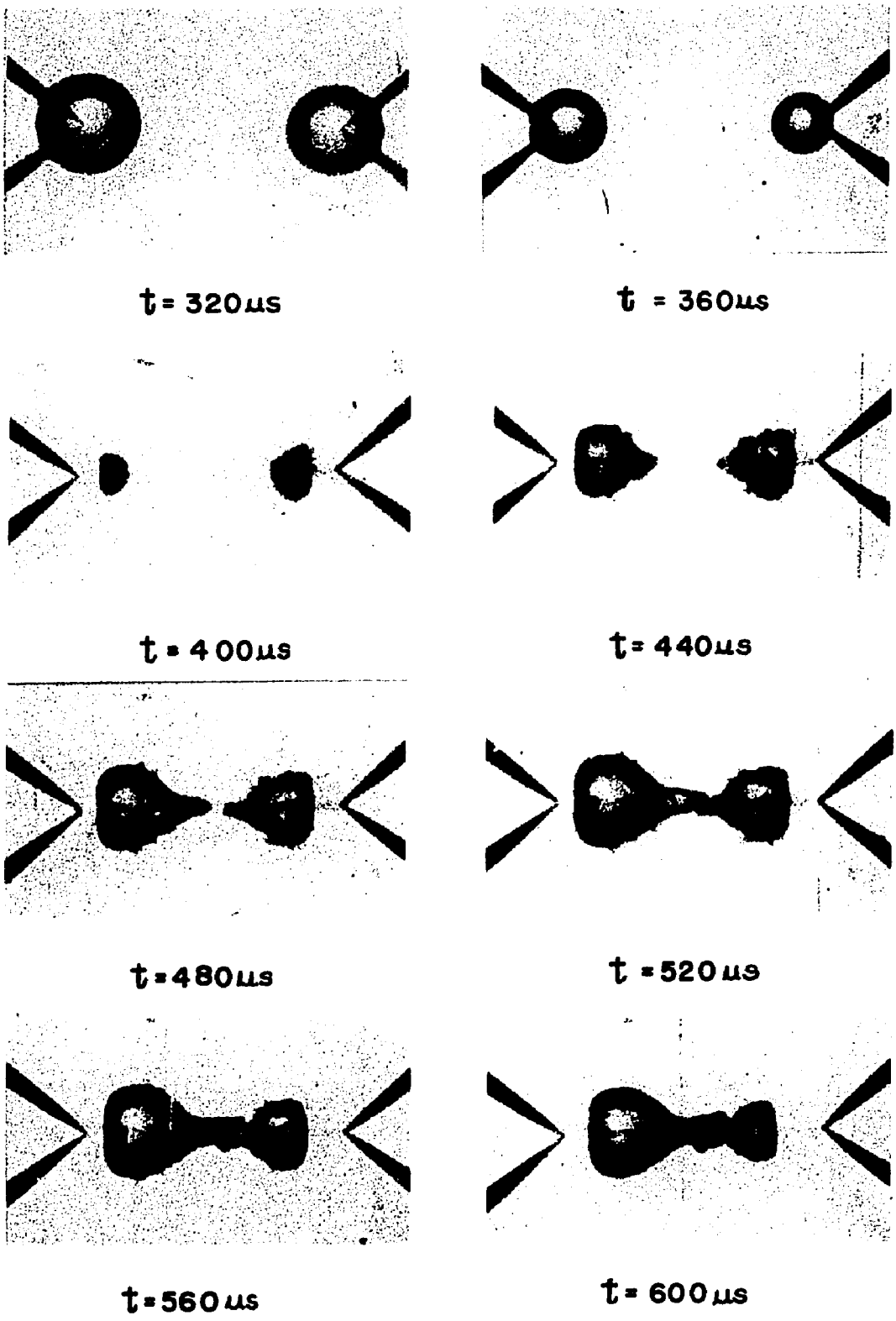


Figure 4.7 Prints, Run 10210-DSB-2, p.2

10210-2 4232

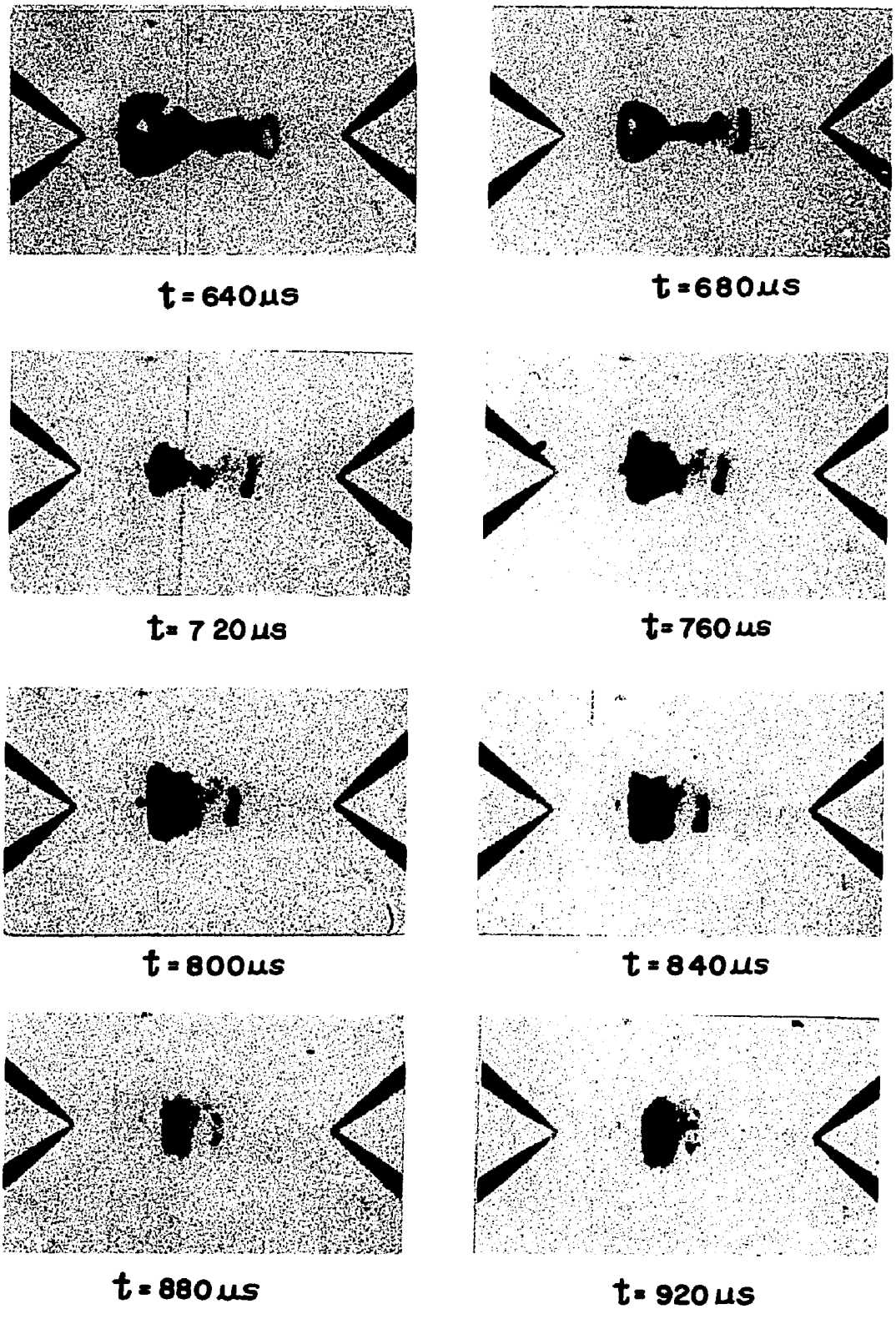


Figure 4.7 Prints, Run 10210-DSB-2, P.3

10210– 2 4233

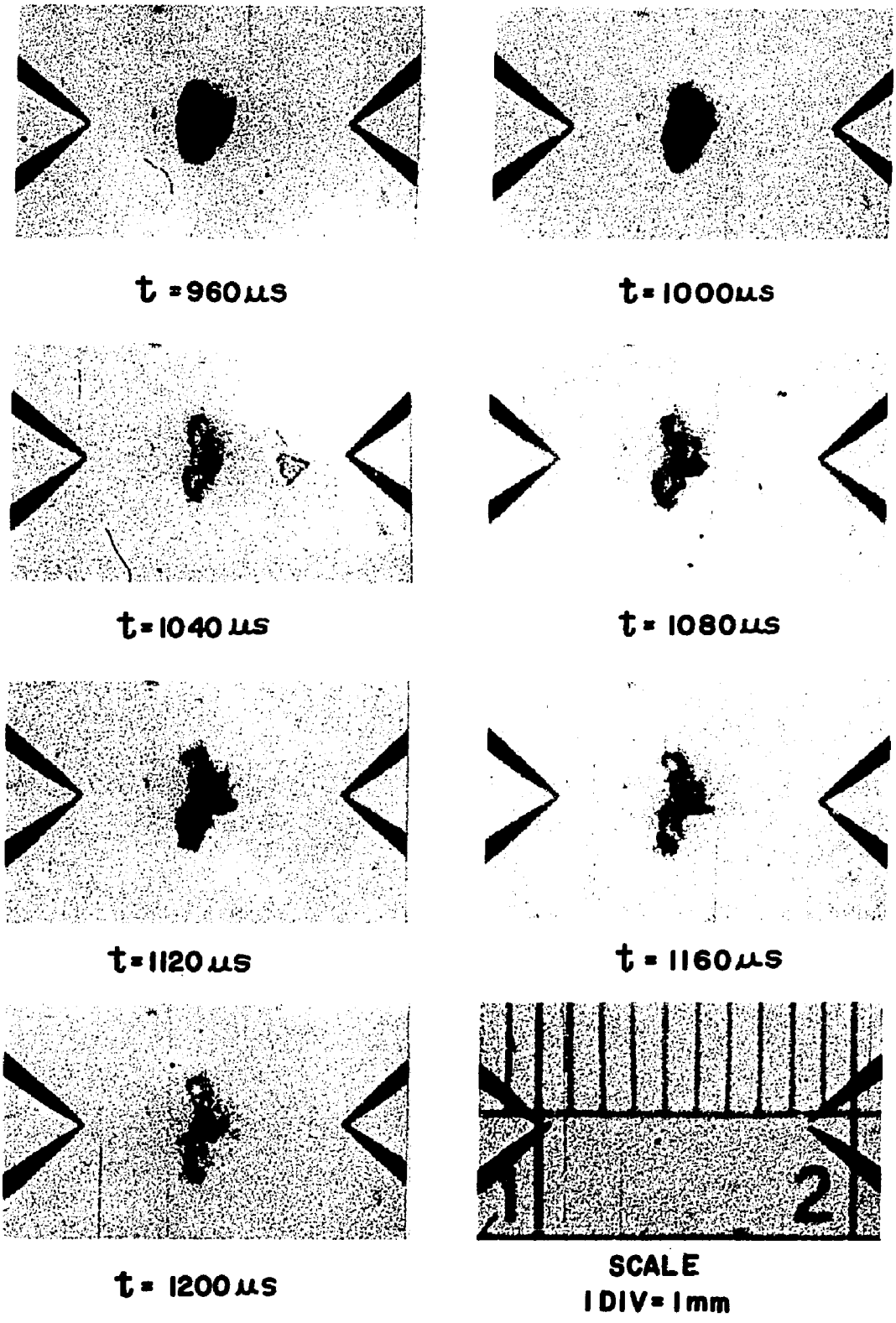


Figure 4.7 Prints, Run 10210-DSB-2, p.4

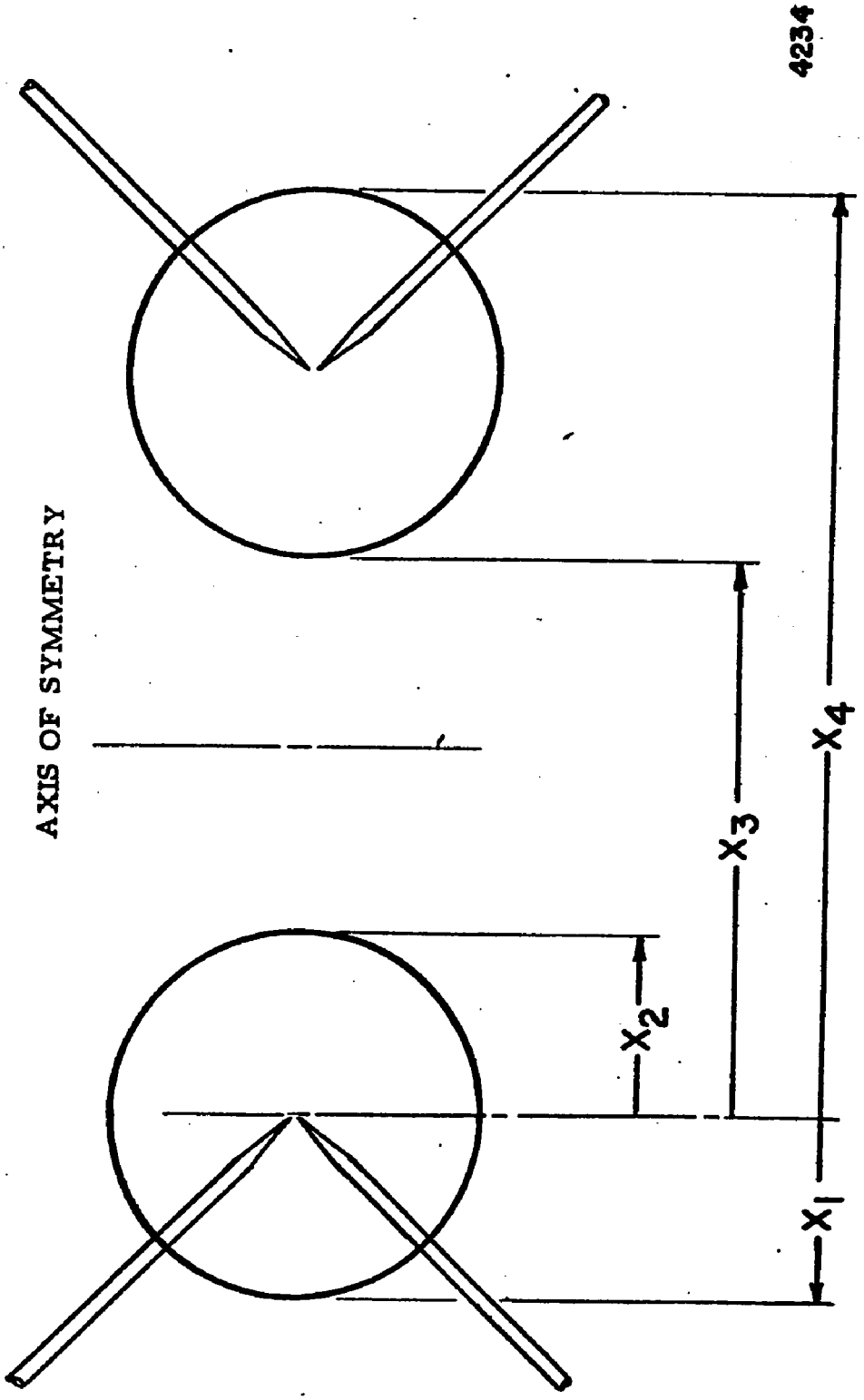


Figure 4.8 Double Bubble Measurement Diagram

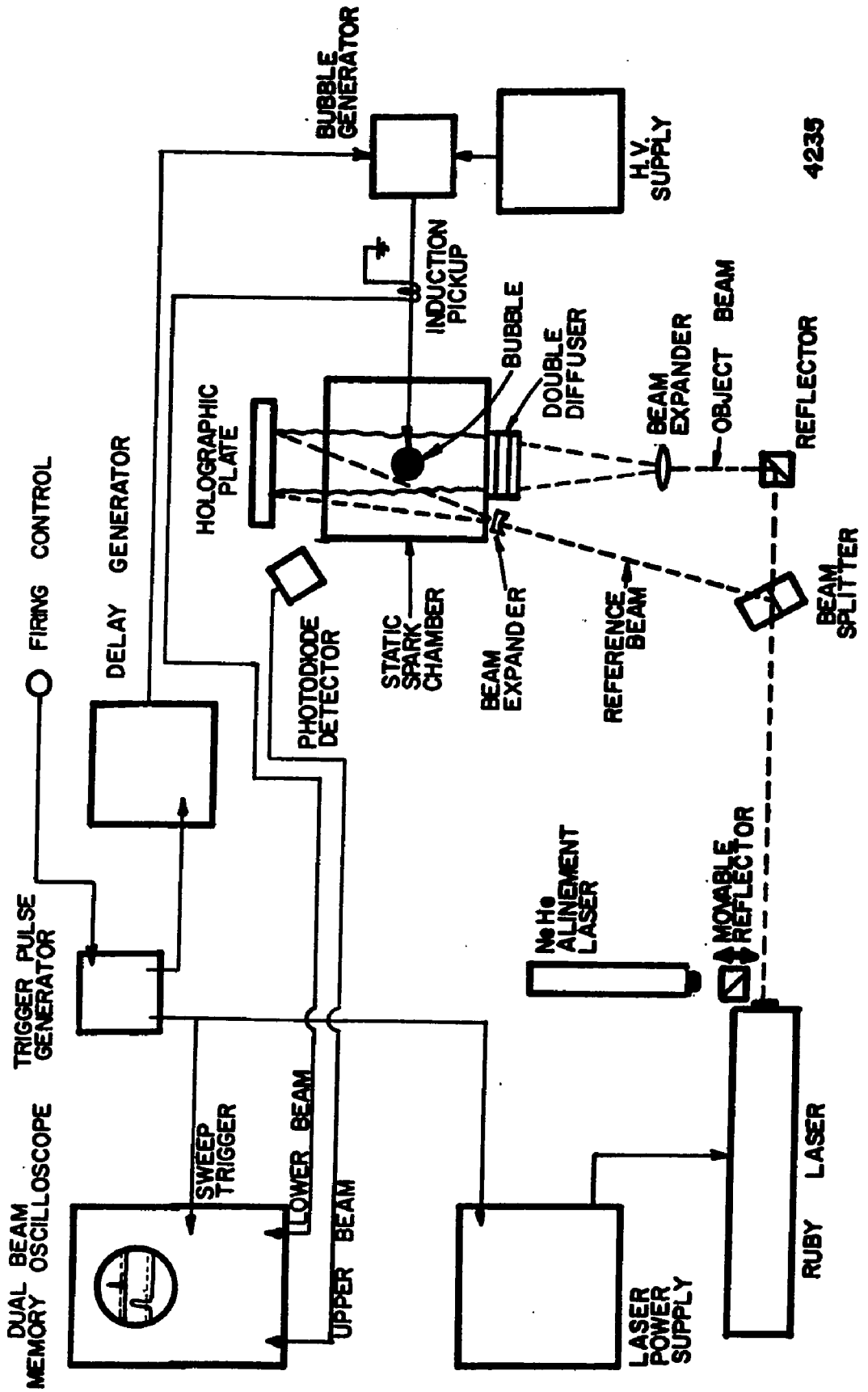
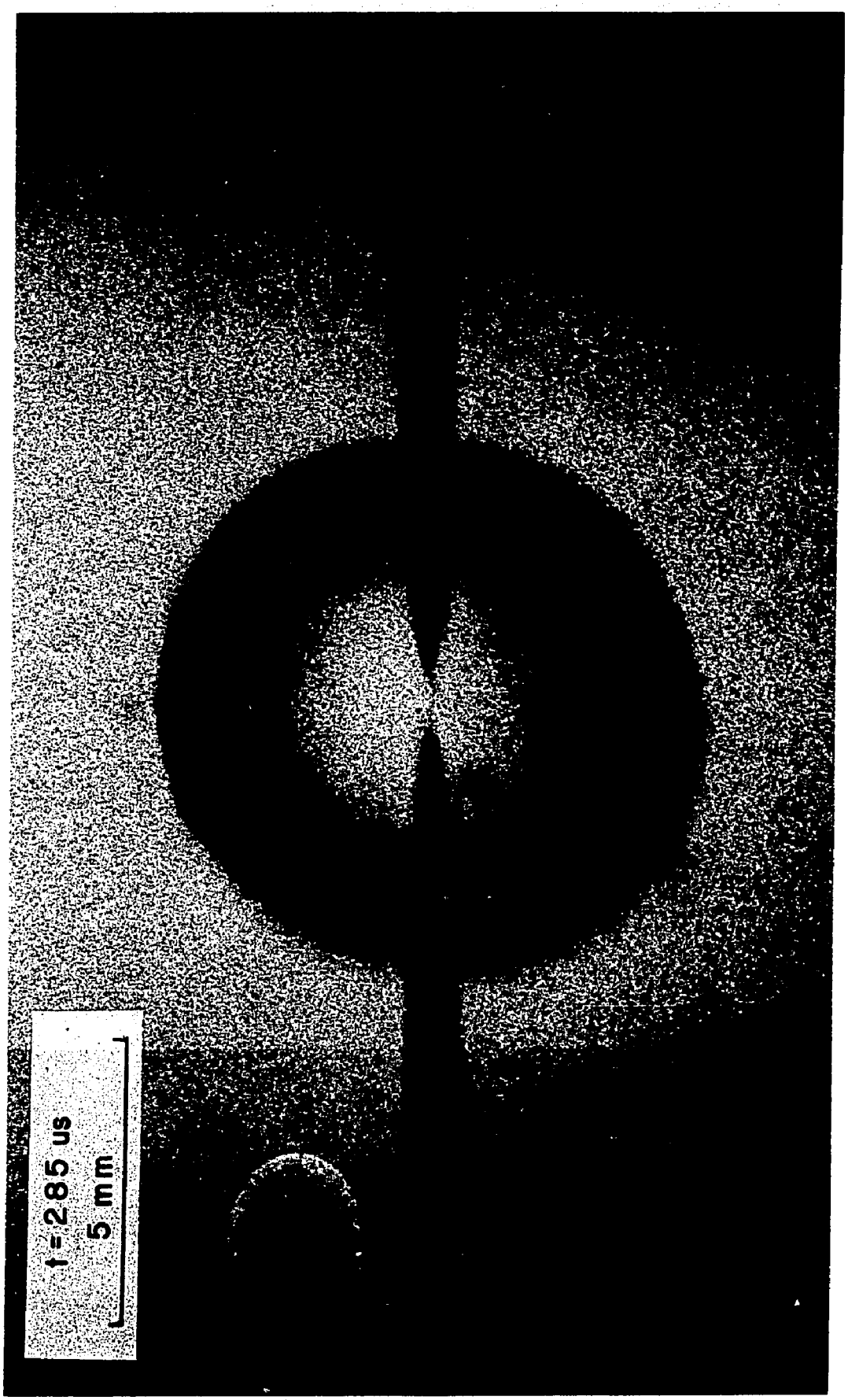


Figure 4.9 Schematic of Holographic Facility



4236

Figure 4.10 Photograph of Hologram, Run1229-H-SB-5

RUN 1191-D-FB-1
ΔP= 3.44 Atm
V= 23 m/s
AIR= 0.31 %

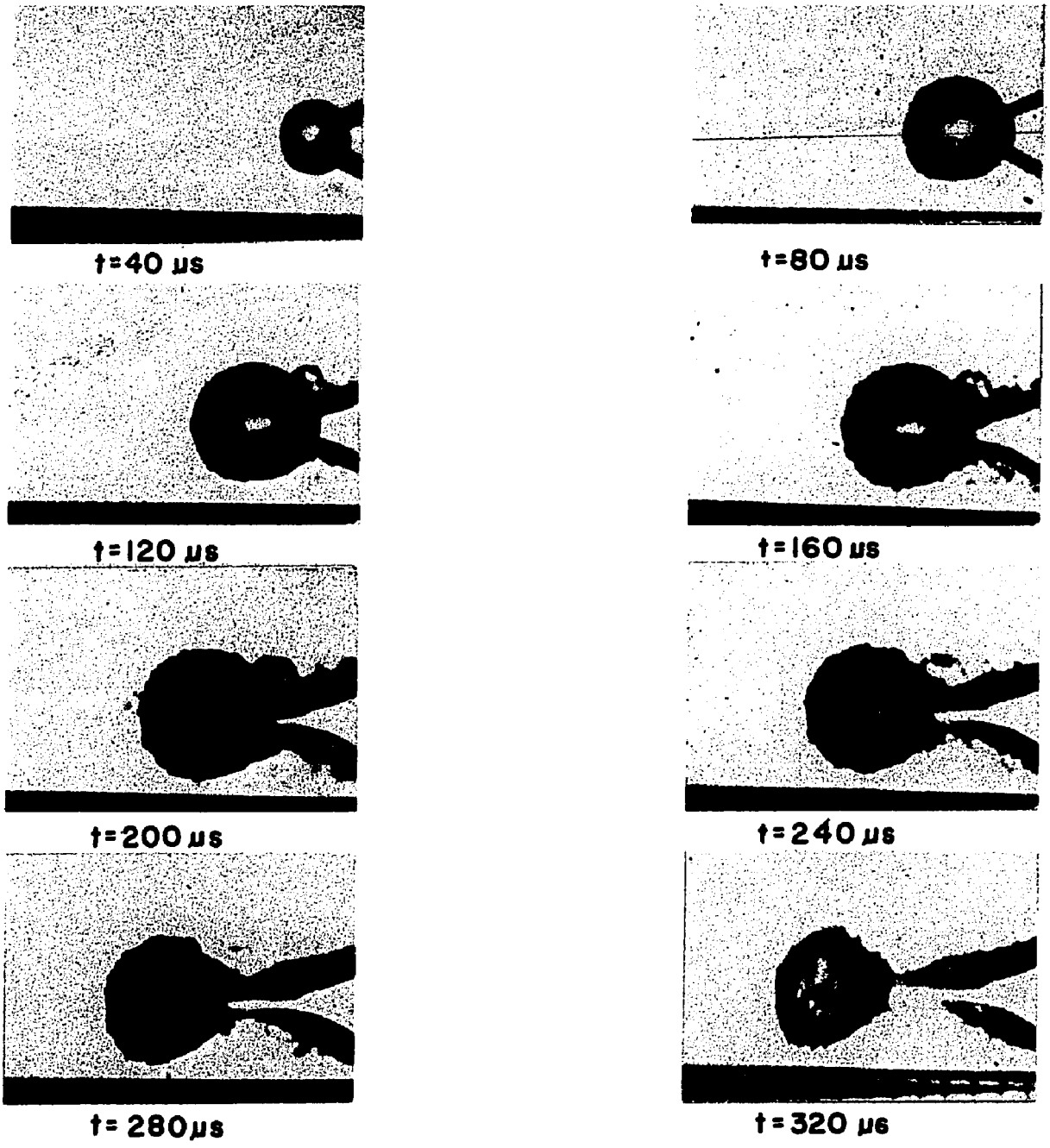
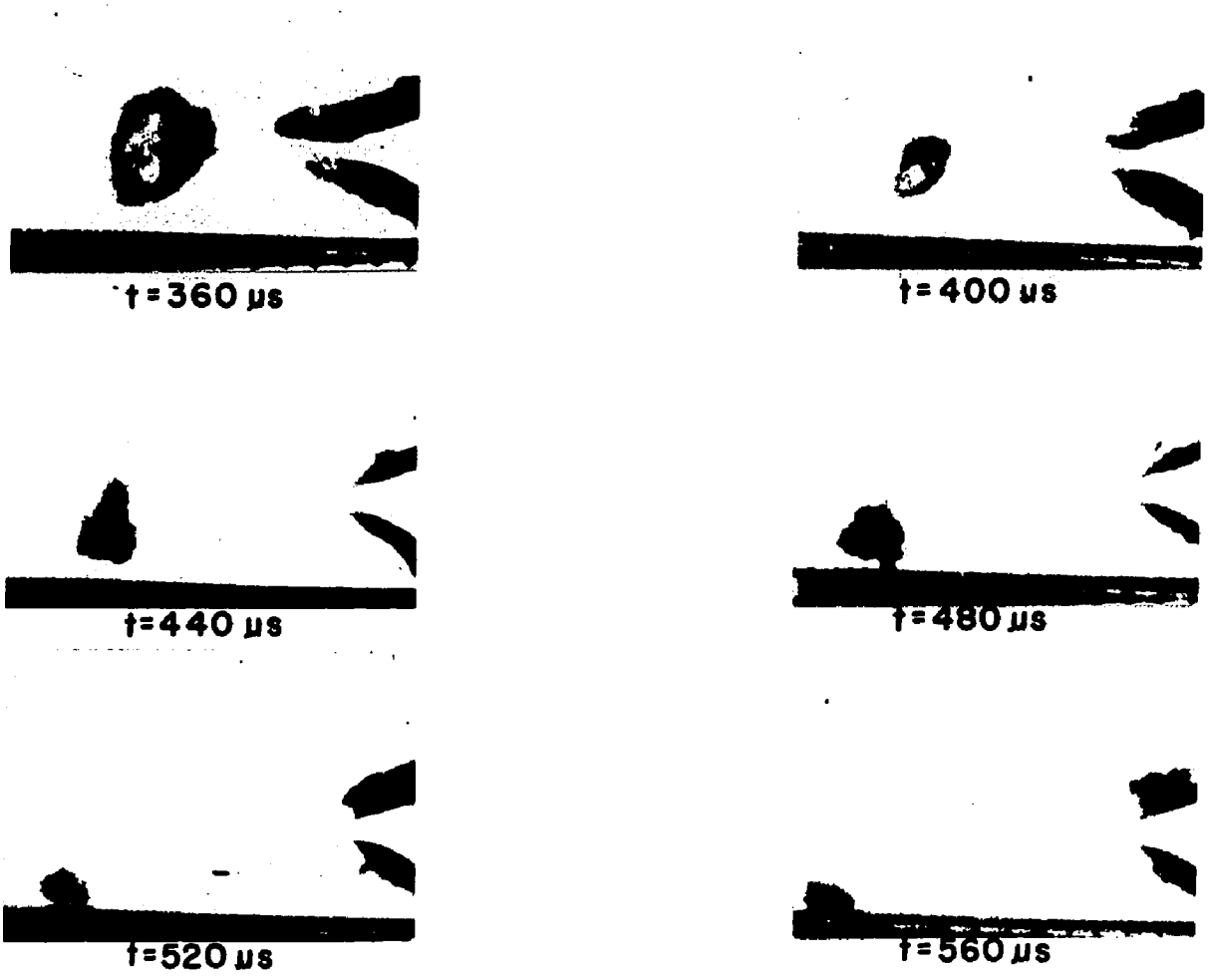


Figure 4.11 Prints, Run 1191-DFB-1, p. 1

4237

1191--1



4238

Figure 4.11 Prints, Run 1191-DFB-1, p. 2

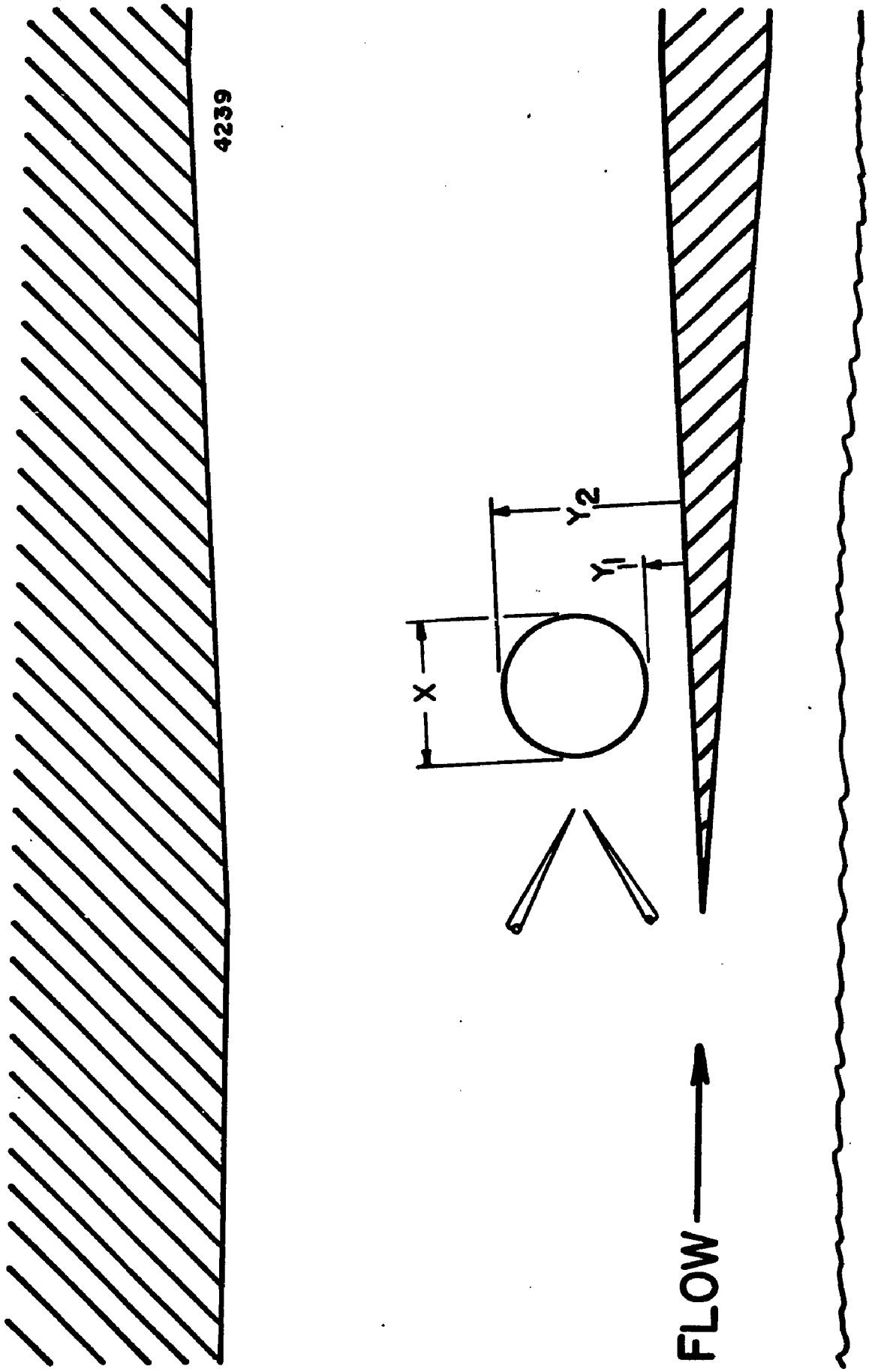
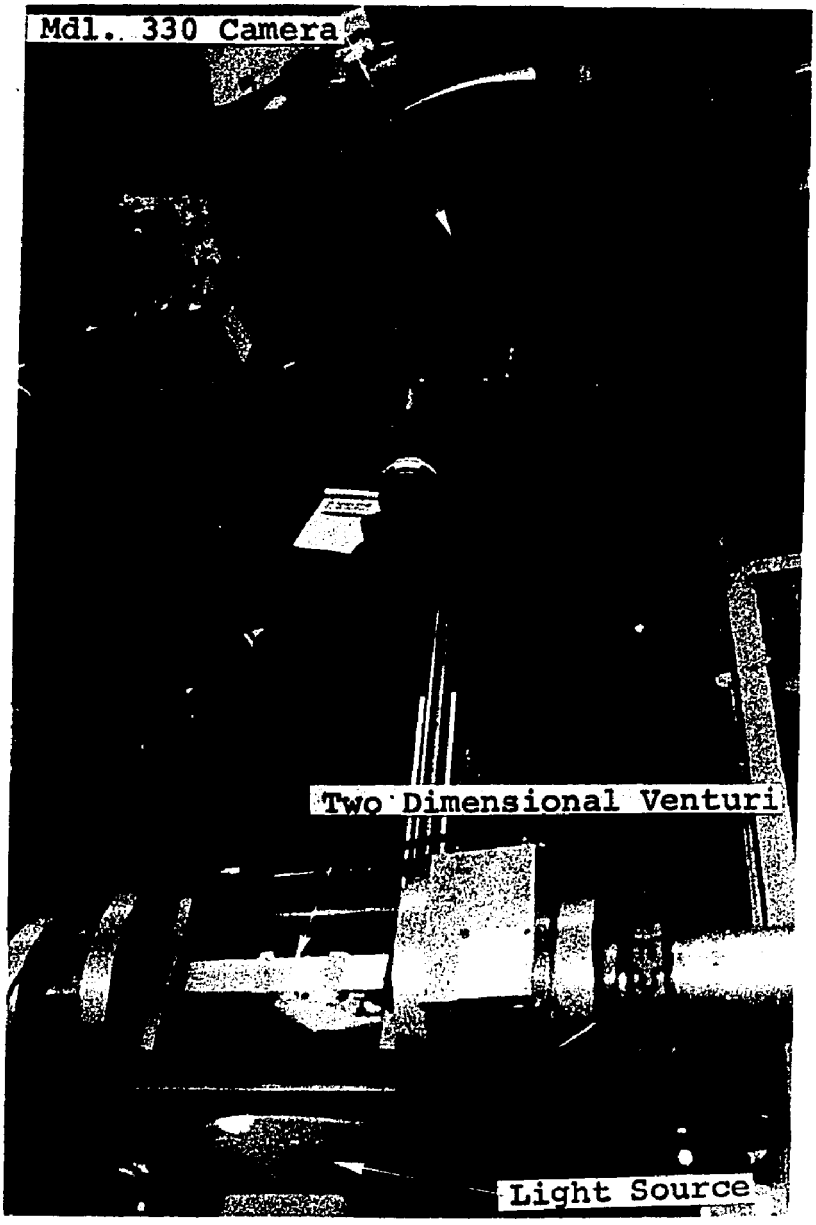


Figure 4.12 Two Dimensional Venturi Measurement Diagram



4240

Figure 4.13 Two Dimensional Venturi w/Model 330 Camera

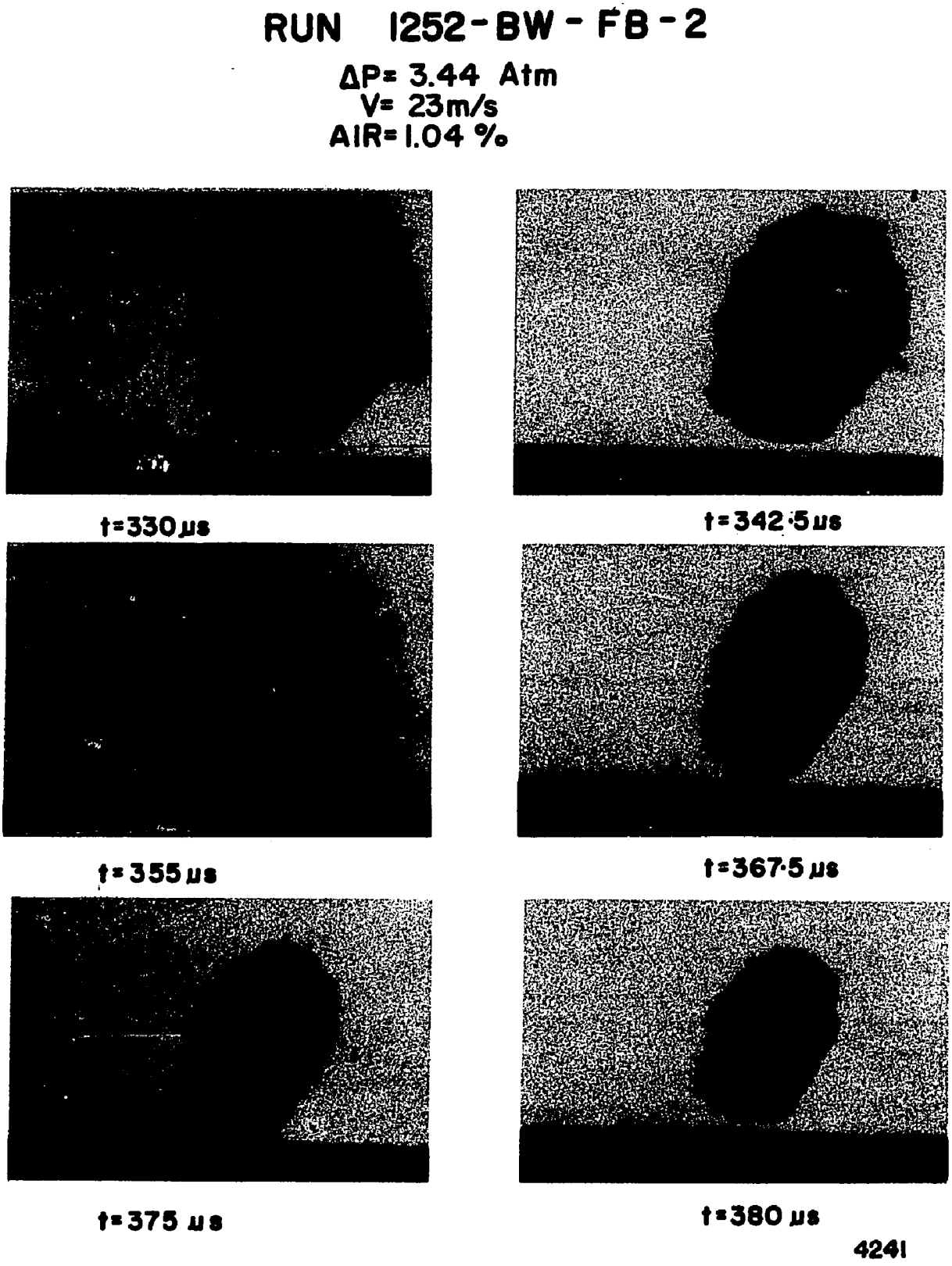


Figure 4.14 Prints, Run 1252-BW-FB-2, p. 1

1252--2

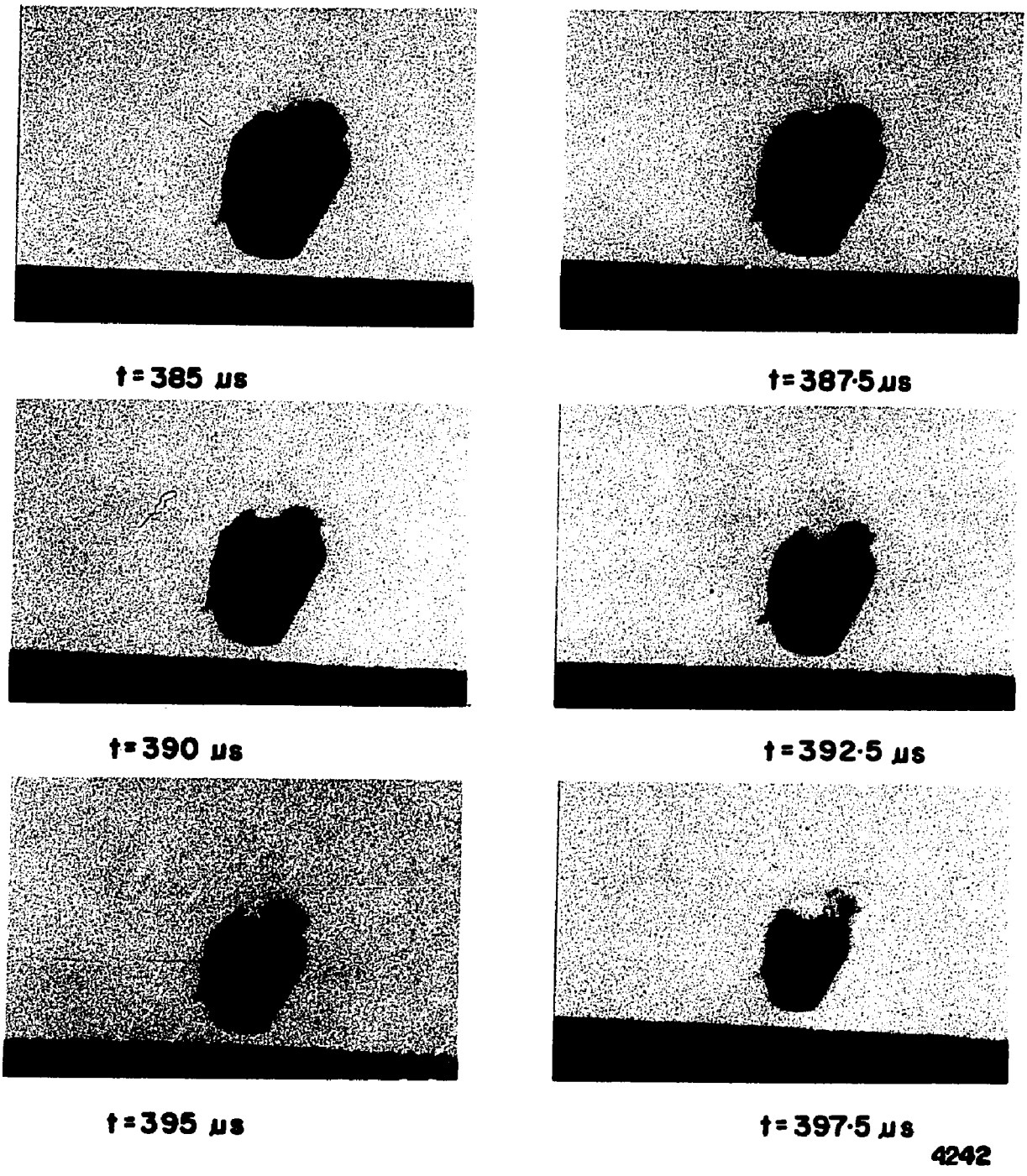


Figure 4.14 Prints, Run 1252-BW-FB-2, p. 2

1252--2

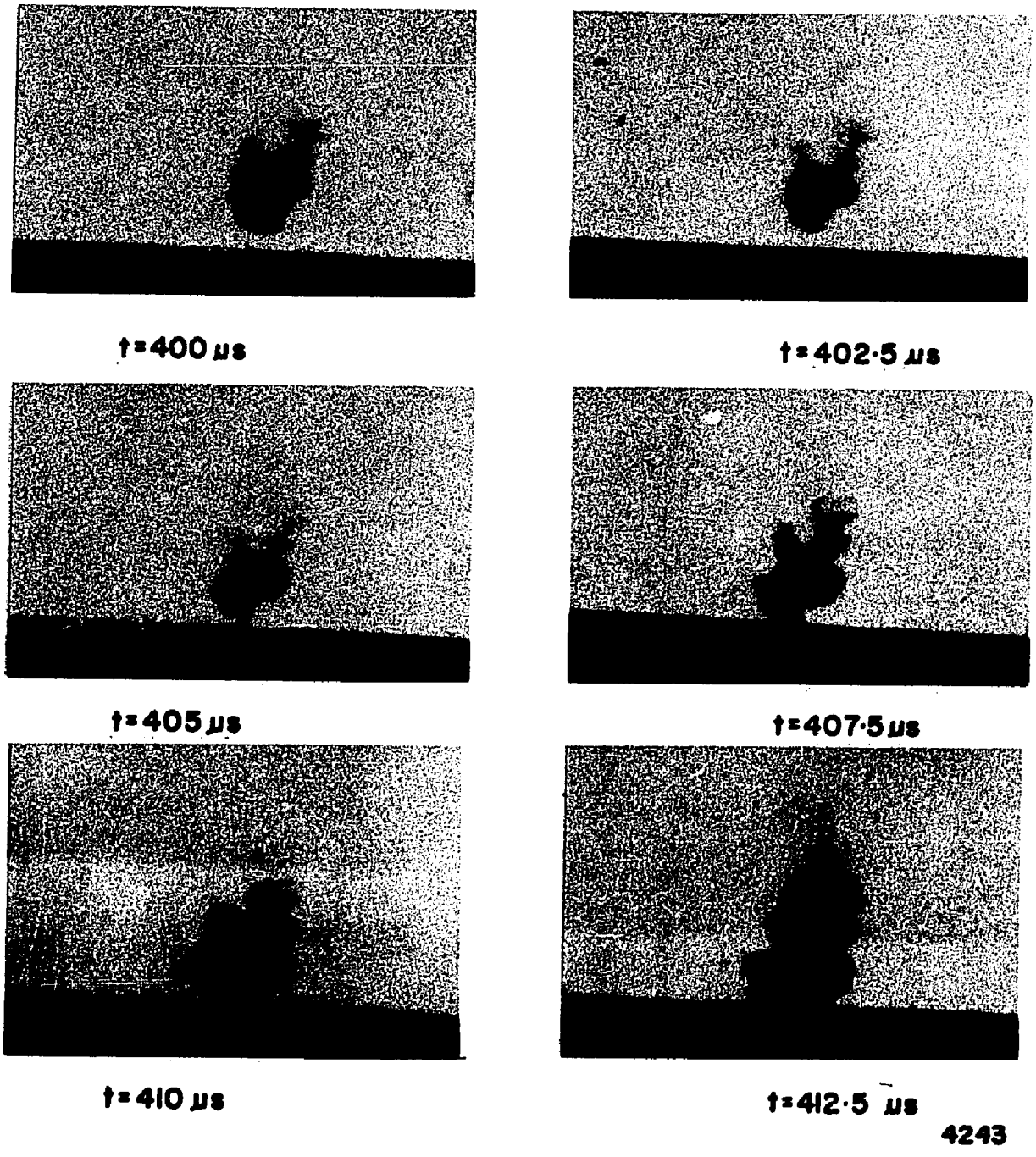
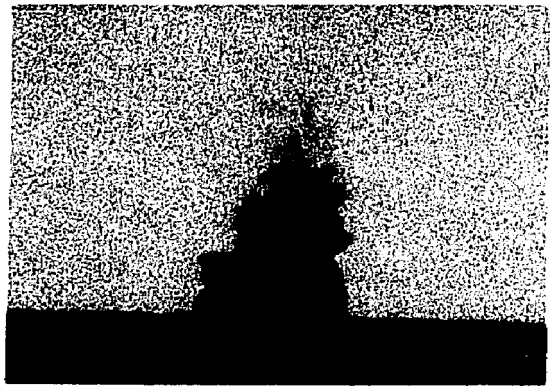


Figure 4.14 Prints, Run 1252-BW-FB-2, p. 3

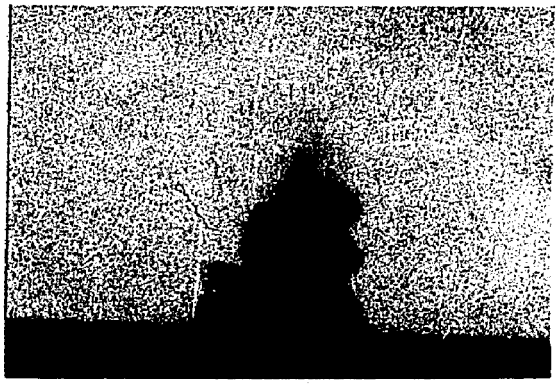
1252--2



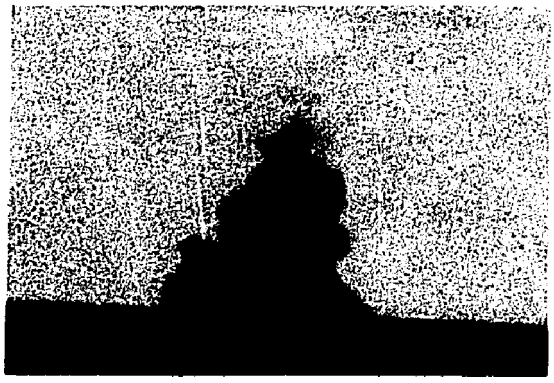
t = 415 μs



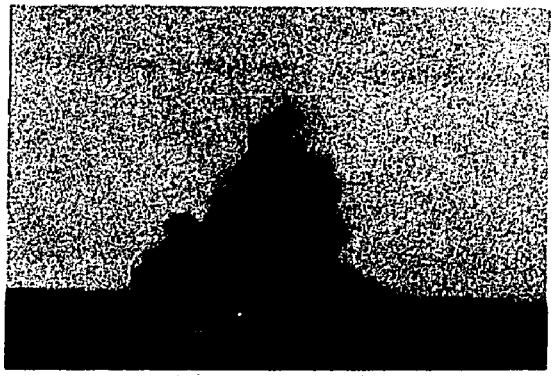
t = 417·5 μs



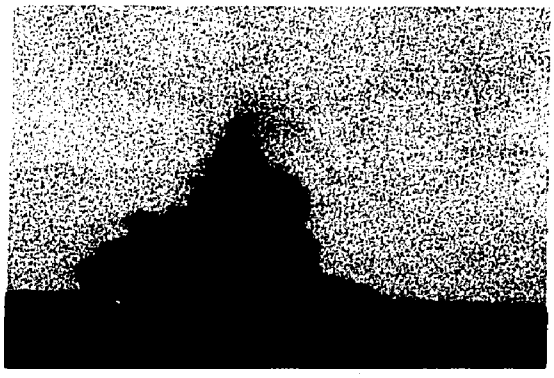
t = 422·5 μs



t = 430 μs



t = 442·5 μs



t = 467·5 μs

4244

Figure 4.14 Prints, Run 1252.-BW-FB-2, p. 4

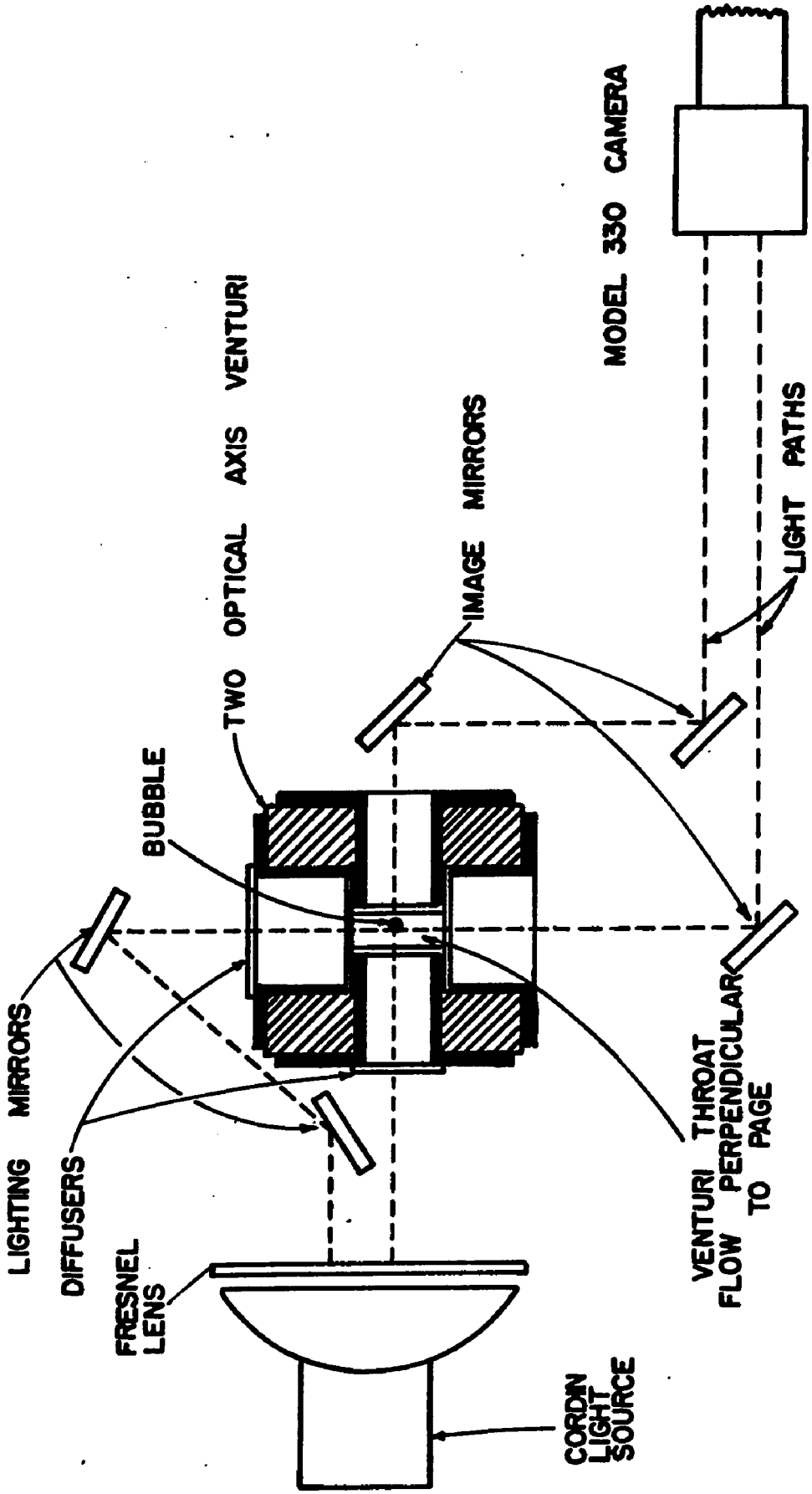


Figure 4.15 Schematic of Two Optical Axis Venturi Setup

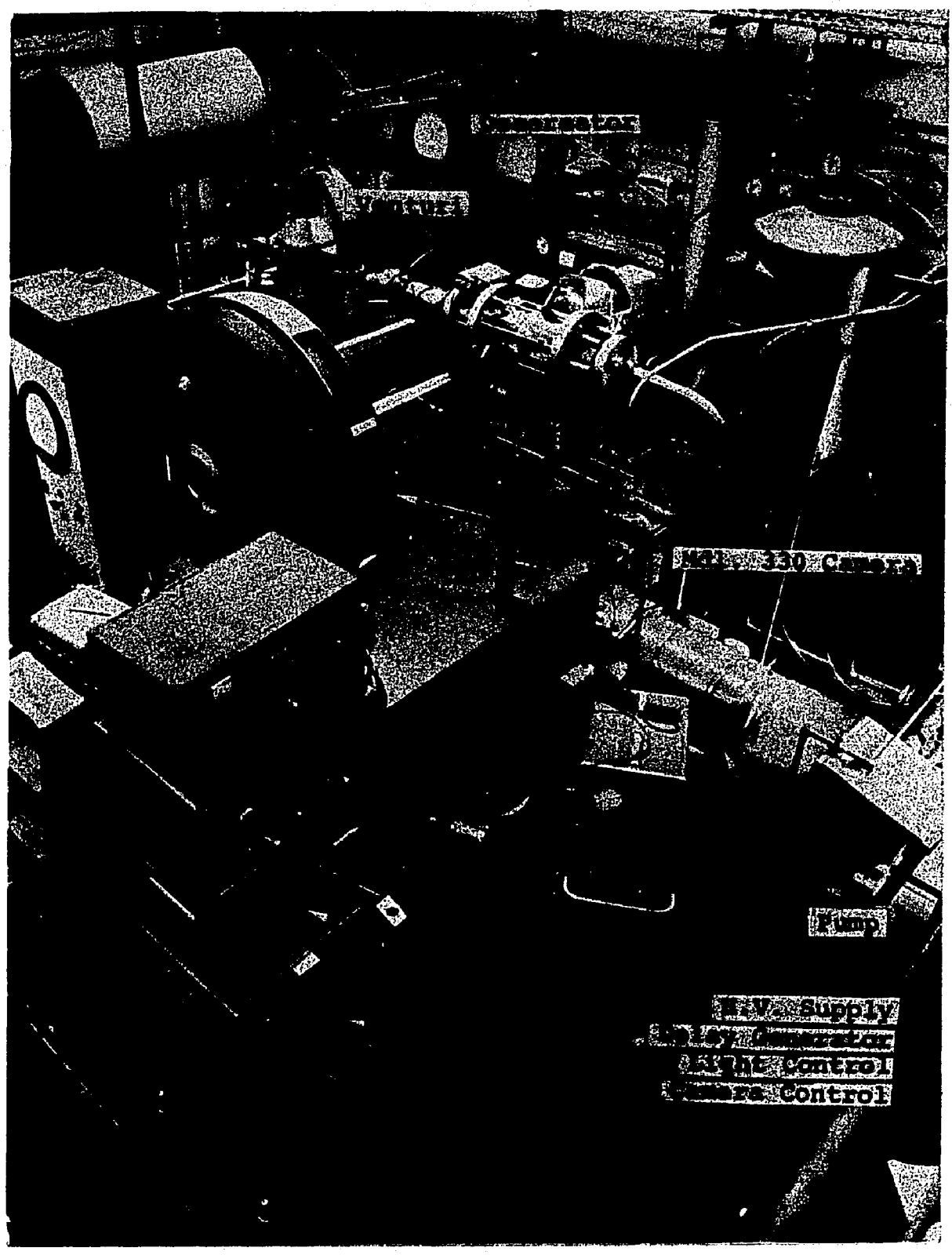


Figure 4.16 Two Optical Axis Venturi w/Model 330 Camera

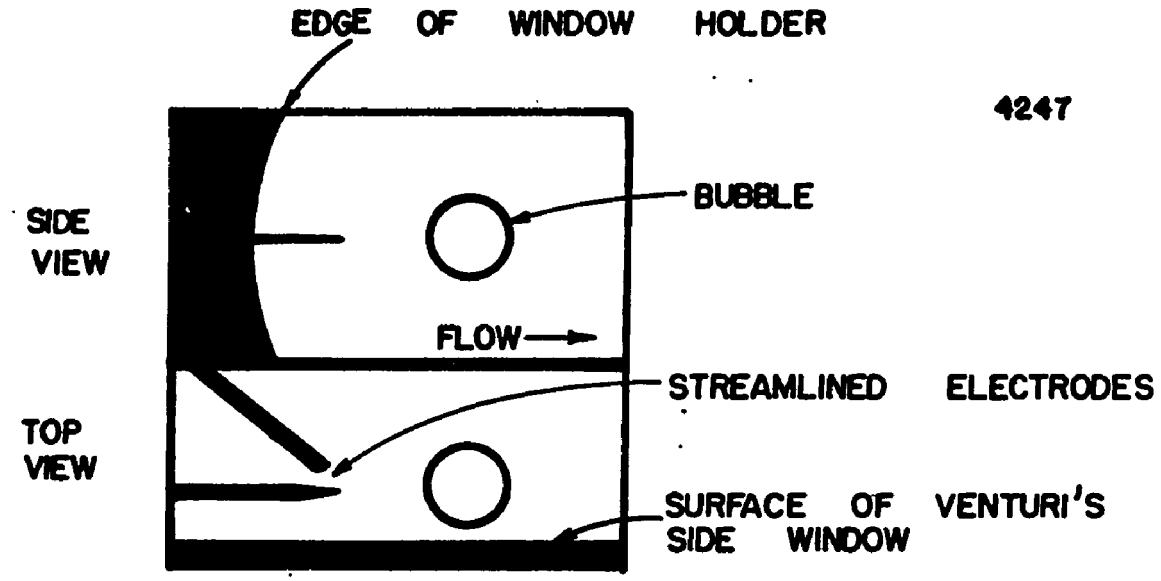


Figure 4.17 Interpretation of Two Optical Axis Prints

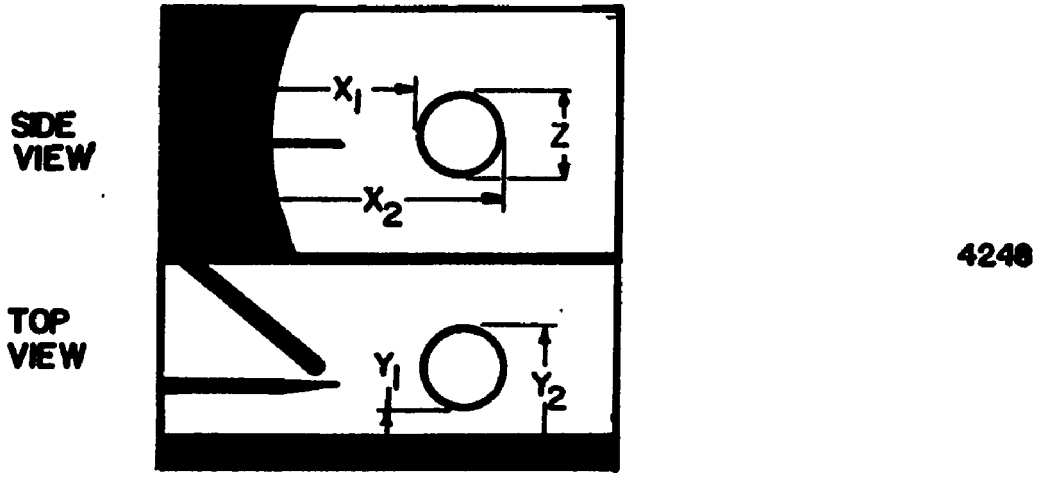


Figure 4.18 Two Optical Axis Measurement Diagram

RUN 7102-BW-2D-4

ΔP=2.03 Atm
V= 18.3 m/s
AIR = 0.68 %

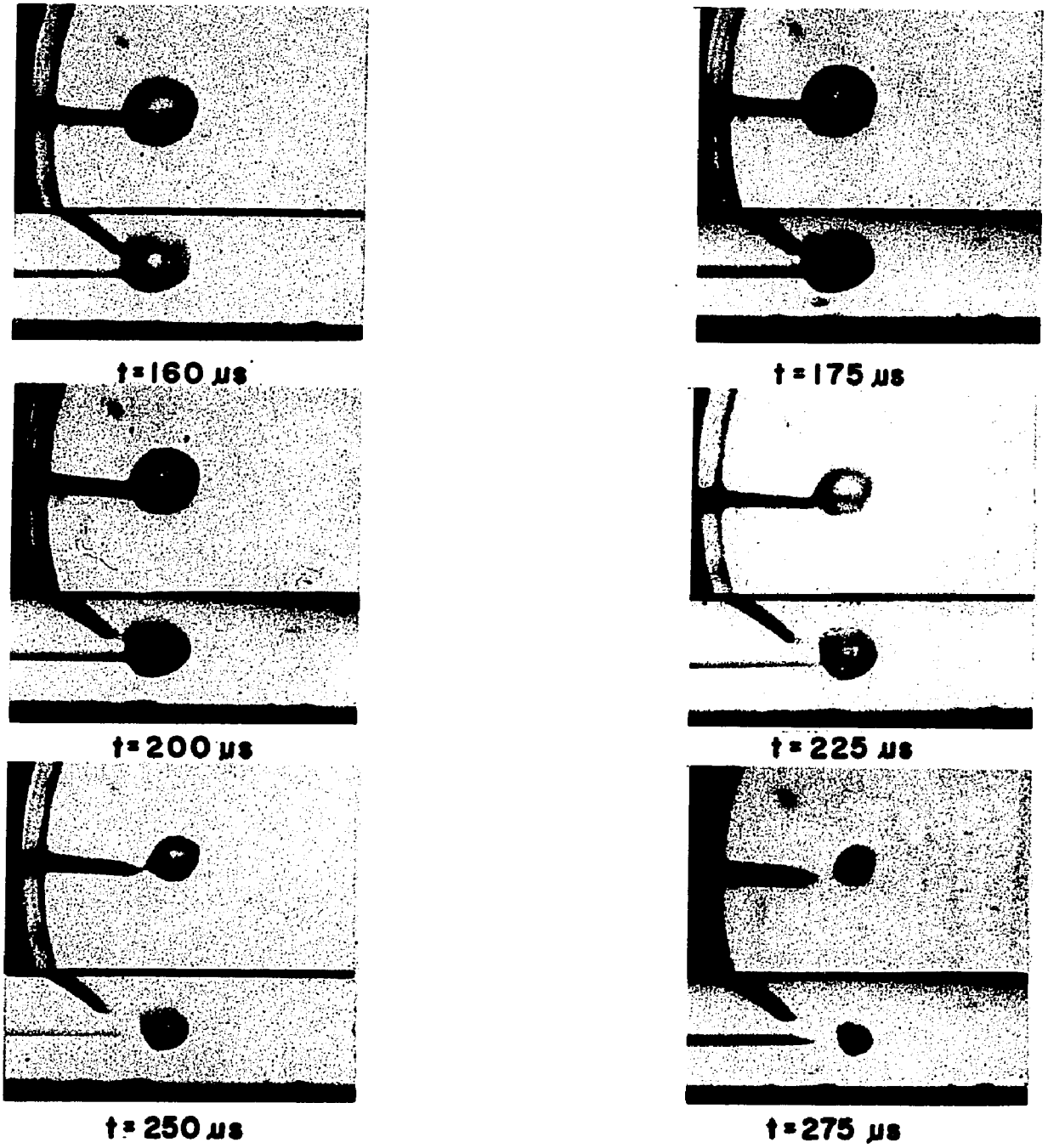


Figure 4.19 Prints, Run 7102-BW-2D-4, p. 1

4249

7102-- 4

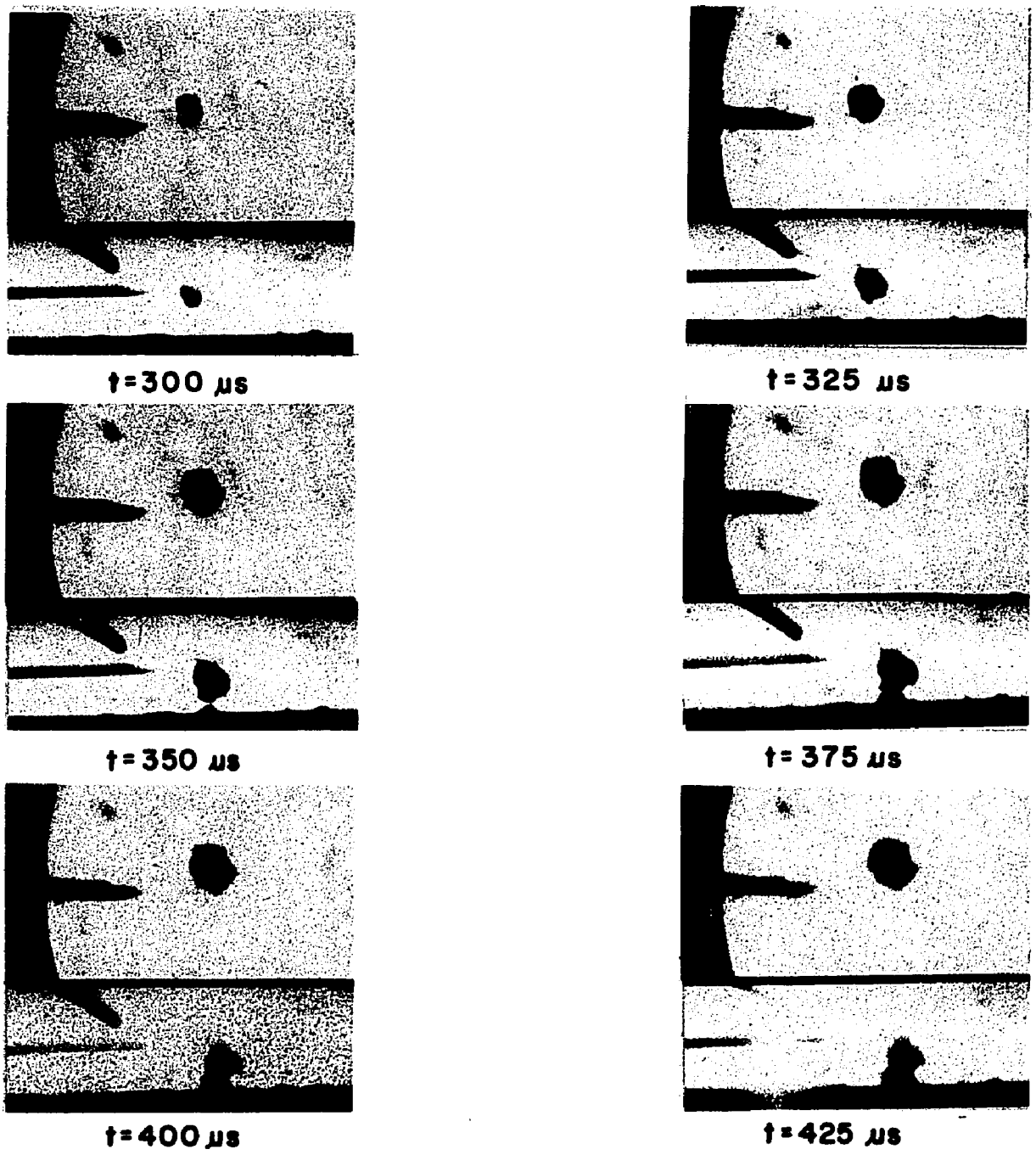
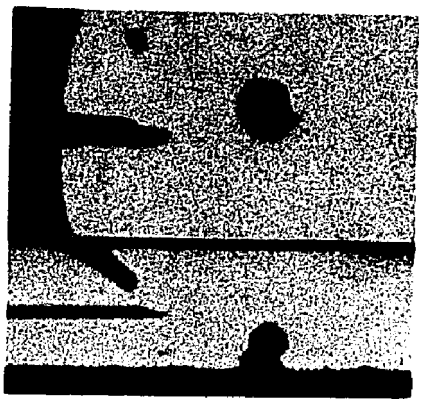


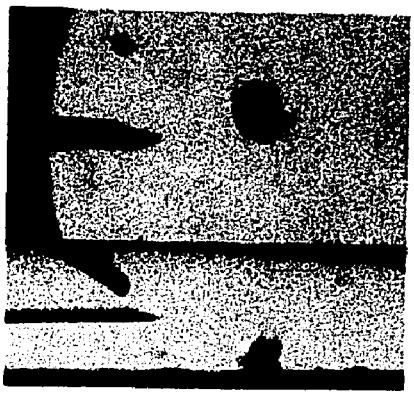
Figure 4.19 Prints, Run 7102-BW-2D-4, p. 2

4250

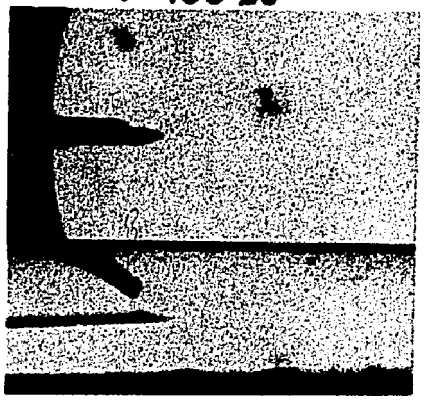
7102--4



t=450 μs



t=475 μs

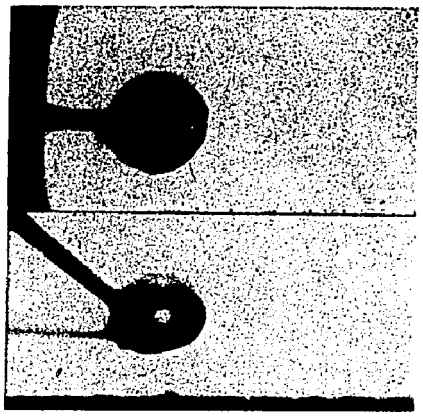


t=500 μs

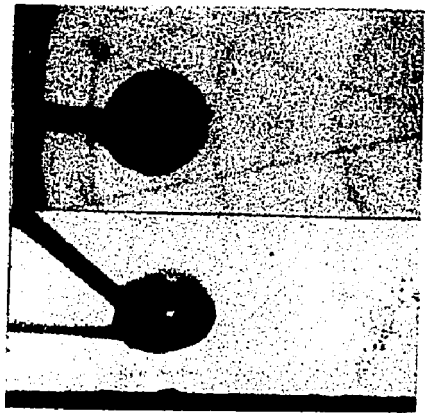
Figure 4.19 Prints, Run 7102-BW-2D-4, p. 3

RUN 842-BW-2D-5

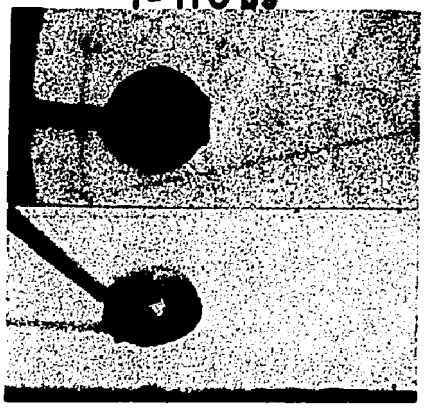
ΔP = 1.98 Atm
V = 18.3 m/s
AIR = 0.49 %



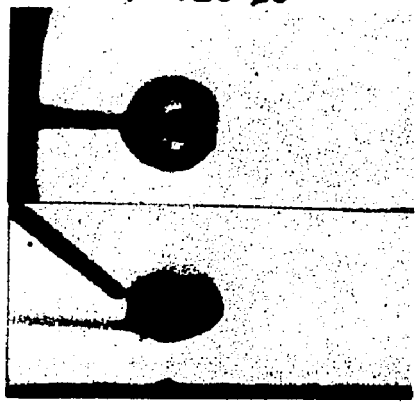
t = 110 μs



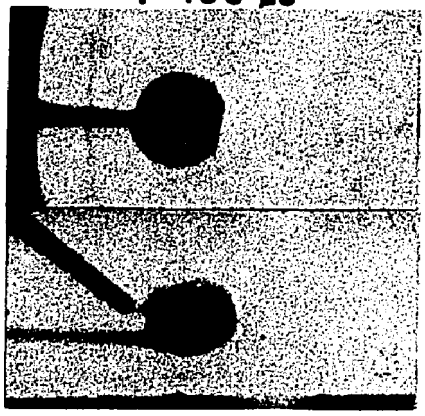
t = 125 μs



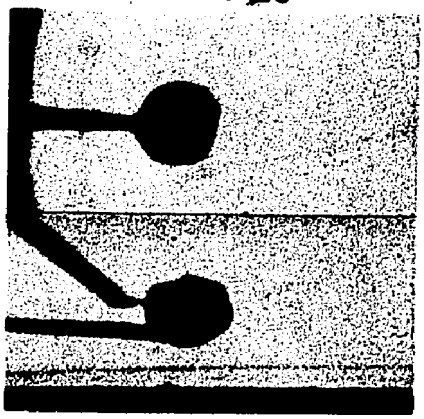
t = 150 μs



t = 175 μs



t = 200 μs



t = 225 μs

Figure 4.20 Prints, Run 842-BW-2D-5, p. 1 4252

842- -5

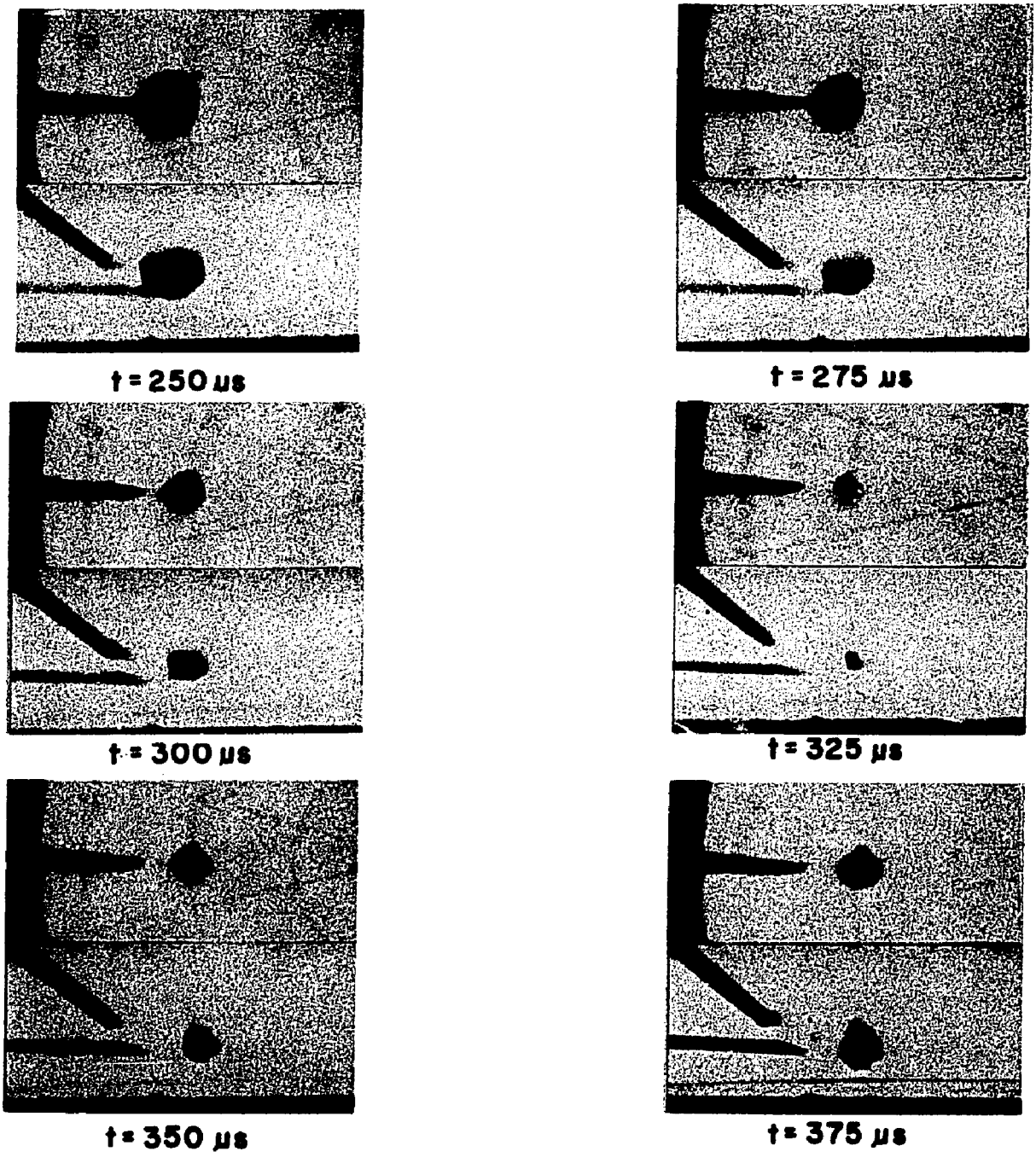
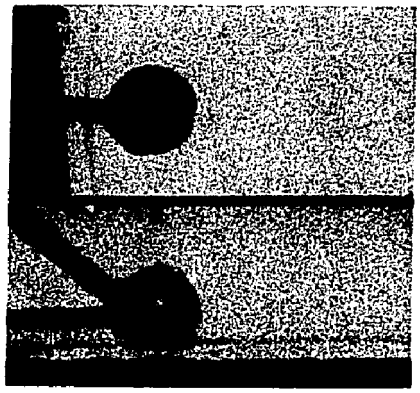


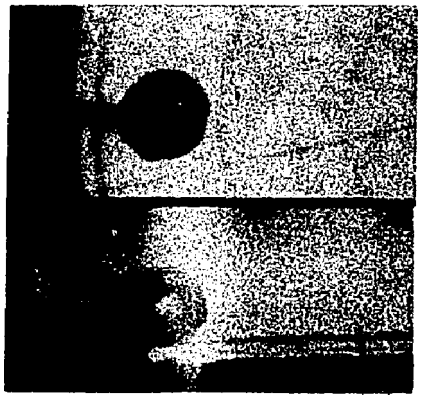
Figure 4.20 Prints, Run 842-BW-2D-5, p. 2

RUN 852-BW-2D-3

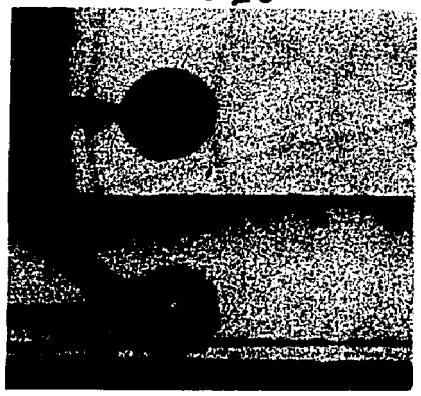
ΔP = 2.01 Atm
V = 18.3 m/s
AIR = 0.46 %



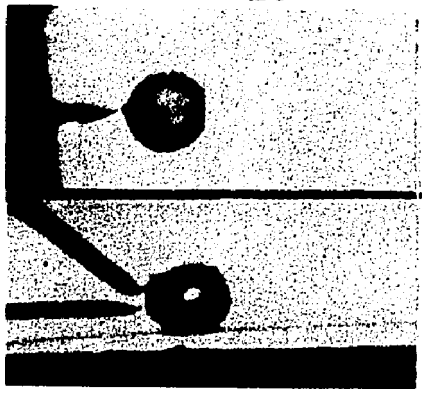
t = 110 μs



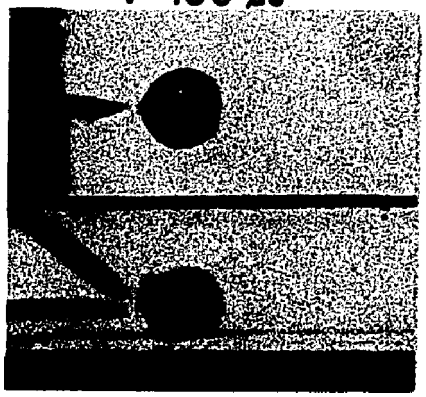
t = 125 μs



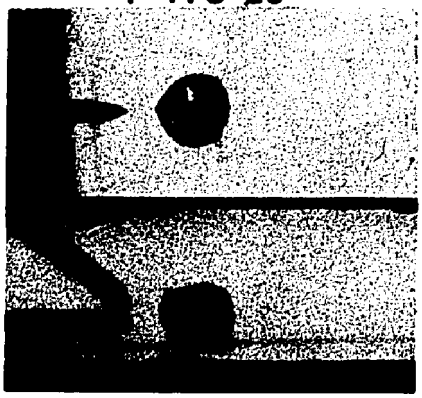
t = 150 μs



t = 175 μs



t = 200 μs

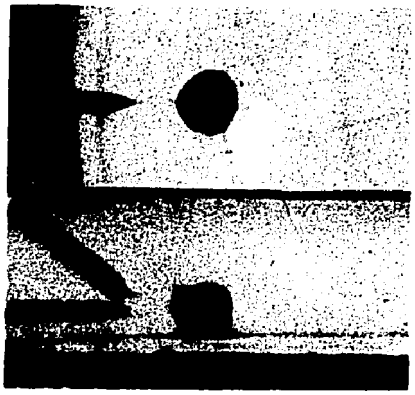


t = 225 μs

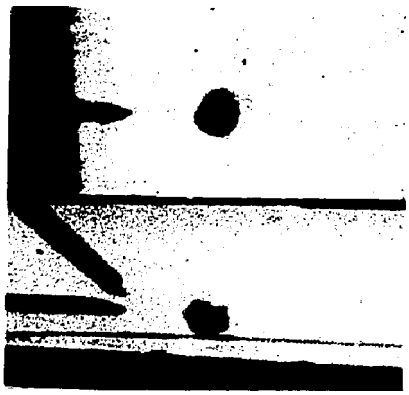
Figure 4.21 Prints, Run 852-BW-2D-3, p. 1

4254

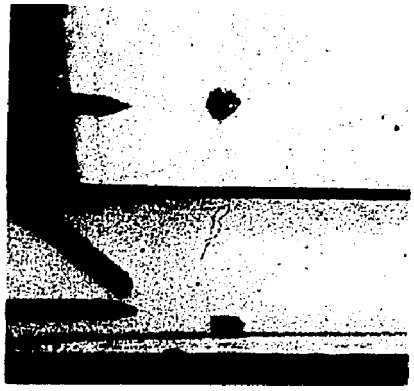
852- - 3



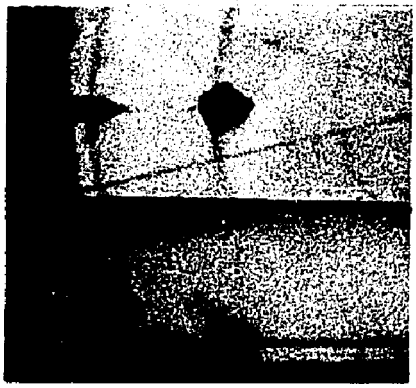
t = 250 μs



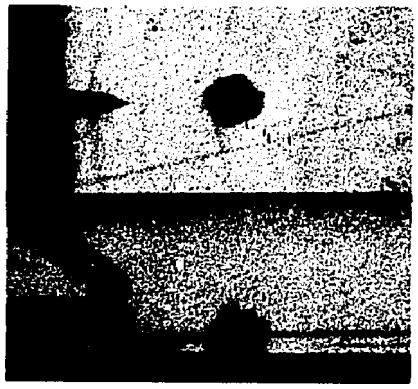
t = 275 μs



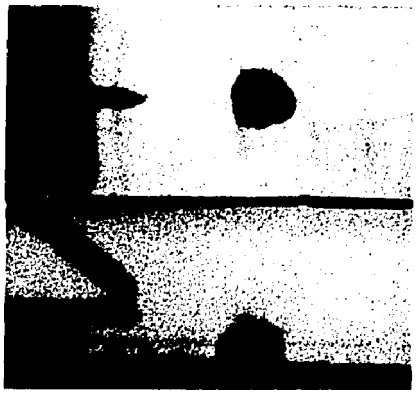
t = 300 μs



t = 325 μs



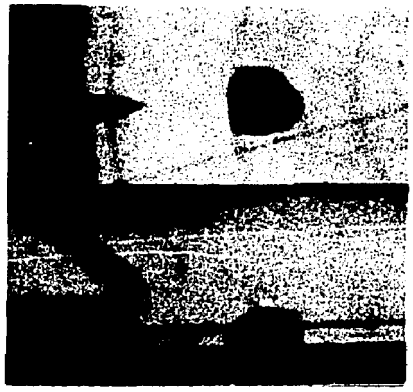
t = 350 μs



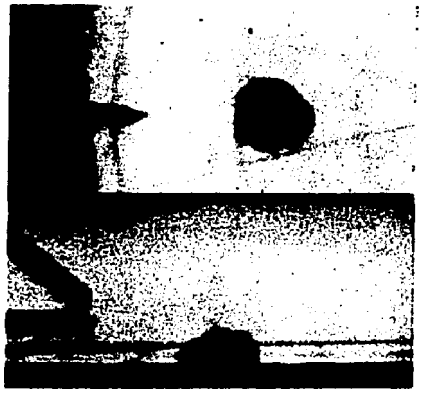
t = 375 μs

Figure 4.21 Prints, Run 852-BW-2D-3, p. 2

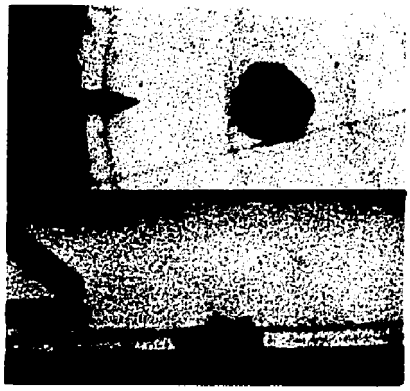
852--3



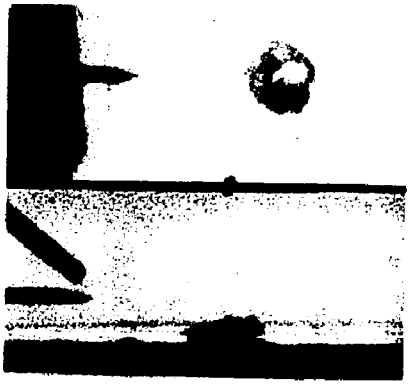
t = 400 μs



t = 425 μs



t = 450 μs



t = 475 μs

4256

Figure 4.21 Prints, Run 852-BW-2D-3; p. 3

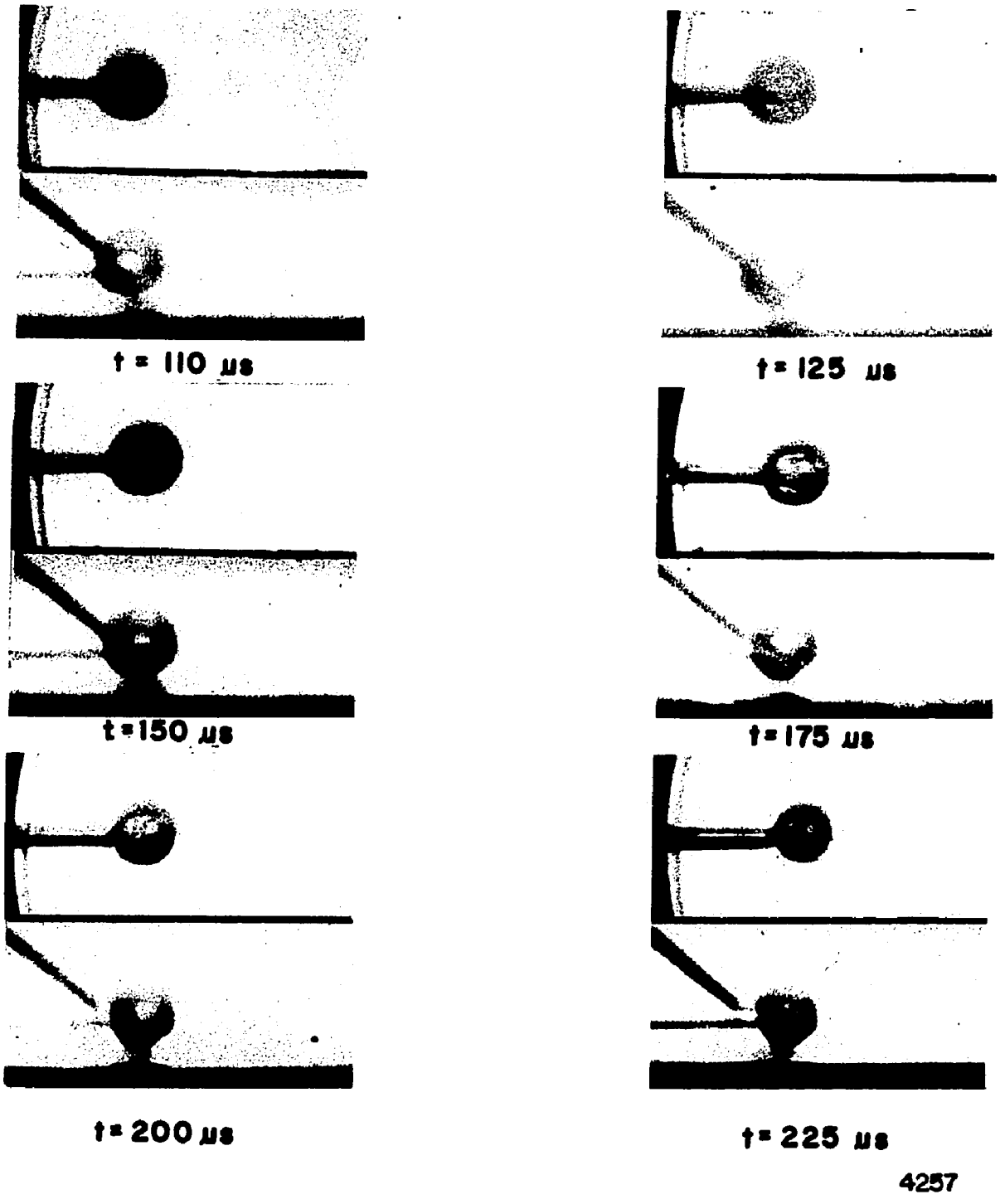


Figure 4.22 Prints, Run 7312-BW-2D-1, p. 1

7312--1

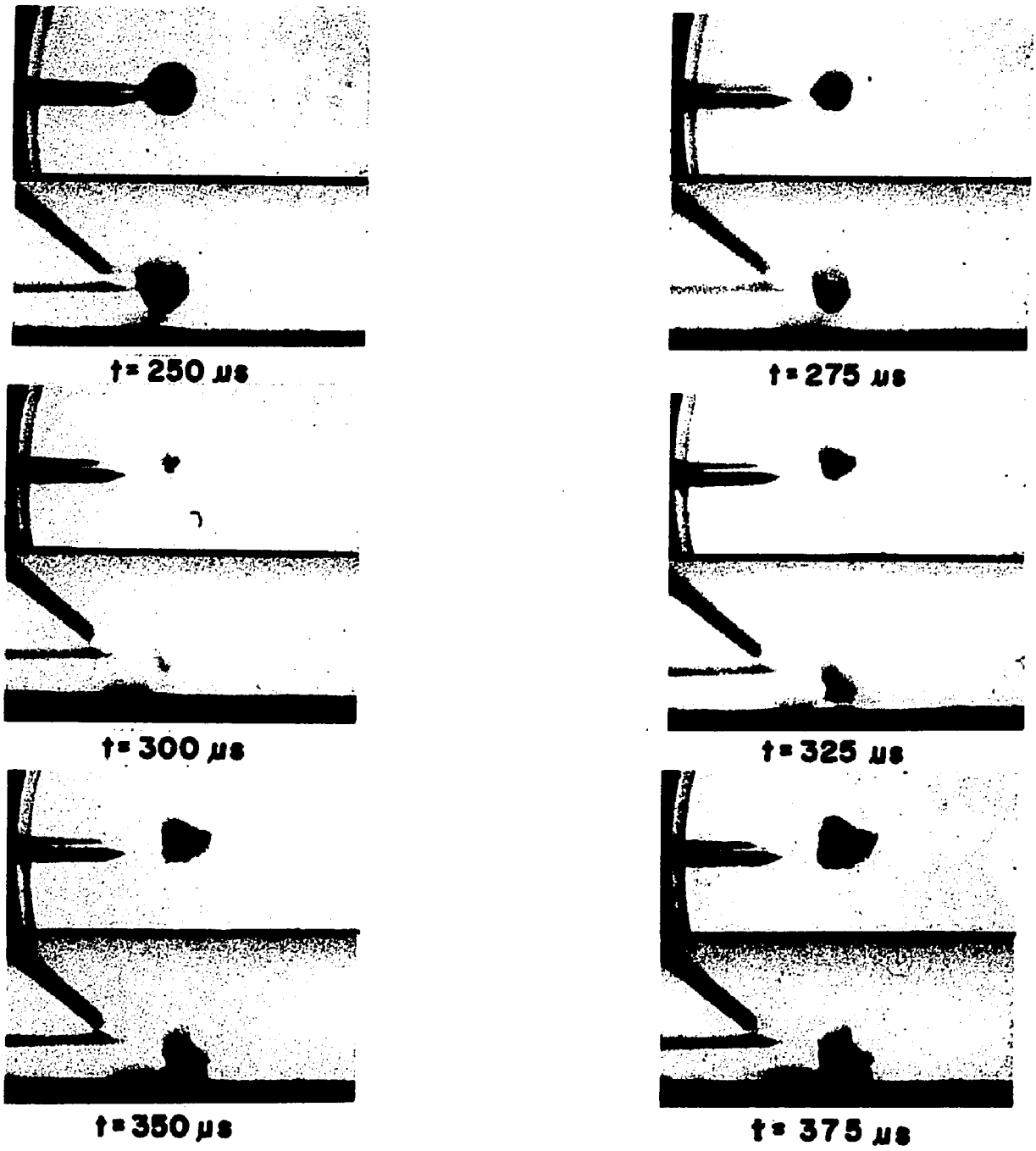
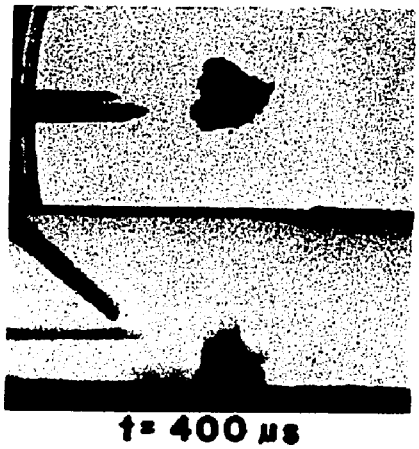
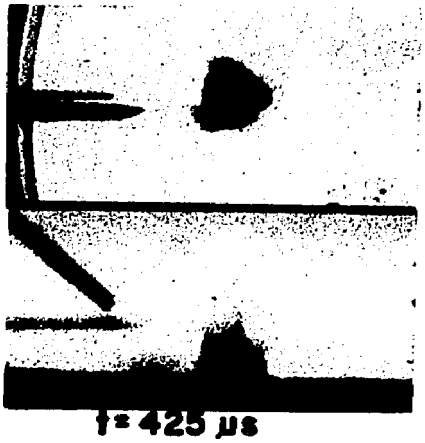


Figure 4.22 Prints, Run 7312-BW-2D-1, p. 2

7312--1





4259

Figure 4.22 Prints, Run 7312-BW-2D-1, p. 3

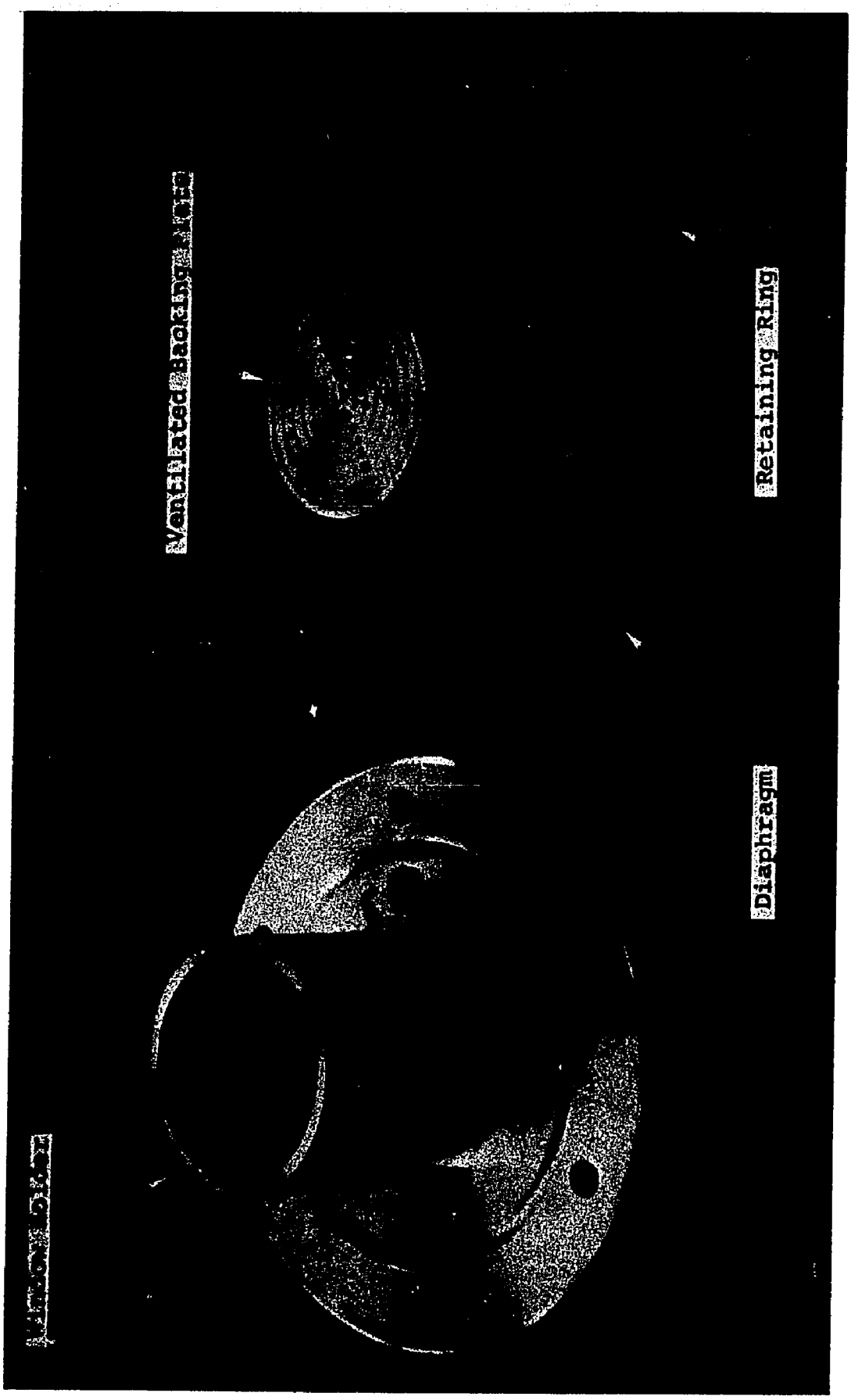


Figure 4.23 Partially Compliant Window-Disassembled

4260

RUN 842-BW-2D-2

ΔP=2.00 Atm
V=18.3 m/s
AIR=0.61 %

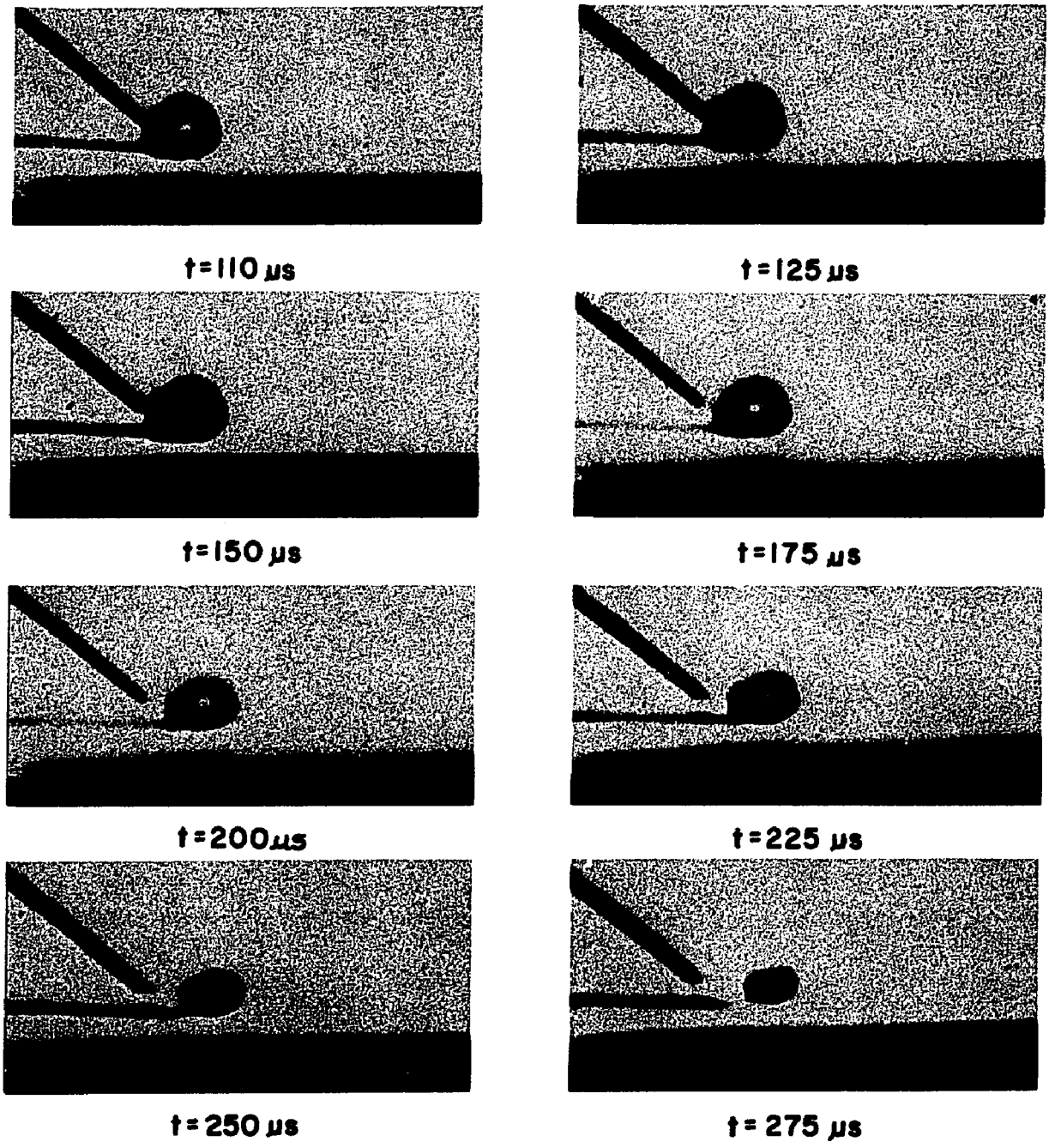
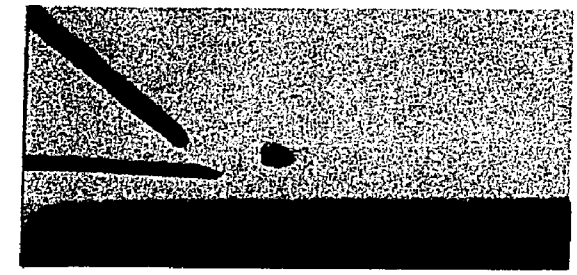


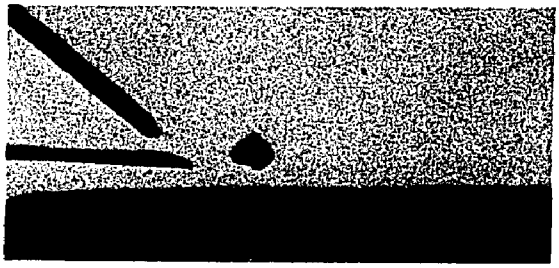
Figure 4.24 Prints, Run 842-BW-2D-2, p. 1

4261

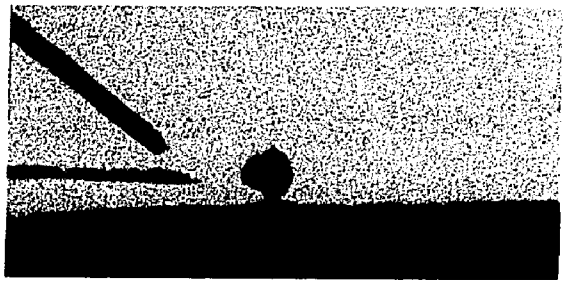
842--2



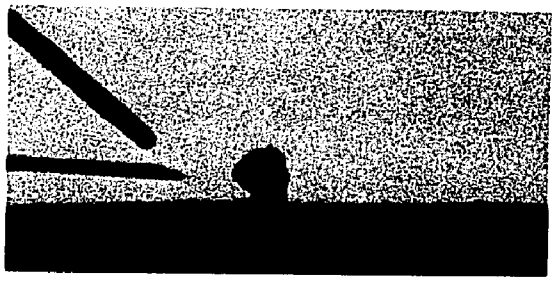
t=300 μs



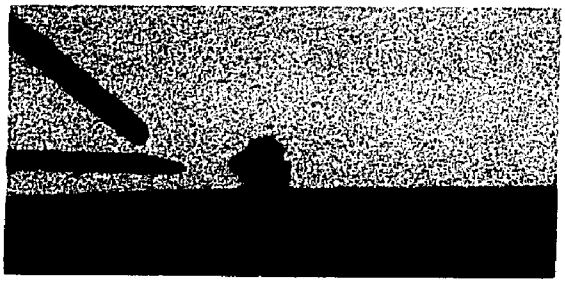
t=325 μs



t=350 μs



t=375 μs



t=400 μs

Figure 4.24 Prints, Run 842-BW-2D-2, p. 2

4262

CHAPTER 5

RESULTS AND DISCUSSION OF EXPERIMENTAL INVESTIGATION OF VAPOR BUBBLE COLLAPSE

5.1 PROBLEMS IN INTERPRETATION OF PHOTOGRAPHIC RECORDS

The interpretation of photographic records has always presented the researcher with a number of problems. The object of interpretation in usually to reduce a photograph, through a mensuration process, into numerical data that may be used to construct or verify a theoretical model of the event under scrutiny. Due to the finite resolution of any photographic system there is always a certain amount of subjectivity involved in saying a particular grey blotch on the photograph is actually a particular object of certain dimensions. This problem could be severe in the interpretation of photographs of translucent vapor bubbles contained in a transparent liquid, with the intent of numerically defining the bubble-wall position. However, experience in this laboratory has demonstrated different interpretors come to remarkably consistent conclusions when measuring identical photographic records of collapsing bubbles. Consequently, all photographic interpretation in this study was done by the author.

As mentioned previously, the greatest source of error in photographic interpretation results from unpredictable dimensional changes in the photorecording media upon processing. When utilized as in this study, the effect of dimensional changes in photorecording media should be no greater than approximately 1% of any measured spatial dimension. A

group of images processed together, like the individual frames of a cine record, are even more consistent. The recording, processing, and interpretation techniques utilized in this study should result in values of spatial dimensions within 1 - 2% of their unknown true values.

An additional problem in interpreting bubble photographs results from the nature of the event. During the involute stage of an asymmetric collapse the bubble assumes an involute shape. Since the walls of the bubble are translucent at best, it is impossible to record clearly the involute area of the bubble. Consequently, little can be discovered about the location or shape of the involute area of the bubble through photographic techniques. Following the involute stage of collapse, the bulk of the bubble is hypothesized to take on a toroidal shape with a high velocity liquid jet penetrating the center of the bulk of the bubble. This jet is thought to be visible in photographic records because it entrains a film of gas from the inside of the bubble as it pierces the bubble wall during the collapse. A similar phenomena has been observed when a drop strikes a liquid surface and forms a cavity in the bulk of the liquid. From photographic records it is impossible to determine whether the object piercing the bubble wall is a drop or a jet. Since the models of asymmetric bubble collapse show jet formation, (34, 48) and all previous experimental photographic studies (45, 47, 49) of asymmetric bubble collapse have assumed this object to be a jet and not a drop; this precedent will be followed in this study.

5.2 PRESENTATION OF RESULTS

Numerical results obtained from interpretation of bubble photographs are best presented graphically. The direct result of photographs taken of collapsing bubbles is information about bubble wall location as a function of time. This information is presented in the form of wall position diagrams which are no more than graphs of the apparent location of selected segments of the bubble wall as a function of time. The apparent location of the walls of an involuted bubble is illustrated in Figure 5.1. In most of these wall position diagrams, spatial dimensions, either diameters or distance from some reference point, are expressed in units of millimeters. The dimensions used in deriving each wall position diagram, along with the photographic sequences from which they were taken, are contained in Chapter 4.

Three quantities of importance were derived from measurements of bubble wall position; mean wall velocity, centroid position, and eccentricity. The mean wall velocity was calculated by division of the difference between two measured wall positions by the appropriate time interval. Mean wall velocities are plotted at the midpoint of this time interval. Since these velocities are the result of a difference technique, their accuracy is a function of the size of this difference and the magnitude of the quantities involved. Typically, due to the nature of bubble collapse, high velocities are measured more accurately than low ones. Most of the measured velocities should be accurate within 3 m/s. Velocities directed away from the bubble's centroid

are considered positive. Thus, a collapsing wall has a negative velocity.

The centroid of a bubble is defined as the point equidistant between the opposite wall segments of the bubble along the axis of interest. For the purposes of this study, the centroid of a bubble is calculated to be the point midway between the apparent wall positions along the axis of interest. When the centroid position of a bubble with an involute shape along the axis of interest is calculated, the centroid position is the arithmetic average of the positions of the extremes of the bubble as projected on a plane. The accuracy of calculated centroid positions is similar to that for wall positions.

Mitchell[34] and others have used eccentricity as a measure of a bubble's asymmetry. Eccentricity in a particular plane is defined as:

$$Exy = \frac{Dx - Dy}{Dx + Dy}$$

Dx = Apparent Bubble Diameter along x axis,

Dy = Apparent Bubble Diameter along y axis.

For this case, and similarly in others, a positive value of Exy means the bubble is elongated along the x axis as compared to a sphere. In three dimensions the shape of an asymmetric bubble is fairly well described by Exy, Exz, and Ezy; this, however, is only true until the bubble takes on an involute shape. When involution occurs the bulk of the bubble is still described since apparent diameters are used in calculating the eccentricity.

5.3 RESULTS AND DISCUSSION OF EXPERIMENTS IN A STATIC FLUID ENVIRONMENT UTILIZING HIGH SPEED CINEMATOGRAPHY

5.3a BUBBLE GENERATOR CHARACTERIZATION

Figure 5.2 illustrates the horizontal and vertical diameters of a bubble as a function of time from spark initiation. This bubble was selected as typical of the thirteen analyzed. From statistical analysis of these thirteen runs the following conclusions were drawn about the consistency of the bubble generator's performance:

1. At a 95% confidence level the bubble generator produces bubbles with a maximum horizontal or vertical diameter within 6% of the mean maximum horizontal or vertical diameter,
2. At a 95% confidence level the bubble generator produces bubbles which achieve maximum diameter at a time within 10% of the mean time required to reach maximum diameter,
3. At a 95% confidence level there is no significant difference between the maximum horizontal and vertical diameters.

Physically, these conclusions mean the bubble generator produces spherical bubbles, but misfires once in every twenty shots. As may be seen in Figure 4.4, the spark electrodes have a small but significant effect on the shape of the collapsing bubble. The electrodes serve to restrict flow to the segment of bubble-wall adjacent to the electrodes and, consequently, this portion of the wall collapses slower than segments further removed from the vicinity of the electrodes.

5.3b BUBBLE COLLAPSE ADJACENT TO A RIGID SURFACE

Figure 5.3 is a wall position diagram for bubble 1120-DSB-1. It illustrates the retarding effect of a solid surface on the collapse of the wall segment adjacent to the surface, and the resultant asymmetric collapse mechanism with

jet formation. The characteristic collapse time as calculated from the Besant - Rayleigh Model for spherical collapse is shown as t_{BR} on Figure 5.3, and the collapse occurs in approximately this time period. The jet formed during collapse has a velocity of approximately 33 m/s, which is perhaps no greater than the velocity of the segment of bubble wall opposite the solid surface prior to jet formation. However, this conclusion is subject to some doubt due to the insufficient time resolution of the camera system employed. The initial centroid distance (bo) for this bubble is 1.39, which is in the range which Kling asserts is significant in causing damage. No trace of material damage could be found on the brass surface upon microscopic examination. In the later stages of collapse the centroid of the bubble migrates strongly towards the solid surface and, following collapse, the bubble seems to become attached to the solid surface. No appreciable rebound of the bubble from the surface is visible although it appears the bubble may have fragmented into many small bubbles which rebound individually.

5.3c BUBBLE COLLAPSE ADJACENT TO A COMPLIANT SURFACE

Figure 5.4 is a wall position diagram for bubble 10300-DSB-1. The effect of the compliant surface is evident in that the bubble is strongly repelled from the surface during collapse. Examination of the photographs of this bubble (Figure 4.6) reveals asymmetric collapse with the bubble-wall segment adjacent to the compliant surface collapsing much faster than other segments. The frame taken at t = 440 μs shows the compliant surface bulging upward to facilitate flow to the

segment of the bubble wall adjacent to the compliant surface. From Figure 5.4 it appears as if the time required for this bubble to collapse to minimum diameter is about that predicted by the Besant-Rayleigh Model. From Figures 4.6 and 5.4 it appears as if this bubble collapses asymmetrically and forms a jet directed away from the compliant surface. This jet is visible in Figure 4.6 at t = 760 μs. The velocity of this jet is 7.5 m/s. This velocity is much lower than both the velocity of the wall segment adjacent to the compliant surface before jet formation (25 m/s), and the jet velocity found for bubble 1120-DSB-1 (33 m/s) which collapsed adjacent to a rigid surface under similar conditions. The centroid of this bubble migrates away from the compliant surface at a relatively constant rate (7.5 m/s) following the initial collapse.

Two aspects of these experimental results are of prime interest. The fact that a bubble collapsing adjacent to a sufficiently compliant surface forms a jet directed away from the compliant surface has been demonstrated by both this work and that of Gibson.[43] The implications of the phenomena as a means of reducing cavitation damage are discussed in sections 5.6 - 5.8. The jet formed during the collapse of this bubble is measured to have a velocity of 7.5 m/s as it pierces the opposite wall of the bubble; the velocity of the wall segment adjacent to the compliant surface prior to involution is measured to have a velocity of 25 m/s. Why the jet has a velocity lower than that of the wall segment from which it was formed is discussed in Section 5.7.

5.3d BUBBLE COLLAPSE ADJACENT TO ANOTHER BUBBLE

In the construction of mathematical models of bubble collapse adjacent to a solid surface, the fluid mechanics principle that no flow occurs across a plane of symmetry is often used. In these models the plane of symmetry is provided by another collapsing bubble a suitable distance from the first. This is called the method of images, and the plane of symmetry midway between the bubbles simulates a solid surface. Figure 5.5 is a wall position diagram for the double bubble collapse experiment photographed in Run 10210-D-SB-2. As can be seen from both the collapse photographs and the wall position diagram the bubbles behave as would be expected if there was a solid surface between them, illustrating the well known validity of the method of images. The simulation in this case is not perfect, as the bubbles are neither exactly the same size nor start collapsing at exactly the same time, nor are viscous effects necessarily negligible. The left bubble forms a jet with a velocity of 40 m/s while the right bubble forms a jet with a velocity of 27 m/s. Also, the jets do not form symmetrically and one passes behind the other instead of colliding with it directly. Following collapse the bubbles agglomerate into a mass, a situation similar to the attachment to a solid surface seen following the collapse of an adjacent bubble. The tips of the two jets formed by collapsing adjacent bubbles are seen to decelerate as one passes behind the other. The initial non-dimensional centroid distance (bo) for these bubbles was 2, illustrating that strong asymmetric behavior can occur even at large initial centroid distances.

5.4 RESULTS AND DISCUSSION OF EXPERIMENT IN A STATIC FLUID ENVIRONMENT UTILIZING HOLOGRAPHY

One advantage of holography when applied to fluid mechanics studies is that a hologram may be used to construct shadowgraphs, schlieren photographs, and interferographs of the event recorded on the hologram. The researcher needs only to make a good hologram and then, at his leisure, manipulate the hologram to yield all the more conventional experimental photographic results. As may be seen from the photograph appearing as Figure 4.8, which was reconstructed from a hologram of a collapsing spherical bubble, the problem with this technique is to produce a good hologram. This photograph is far inferior in quality to those which could be obtained by direct photography of the bubble and the hologram from which it was taken is so inferior as to make further optical manipulation useless. The reasons for this lack of quality are manifold, and foremost among them is the rapid motion of the bubble wall. Holograms are sensitive to movements on the order of a wavelength of light and, even though the exposure time for this hologram was on the order of 100 ns, the wall motion during exposure was excessive. Laser technology has progressed remarkably since the laser used in this study was constructed, and pulsed lasers are now available which have output pulses sufficiently narrow to avoid this problem. It is technically feasible to conduct a study of bubbles collapsing adjacent to a solid surface utilizing holography which would result in much more knowledge of bubble shapes and the associated pressure fields than can be obtained through conventional photographic processes. Such a study

would be neither simple nor inexpensive. A brief review of some applications of holography in fluid mechanics was published by Tanner[85].

5.5 RESULTS AND DISCUSSION OF EXPERIMENTS IN A FLOWING FLUID ENVIRONMENT CONTAINED BY THE TWO DIMENSIONAL VENTURI

Figure 5.6 is a wall position diagram for bubbles 1191-D-FB-1 and 1252-BW-FB-2. These bubbles will be referred to as FB-1 and FB-2 in the following text. From this figure and the photographs of these bubbles two things are obvious: the Dynafax Camera has insufficient temporal resolution to visualize the final stages of collapse and the Model 330 Camera, when operated at a framing rate sufficient to visualize the final stages of collapse, has insufficient writing time to record the whole of the collapse. At t = 330μs bubble FB-1 has the same diameter as bubble FB-2, but bubble FB-2 is about 0.5 mm. closer to the solid surface. The bubble generator was found to produce bubbles of consistent diameter in a flowing system but, for unknown reasons the initial centroid distance was uncertain. This required that a large number of camera runs be made to get bubbles with similar initial centroid distances.

From the photographs it appears that spark generated bubbles in a flowing system are less symmetrical than bubbles produced in a static fluid environment. Figure 5.7 is an expanded scale wall position diagram of bubble FB-2. From it the collapse adjacent to a solid surface appears similar to that of a bubble in a static fluid environment. The initial centroid distance for bubble FB-2 is uncertain, but from

Figure 5.6 it is estimated to be 1.1. The collapse progresses in a highly asymmetrical mode and a jet is formed which penetrates the opposite bubble wall at t = 400μs. The moment at which the jet pierces the opposite wall is more obvious from the wall position diagram than from the photographs.

Figure 5.8 is a plot of the mean apparent wall velocity as a function of time for bubble FB-2. Two observations may be made from Figure 4.11: the collapse proceeds more in a pulsating mode than a continuously accelerating mode, and the jet velocity (52 m/s) appears to be significantly lower than the velocity of the segment of bubble wall opposite the solid surface prior to jet formation (78-148 m/s). Both of these phenomena are apparent in the static fluid case, but are much more pronounced in the flowing fluid. Figure 5.8 is a plot of the eccentricity for the main bulk of bubble FB-2 as a function of time. At the start of the camera run the collapse appears to have progressed to a point where the bubble is oblate with respect to the solid surface, as is indicated by a negative value of eccentricity. As the jet is formed the bubble takes on a prolate shape and the eccentricity takes on a positive value at the same time (t = 400 μs) as the jet is observed to pierce the opposite wall.

Two further observations may be made concerning Figures 4.11 and 4.14: the apparent diameter of the jet formed during the collapse of these bubbles is about 1/10 the maximum radius of the bubble and, following jet formation, a portion of the bulk of the bubble appears to break into numerous smaller bubbles.

5.6 RESULTS AND DISCUSSION OF EXPERIMENTS IN A FLOWING FLUID ENVIRONMENT CONTAINED BY THE TWO OPTICAL AXIS VENTURI

Of the experimental runs made utilizing the two optical asix venturi, five were selected as being suitable for further analysis. Table 5.1 lists the important characteristics of the bubbles produced during these runs and the conditions under which the runs were made. Two of the bubbles studied were relatively close to the solid surface with an initial centroid distance (bo) of about 1.5, while the other three bubbles were further from the surface with an initial centroid distance of about 1.8.

Figure 5.10 is a wall position diagram for bubble 7312-BW-2D-1 (bo = 1.45) and Figure 5.11 is a wall position diagram for bubble 852-BW-2D-3 . These bubbles will be referred to as 2D-1 and 2D-3 in the following text. Both of these bubbles collapsed in a highly asymmetric mode resulting in jet formation. Wall velocities for bubble 2D-1 are presented in Figure 5.12 while wall velocities for bubble 2D-3 are presented in Figure 5.13. Of these two bubbles, 2D-1 was found to be the most spherical at maximum diameter with an initial eccentricity (Exyo) of 0.007, as compared to bubble 2D-3 with Exyo = 0.057. Eccentricity as a function of time in the three observable planes (Exy, Exz, Ezy) is plotted as Figure 5.14 for bubble 2D-1, while Figure 5.15 is a similar eccentricity diagram for bubble 2D-3.

From the wall velocity diagrams for these two bubbles, it is apparent that the velocity of the bubble wall opposite the solid surface just prior to jet formation (47 m/s & 39 m/s)

is greater than the observed jet velocity (15.5 m/s & 18.5 m/s). Additionally, as the bulk of bubble 2D-3 collapses to a minimum diameter and then rebounds due to the presence of non-condensible gas in the bubble,the rebound velocity of the bubble wall adjacent to the solid surface prior to penetration by the jet (19 m/s) is about the same as the jet velocity (18.5 m/s). The rebounding bubble wall, however, is slowed by its proximity to the solid surface, and consequently the jet catches and penetrates it. Similar information is not available for bubble 2D-1, but careful examination of the photographs of this bubble reveals the jet formed during collapse is not directed at right angles to the solid surface; rather the jet appears to be directed along an axis 35^{o} from the perpendicular. If cavitation damage pits are assumed to be caused by the impact of jets produced by collapsing bubbles, then this observation is consistent with the often asymmetrical nature of cavitation damage pits.

Of the three bubbles analyzed with an approximate initial centroid distance of 1.8, two (7102-BW-2D-4, 842-BW-2D-5) were studies of collapse adjacent to a solid surface and the other (842-BW-2D-2) was a study of collapse adjacent to what may have been a compliant surface. These bubbles will be referred to as 2D-4, 2D-5, and 2D-2 in the remainder of this text. Following is a list of figures containing numerical information resulting from analysis of these bubbles.

BUBBLE	bo	TYPE OF FIGURE	FIGURE NO.
7102-BW-2D-4 (2D-4)	1.75	Wall Position Diagram	5.16
		Wall Velocity Diagram	5.19
		Eccentricity Diagram	5.22
842-BW-2D-5 (2D-5)	1.80	Wall Position Diagram	5.17
		Wall Velocity Diagram	5.20
		Eccentricity Diagram	5.23
842-BW-2D-2 (2D-2)	1.80	Wall Position Diagram	5.18
		Wall Velocity Diagram	5.21
		Eccentricity Diagram	5.24

For bubbles 2D-4 and 2D-5 the collapse velocities follow a pattern similar to that for bubbles 2D-1 and 2D-3. The velocity of the bubble wall opposite the solid surface prior to jet formation (37 m/s & 33 m/s) is greater than the observed jet velocity (18 m/s & 17.5 m/s), and the rebound velocity of the bubble wall prior to jet penetration (30 m/s & 35 m/s) is also greater than the jet velocity. Again, the rebounding wall is quickly slowed by its proximity to the solid surface and consequently the jet catches and penetrates it.

Examination of the wall velocity plots for bubbles 2D-1, 2D-3, 2D-4, and 2D-5 (Figures 5.12, 5.13, 5.19, and 5.20) reveals that none of these bubbles collapsed with smoothly accelerating wall velocities. This phenomena is visible to a lesser extent in the wall position diagram for bubble 1120-DSB-1 (Figure 5.3). Plesset and Mitchell[16] have suggested that bubble collapse adjacent to a solid surface proceeds with an oscillatory component superimposed upon the accelerating wall collapse velocity. The frequency of this oscillatory component is an inverse function of the bubble

radius. The temporal and spatial resolution of the camera system used in this study was insufficient to quantify whether or not the bubbles photographed in this study had an oscillatory component superimposed upon their collapse. However, the resolution was sufficient to demonstrate the bubbles observed in this study collapsed irregularly and this fact lends credence to the hypothesis of Plesset and Mitchell.[16]

All of the bubbles observed during collapse adjacent to a rigid surface were found to collapse asymmetrically and form a jet directed at the rigid surface. The exact size and shape of this jet could not be quantified due to lack of resolution but as a general conclusion the diameter of this jet was observed to lie between 0.1 and 0.3 of the maximum bubble radius.

Following collapse and jet formation bubbles collapsing adjacent to a rigid surface become attached to the rigid surface. The two-optical-axis venturi was designed so that photographic information could be obtained concerning the shape and optical density of a bubble collapsing adjacent to a rigid surface in the plane of that surface. Through this method it was hypothesized that it could be determined whether the object which becomes attached to the rigid surface following collapse is composed of a single bubble or a number of smaller bubbles formed from the original bubble. All of the photographs taken of this attached object show uniform optical density across the object. Since both an irregular single bubble and a cloud of small bubbles could show this

characteristic it is impossible to determine the nature of the attached object from this experiment.

In the case of collapse adjacent to a compliant surface the pattern set by bubble 10300-D-SB-1 in a static fluid was not followed by bubble 2D-2 in a flowing fluid environment. Bubble 2D-2 collapsed in an asymmetric mode and formed a jet directed towards the compliant surface, as opposed to static bubble 10300-D-SB-1, which formed a jet away from the compliant surface. These two bubbles were similar except for the nature of the compliant surface adjacent to which they collapsed, the fluid flow condition, and the collapse driving force (ΔP). Since other bubbles which collapsed in differing flow fields and with different driving forces have not shown this type of jet behavior, it is probably this behavior is due to differences in the nature of the compliant surface.

Both compliant surfaces were similar rubber diaphragms but there were significant differences between the experimental designs for these bubble collapse experiments. Bubble 10300-DSB-1 collapsed adjacent to a rubber surface which was backed by air at the ambient pressure of the bulk of the liquid. Bubble 2D-2 collapsed adjacent to a rubber surface backed by a perforated and grooved metal plate which served to support the rubber diaphragm. This support was necessary because the liquid in the test venturi was at 2 Atm. absolute pressure while the gas behind the perforated metal plate was at 1 Atm. absolute pressure. This difference in experimental designs makes it possible to attribute the opposite behavior

of bubbles 10300-DSB-1 and 2D-2 to either or both of two explanations. One explanation of this behavior is that the failure of the compliant surface used in Run 2D-2 to cause jet reversal is due to the 1 Atm. pressure differential across the rubber diaphragm used as the compliant surface in Run 2D-2. The other explanation for this behavior is that the compliant surface used in Run 2D-2 behaved as a rigid surface because bubble 2D-2 collapsed over an area of the surface that was backed by solid metal instead of over an area of the surface that was backed by gas admitted through the system of grooves and perforations in the metal backing plate. What has been verified by comparison of these experiments is that a bubble collapsing adjacent to a sufficiently compliant surface forms a jet directed away from the compliant surface.

The jet velocity for bubble 2D-2 (32.5 m/s) was similar to the velocity of the opposite wall prior to impact (35 m/s), and was the highest jet velocity observed in the two optical axis venturi. The rebound velocity of the adjacent wall prior to jet penetration (14 m/s) was significantly lower than the jet velocity which stands in contrast to the pattern observed for other bubbles where these velocities were comparable to or the rebound velocity was greater than the jet velocity. Figure 5.25 is a plot of the centroid position of the three bubbles observed with bo = 1.8 in the two optical axis venturi. From this figure it is evident that the surface used in run 2D-2 had little effect on bubble centroid migration as compared to a rigid surface.

Three types of solid surfaces (glass, plexiglass, and laquer coated plexiglass) were subjected to the forces produced by the nearby collapse of spark generated bubbles in the two optical axis venturi. Following the bubble collapse each surface was microscopically inspected for damage in the area where the jet formed by the collapsing bubble was observed to impact. The microscopic examination was conducted utilizing front, back, oblique, and polarized lighting. No trace of damage was evident on any of the surfaces, although, the surface finish on the laquer coating plexiglass window was so irregular that it is doubtful the presence of damage could have been detected if present. Additionally, no damage could be found in the area directly under the bubble producing arc. One plexiglass window was subjected to attack by over a hundred bubbles similar to those reported in this section. No trace of damage, either in the area of jet impact or directly under the arc, could be found. However, it has been observed before in this laboratory that plexiglass venturis are quite resistant to low intensity cavitation fields.

5.7 DISCUSSION AND CONCLUSIONS CONCERNING INVESTIGATION INTO VAPOR BUBBLE COLLAPSE

The principal difference between spark generated bubbles and natural cavitation bubbles is that spark generated bubbles contain more non-condenseble gas due to electrolysis than natural cavitation bubbles and are formed at high temperature so that heat transfer restraints on collapse rates may be present. Utilizing a series of questionable assumptions, Kling[49] (working in this laboratory) estimated the

permanent gas content of spark generated bubbles and came to the following conclusion:

> "For typical spark generated bubbles the partial pressure of the permanent gas is approximately half of the total pressure at maximum volume. This partial pressure of permanent gas, which is the same order of magnitude as the water vapor pressure, is about 10^3 times the partial pressure expected from the naturally occurring gas nuclei present in the water tunnel facility. This estimate of the permanent gas is quite high due to the assumptions made. However, the possibility of a substantial amount of permanent gas formation is shown and a large amount of water vapor is also formed which conceivably may not condense rapidly enough during bubble collapse to prevent retardation of this collapse. If so, the damage potential of the bubble could be greatly reduced compared to a natural cavitation bubble. Therefore, the damage potential of the spark generated bubble could be much less than that of a natural cavitation bubble which collapses in the same hydrostatic pressure and contains little or no permanent gas."

However, Mitchell,[34] also working in this laboratory, came to the following conclusion from study of his mathematical model which allows for both asymmetric and thermodynamic effects:

> "These asymmetries are produced with such small volume changes ($R/Ro < 0.25$) that we can assume the internal gas and vapor content of cavitation bubbles have no substantial effect on such jets."

In reality, it is probable that the truth of this matter lies somewhere between the views of Kling and Mitchell. The internal gas content of a bubble collapsing adjacent to a solid surface does play a role in that it cushions the collapse of the bulk of the bubble in the later stages of collapse and causes the bulk of the bubble to rebound following collapse to some minimum diameter. Of course, many photos of natural cavitation bubbles also show a similar

rebound behavior. However, since the jet forms relatively early in the collapse and, as Chapman[48] states, once the jet is formed its velocity is fairly constant, it is probable that the effect of spark generation is less than that expected by Kling. Therefore, when spark generated bubbles are compared to natural cavitation bubbles, the following may be expected: (1) Wall collapse velocities for spark generated bubbles are less than for natural cavitation bubbles; (2) Rebound phenomena are more pronounced, occurring earlier for spark generated bubbles than for natural cavitation bubbles.

Careful examination of all the venturi windows subjected to attack by both the collapsing bubbles and the shockwaves produced by the bubble initiating arcs failed to reveal any trace of damage. Kling,[49] in a similar series of experiments, demonstrated damage to adhesive backed aluminum sheet, produced by both the initiating arc and the collapsing bubble. In the two-optical-axis venturi the initiating arc electrodes are placed in a plane perpendicular to the adjacent surface and the possibility of damage to this surface due to the shockwave produced by the initiating arc is greatly reduced.

Chapter 7 contains the results of jet impact damage studies on plexiglass and other materials. Plexiglass was found to be quite resistant to damage by jet impact. It required over a hundred impacts by 1 mm. diameter water jets travelling at 200 m/s to produce measurable damage on a plexiglass specimen. All of the liquid jets due to bubble

collapse photographed in the two-optical-axis venturi were observed to impact on the plexiglass window surface with a velocity on the order of 20 m/s. Consequently, it would be surprising if damage were observable on the plexiglass window due to the impacting jets produced by collapsing bubbles. All of these bubbles had initial centroid distances (bo) greater than the range (bo = 1.1-1.4) thought most likely to result in surface damage by Kling.[49] The jets from these bubbles had to penetrate a considerable film of water in order to reach the solid surface. Table 5.1 shows the measured jet velocity for all of the bubbles photographed in the two axis venturi to be about half the collapse velocity of the bubble wall opposite the solid surface prior to involution. It is unlikely that the collapsing wall could provide jets with a velocity lower than the wall velocity prior to involution; therefore, the low observed jet velocities probably are due to slowing of the jet following its penetration of the bubble wall adjacent to the solid surface.

Figure 5.26 is a centroid position diagram showing the centroid position (b) as a function of time for bubbles 2D-1 (bo = 1.45), 2D-3 (bo = 1.43), 2D-4 (bo = 1.75), and 2D-5 (bo = 1.80). Also appearing on Figure 5.26 are theoretical predictions of centroid position as a function of time for a bubble with an initial centroid distance of 1.5; these predictions are derived from the work of Mitchell[34] and Chapman[48]. It is difficult to define exactly when an experimentally observed bubble starts to collapse and for this reason some inconsistency in the time scale is to be

expected when comparing theoretical results to experimental observations. Figure 5.26 indicates that the Mitchell calculation fits the observed results better in the early states of collapse, while the Chapman calculation results in a better fit in the later stages after gross asymmetries in the bubble's shape have developed. Due to the singularity at the origin of its coordinate system the Mitchell calculation does not go far enough in time to show the development of gross asymmetries with the consequent strong centroid migration.

Figure 5.27 is a plot of the wall velocities in the x and y planes predicted by Chapman and corrected to the ambient conditions of the two-axis venturi. Figure 5.28 consists of three wall velocity plots with one of Chapman's wall velocity predictions and the corresponding experimentally observed wall velocities for the two bubbles closest to Chapman's initial conditions (2D-1, 2D-3) on each. Chapman's model differs from this experiment in three major ways: it assumes the bubbles to be spherical initially, it assumes the bubbles to contain no noncondensible gas, and it assumes the bubble to be in a static fluid environment. The effect of initial asymmetry, noncondensible gas, and a flowing fluid environment on a collapsing bubble should be to retard the collapse and result in measured velocities lower than those predicted by Chapman's model. Nevertheless, examination of Figure 5.28 reveals measured wall collapse velocities quite similar to those predicted by Chapman's model up until the time the bulk of the bubble is observed to rebound.

This study of spark produced vapor bubbles in both flowing and static liquid environments has led to conclusions in three areas: (1) The effect of a nearby rigid surface on the bubble collapse mechanism; (2) The effect of a nearby compliant surface on the bubble collapse mechanism; and (3) The accuracy with which the mathematical models of Chapman[48] and Mitchell[34] predict the collapse of spark generated vapor bubbles in a flowing liquid adjacent to a solid surface. Following, in summary form, is a list of these conclusions.

I. Effect of nearby rigid surface

(1) Spark generated vapor bubbles collapsing adjacent to a rigid surface do so asymmetrically with the formation of a liquid jet which strikes the rigid surface. This jet slows down as it penetrates the liquid layer between the bubble and the rigid surface.

(2) The diameter of this jet is on the order of from 0.1 to 0.3 of the maximum bubble radius.

(3) For bubbles with a maximum radius of 2.3 mm. and an initial nondimensional centroid distance of 1.4 - 1.8 collapsing in a flowing fluid stream at 2 Atm. absolute pressure, the velocity of this jet is typically 17 m/s. Under the same conditions the bubble wall opposite the rigid surface, which eventually forms the jet, has a typical collapse velocity of 40 m/s prior to jet formation.

(4) Following jet formation and collapse to some minimum diameter the bulk of the bubble rebounds. The bubble wall adjacent to the solid surface has a typical maximum rebound velocity of 30 m/s under the above conditions. This rebounding wall is quickly slowed by the presence of the rigid surface so that the jet catches and penetrates it.

(5) Following jet impact on the rigid surface the bulk of the bubble becomes attached to the rigid surface. Whether the attached object is a single bubble or a cluster of small bubbles is not known.

(6) No trace of damage either in the location of jet impact or directly under the bubble generating arc discharge could be found on plexiglass and glass rigid surfaces. This observation is consistent with the low observed jet velocity and geometry of the arc discharge electrodes.

II. Effect of Nearby Compliant Surface

(1) Spark generated vapor bubbles collapsing adjacent to a sufficiently compliant surface do so asymmetrically with the formation of a liquid jet which travels away from the compliant surface.

(2) The degree of surface compliancy necessary to cause jet reversal is less than that of a free surface.

III. Comparison of Results with Models of Chapman and Mitchell

(1) The collapse velocities measured for spark generated bubbles collapsing adjacent to a rigid surface are similar to those predicted by the model of Chapman up to the time the bulk of the collapsing bubble is observed to rebound.

(2) The centroid of a bubble collapsing under the above conditions migrates towards the rigid surface during collapse. This centroid migration is best predicted by the Mitchell Model in the early stage of collapse and the Chapman Model in the later stages of collapse.

(3) Rebound phenomena are an important part of the bubble collapse mechanism. Neither the model of Mitchell nor that of Chapman predict rebound phenomena.

5.8 FURTHER DIRECTIONS IN BUBBLE COLLAPSE RESEARCH

There is much room for further research into bubble collapse. The motivation for this research might be academic, but it would probably be of a practical nature based on a desire to reduce cavitation damage in some particular application. A thorough understanding of the mechanics of bubble collapse and the effect of nearby surfaces on the collapse mechanism might result in a large reduction of cavitation damage through knowledgeable modification of local surface characteristics.

The experiments reported here, some of which investigated the effect of surface compliancy on the collapse mechanism of a bubble, suggest further experimentation. It was demonstrated that a compliant surface under some conditions causes a collapsing bubble to form a liquid jet directed away from the surface while under less compliant conditions the jet formed is directed towards the surface. What is needed is further quantitative information on the degree of compliancy needed to cause this jet reversal under arbitrary ambient conditions. An experimental approach to this problem could involve a photographic study in a flowing fluid environment. One means of constructing a variable compliancy surface is to stretch a rubber diaphragm over a suitable metal backing screen and arranging this surface so the pressure differential between the liquid on one side of the diaphragm and the gas on the other side of the diaphragm is variable. The metal backing screen must be sufficiently porous so the objections to this experiment discussed in Section 5.6 are overcome. By varying this pressure differential and the rubber surface (thickness, density, prestress, etc.) and monitoring the results photographically, data might be taken which could result in a model of the surface characteristics necessary to achieve jet reversal. A theoretical approach to this problem might involve a fluid flow model of bubble collapse similar to that of Mitchell[34] or Chapman[48], but allowing for a compliant surface. For greatest practical significance it would be desirable to include the effect of internal non-condensible gas in the model. Computer solution

of this model could quantify the degree of surface compliancy necessary to achieve jet reversal. It appears, on first examination, that a compliant surface that acted as if it were a long column of water might represent the degree of surface compliancy necessary to achieve spherical collapse or jet reversal. Regardless of what approach to this problem is taken, quantification of the surface compliancy necessary to achieve jet reversal under various ambient conditions might result in the synthesis of new surface coatings which could greatly reduce cavitation damage when tailored to a specific environment.

Other directions further bubble collapse research may advantageously take include holographic studies of collapsing bubbles with the goals of determining involuted bubble shapes, pressure profiles, etc. and studies of the effect of initial bubble shape on jet direction, velocity, etc.

Run	b_o	t_o μs	R_o mm	xyo	Jet Velocity m/s	Adjacent Wall Rebound Velocity m/s	Opposite Wall Collapse Velocity m/s	Bubble Slip Velocity m/s	Fluid Air Content Vol. %
7312 BW-2D 1	1.45	150	2.23	0.007	15.5		47	3.4	0.49
852 BW-2D 3	1.43	150	2.26	0.057	18.5	19	39	1.8	0.46
7102 BW-2D 4	1.75	163	2.17	0.072	18	30	37	3.0	0.68
842 BW-2D 5	1.80	138	2.43	0.120	17.5	35	33	2.8	0.49
842 BW-2D 2 (Compliant Wall)	1.80	163	2.24	0.085	32.4	14.1	35		0.61

Conditions in Venturi: Pressure = 2 Atm Abs, Velocity = 18 m/s

Table 5.1 Bubble Characteristics

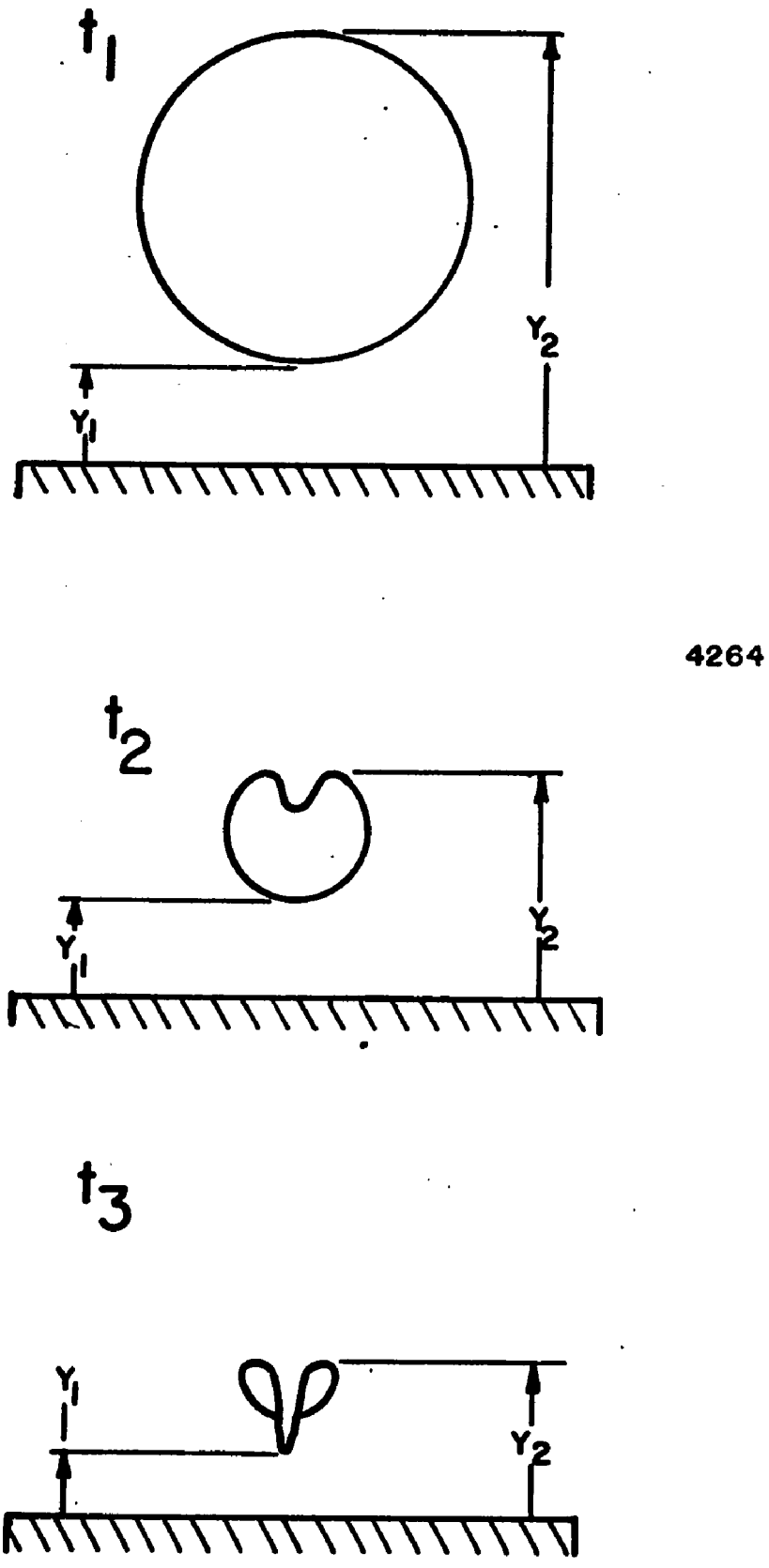


Figure 5.1 Illustration of Apparent Bubble Wall Position

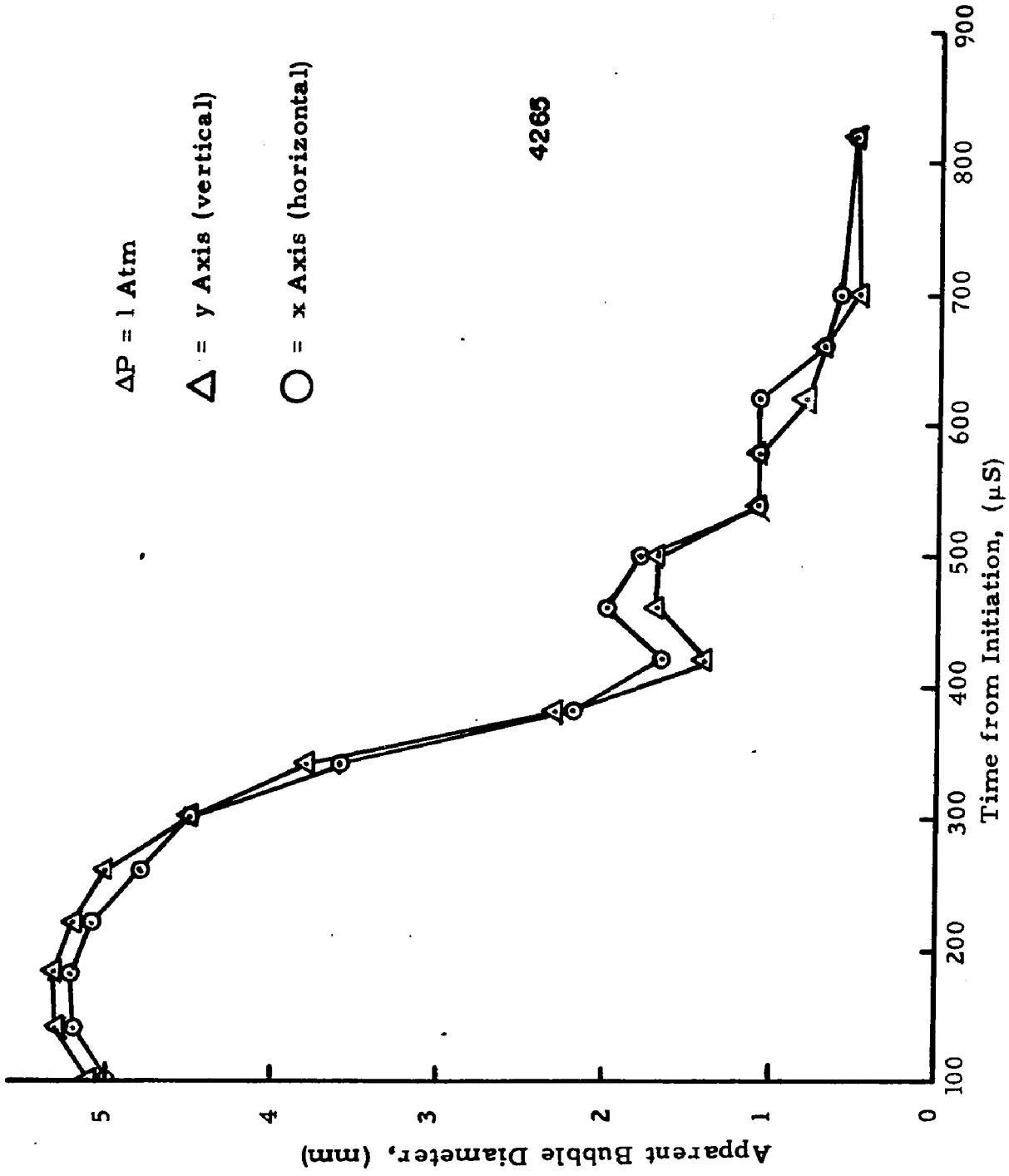


Figure 5.2 Wall Position, Run 1099-DSB-3

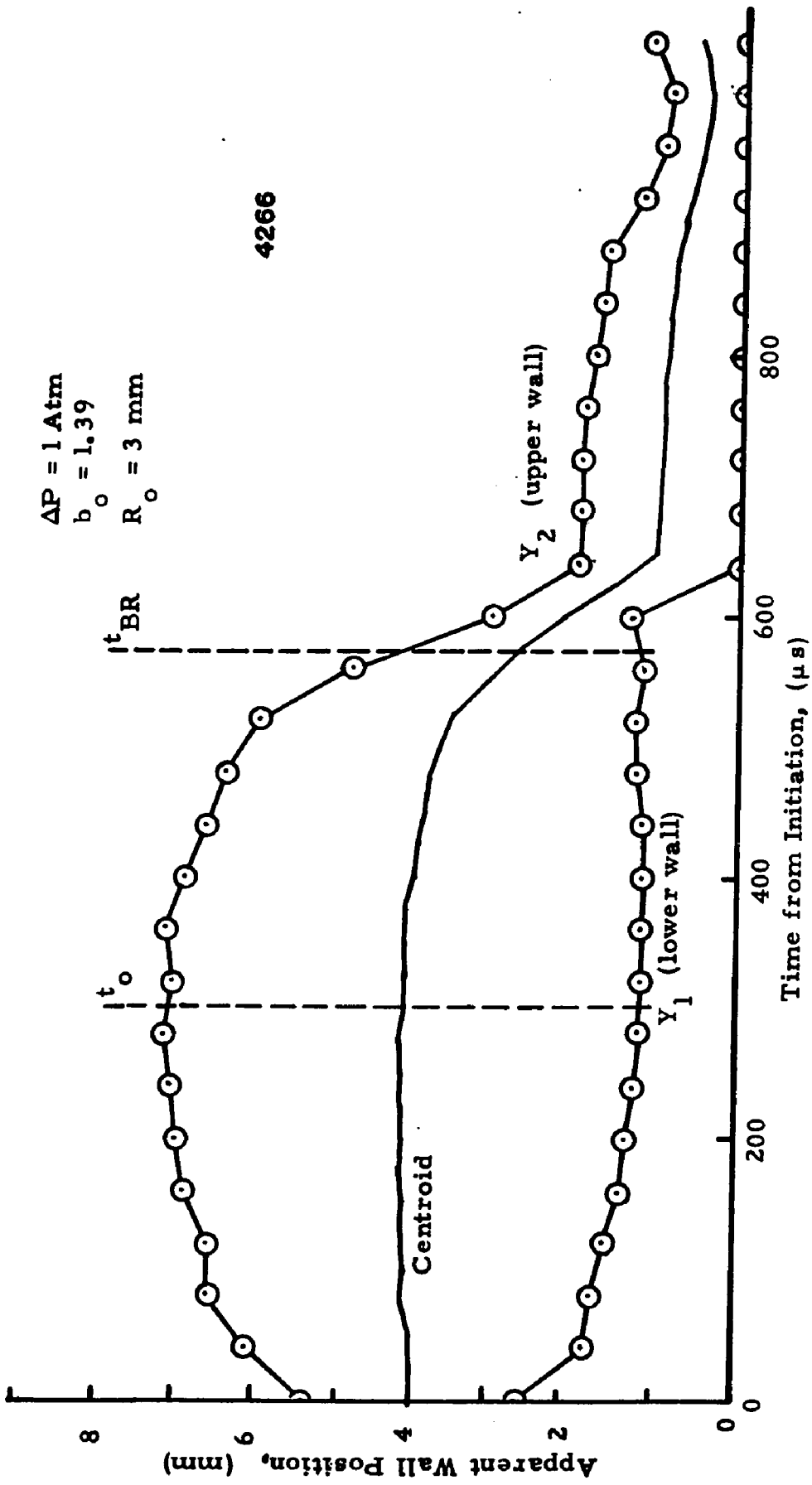


Figure 5.3 Wall Position, Run 1120-DSB-1

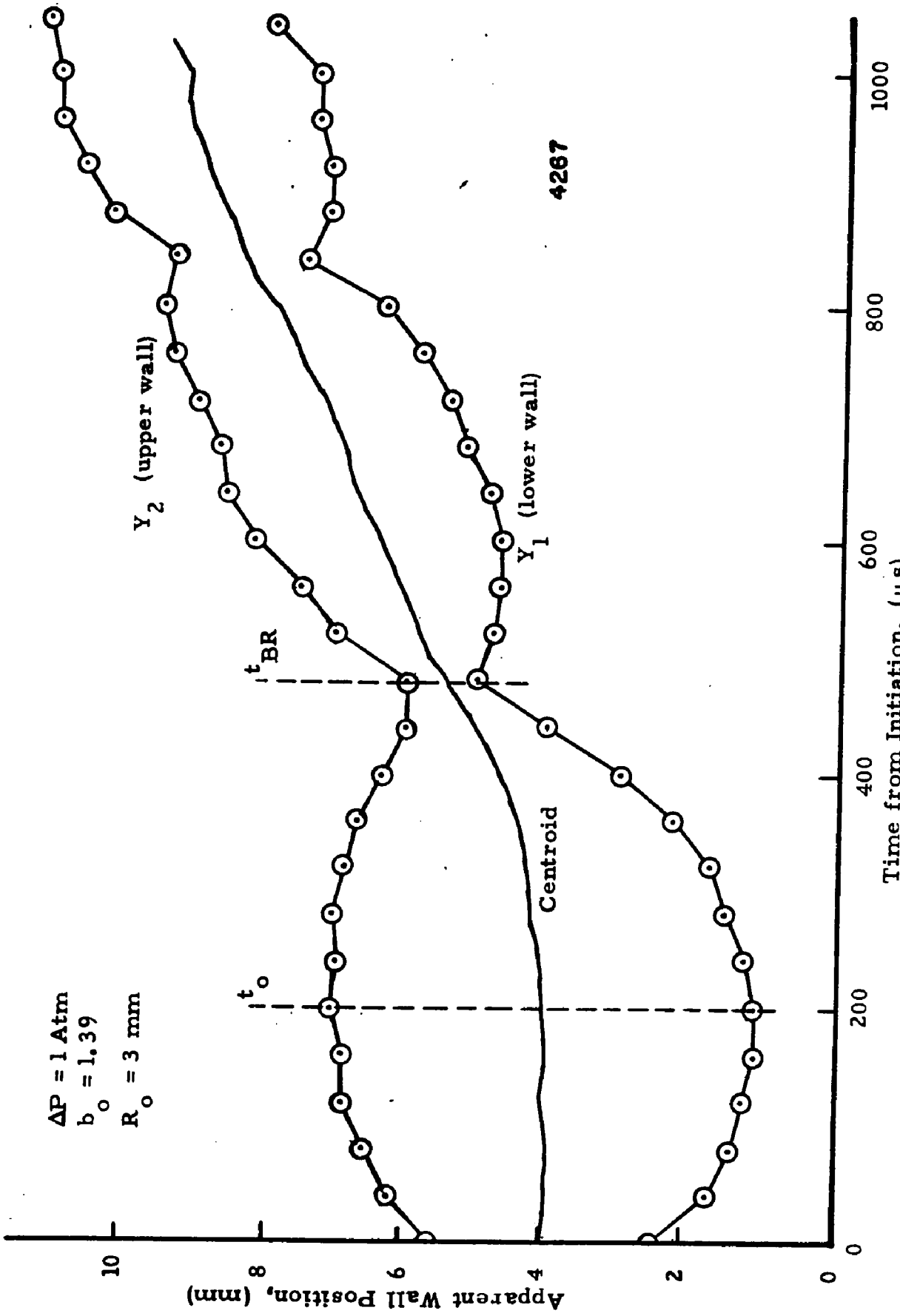


Figure 5.4 Wall Position, Run 10300-DSB-1

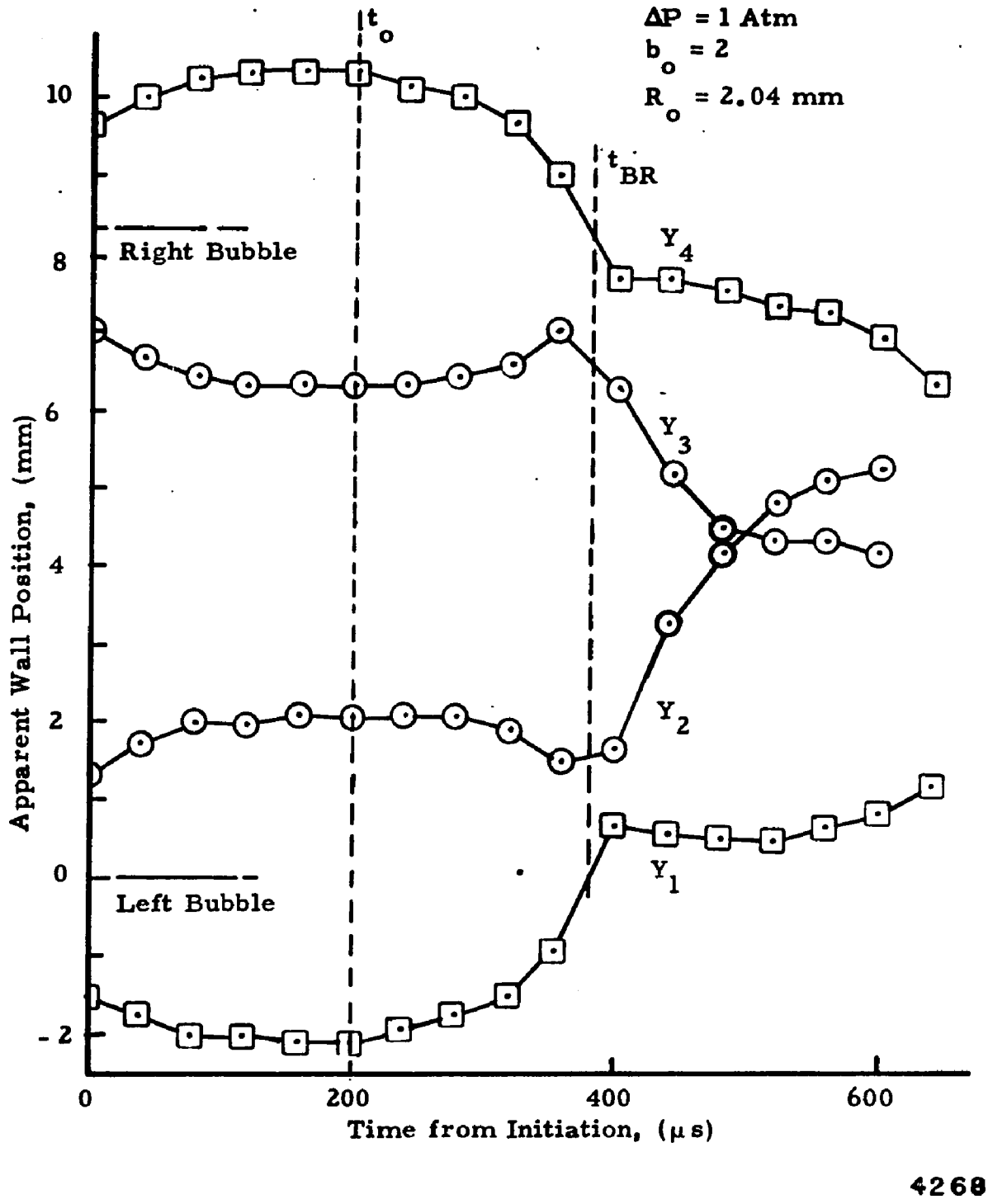


Figure 5.5 Wall Position, Run 10210-DSB-2

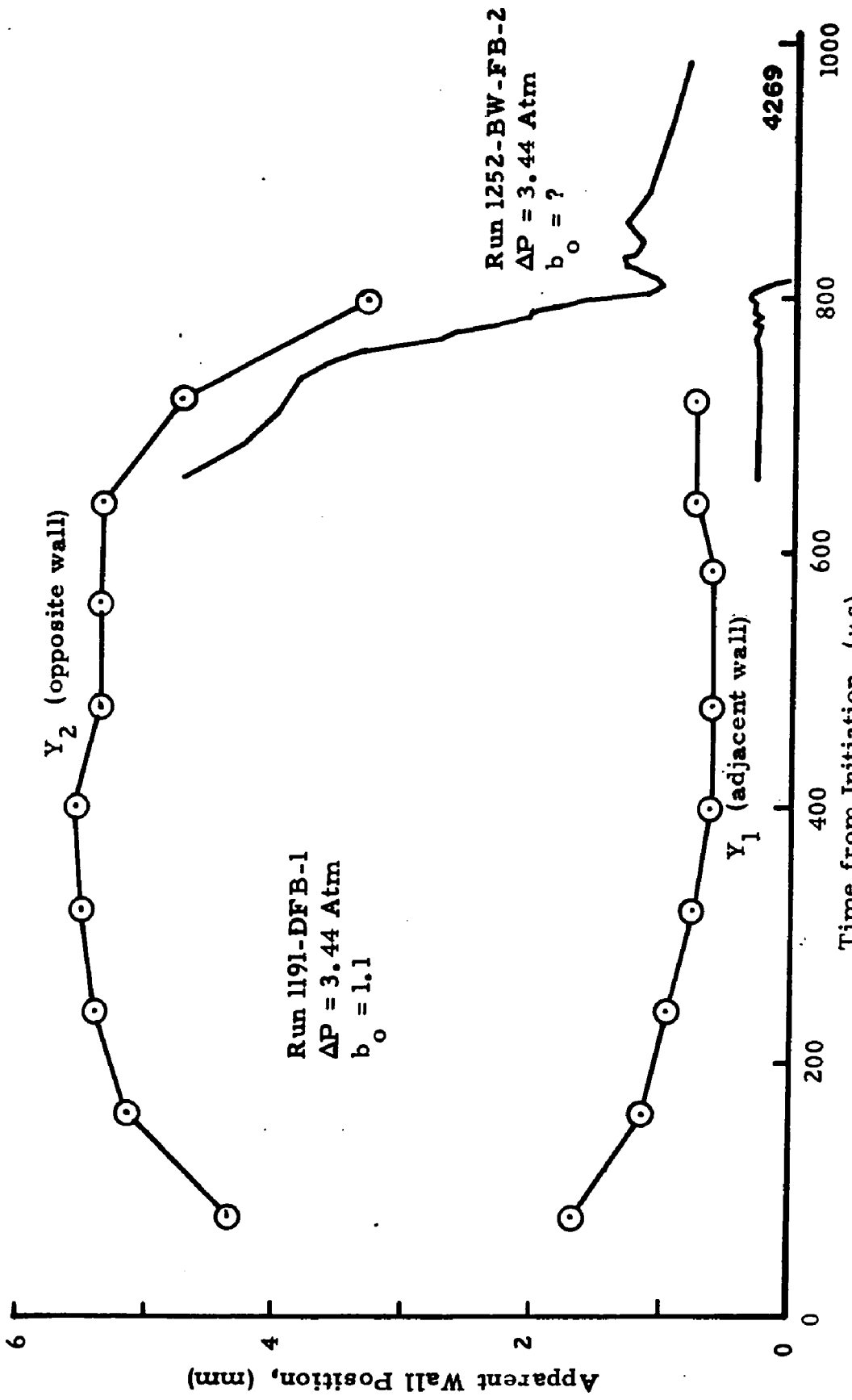


Figure 5.6 Wall Position, Runs 1191-DFB-1 and 1252-BW-FB-2

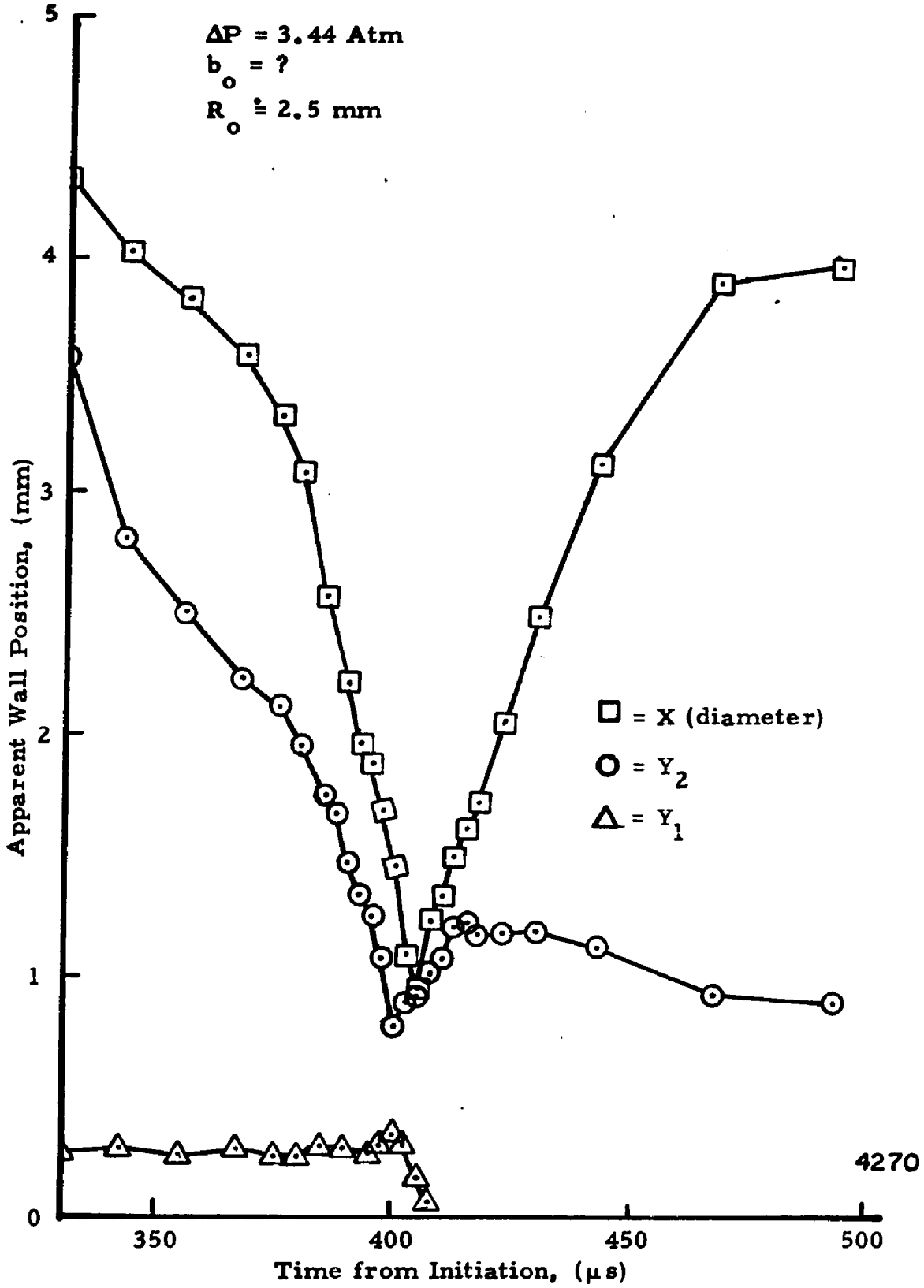


Figure 5.7 Wall Position, Run 1252-BW-FB-2

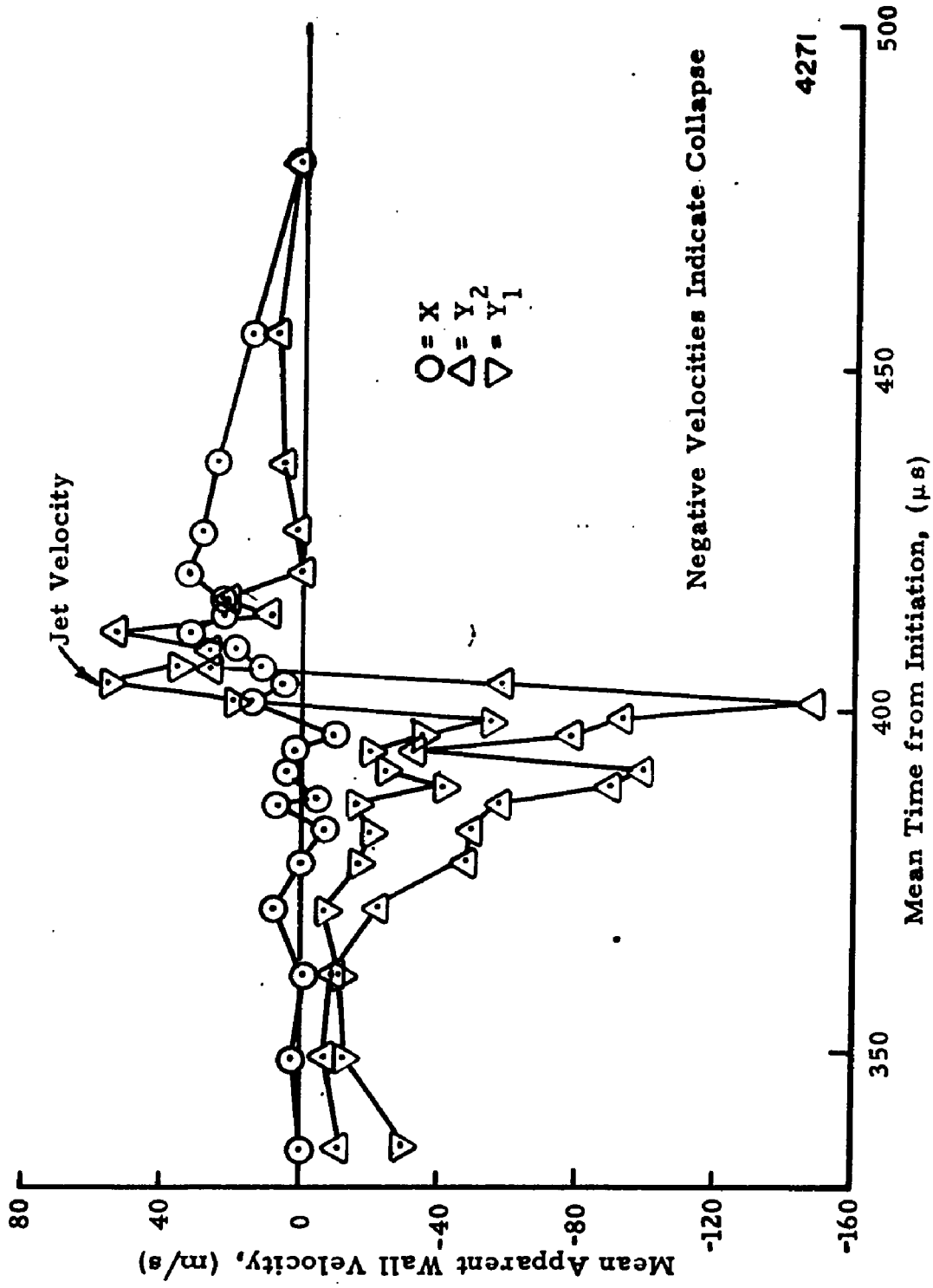
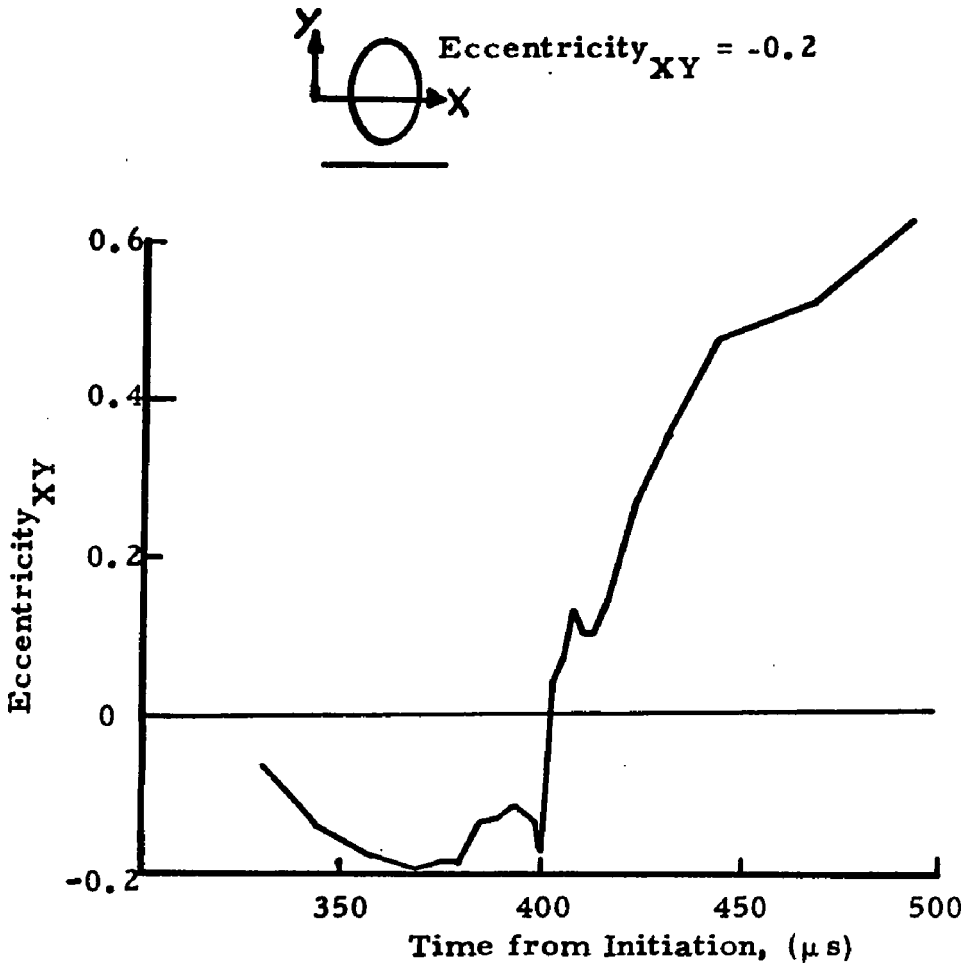


Figure 5.8 Wall Velocity, Run 1252-BW-FB-2



4272

Figure 5.9 Eccentricity, Run 1252-BW-FB-2

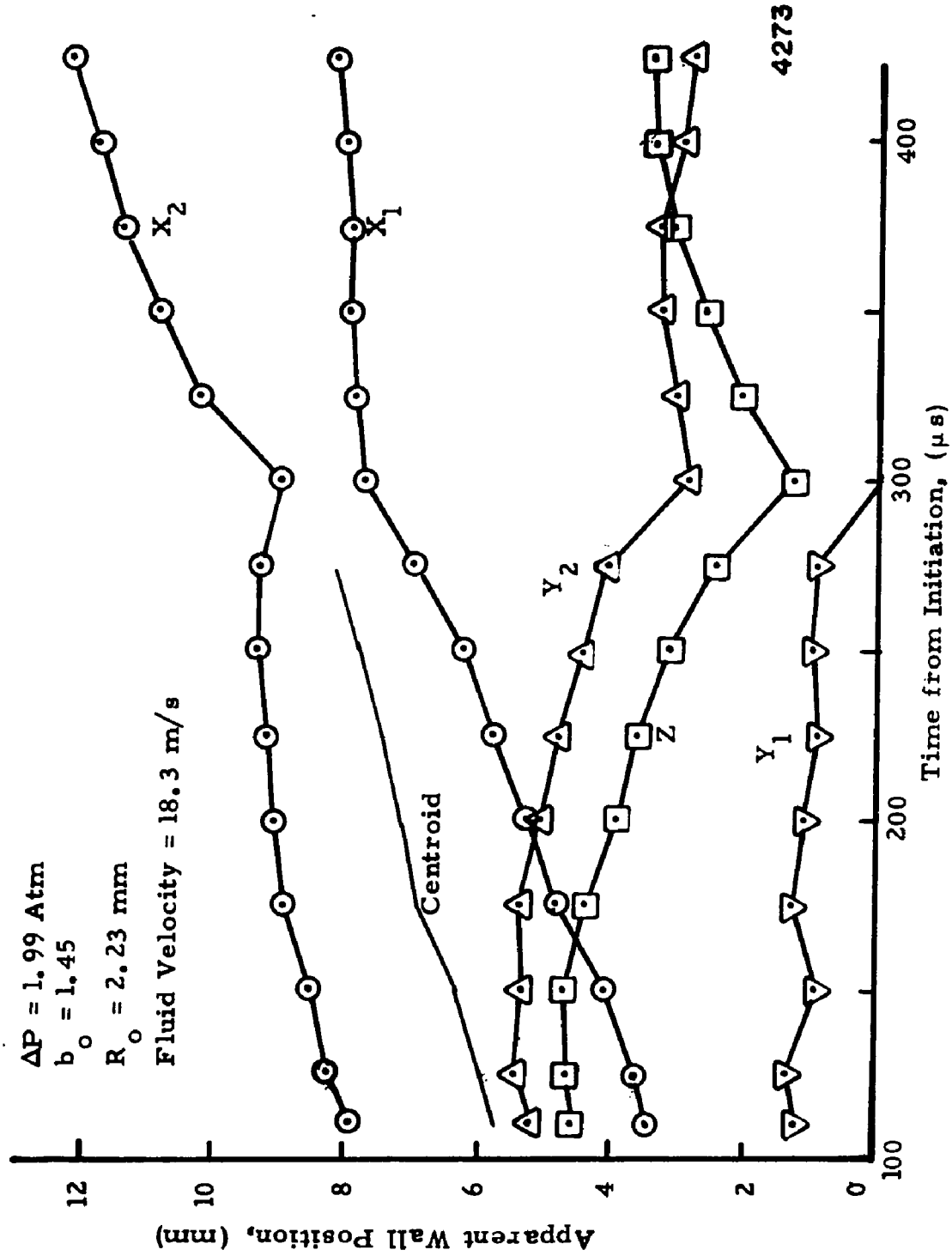


Figure 5.10 Wall Position, Run 7312-BW-2D-1

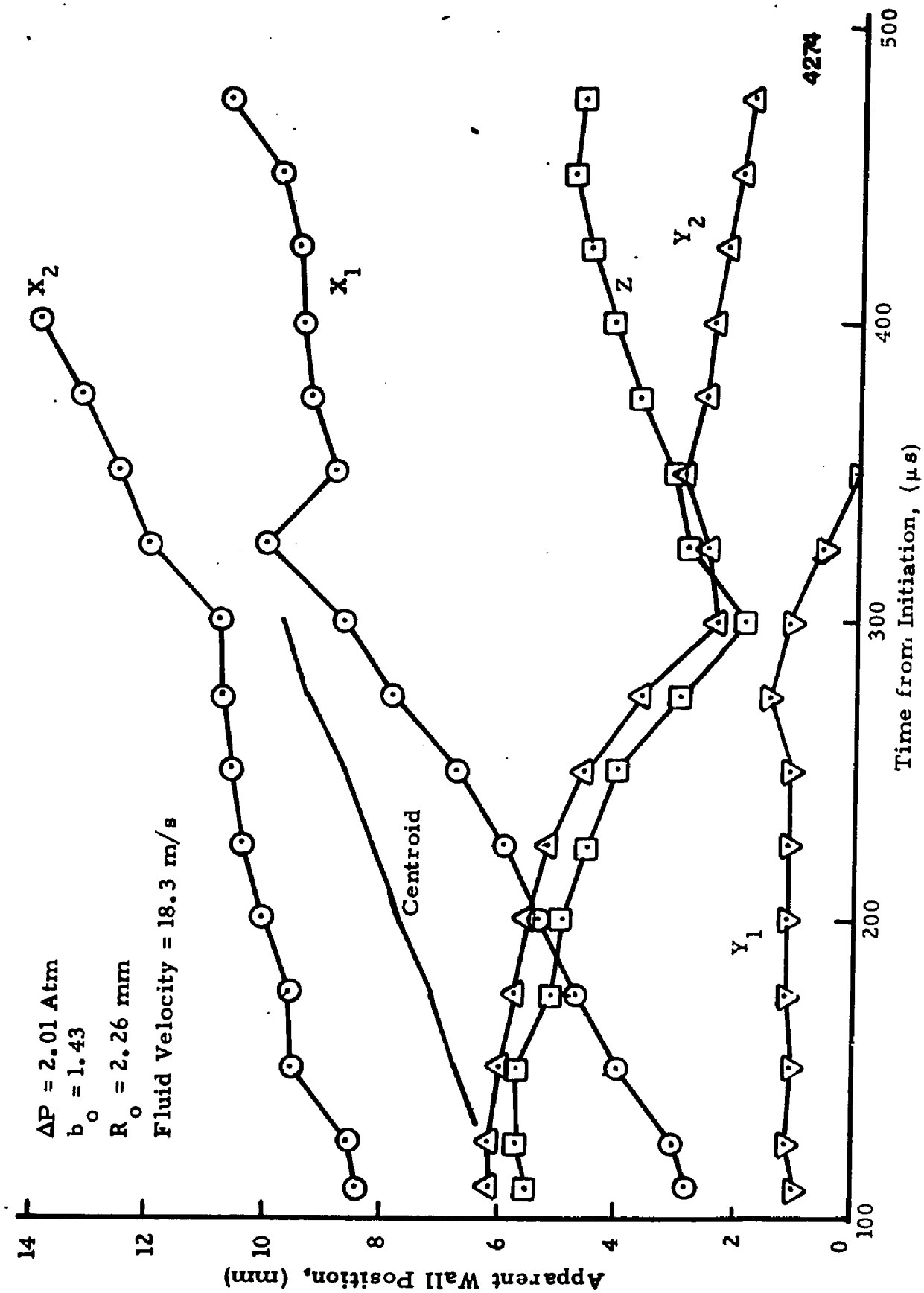


Figure 5.11 Wall Position, Run 852-BW-2D-3

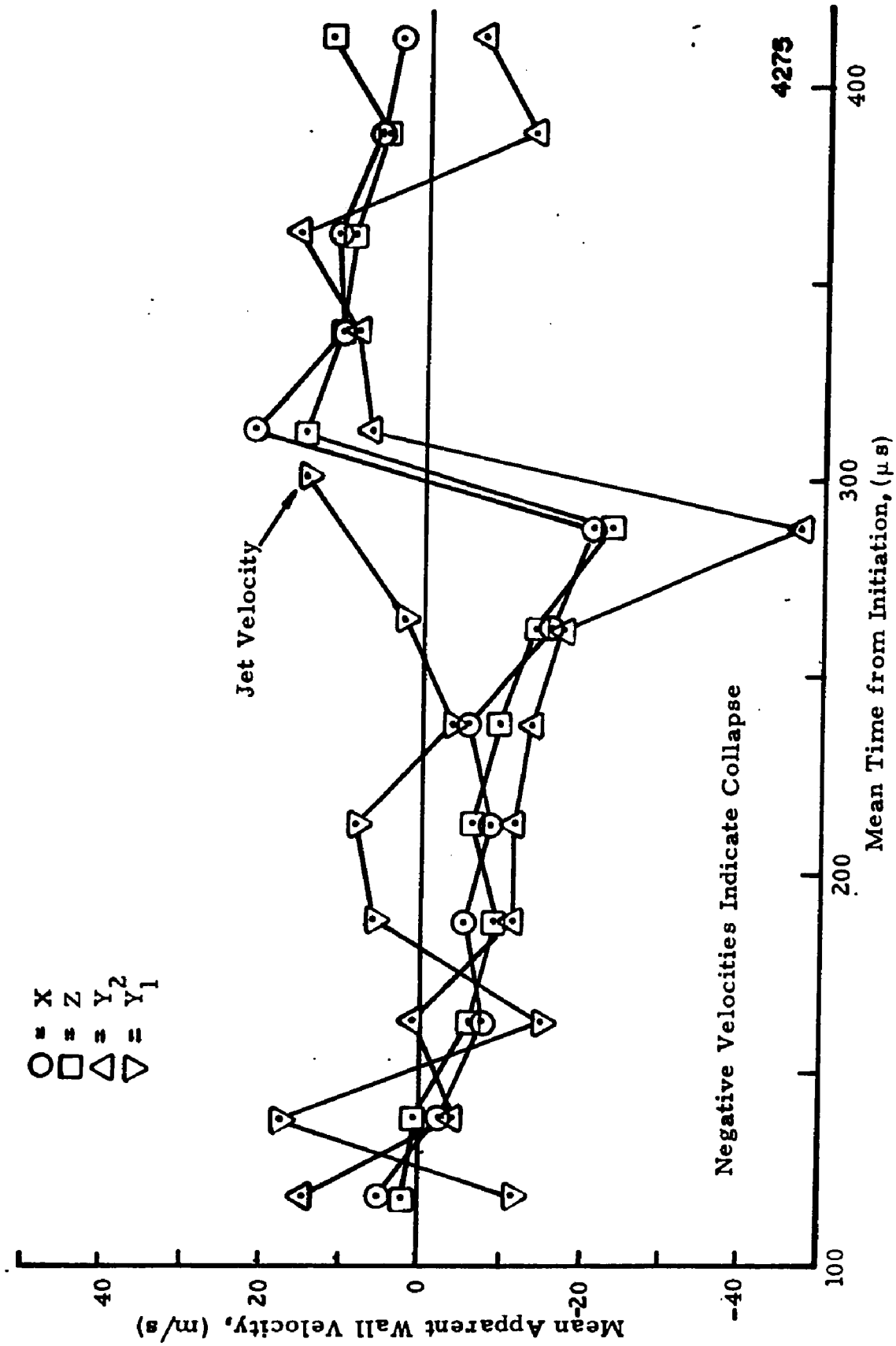


Figure 5.12 Wall Velocity, Run 7312-BW-2D-1

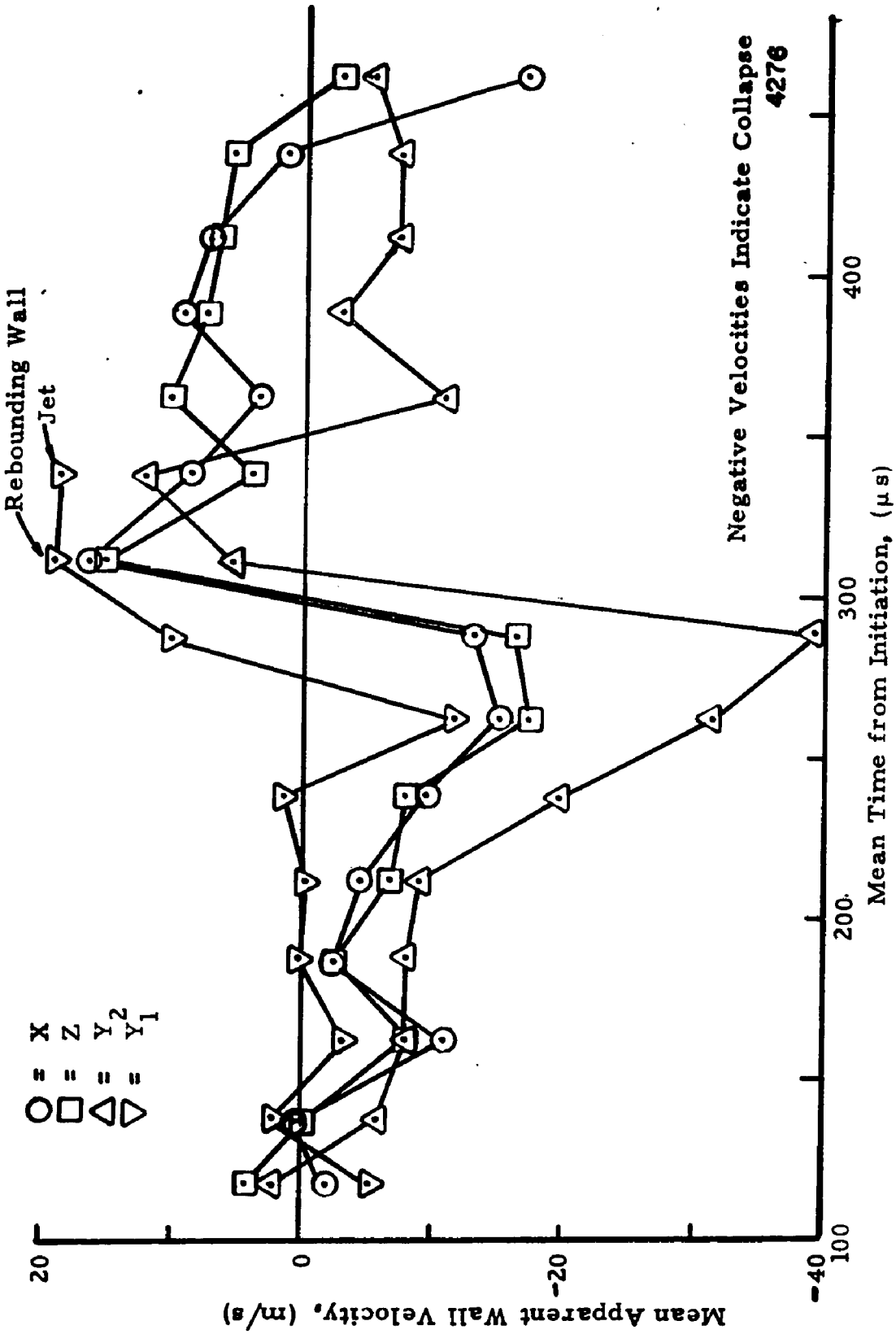


Figure 5.13 Wall Velocity, Run 852-BW-2D-3

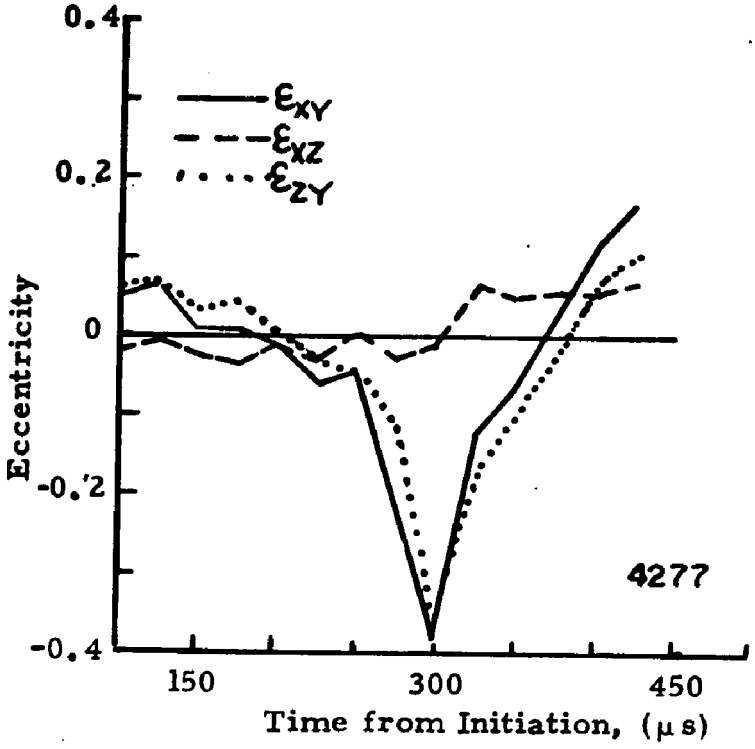


Figure 5.14 Eccentricity, Run 7312-BW-2D-1

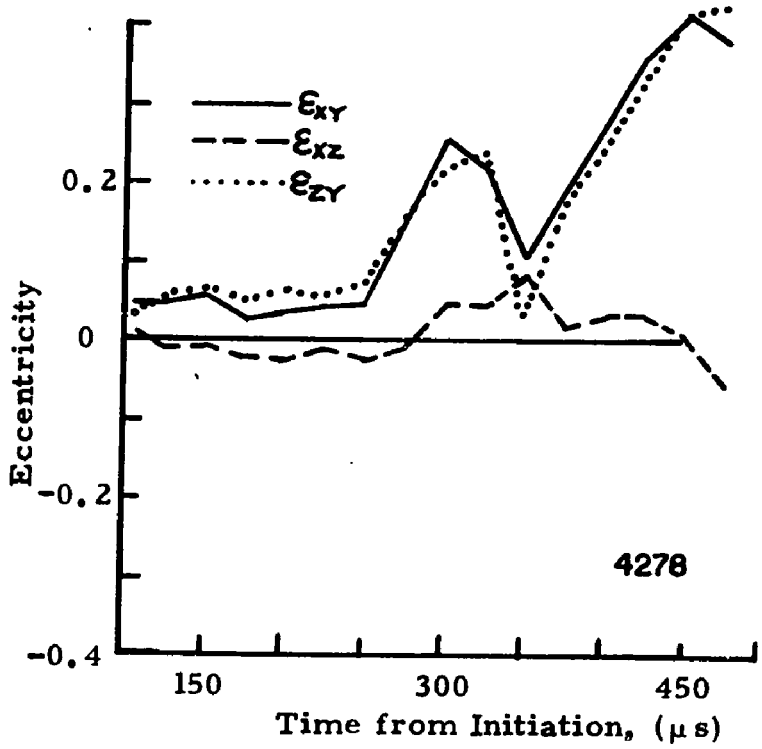


Figure 5.15 Eccentricity, Run 852-BW-2D-3

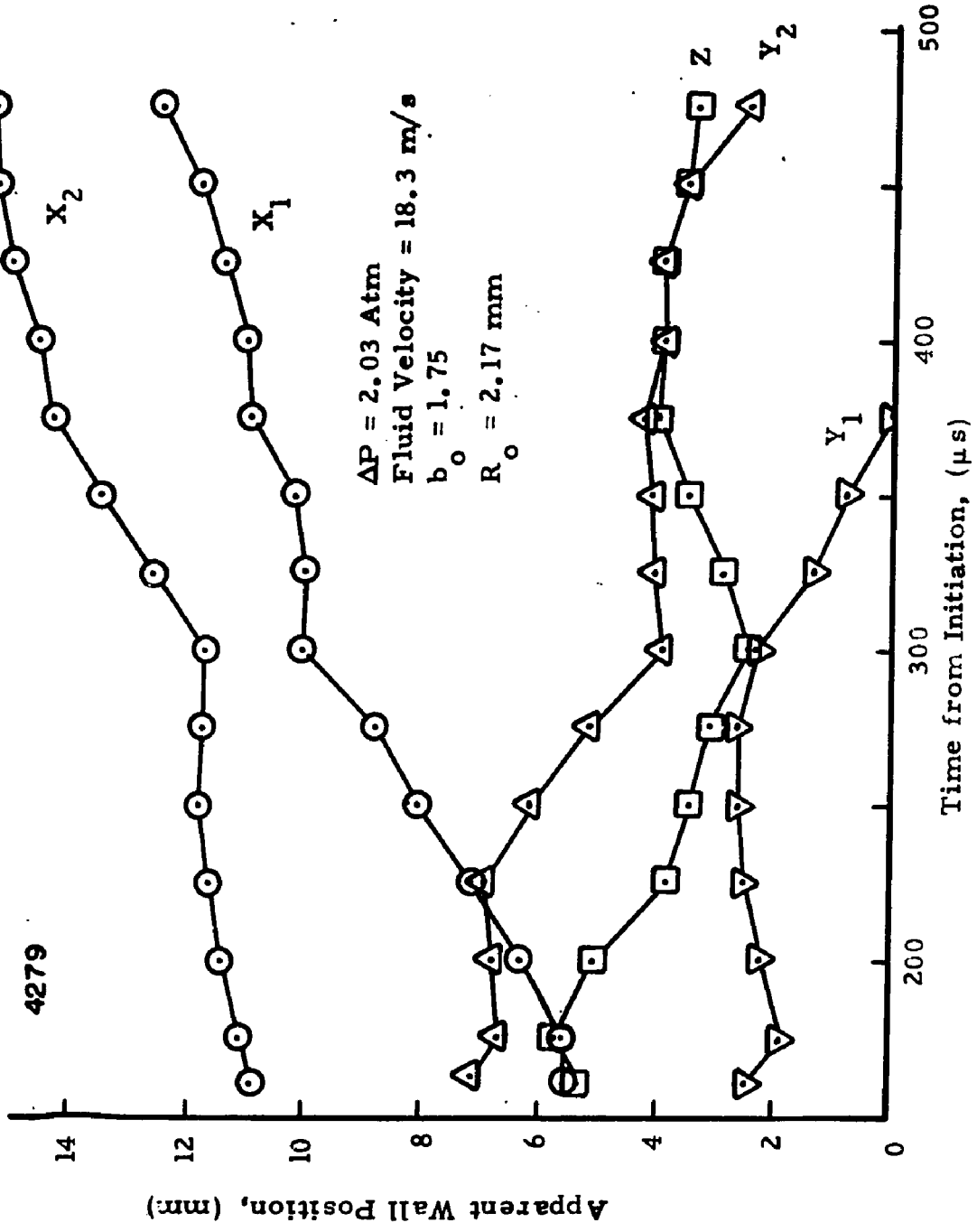


Figure 5.16 Wall Position, Run 7102-BW-2D-4

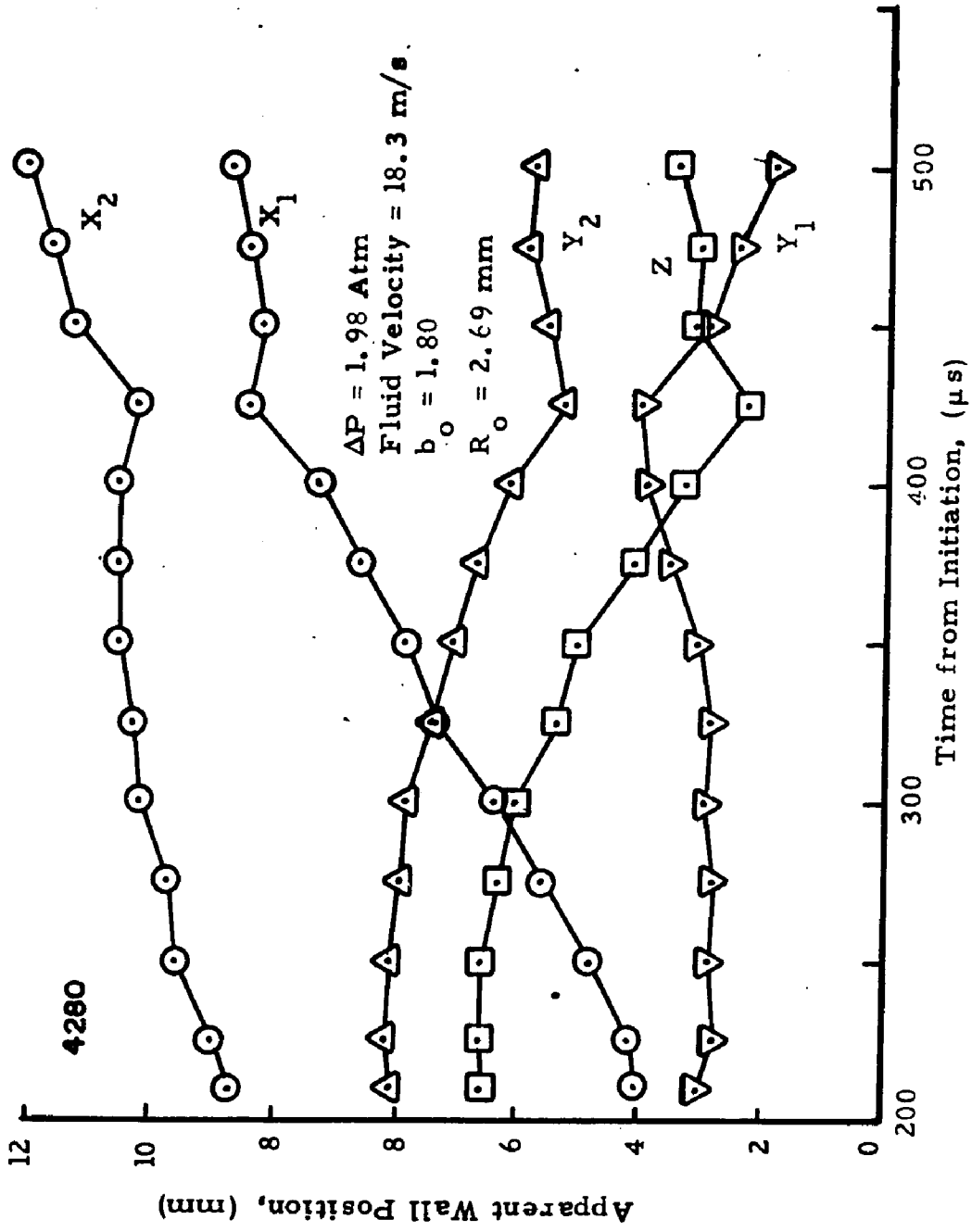


Figure 5.17 Wall Position, Run 842-BW-2D-5

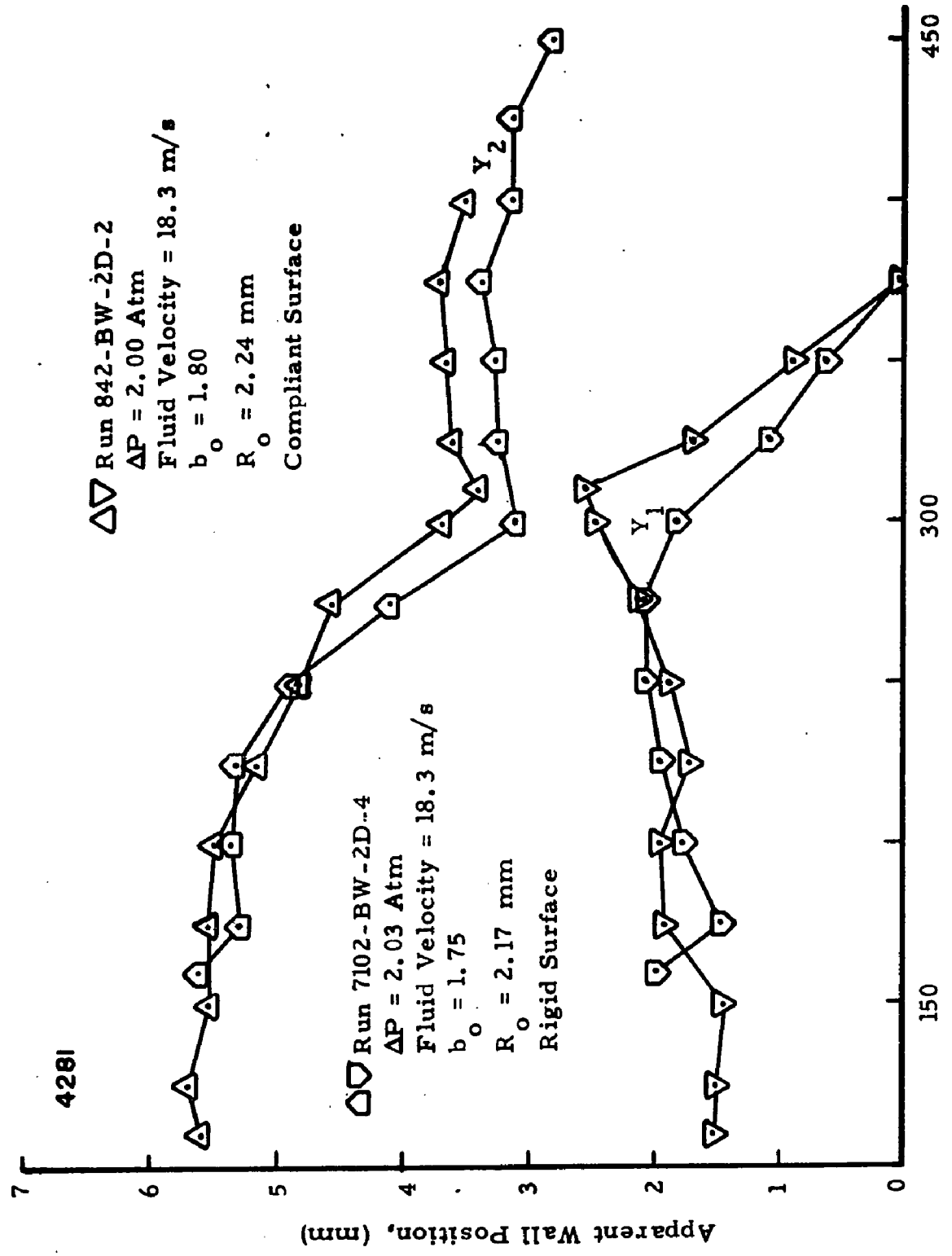


Figure 5.18 Wall Position, Run 842-BW-2D-2

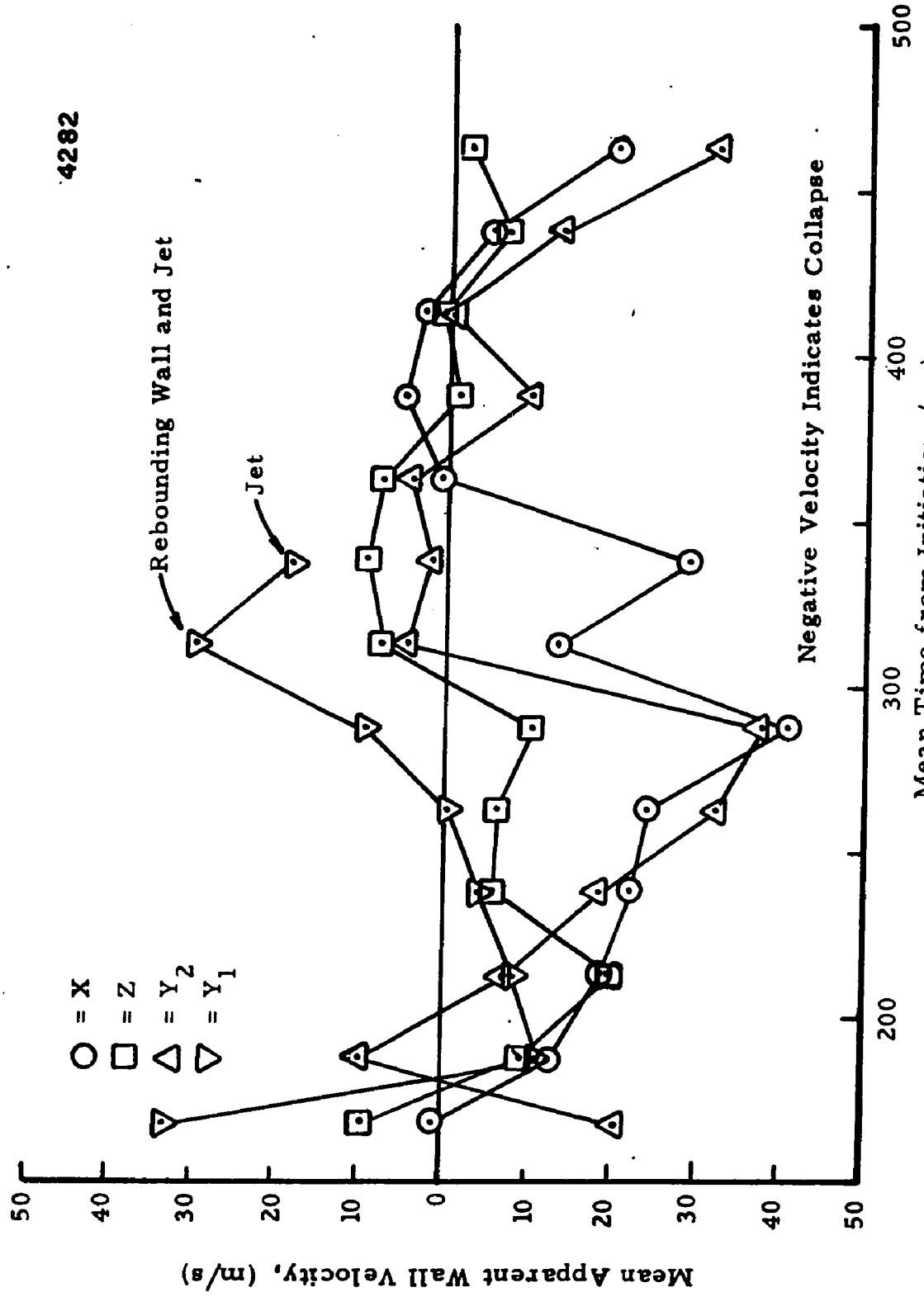


Figure 5.19 Wall Velocity, Run 7102-BW-2D-4

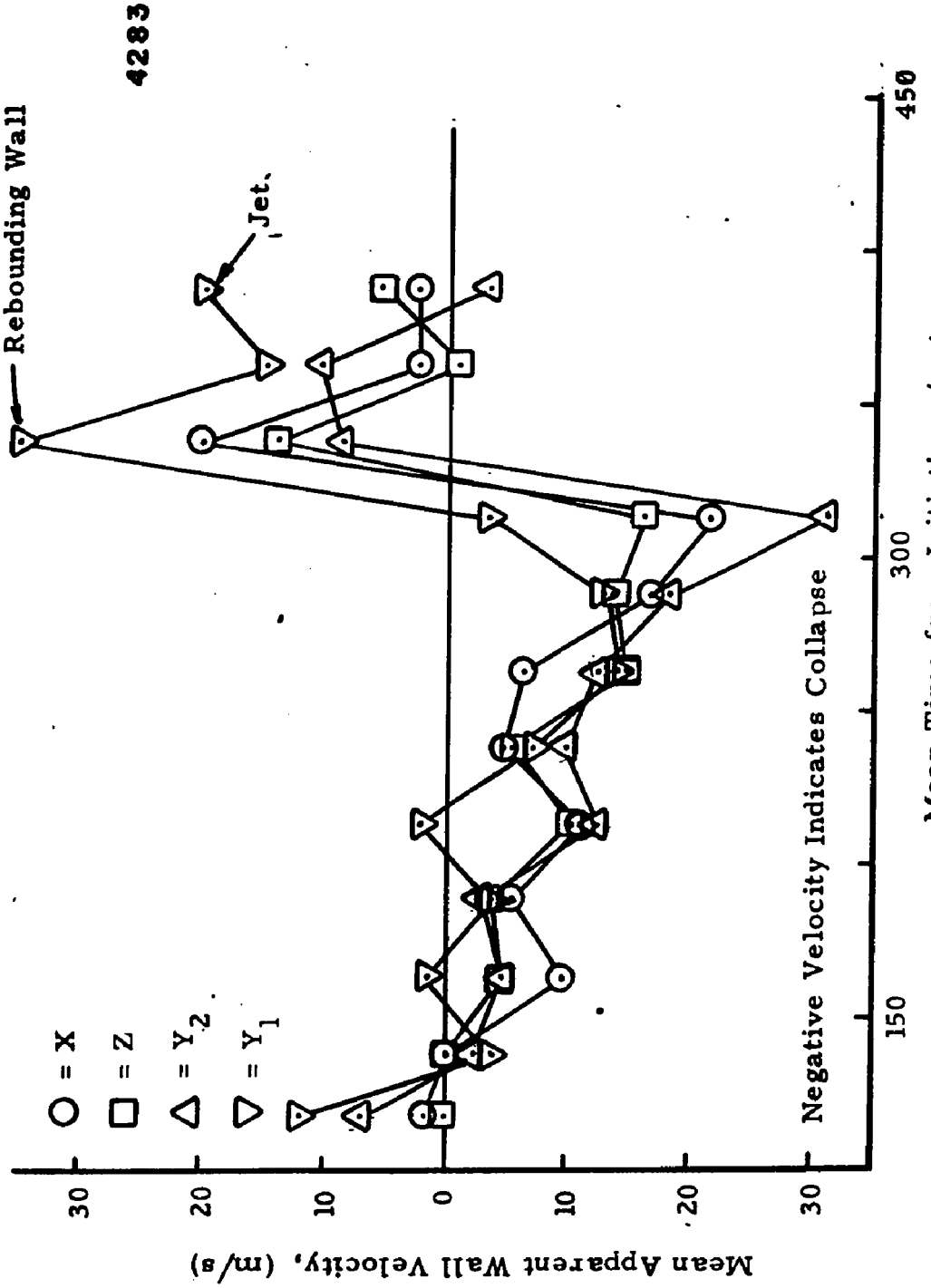


Figure 5.20 Wall Velocity, Run 842-BW-2D-5

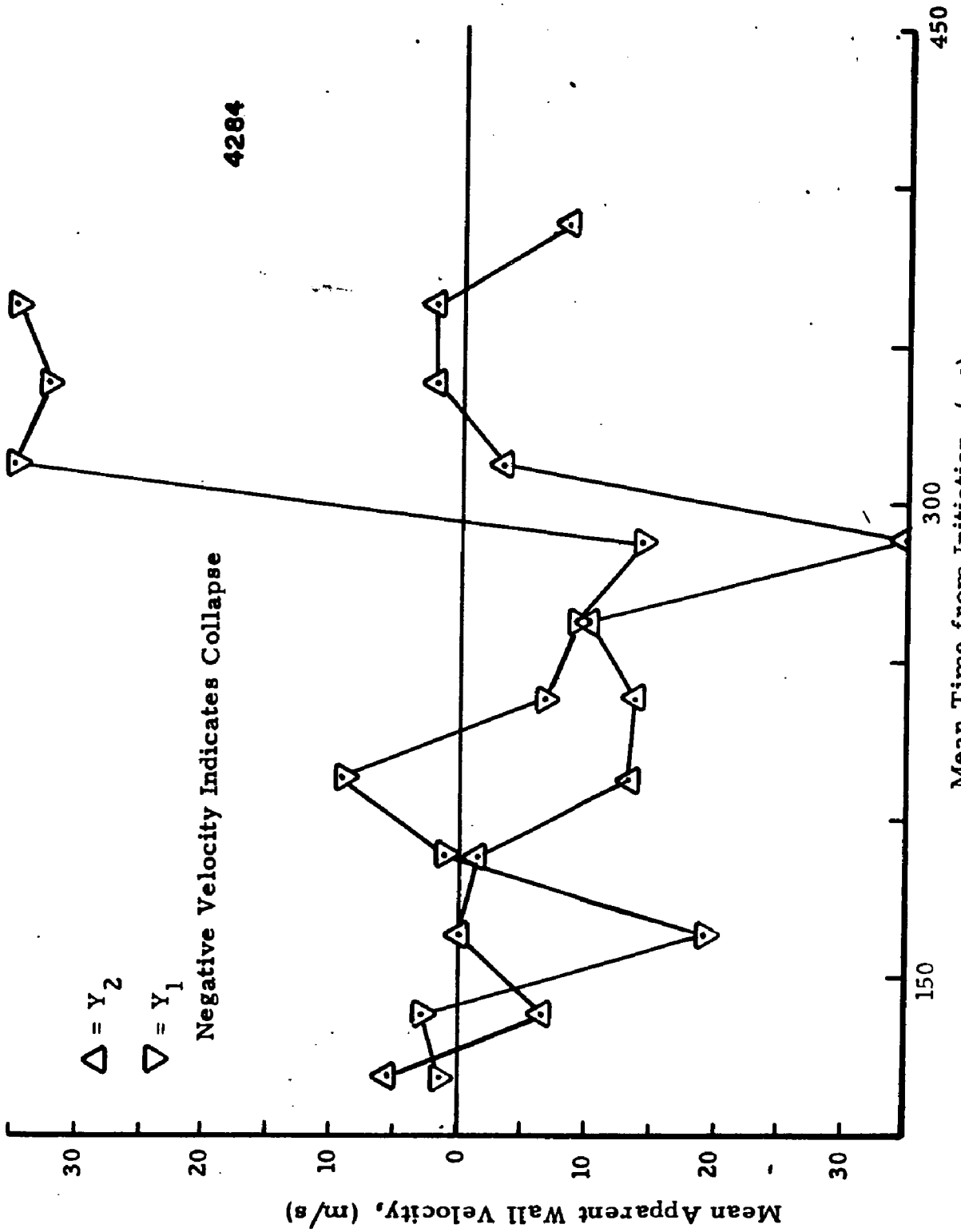


Figure 5.21 Wall Velocity, Run 842-BW-2D-2

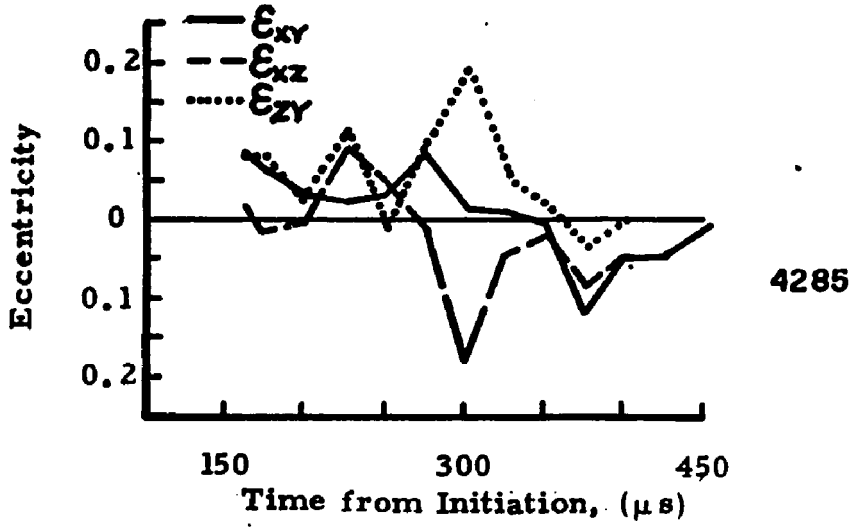


Figure 5.22 Eccentricity, Run 7102-BW-2D-4

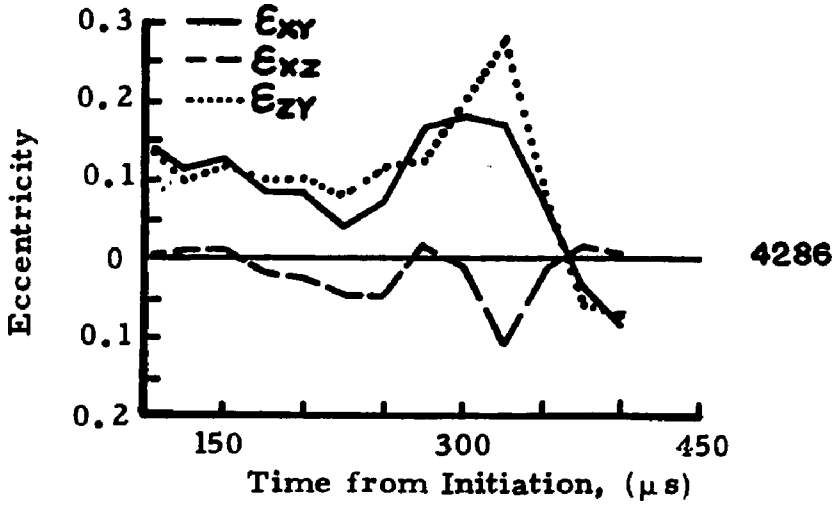


Figure 5.23 Eccentricity, Run 842-BW-2D-5

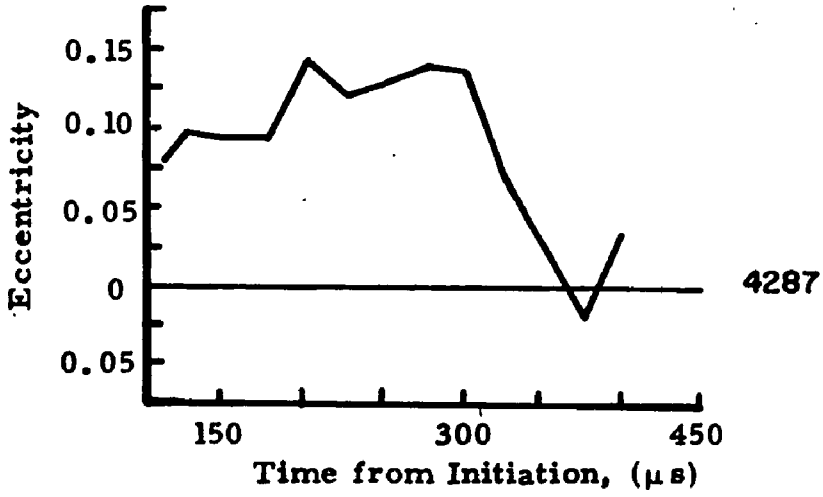


Figure 5.24 Eccentricity, Run 842-BW-2D-2

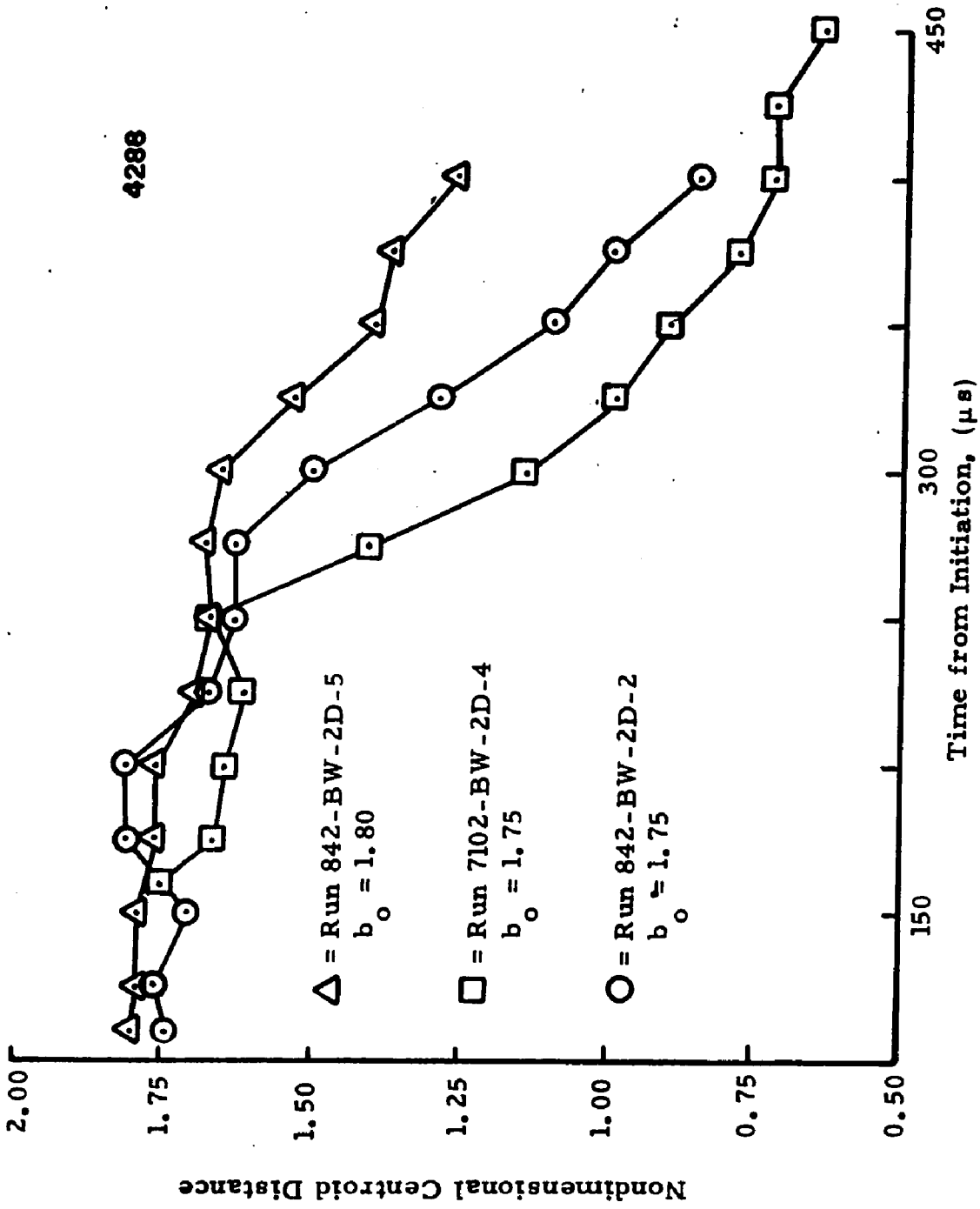


Figure 5.25 Centroid Position

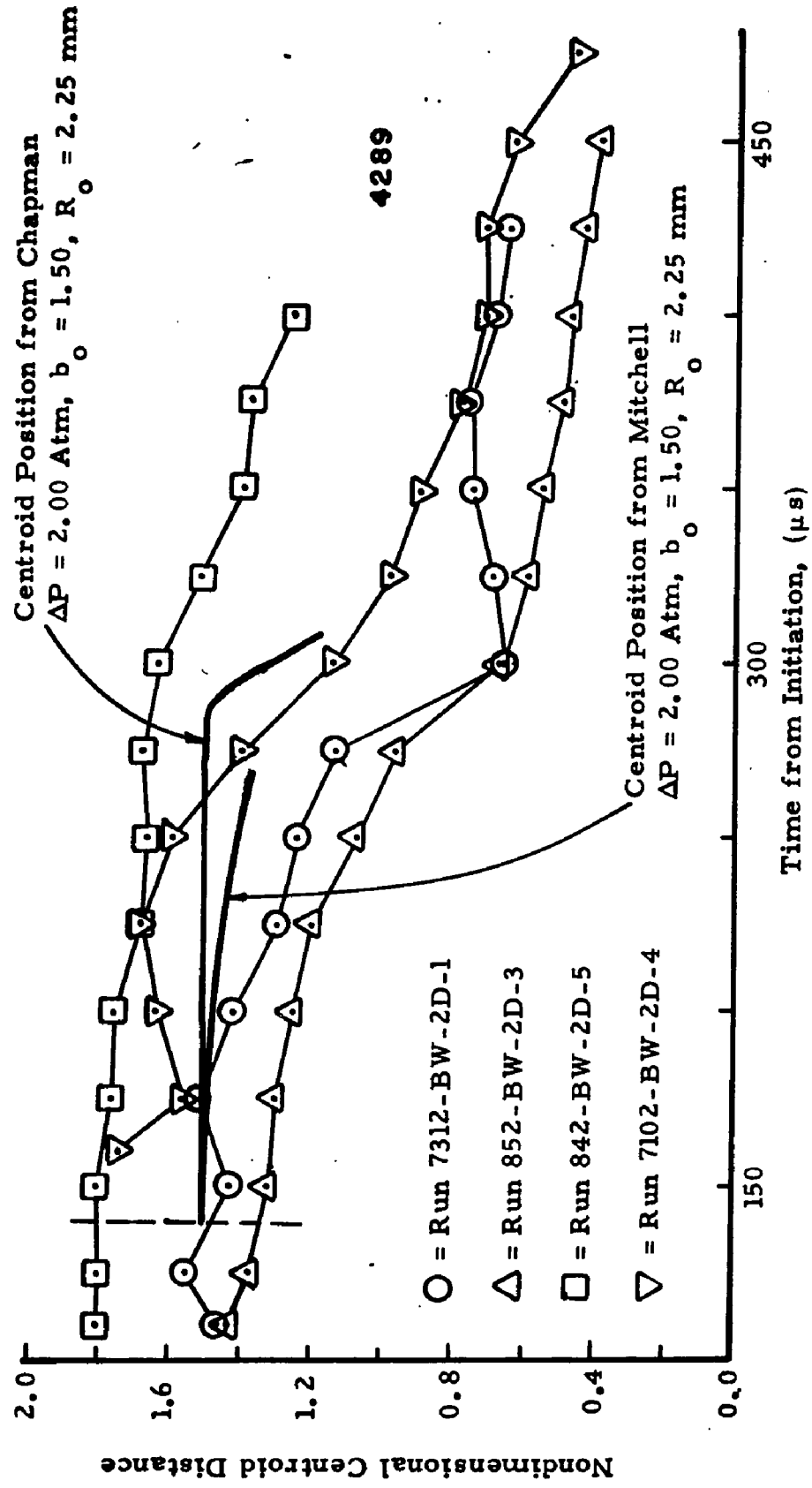


Figure 5.26 Centroid Position Comparision

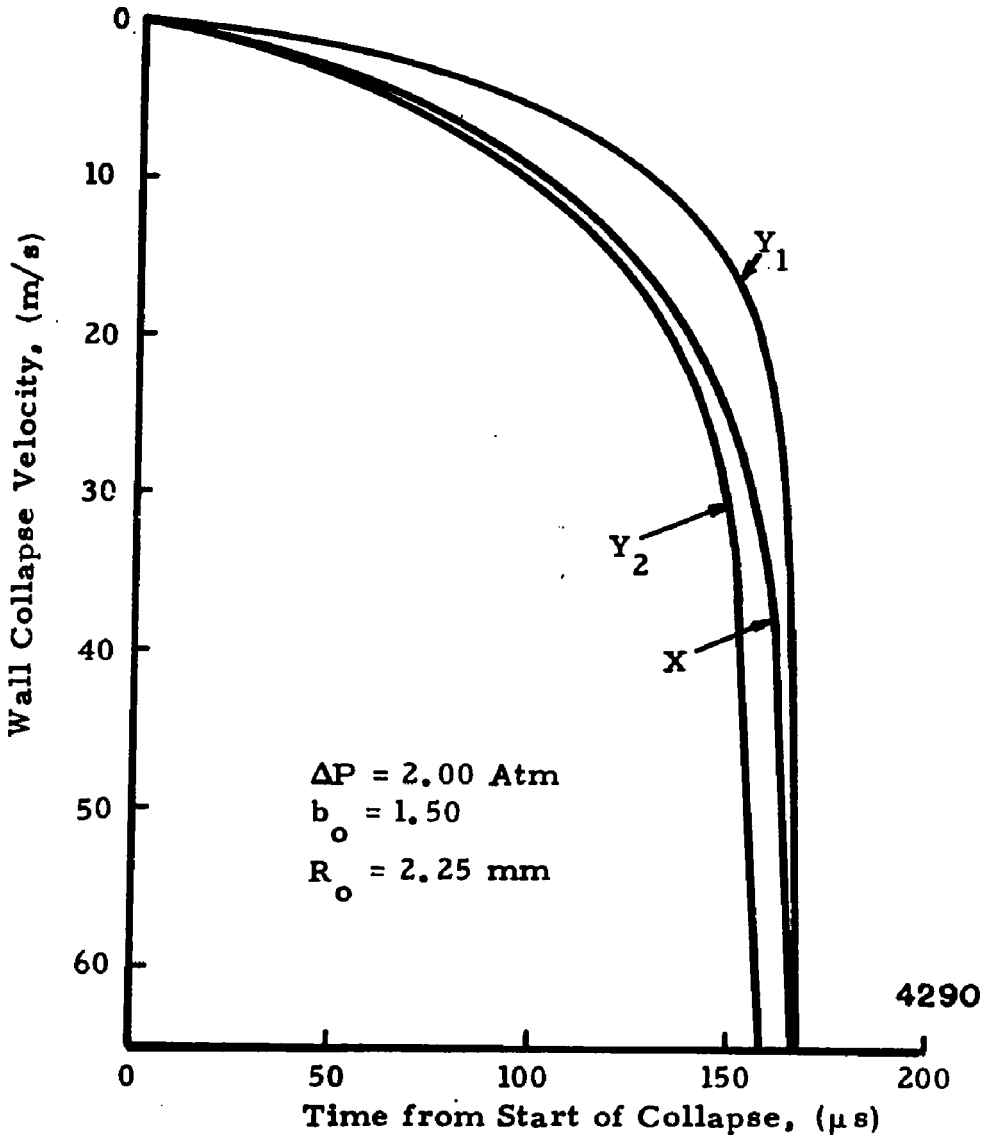


Figure 5.27 Wall Velocities from Chapman

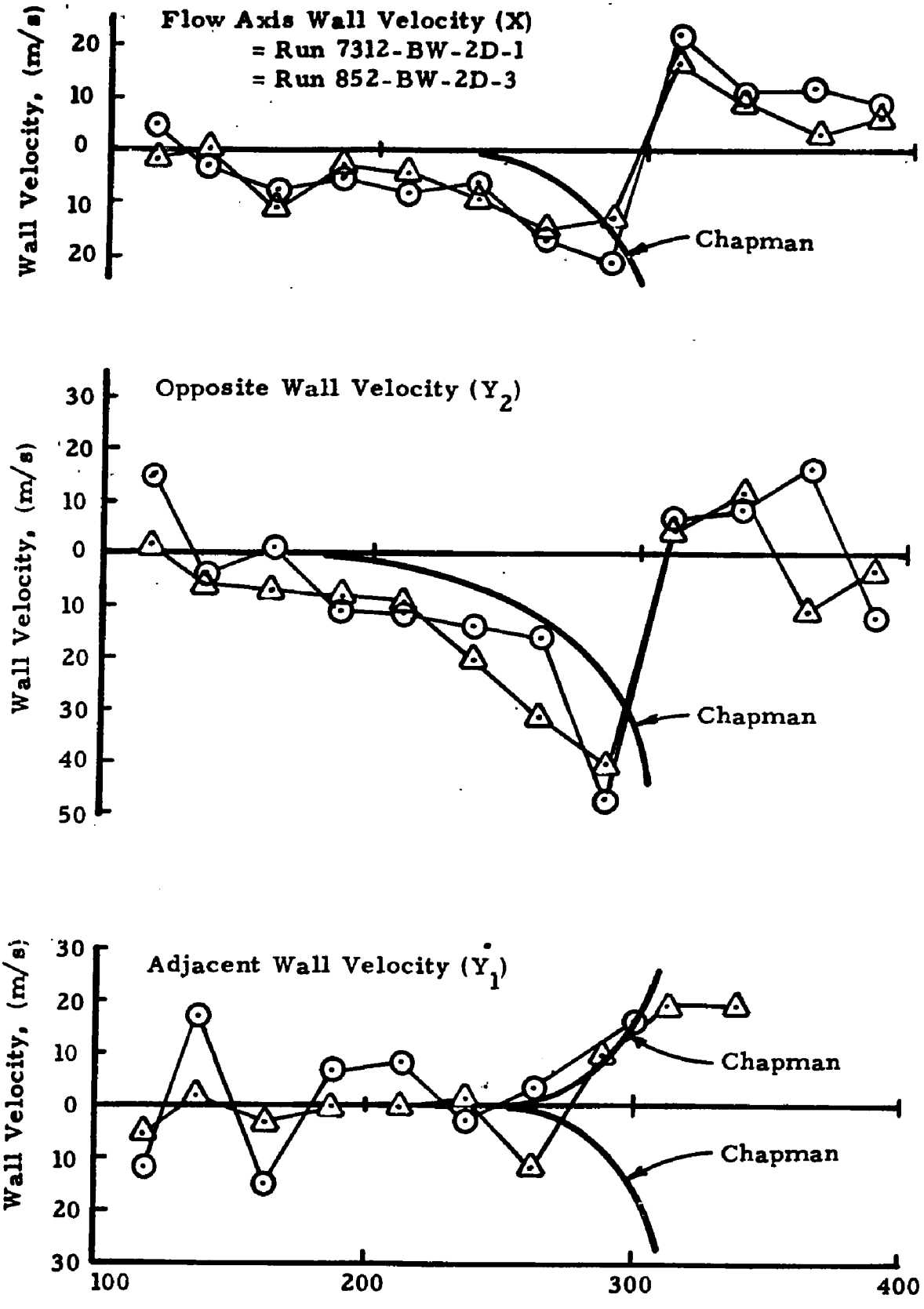


Figure 5.28 Wall Velocity Comparision, $\Delta P = 2.00$ Atm, $b_o = 1.50$ $R_o = 2.25$ mm

4291

CHAPTER 6

EXPERIMENTAL INVESTIGATION OF WATER JET IMPINGEMENT

6.1 GENERAL PROCEDURE

Experiments were conducted to investigate the collision between a high speed water jet and a solid surface. These investigations were directed into two areas: photographic studies of the impact, and studies of the damage produced by multiple impacts. The experimental photographic procedures utilized to study the impact phenomena were similar to those utilized in the investigation of bubble collapse, described in Section 4.1. Experiments were conducted to determine how susceptible to water impact damage the materials described in Section 3.2b are. General procedure consisted of repeated bombardment of the specimen with water jets generated by the high speed water jet gun. Material damage was measured qualitatively by visual inspection and quantitatively by weighing the specimens at selected intervals. Detailed discussion of these experiments is given in the following sections.

6.2 PHOTOGRAPHIC INVESTIGATION OF IMPACT PHENOMENA

It was decided to limit the investigation of water jet impact phenomena to a study utilizing jets of a typical, nominal velocity. This velocity was chosen to be one typical of the impact velocities thought involved when the jet from a collapsing bubble strikes a nearby surface or when a surface on a commercial aircraft strikes a raindrop, approximately 220 m/s. At this jet velocity the collision and resultant splash show temporal detail for a period of

about 100 microseconds when the Model 330 Camera is used for the study at a magnification sufficient to show fine spatial detail. Therefore, a camera framing rate on the order of 5×10^5 f/s was utilized, with a resultant camera writing time of 160 microseconds. Preliminary studies indicated that partially diffused back light was the best type of illumination and therefore the Model 450 light source was set up with a collimating lens and a ground glass diffuser, as pictured in Figure 6.1. The jet gun was fired, after manual cocking and loading, by an electrical impulse to its firing solenoid, which also served to actuate the capping shutter solenoid in the Model 330 Camera. The output beam from the laser was directed across the jet's path and into the photodiode sensor. When the jet interrupted the light beam, a pulse was generated which, after suitable delay and shaping, was used to trigger the light source. After exposure, the film was developed and prints were made. The measurements indicated in Figure 6.2 were taken from each print. This procedure was applied to all of the materials studied. Figures 6.3 through 6.7 consist of the prints for photographic runs on, respectively: Aluminum, Epon 828; Plexiglass; Rubber A; and Rubber B. Figure 6.8 shows the collision of the jet with an aluminum specimen upon which a drop of water is suspended.

6.3 EXPERIMENTAL INVESTIGATION OF IMPACT DAMAGE SUSCEPTIBILITY

The high speed water jet gun was set up to produce, repetitively, water jets with a nominal velocity of 220 m/s.

The material samples used in the photographic study were cleaned, dried, and weighed on a Mettler balance which is accurate within 0.05 milligram. The samples were then bombarded several times, cleaned, dried, and re-weighed. This procedure was repeated until curves of weight loss as a function of number of impacts had been developed for all the materials. The number of impacts necessary to damage the samples differed for each material, so the number of impacts each material was subjected to between weighings was adjusted for each material. During these tests the jet velocity was periodically monitored for consistency with the photoelectric velocity sensor. Since only one sample of some of the materials was available, every effort was made to insure against the introduction of uncontrolled variables into the tests. The preparation of the samples before weighing was given utmost attention and the following procedure was adopted: the sample was rinsed with tap water; the sample was rinsed with anhydrous methanol; the sample was dried for 5 minutes in a vacuum oven; and finally the sample was carefully transferred to the balance room for weighing. All tests were conducted at room temperature using the same batch of tap water in the jet gun.

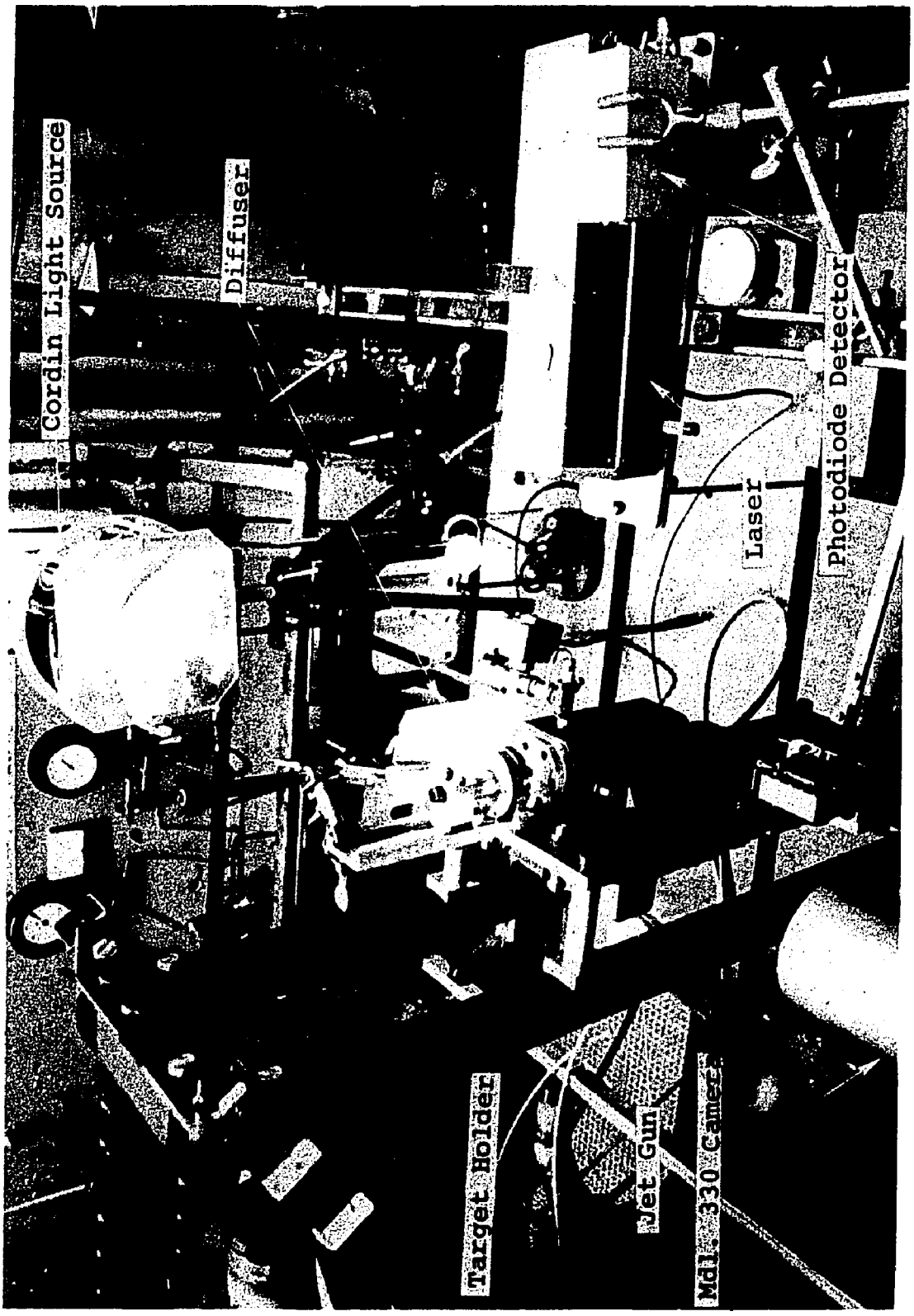


Figure 6.1 Jet Gun w/Model 330 Camera

4292

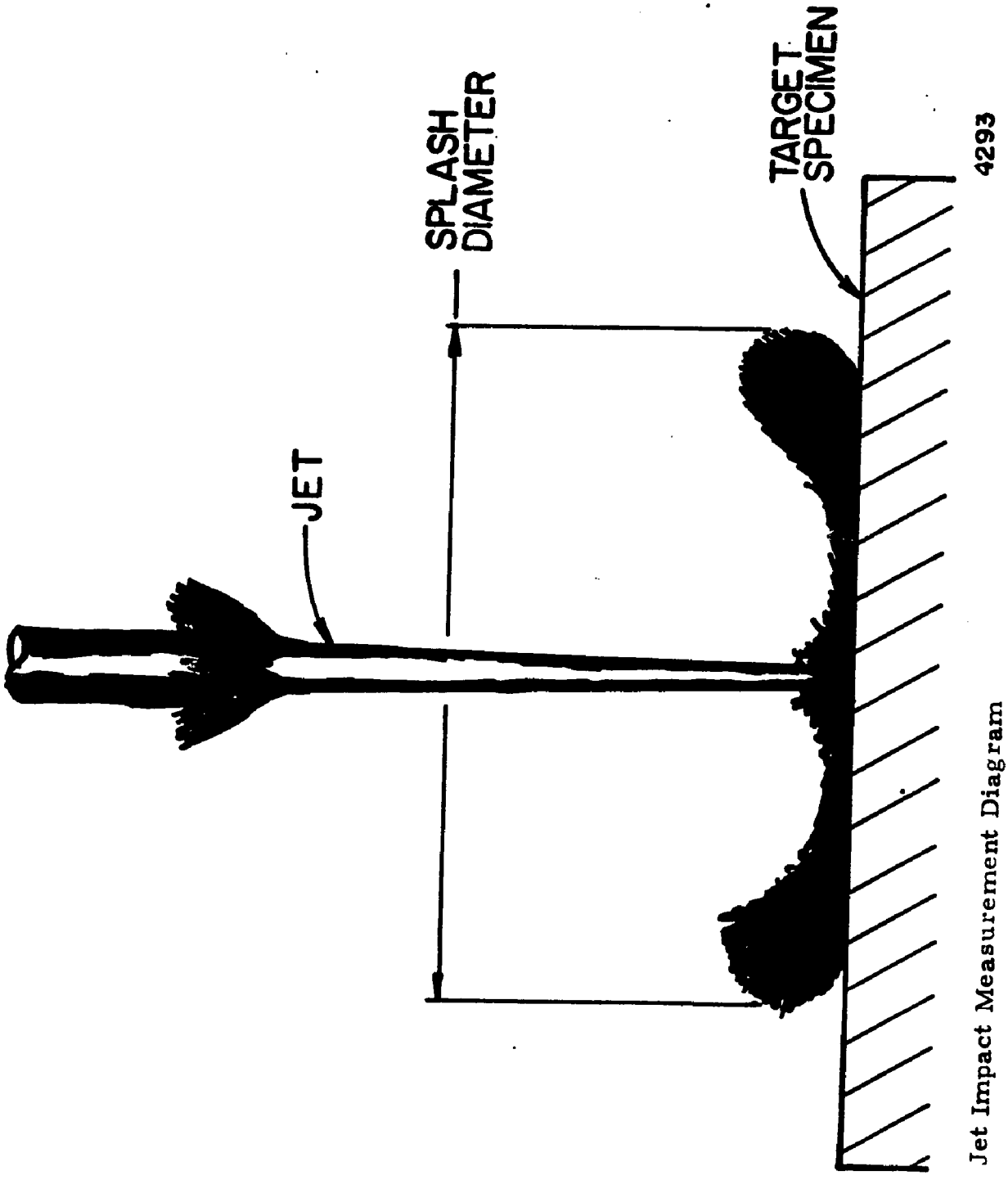


Figure 6.2 Jet Impact Measurement Diagram

RUN 892-BW-I-1

JET VELOCITY = 228 m/s
TARGET MTL = 1100 ALU

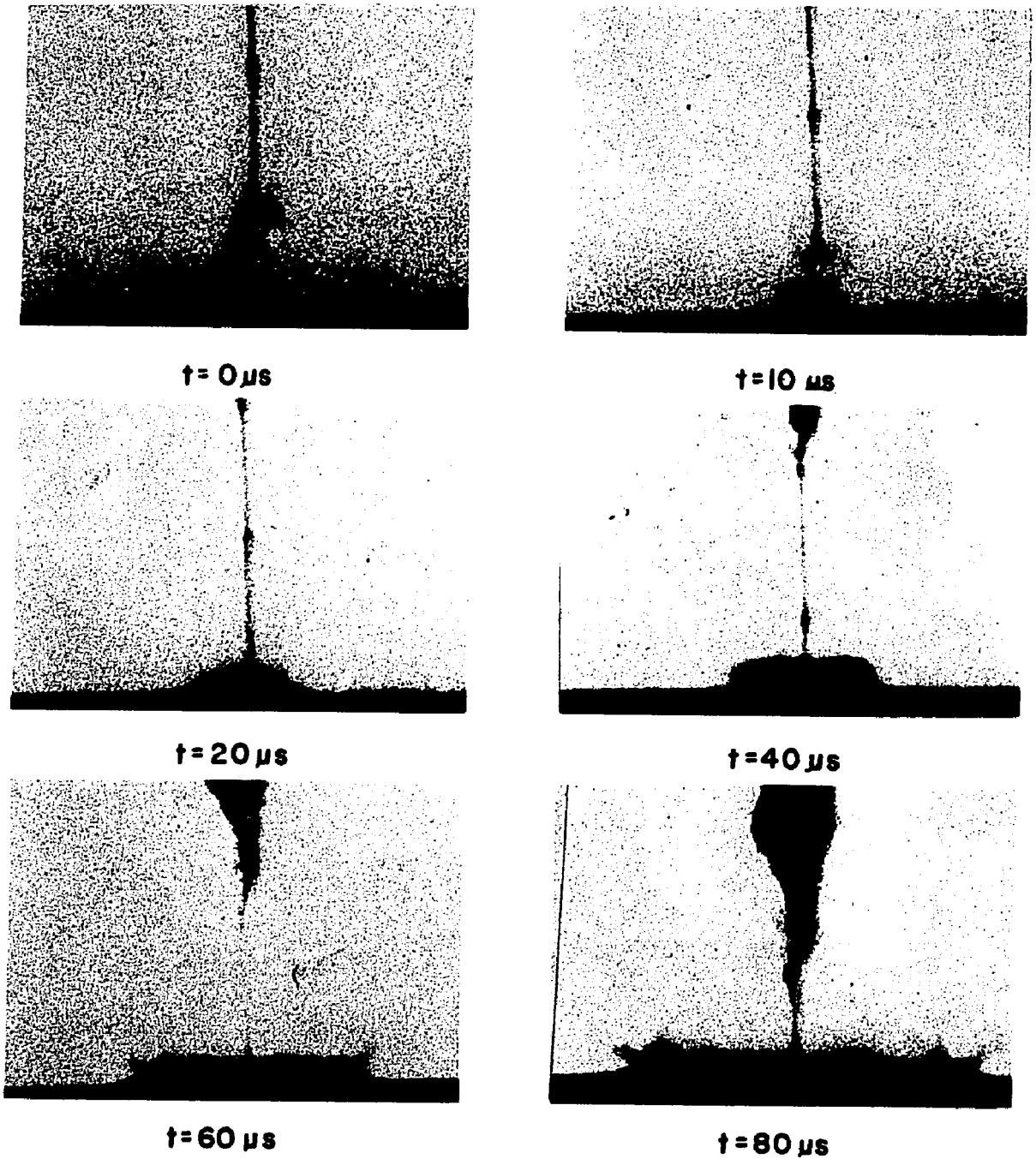


Figure 6.3 Prints, Run 892-BW-I-1

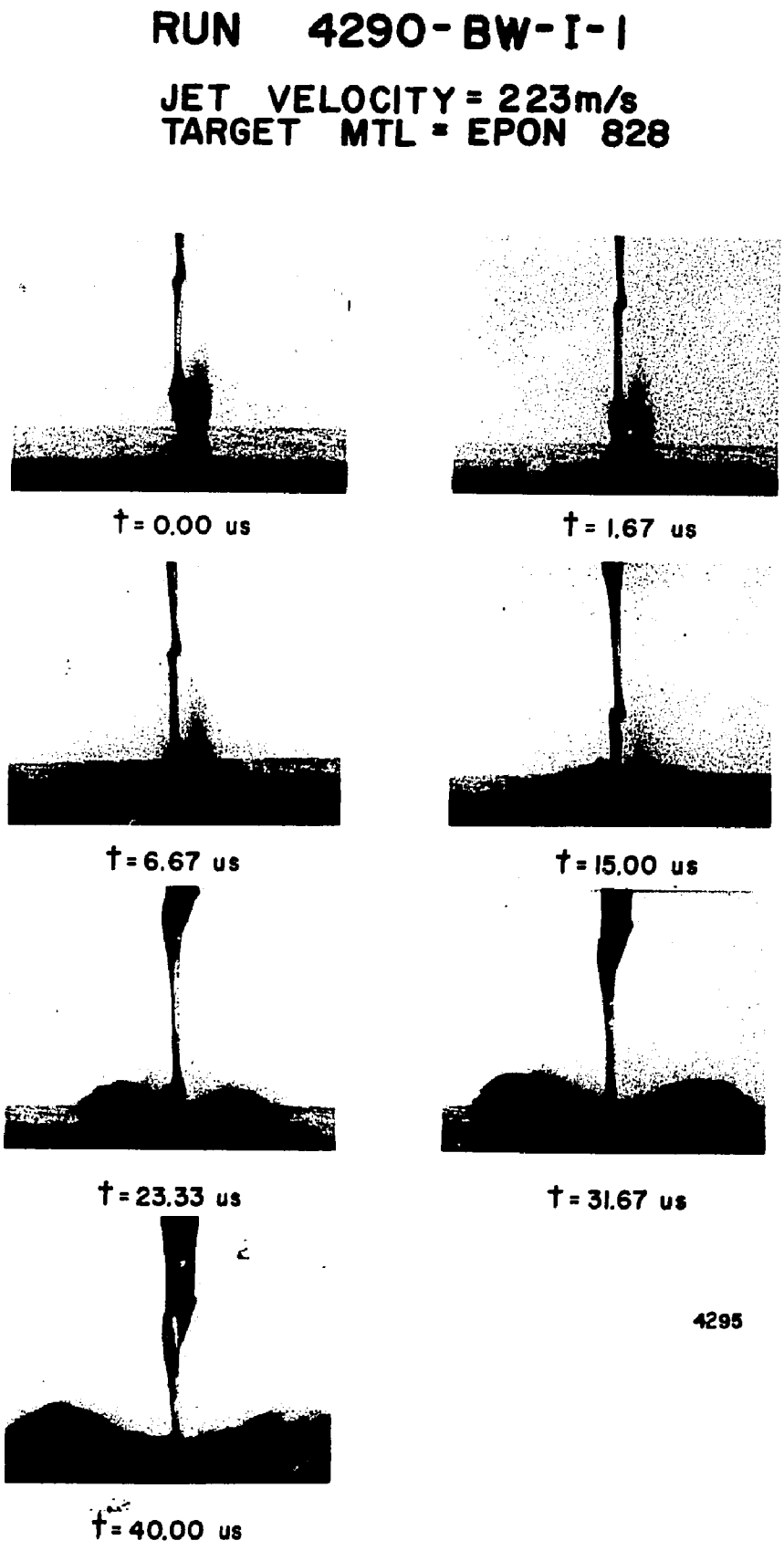


Figure 6.4 Prints, Run 4290-BW-I-1

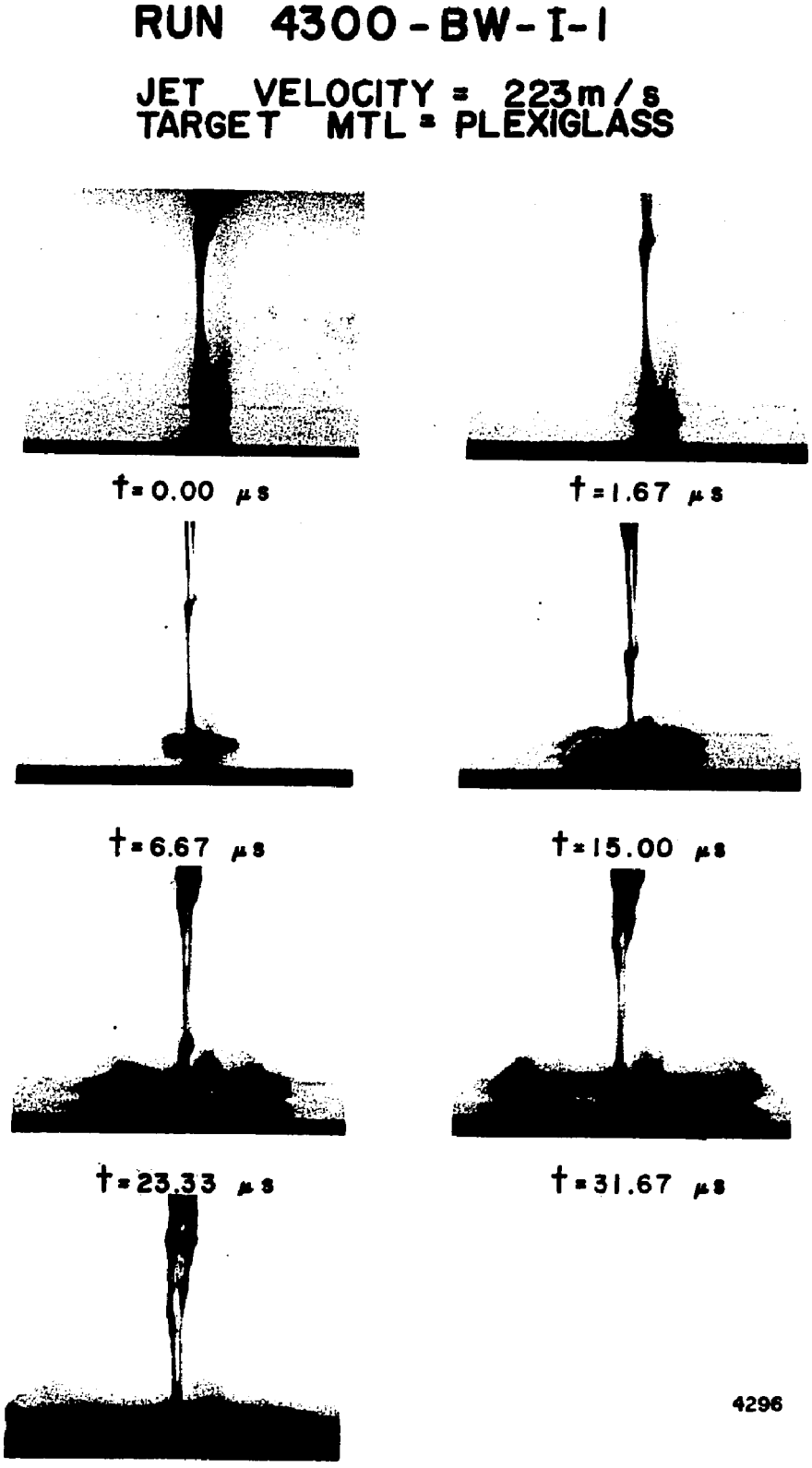


Figure 6.5 Prints, Run 4300-BW-I-1

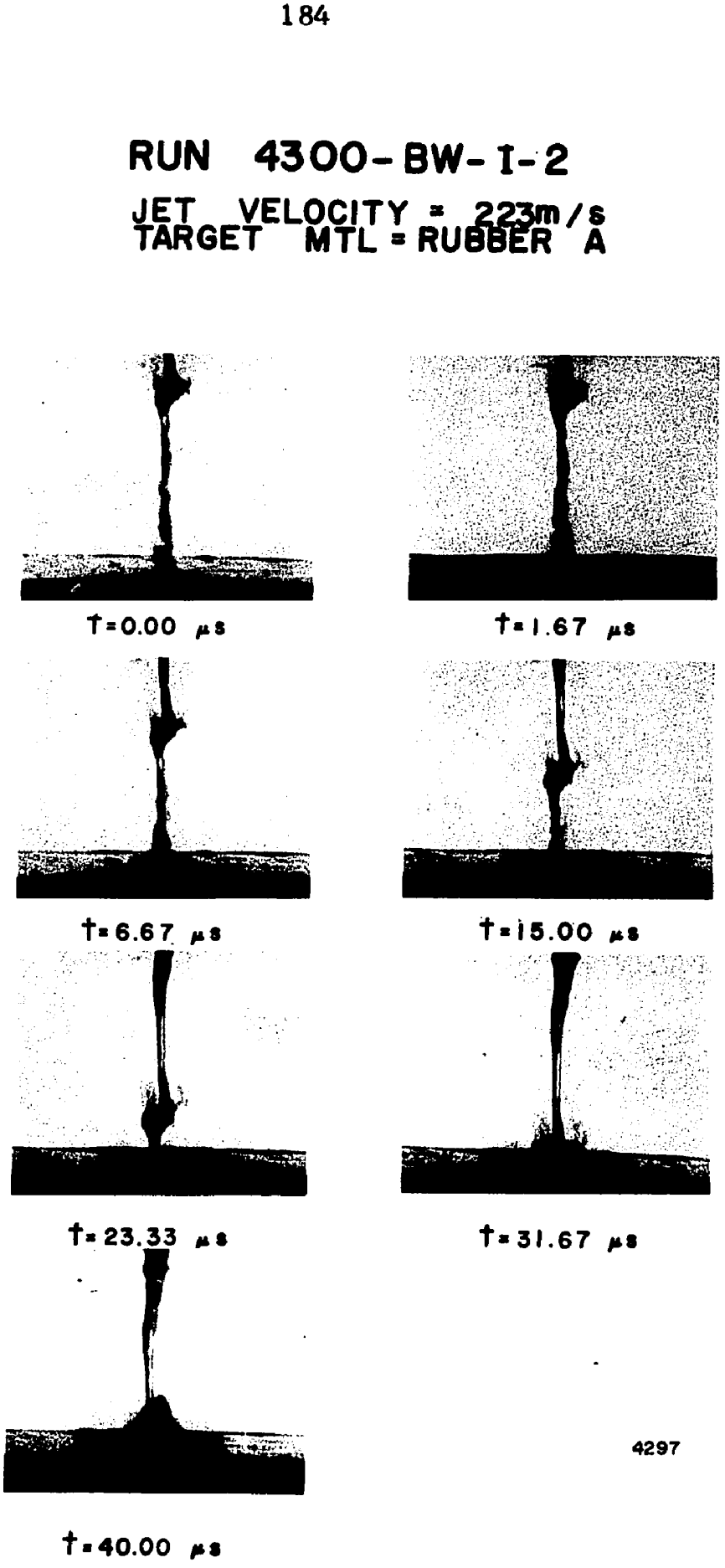


Figure 6.6 Prints, Run 4300-BW-I-2

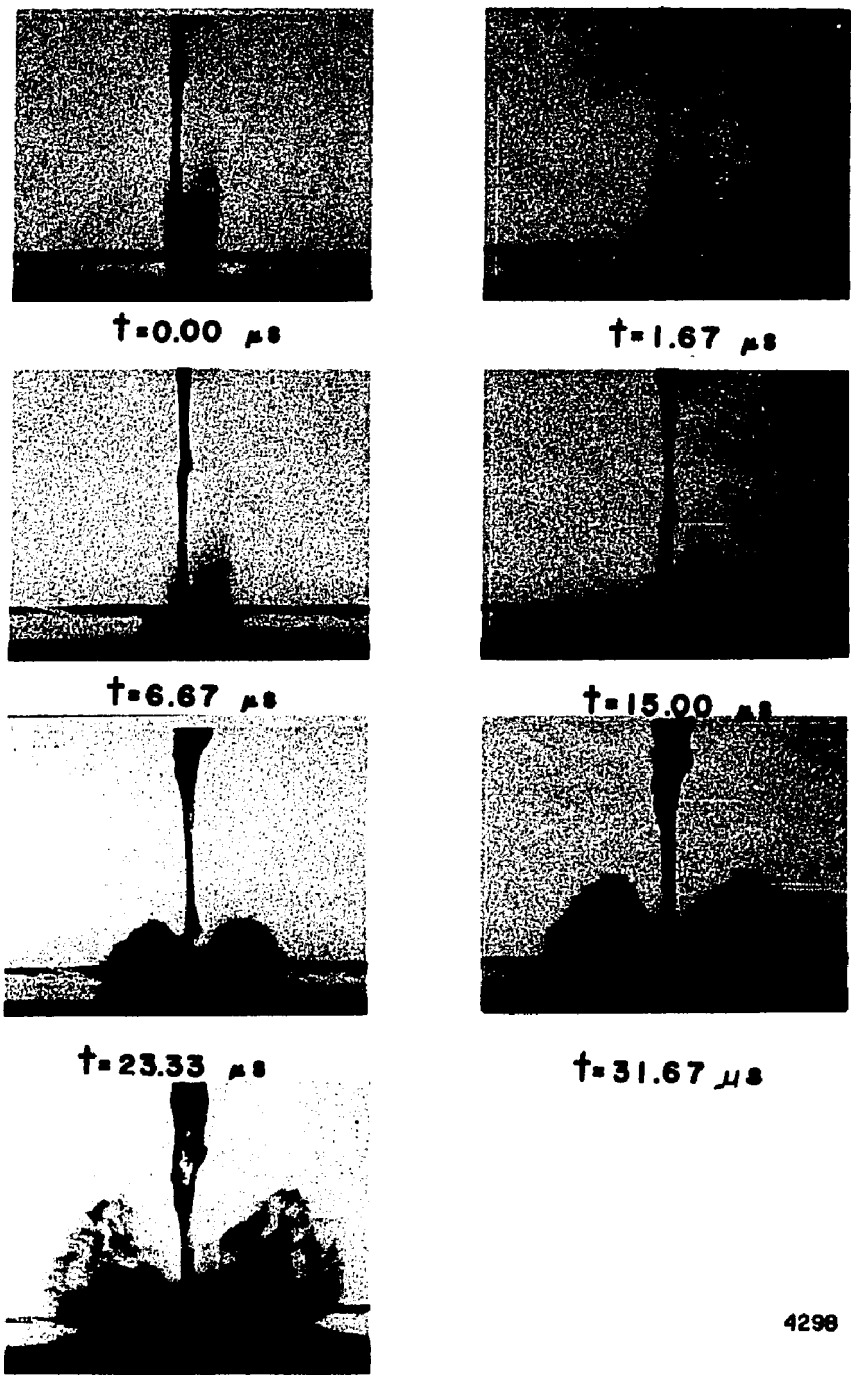


Figure 6.7 Prints, Run 510-BW-I-4

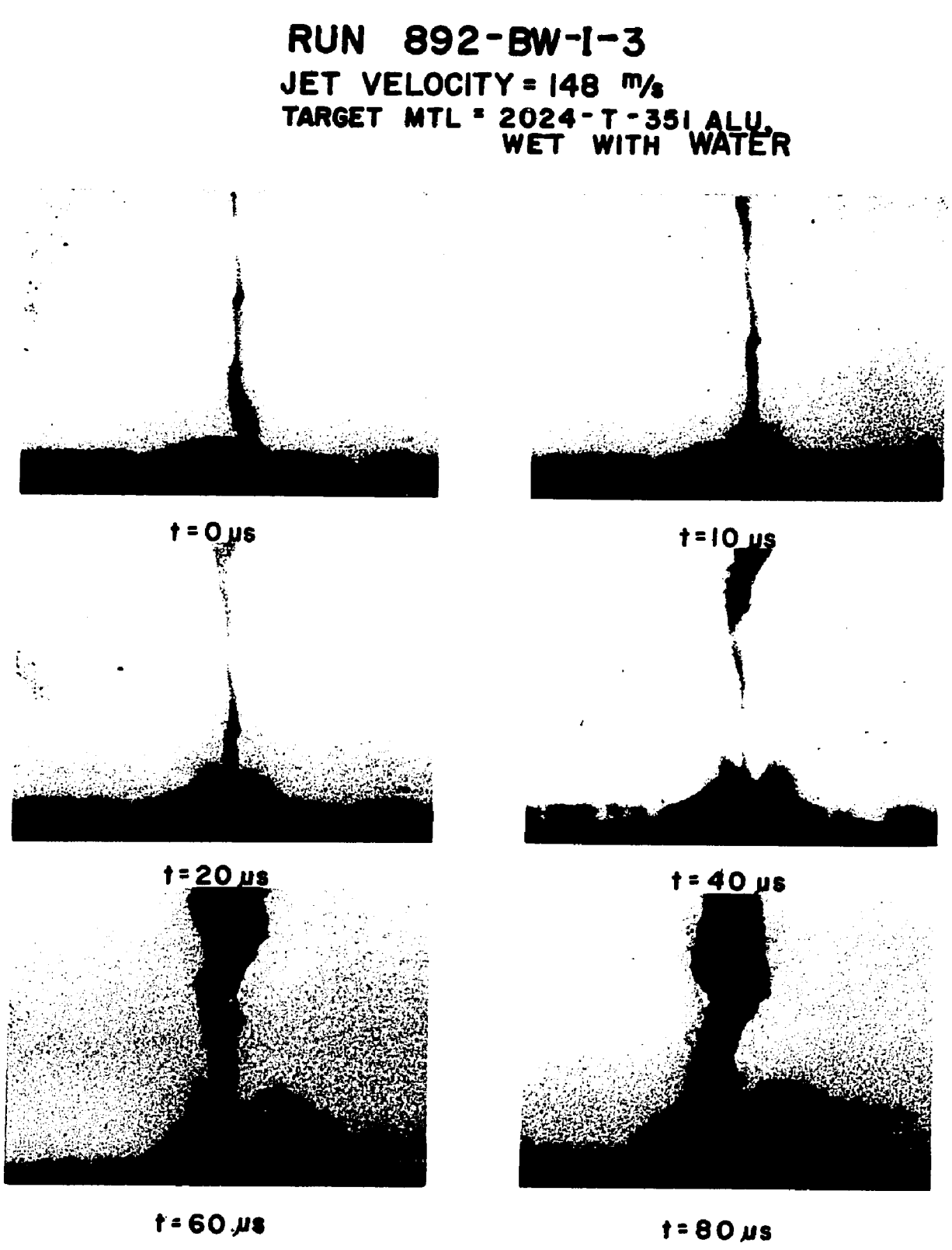


Figure 6.8 Prints, Run 892-BW-I-3

CHAPTER 7

RESULTS AND DISCUSSION OF EXPERIMENTAL INVESTIGATION OF WATER JET IMPINGEMENT

7.1 PHOTOGRAPHIC INVESTIGATION INTO WATER JET IMPINGEMENT

7.1a PROBLEMS IN INTERPRETATION OF PHOTOGRAPHIC RECORDS

All of the general discussion concerning the interpretation of photographic records that is contained in Section 5.1 applies to the interpretation of photographic records of liquid - solid impact phenomena. Additionally, the interpretation of photographic records of liquid - solid impact involves some complexities which are considered in the following paragraphs of this section.

The event of interest in this study was the collision between a small (1 mm.) diameter water jet and a solid surface. It was desired to record the moment of impact, and the subsequent splash, in sufficient detail for analysis. The procedure and photographic results of this investigation are presented in Section 6.2; the interpretation of these records for analysis involves several considerations.

Because water is a transparent medium, careful consideration must be given to illumination if the liquid jet is to be clearly visible in the photographic record. Additionally, because the impact generates a great deal of spray, it is desirable to illuminate the event so that the spray cloud will be translucent, and some details of the impact become visible. Under these conditions collimated back light defines the jet well but makes the spray cloud opaque, while diffuse back light (or front light) results in a translucent spray cloud and an ill-defined jet. Experimentation showed the best

compromise for illumination resulted when a diffuse source of restricted dimensions was used.

The splash resulting from liquid - solid impact consists of a cloud of spray which is detached from the target surface to some degree, and a spreading disc of liquid which remains attached to the target surface. The biggest problem in interpreting records of liquid - solid impact is in deciding which part of the photographic record represents liquid and which part represents spray. One means of approaching this problem is to place the plane of the target surface off the optical axis of the camera system so that in the resultant record the target surface is not viewed edge on, but rather is viewed from a slight elevation above the surface. The result of this is better visualization of the three dimensional nature of the splash. For purposes of comparison, Figures 6.4 - 6.7 were photographed from about 2^{o} above the target surface. Unfortunately, when the event is viewed from this angular perspective, the shadow cast by the spray cloud on the target surface obscures the fluid attached to the surface. Consequently, once the spray cloud forms about the splash site, the details of the fluid flow attached to the target surface are beyond the reach of this type of photographic investigation.

A further complication results from the use of a high velocity liquid jet in this liquid - solid impact study. The moving tip of the jet is subject to aerodynamic drag and, being liquid, disintegrates into spray continuously during its passage from the jet gun's muzzle to the target surface.

This cloud of spray masks the shape of the tip of the jet so that the geometry of the impacting liquid surface is unknown. Examination of many photographic negatives taken of jets before impact has led to the conclusion that the jets in this study have rounded tips and are about 0.5 to 1.0 mm. in diameter at the tip. Careful examination of Figures 6.3 - 6.8 leads to the conclusion that all the jets impacted on target materials in this study are geometrically similar but not identical. This means it is impossible to attribute variations in splash patterns on the different target materials solely to differences in the target materials. One way around this difficulty would have been to record a number of impacts on each material so that the effect of variations between individual impacts could be averaged out. However, time limitations prevented this from being done and, consequently, the subject of cause and effect relationships between target material parameters and splash patterns must be approached very cautiously. It was believed that optimum use of the available experimental time could be made by investigating the effect of a wide range of material parameters under the assumption of similar jets in order to mark the way for further research in this relatively unexplored area.

7.1b RESULTS OF PHOTOGRAPHIC INVESTIGATION

The photographs printed as Figures 6.3 - 6.8 were measured, as illustrated in Figure 6.2, in order to determine splash diameter as a function of time. From this data mean radial splash velocities were computed for each material. Figure 7.1 is a plot of these computed radial splash

velocities, normalized by division by the jet velocity, as a function of time. Velocities are plotted at the midpoints of the time intervals from which they were computed. The measurements from which these velocities were computed represent the maximum diameter of the splash pattern at the time the negative was exposed. As discussed in Section 7.1a, it was impossible to determine the diameter of the disc of liquid which remained attached to the target surface once the spray cloud obscured the target surface. This occurred about 10μs after initial contact between the jet's tip and the target surface. Consequently, the radial velocities calculated after 10 μ s from impact are the radial velocities of the spray cloud. Due to the nature of the splash it was not possible to exactly define its outer limits when measuring the photographs. This results in approximately 20% uncertainty in the computed radial velocities. Uncertainty in time measurement is negligible.

As may be seen from Figure 7.1, the radial splash velocity observed for single impacts on the various target materials differs significantly between materials. Also plotted on Figure 7.1 is the instantaneous radial velocity at the extreme splash diameter as computed by Huang[81] for a right cylindrical water slug impacting at 300 m/s on a rigid target with a free slip boundary condition. Huang's calculation does not extend far enough in time to permit direct comparison between his results and the results of this study but, from Figure 7.1, it appears that there is no conflict between these works.

By comparison of Figures 6.3 - 6.8, at t = 40 μs, it may be seen that there are substantial differences between the shapes of the spray clouds produced by impacts on different materials. Of particular significance in this comparison is the degree to which the spray cloud lifts from the target surface following impact. If it is assumed the degree of spray cloud lifting reflects the amount of target surface deformation, then the softer target materials would be expected to produce spray clouds which lift from the target surface more than the spray clouds resulting from impacts on harder surfaces. This expected pattern of spray cloud behavior is demonstrated by comparison of impacts on the harder materials (Aluminum, Plexiglass, Epon 828) with impacts on the softer elastomeric materials. However, as may be seen from careful comparison of the splashes on the elastromeric materials, the impacts on the two elastomers result in greatly different splash behavior. The impact on rubber B results in a splash with a well formed spray cloud which lifts from the target surface, while the impact on Rubber A results in a spray cloud which humps up around the impacting jet. This behavior might be explained by the difference in hardness between these materials, but a more probable explanation is that the impacting jets are of significantly different geometry. This conclusion is supported by examination of Figures 6.6 and 6.7 which show the jet impacting on Rubber A to be fragmented and to have a large discontinuity which strikes the target surface prior to the formation of Rubber A's anomalous spray cloud. The subject of effects due to

jet geometry is further explored in Section 7.3.

7.2 EXPERIMENTAL INVESTIGATION INTO MATERIAL DAMAGE RESULTING FROM WATER JET IMPINGEMENT

7.2a PROBLEMS IN INTERPRETATION OF MATERIAL DAMAGE DATA

The main problem in interpreting damage data generated by repeated impingement at the same location on a material specimen with an interrupted water jet is a direct consequence of the means chosen to characterize the damage. Conventionally, specimen weight loss, or volume loss computed from weight loss, has been used to characterize liquid impingement erosion damage. This method is useful when applied to similar materials which fail by similar mechanisms, but can be misleading when used to compare materials which fail by different mechanisms. For example, plastic materials like aluminum often show no measurable weight loss until the impacted surface has been sufficiently work-hardened for the material to become brittle; only then can cracks form and link up with the subsequent ejection of material. Frequently this does not occur until well after the material is so cratered as to have lost all structural integrity. Brittle materials in which cracks propogate easily show measurable weight loss as soon as the structural integrity of the material is modified, and elastomeric coatings frequently rupture, losing all structural integrity and leaving the substrate unprotected, without showing any weight loss.

The goal of material testing on the water jet gun is to rank materials according to their useful lifetime in practical application. The use of a device which repeatedly

impacts jets at the same location, coupled with the effect this bombardment of the same location has on failure mechanism, and the use of weight loss to characterize failure, sometimes results in material rankings which are not born out in practice.

A further complication in the use of the jet gun as a device to test materials results from the nature of the load it applies to the material under test. In applications, whether in the low pressure end of a steam turbine or on a leading edge of an aircraft, a material is loaded by the collision between the material and a spheroidal mass of water. On the jet gun a material is loaded by a collision between the material and a slug of water of relatively great length and varying diameter. Consequently, the pressure distribution on the surface of the target material, as a function of both location and time from impact, is somewhat different on the jet gun as opposed to the "in application" situation. The question of whether the mechanism by which a material fails under liquid impingement attack is affected by these different means of loading is of importance to interpreting data generated on the jet gun.

The point of the foregoing discussion is to outline a few of the considerations which complicate the direct interpretation of data generated on the jet gun device for simulating liquid impingement erosion. The laboratory scale device which most closely simulates "in application" conditions of liquid impingement erosion is the whirling arm type of apparatus, where material specimens are mounted at the

end of a rotating arm and whirled through a simulated rain storm. A device of this nature capable of propelling material specimens at velocities comparable to the jets generated by the jet gun costs from 10 to 1000 times the amount required to build a jet gun, depending on its final performance parameters. Consequently, few whirling arm devices exist* and much of the erosion data generated by them is proprietary. A cheap laboratory test device (such as the jet gun) which adequately models "in application" liquid impingement erosion conditions could contribute to the understanding which would result in superior materials. Conclusions arrived at during the course of this work concerning the development of such a device are discussed in Section 7.3

7.2b RESULTS OF INVESTIGATION INTO MATERIAL DAMAGE

The material specimen described in Table 3.1 were tested for liquid impingement erosion resistance utilizing the jet gun and the procedure outlined in Section 6.3. Measurements of specimen weight loss were made at intervals during the bombardment procedure and these measurements were converted into volume loss through the known density of each target material. Figure 7.2 is a logarithmic plot of the volume loss data generated on the jet gun for the various target material samples. This data is presented in Table 7.1 under the heading "Incubation Period."

*One is now being developed in this laboratory for nominal 600 m/s capability.

Table 7.1. Incubation Period Data

MATERIAL SAMPLE (Impact Velocity = 223 m/s)	INCUBATION PERIOD (Number of Impacts)
1100-0 Aluminum	1500
Plexiglass	1500
Epon 828	900
Rubber A	10
Rubber B	2200

Photographs of the material specimens after testing are shown in Figure 7.3.

The materials tested in this study can be divided into four distinct classes: Metallic (Aluminum); Plastic (Plexiglass); Fiber Reinforced Plastic (Epon 828); and Elastomeric coating (Rubbers). Examination of the specimens following testing resulted in the conclusion that each of these four groups appeared to have failed by a different macroscopic mechanism. Damage to the aluminum specimen took the form of a jagged central pit with a raised rim. The specimen lost little mass even though the central damage pit is more than 1 mm. deep. The material from the central damage pit was plastically deformed by the impacting jet into the raised rim around the pit. This process resulted in little material loss as it is more of a flow process than a material removal process. However, the more the aluminum was deformed the more brittle it became which resulted in increased material loss due to the increased probability of cracking in the embrittled material. Plexiglass is a relatively brittle material as is indicated by its low (4%) elongation to failure, but it is also much stronger in compression than in tension. Consequently, as has been

discussed by Bowden and Brunton[57], liquid impingement results in a ring type failure with a central undamaged area surrounded by a ring of crazed plexiglass. The explanation for this behavior is that the plexiglass directly under the point of impact is depressed and stressed in compression while the ring around this depressed area is stressed in tension. The ring put into tension fails and the resulting damage consists of small cracks oriented parallel to the impacted surface in a circular ring. When under repeated impact these cracks grow to the point where they link up, large pieces of the target are lost. Damage to the composite material (Epon 828 Epoxy-Glass Laminate) is a result of failure of the epoxy phase, which is similar in properties to plexiglass, compounded by interactions between the glass phase and the pressure pulse generated by the impact.

Damage to composite materials has been studied by Mok[70] and others with the conclusion that the presence of the reinforcing phase has little effect on the erosion resistance of the material, but in many cases it increases the possibility of catastrophic interlaminar failures. Damage to the elastomeric materials can be divided into two phases. In the early phase of damage the material is subjected to strong shear loads in the vicinity of impact. Eventually this leads to rupture of the material which gives the impacting jet access to the surface underneath the layer of rubber. In the second phase of damage the liquid jet spreads radially from its point of impact on the substrate material and causes radial tears in the rubber coating.

Often these tears link up with the resultant removal of a large piece of elastomeric coating. The material damage tests on the elastomeric materials were terminated upon the appearance of significant amounts of radial tearing of the elastomeric coating.

From the data the materials tested may be ranked for erosion resistance by two criteria.[86] The first of these is the number of impacts required for the loss of an arbitrary volume of material and the second is the incubation period. Relative rankings between materials may be assigned as a figure of merit resulting from normalizing the measured damage parameters by dividing by the damage parameter for a particular material. Rankings for the materials tested are presented in Table 7.2.

Table 7.2. Damage Rankings of Materials

	CRITERION: IMPACTS TO 3μl VOLUME LOSS		CRITERION: INCUBATION PERIOD (NUMBER OF IMPACTS)	
MATERIAL	IMPACTS	FIGURE OF MERIT	IMPACTS	FIGURE OF MERIT
Rubber A	84	1	10	1
Epon 828	750	8.9	890	89
Plexiglass	770	9.2	1500	150
Aluminum	9700	115	1500	150
Rubber B	1200	14.3	2200	220

It is probable that the particularly high rating aluminum gets when ranked on the basis of number of impacts to 3μl volume loss is a result of the test procedure. If the liquid impacts were distributed more evenly over the surface of the test specimen rather than in one location, the raised crater rims formed by plastic flow upon impact would then be

removed by subsequent impacts upon sensitive locations on the rim, which would result in a much greater material loss rate. Consequently, when ranking grossly dissimilar materials utilizing the jet gun, use of the incubation period may result in more accurate rankings than does the use of folume loss. However, when developing rankings for dissimilar materials, the use to which the material will be put must be considered. For example, no one would consider making aircraft structures of glass or antenna radomes of aluminum. The tremendous difference in erosion resistances of the two elastomeric materials cannot be explained on the basis of their physical properties. Perhaps the tear strengths of the elastomeric materials might explain this difference in erosion resistance, but this data is unavailable. What is of particular importance is that Rubber B possesses very good erosion resistance and is an elastomeric material. This illustrates the possibility of coating a dielectric structural material like Epon 828 with an erosion resistant dielectric coating like Rubber B to obtain a composite material which is strong, erosion resistant, and transparent to microwave energy. Composite materials like this have been used as antenna radomes for years, but their development has always been a hit or miss proposition. Recent work by Field, Camus, and Gorham[71] has started to put this development program on a more scientific footing. However, experimental work will remain the mainstay of rain erosion resistant material development for some time. This again points to the importance of the development of laboratory scale devices

for erosion resistance testing. Modifications to the jet gun which might make it more suitable for testing different classes of materials are discussed in Section 7.3.

7.3 DISCUSSION AND CONCLUSIONS CONCERNING INVESTIGATION INTO WATER JET IMPINGEMENT

The results of this investigation into water jet impingement phenomena are not nearly as easily categorized as were the results of the investigation into vapor bubble collapse phenomena contained elsewhere in this work. Due to the wide range of jet impact phenomena studied it was impossible to repeat experiments and, consequently, the subject of cause and effect relationships between experimentally observed phenomena must be approached very cautiously. However, much of value was learned which, as is typical in such exploratory studies, points the direction for further research in the general area of liquid-solid impact phenomena.

The photographic investigation of liquid-solid impact has provided information about questions in the following three areas: (1) The utility of the jet gun device as a source of high velocity liquid jets for the purpose of studying the hydrodynamics of liquid-solid impact; (2) The utility of high speed cinematography as a tool to investigate the hydrodynamics of liquid-solid impact; and (3) The effect of various target materials on the hydrodynamics of liquid-solid impact.

The use of the jet gun as a device to provide a liquid mass with a high velocity relative to a solid surface for the purpose of obtaining data which could be used to verify

mathematical models of liquid-solid impact phenomena has an overwhelming drawback. The jet produced by the jet gun is very irregularly shaped and cannot be reproduced repeatably from a microscopic viewpoint. This drawback means that hydrodynamic data generated through the use of the jet gun will always be open to question. The experimental approach taken by Fyall[61] and others, where a droplet is suspended in place and a solid projectile is fired into it, results in an experimental design with clearly defined hydrodynamics. The situation where this type of experimental design cannot be used is when it is desired to instrument the solid target surface with pressure probes in order to record the pressure produced by the impact at the liquid-solid interface. In this situation, because it would be very difficult to so instrument the moving solid projectile in a Fyall-type experiment, the vagaries of the liquid jets produced by the jet gun would have to be accepted. The principal difference between pressures measured in a droplet impact experiment and pressures measured in a jet impact experiment should result from the steady state stagnation pressure component imposed upon the instrumented surface by the body of the jet. Other differences would be expected because the jet does not have a trailing edge close to the leading edge which reflects the impact pressure pulse. An impact pressure experiment of this nature would be the most direct way to demonstrate the accuracy of Huang's model for liquid-solid impact. However, the state of the art in pressure transducer design results in available transducers with a rise time on the

order of a microsecond. Since both photographic experiments and mathematical models indicate the maximum pressure in a typical high velocity liquid-solid impact occurs within 0.3μs after impact, the state of art in transducer manufacture must improve by an order of magnitude before reliable pressure measurement experiments can be undertaken. The use of available pressure transduces above their resonant frequency in this type of experiment results in unreliable data.

The use of high speed cinematography in the study of liquid-solid impact phenomena runs into several problems. When used as a tool to study the initial few microseconds after impact, in order to confirm mathematical models of liquid-solid impact phenomena, high speed cinematography runs into the problems that have plagued it since its invention: insufficient temporal and spatial resolution. Huang has noted, concerning the use of photography to study the shapes taken by a liquid mass upon high speed impact, that "The early protrusion (above the solid surface) in the contract periphery (of the liquid mass) is so slight that it is almost impossible to detect by experiments or photographical means." Additionally, the most important events that occur when a liquid strikes a rigid surface take place in the first microsecond after impact. If a number of exposures are to be made of this critical period a camera framing rate on the order of 10^7 frames/second is required. A framing rate of this magnitude represents the state of the art of high speed cinematography and, no matter whether conventional or electronic image conversion cameras are considered for application

in this area, spatial resolution and timing problems become very complex and perhaps insuperable.

The area in which high speed cinematography appears to have significant application in the study of liquid-solid impact phenomena concerns the effect of non-rigid target surfaces on the hydrodynamics of the impact process. This area is especially important because many materials which have shown much promise in reducing damage resulting from liquid impingement and/or cavitation attack are non-rigid materials. One approach to the study of the effect non-rigid surfaces have on the hydrodynamics of liquid-solid impact would be through the modification of mathematical models of the process to include non-rigid surfaces. However, this modification of the simple rigid boundary condition presently used in these models involves a great deal of additional complexity. For example, information is needed on how flexible materials respond at loading rates approaching their relaxation times. Good information of this type is not readily available. Consequently, the use of high speed cinematography to study the effect of flexible materials on the impact process represents an approach to this problem which would probably bear fruit.

In Section 7.1 the results of photographic investigation of waterjet impacts on two flexible materials, Rubber A and Rubber B, are discussed. It is noted there that even though these two materials are reasonably similar with respect to physical properties the splashes produced by the impact of high velocity water jets on them are grossly

dissimilar. The conclusion drawn is that the difference in splash behavior between the two materials is most probably due to differences between the type of jets impacting on them. When Rubber A and Rubber B were tested for erosion resistance on the jet gun, Rubber B was found to be nearly a hundred times more erosion resistant than Rubber A. This disparity in erosion rates is not reflected in the physical properties of these materials but serves to substantiate the hypothesis that the observed difference in splash behavior between Rubber A and Rubber B is due to differences in the materials and not the impacting jets. The best way to investigate this hypothesis would be through the use of high speed cinematography in conjunction with an impact device similar to Fyall's, where the geometry of the impacting liquid mass is very well defined. A study of this nature would permit the effect of various materials on the hydrodynamics of liquid-solid impact to be quantized, and might lead to understanding which would result in better materials. The data from this experiment could be correlated with the dynamic physical properties of the target materials in order to gain insight into the mechanism of impact damage.

The two principal objections to the use of the water jet gun as a test device to simulate liquid impingement erosion on a laboratory scale are: (1) The gun repeatedly impacts the material specimen in the same location, and (2) The gun impacts the specimen with a relatively long slug of water with a varying diameter as opposed to the real life situation where materials are impacted with compact masses of

water. The first of these objections could be removed by modifying the sample holder of the gun assembly so that the sample is shifted within a limited area between impacts. A device which caused the target material sample to be rotated and translated within limits could easily be attached to the jet gun and, if properly designed, would result in a relatively random impact location within a representative area on the target material. The problem of the shape of the jet produced by the jet gun is much more complex. As may be seem from Figures 6.3 - 6.8, the tip of the jet produced by the jet gun is of reasonably regular shape. If some means could be found to chop this leading section from the jet and allow it alone to impact the target, the impacting mass of liquid would be reasonably similar to those found in applications. However, as the jet is travelling at several hundred meters/second no mechanical device could repeatedly respond fast enough to chop off a section of it that is only a few millimeters long. One possible approach to this problem might be through an application of the principles of fluidics. It might be possible to construct a chamber for the jet gun which would produce a second jet with the correct orientation and timing to steer the primary jet into a collector a few microseconds after the tip of the primary jet has passed the collector. This would result in a short, high velocity liquid slug which could be impacted on material test specimens. A schematic illustration of how this device might be constructed, as well as illustrations of its function, is given in Figure 7.4. The practical aspects of making this device function

would be very complex but, in theory, it should work.

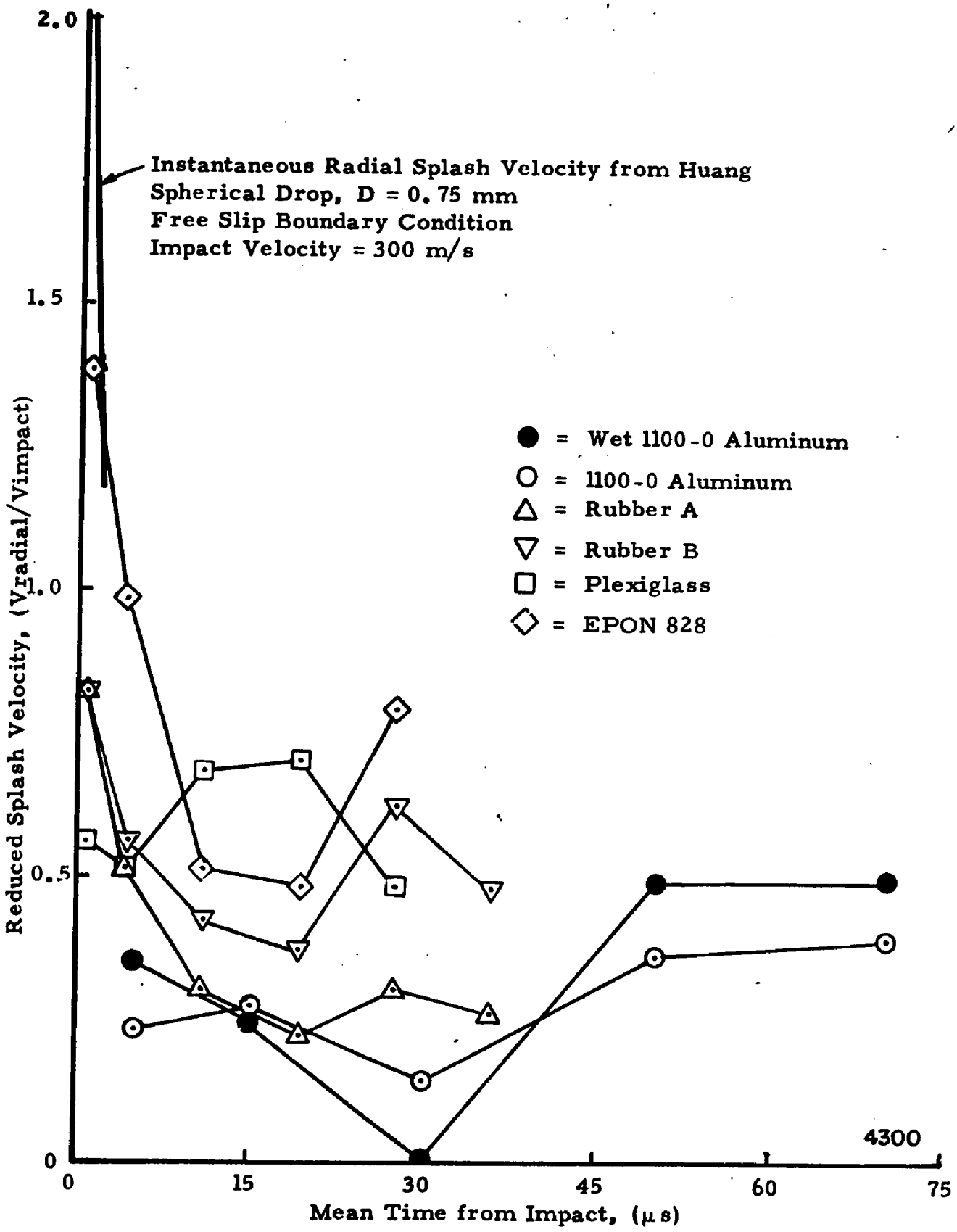


Figure 7.1 Liquid Impact Radial Splash Velocity

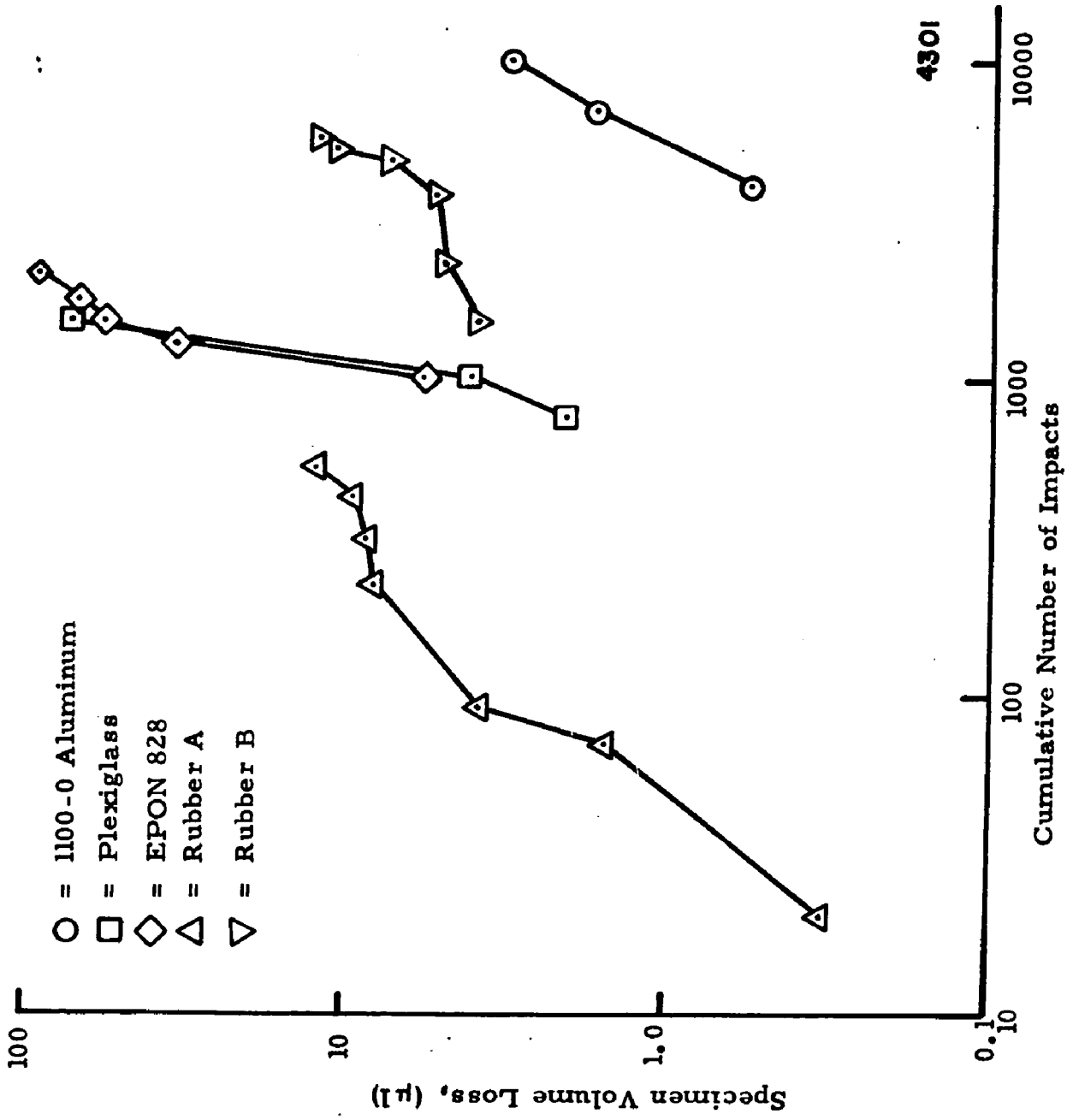
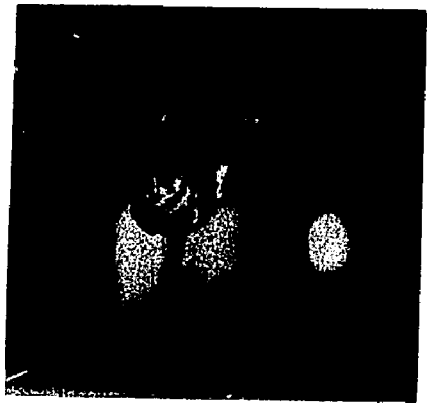
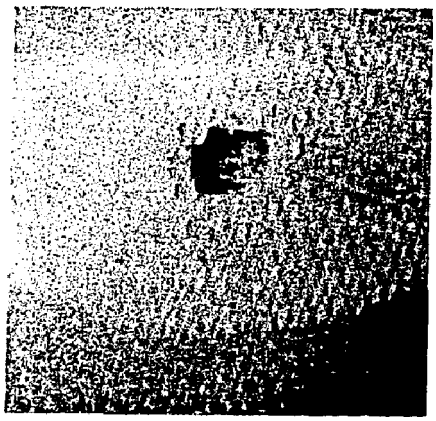


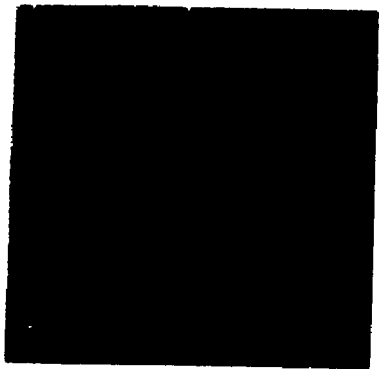
Figure 7.2 Liquid Impact Specimen Volume Loss



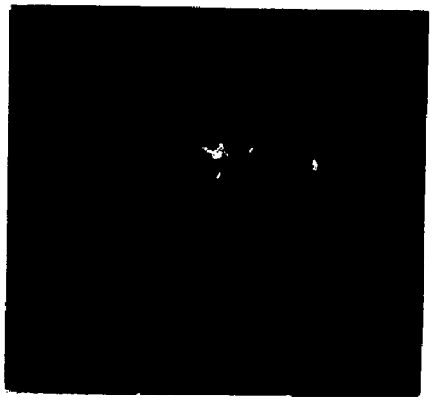
Plexiglass



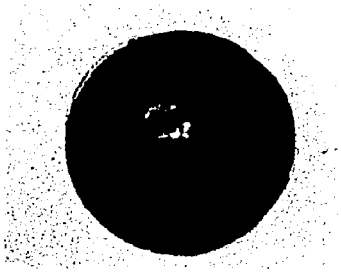
EPON 828



Rubber A



Rubber B



1100-0 Aluminum

4302

Figure 7.3 Liquid Impact Specimens

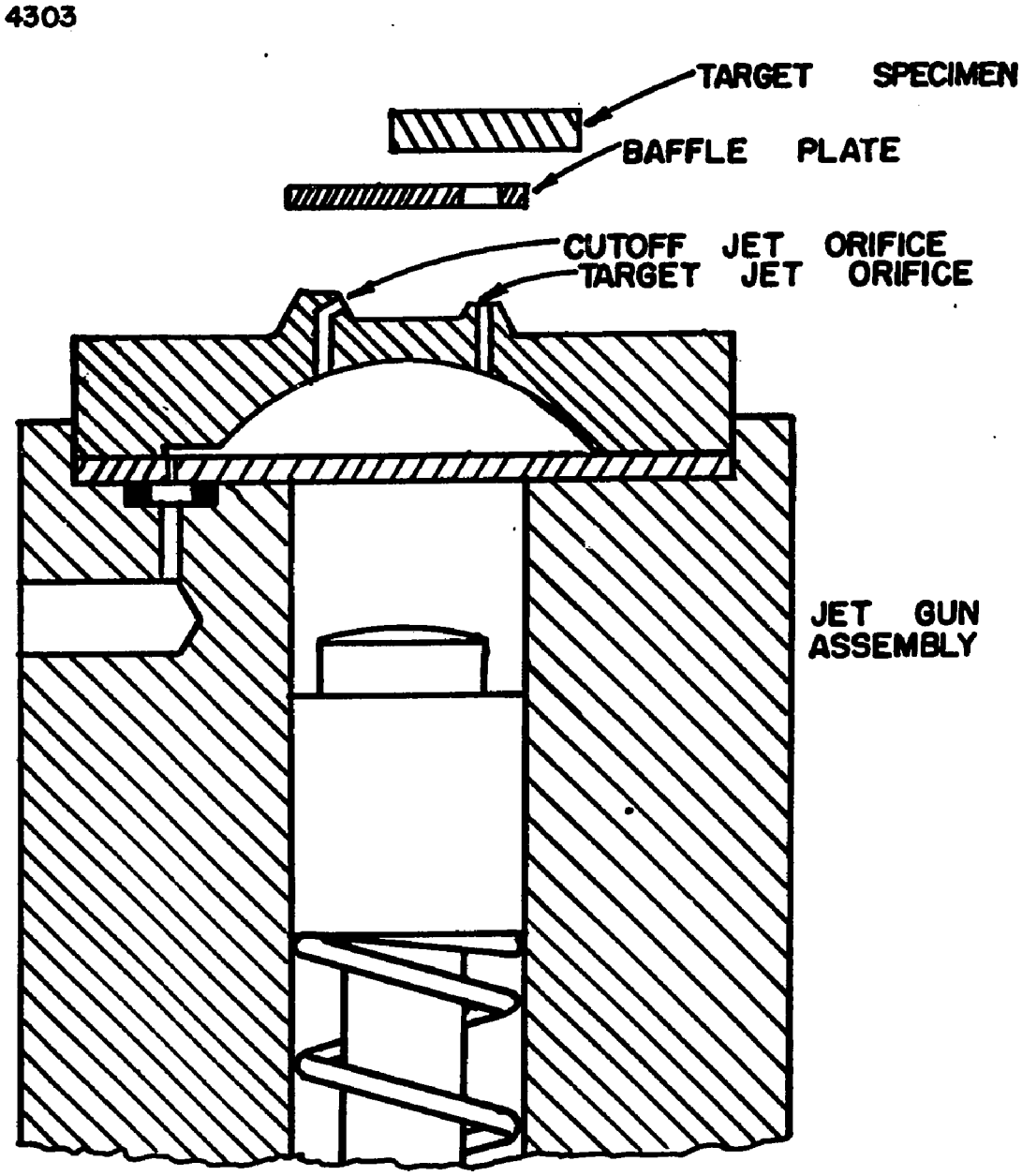


Figure 7.4 Schematic of Proposed Fluidic Cutoff for Jet Gun

1. Euler, Leonhard, "Theorie plus complete des machines, qui sont mises en mouvement par las reaction de l'eau," Historie de l'Academia Royale des Sciences at Belles Lettres, Classe de Philosophie Experimentale, Men 10, 1754, Berlin, 1756, pp. 227-295.

2. Besant, W. H., A Treatise on Hydrodynamics, Cambridge Univ. Press, Cambridge (1859), 198.

3. Lord Rayleigh, "On the Pressure Developed in a Liquid During the Collapse of a Spherical Cavity," Phil. Mag., Vol. 34, No. 200 (1917), 94-98.

4. Reynolds, Osborne, "Experiments Showing the Boiling of Water in an Open Tube at Ordinary Temperatures," Scientific Papers, 2 (1901), 578-587.

5. Parsons, Sir Charles, and Cook, S. S., "Investigations into the Causes of Corrosion or Erosion of Propellers," Trans. Inst. Nav. Arch., 61 (1919), 223-247.

6. Burrill, L. C., "Sir Charles Parsons and Cavitation," Trans. Inst. Marine Engrs., 43, No. 8, (1951) 149-167.

7. Barnaby, Sydney W., "On the Formation of Cavities in Water by Screw Propellers at High Speed," Trans. Inst. Nav. Arch., 39 (1897), 139-144.

8. Beeching, R., "Resistance to Cavitation Erosion," Trans. Inst. of Eng. and Shipbuilders in Scotland, 85 (1942) 210-276.

9. Herring, Conyers, "Theory of Pulsations of the Gas Bubble Produced by an Underwater Explosion," Report C4-Sr20-010, Columbia Univ. (1941).

10. Silver, R. S., "Theory of Stress Due to Collapse of Vapour Bubbles in Liquid," Engineering, (Dec. 25, 1942) 501-502.

11. Kornfeld, M., and Suvorov, L., "On the Destructive Action of Cavitation," J. Appl. Phys., 15 (1944), 495-506.

12. Cole, R. H., Underwater Explosions, Princeton University Press, 1948.

13. Plesset, Milton, "The Dynamics of Cavitation Bubbles," J. Appl. Mech., 16 (1949), 277-282.

14. Eisenberg, Phillip, "On the Mechanism and Prevention of Cavitation," David Taylor Model Basin Report 712, Washington (1950).

15. Rattray, Maurice, "Perturbation Effects in Cavitation Bubble Dynamics," Aero. Eng. Thesis, Cal. Inst. Tech. (1951).

16. Plesset, M. S., and Mitchell, T. P., "On the Stability of the Spherical Shape of a Vapor Cavity in a Liquid," Quarterly Appl. Math., XII, No. 4, (January, 1956).

17. Poritsky, H., "The Collapse or Growth of a Spherical Bubble or Cavity in a Viscous Liquid," Proc. First National Congress of Appl. Mech., ASME, (1952) 823-825.

18. Shu, S. S., "Note on the Collapse of a Spherical Cavity in a Viscous Incompressible Liquid," Cal. Inst. Tech. Report 26-4 (1952) 823-825.

19. Gilmore, F. R., "The Growth or Collapse of a Spherical Bubble in a Viscous Compressible Liquid," Cal. Inst. Tech. Report 26-4 (1952).

20. Gilmore, F. R., "The Growth or Collapse of a Spherical Bubble in a Viscous Compressible Liquid," 1952 Heat Transfer and Fluid Mechanics Institute, Stanford University Press (1952), 53-64.

21. Ellis, A. T., "Observations on Cavitation Bubble Collapse," C.I.T., Hydrodynamics Lab. Report 21-12 (1952).

22. Zwick, S. A., and Plesset, M. S., "On the Dynamics of Small Vapor Bubbles in Liquids," J. Math. Phys., 33 (1955), 308-330.

23. Benjamin, T. B., (1954). "Cavitation in Liquids," Doctoral Dissertation, Cambridge University.

24. Stahl, H. A., and Stepanoff, A. J., "Thermodynamic Aspects of Cavitation in Centrifugal Pumps," Trans. ASME, 78 (1956), 1691-1693.

25. Flynn, H. G., "Collapse of a Transient Cavity in a Compressible Liquid," Tech. Mem. No. 38, Acoustic Res. Lab., Harvard Univ. (1957).

26. Prudhomme, R. O., and Guilmart, J. Chim. Phys., 54 (1957), 336-340.

27. Jarman, Peter, "Sonoluminescence: A Discussion," J. Acoustical Soc. Am., 32 (1960), 1459-62.

28. Hickling, Robert, "I. Acoustic Radiation and Reflection from Spheres, II. Some Effects of Thermal Conduction and Compressibility in the Collapse of a Spherical Bubble in a Liquid," Ph.D. Thesis, Ca. Inst. Tech. (1962).

29. Hickling, R., and Plesset, M., "Collapse and Rebound of a Spherical Bubble in Water." Phys. of Fluid, Vol. 7, No. 1 (1964).

30. Florschuetz, L. W., and Chao, B. T., "On the Mechanics of Vapor Bubble Collapse," Trans. ASME, J. Heat Transfer, 87, (1965), 209-220.

31. Wittke, D. D., and Chao, B. T., "Collapse of Vapor Bubbles with Translatory Motion," Trans. ASME, J. Heat Transfer, 89 (1967), 17-24.

32. Canavelis, Richard, "Contribution a l'Etude de l'Erosion de Cavitation dans les Turbonmachines Hydrauliques," Ph.D. Thesis, Univ. of Paris (1966.

33. Theofanous, T. G., Biase, L., Isbin, H. S., and Fauske, H. K., "Nonequilibrium Bubble Collapse - A Theoretical Study," AIChE Preprint 1, Presented at Eleventh National Heat Transfer Conference, Minneapolis, August, 1969.

34. Mitchell, T. M., "Numerical Studies of Asymmetric and Thermodynamic Effects on Cavitation Bubble Collapse," Ph.D. Thesis, Univ. of Michigan, (1970).

35. Ivany, R. D., and Hammitt, F. G., "Cavitation Bubble Collapse in Viscous, Compressible Liquids - - Numerical and Experimental Analyses," Ph.D. Thesis, Univ. of Michigan (1965).

36. Ivany, R. D., and Hammitt, F. G., "Cavitation Bubble Collapse in Viscous, Compressible Liquids - - Numerical Analysis," Trans. ASME, J., Basic Eng., 87 (1965), 977.

37. Hickling, R. and Plesset, M. S., "The Collapse of a Spherical Cavity in a Compressible Liquid," California Institute of Technology, Report No. 85-24, Pasadena, California, 1963.

38. Khoroshev, G. A., "The Effect of a Wall on the Process of Collapsing Cavitation Bubbles," Inzhenerno - Fizicheskiy Zhurnal, Vol. 6, No. 1 (1963), 59-65.

39. Korovkin, A. N., and Levkovskiy, Yu. L., "Investigation of the Collapse of a Cavitating Bubble Near a Solid Wall," Inzhenerno - Fizicheskiy Zhurnal, Vol. 12, No. 2 (1967), 246-253.

40. Green, Joseph, "The Hydrodynamics of Spherical Cavities in the Neighborhood of a Rigid Plane," Ph.D. Thesis, Cal. Inst. Tech. (1957).

41. Shima, A., "The Behavior of a Spherical Bubble in the Vicinity of a Solid Wall," Trans. ASME, J. Basic Eng., 90, Series D. (1968), 75-89.

42. Yeh, Hsu-Chieh, and Yang, Wen-Jei, "Dynamics of Bubbles Moving in Liquids with Pressure Gradient," J. Appl. Phys., 39 (1968), 3156-3165.

43. Gibson, D. C., "The Collapse of Vapor Cavities," Ph. D. Thesis, Cambridge University (1967).

44. Naude, C. F., and Ellis, A. T., "On the Mechanism of Cavitation Damage by Nonhemispherical Cavities Collapsing in Contact with a Solid Boundary," Trans. ASME, J. Basic Eng., 83, Series D (1961), 648-656.

45. Shutler, N. D., and Mesler, R. B., "A Photographic Study of the Dynamics and Damage Capabilities of Bubbles Collapsing Near Solid Boundaries," Trans. ASME, J. Basic Eng., 87, Series D (1965), 511-517.

46. Kozirev, S. P., "On Cumulative Collapse of Cavitation Cavities," Trans. ASME, J. Basic Eng., 90, Series D (1968), 116-124.

47. Benjamin, T. B., and Ellis, A. T., "The Collapse of Cavitation Bubbles and the Pressures Thereby Produced against Solid Boundaries," Phil. Trans. Roy. Soc. Lond., A. 260, (1966), 221-240.

48. Chapman, R. B., "Nonspherical Vapor Bubble Collapse," Ph. D. Thesis, Cal. Inst. Tech. (1970).

49. Kling, C. L., "A High Speed Photographic Study of Cavitation Bubble Collapse," Ph.D. Thesis, Univ. of Michigan, (1970).

50. Worthington, A. M., A Study of Splashes, The MacMillan Company, New York, (1963).

51. Honegger, E., "Tests on Erosion Caused by Jets," Brown Boveri Review, 14, 4, pp. 95-104, (1927).

52. Cook, S. S., "Erosion by Water-Hammer," Proc. Royal Society, A, 119, pp. 481-488, (1928).

53. Engel, O. G., "Mechanism of Rain Erosion," WADC Tech. Report 53-192, Part I through XV. (1953).

54. Engel, O. G., "Waterdrop Collisions with Solid Surfaces," J. of Research of the National Bureau of Standards, 54, 5, (May 1955).

55. Savic, P., and Boult, G. T., "The Fluid Flow Associated with the Impact of Liquid Drops with Solid Surfaces," National Research Council of Canada, Report No. MT-26, May 1955.

56. Engel, O. G., "Pits in Metals Caused by Collision with Liquid Drops and Rigid Steel Spheres," J. of Research of the National Bureau of Standards 64A, (1960).

57. Bowden, F. P., and Brunton, J. H., "The Deformation of Solids by Liquid Impact at Supersonic Speeds," Proc. of the Royal Society, A, 263, pp. 433-450.

58. Christie, D. G., and Hayward, G. W., "Observation of Events Leading to the Formation of Water Drops Which Cause Turbine Blade Erosion," Phil. Trans. Roy. Sec., A, Part No. 1110, 260, pp. 73-315, (1966).

59. Caldwell, J., "Description of the Damage in Steam Turbine Blading Due to Erosion by Water Droplets," Phil. Trans. Roy. Soc., A, Part No. 1110, 260, pp. 204-208, (1966).

60. Smith, A., "Physical Aspects of Blade Erosion by Wet Steam in Turbines," Phil. Trans. Roy. Soc., A., Part No. 1110, 260 pp. 209-215, (1966).

61. Fyall, A. A., King, R. B., and Strain, R. N. C., "Rain Erosion Aspects of Aircraft and Guided Missiles," J. Roy. Aero. Sec., 66, pp. 447-453, (1962).

62. Schmitt, G. F. Jr., "Current Investigations in Rain Erosion by the U. S. Air Force," ATSM Meeting in Atlantic City, N. J., June 27 - July 1, 1966.

63. Wahl, N. E., "Investigation of the Phenomena of Rain Erosion at Subsonic and Supersonic Speeds," Air Force Materials Laboratory Report AFML-TR-65-330, (1966).

64. Thiruvengadam, A., Ruby, S. L., and Gunasekaran, M., "Experimental and Analytical Investigations on Liquid Erosion, ASTM Special Technical Publication, 474, (1969).

65. Hobbs, J. M., "Experience with a 20 kh/z Cavitation Erosion Test," Symp. on Erosion by Cavitation or Impingement ASTM STP 408, ASTM, Philadelphia, Pa., (1967).

66. Plesset, M. S. and Devine, R. E., "Effect of Exposure Time on Cavitation Damage," Trans. ASME, J. Basic Engineering, Vol. 88 D., 1966, pp. 691-705.

67. Hammitt, F. G., "Impact and Cavitation Erosion and Material Mechanical Properties," Univ. of Michigan, Report No. 03371-1-T., (Nov. 1969).

68. Canavelis, R., "Jet Impact and Cavitation Damage," Trans. ASME, J. Basic Engineering, Vol. 90D, 1968, pp. 355-366.

69. Hancox, N. L. and Brunton, J. H., "The Erosion of Solids by Repeated Impact of Liquid Drops," Phil. Trans. Royal Soc. of London, Vol. 260 A, 1966, p. 121.

70. Mok, C., "On the Role of Microstructure in Erosion Phenomena," Proc. Third Intl. Conf. on Rain Erosion and Associated Phenomena, Royal Aircraft Establishment, England, 1970, p. 523.

71. Field, J. E., Camus, J. J., and Gorham, D. A., "Single Impact Erosion Processes," Proc. Third. Intl. Conf. on Rain Erosion and Associated Phenomena, Royal Aircraft Establishment, England, 1970, p. 303.

72. Schmitt, G. F., "Polyurethane Coatings for Rain Erosion," Proc. Second Intl. Conf. on Rain Erosion and Associated Phenomena, Royal Aircraft Establishment, England, 1967, p. 329.

73. Brunton, J. H., "Erosion by Liquid Shock," Proc. Second Intl. Conf. on Rain Erosion and Associated Phenomena, Royal Aircraft Establishment, England, 1967, p. 535.

74. Wenzel, H. G., Jr., and Wang, C. T., "The Mechanics of a Drop After Striking a Stagnant Water Layer," Research Report No. 30, Water Resources Center, University of Illinois, (1970).

75. Heyman, F. J., "A Survey of Clues to the Relationship Between Erosion Rate and Impact Parameters," Proc. Second Intl. Conf. on Rain Erosion and Associated Phenomena, Royal Aircraft Establishment, England, 1967, p. 683.

76. Conn, A. F., "Prediction of Rain Erosion Resistance From Measurements of Dynamic Properties," Proc. Third Intl. Conf. on Rain Erosion and Associated Phenomena, Royal Aircraft Establishment, England, 1970, p. 353.

77. Fyall, A. A., "Single Impact Studies of Rain Erosion," Shell Aviation News, 374, (1969).

78. Brunton, J. H. and Camus, J. J., "The Flow of a Liquid Drop During Impact," Proc. Third Intl. Conf. on Rain Erosion and Associated Phenomena, Royal Aircraft Establishment, England, 1970, p. 327.

79. Heymann, F. J., Symposium on Erosion and Cavitation, ASTM STP 408, (1967).

80. Engel, O. G., "A First Approach to a Microscopic Model of Erosion Rate in Drop Impact and Cavitation," Proc. Third Intl. Conf. on Rain Erosion and Associated Phenomena, Royal Aircraft Establishment, England, 1970, p. 447.

81. Huang, Yen-Chen, "Numerical Studies of Unsteady Two Dimensional Liquid Impact Phenomena," Ph.D. Thesis, Univ. of Michigan, (1971).

82. Hammitt, F. G., "Cavitation Damage and Performance Research Facilities," ASME Symposium on Cavitation Research Facilities and Techniques, (May, 1964), pp. 175-84.

83. Timm, E. E., and Hammitt, F. G., "A Repeating Water Gun Device for Studying Erosion by Water Jet Impact," Univ. of Mich., Report No. 02643-1-PR, (1969).

84. Hammitt, F. G., et. al., "Liquid Impingement and Cavitation Studies of Erosion Resistance of Rubber Coated Materials for B. F. Goodrich," Univ. of Mich., Report No. UMICH-324490-1-T, (1970).

85. Tanner, L. H., "Some Applications of Holography in Fluid Mechanics," J. Scientific Instrumentation, 43, (1966), p. 81.

86. Hammitt, F. G., et. al., "Cavitation and Droplet Impingement Damage of Aircraft Rain Erosion Materials," Proc. Third Intl. Conference on Rain Erosion and Associated Phenomena, Royal Aircraft Establishment, England, 1970, p. 907.

APPENDIX

LIQUID RELAXATION PHENOMENA IN LIQUID - SOLID IMPACT

A.1 INTRODUCTION

Under most conditions liquids respond to compression or shear waves according to their equilibrium bulk or shear moduli. However, the propogation of compression or shear waves through a liquid is a non-equilibrium process requiring a finite time for a return to equilibrium. The process by which a liquid returns to its equilibrium state during the passage of a disturbance is called relaxation and the time required for a return to equilibrium following disturbance is called the relaxation time. If a liquid is strained at a sufficiently high rate so that the time scale of the straining process is shorter than the strain relaxation time for that process, then the liquid is unable to respond to the strain according to its equilibrium moduli and, instead, responds with the bulk and shear moduli of a solid.[1] This behavior at high strain rates is called induced glassiness.

Shalnev and Kozirev[2] have proposed that high velocity liquid-solid impact results in strain rates sufficiently high to cause induced glassiness in the liquid. During the period in which the liquid behaves as a solid Newton's Law may be applied to approximate the forces generated during the impact; that is:

$$\text{Force} = M \frac{dv}{dt} \triangleq M \frac{(V_2 - V_1)}{\Delta t} \qquad (1)$$

where M is the mass of the solidified liquid, V_1 and V_2 are the velocities of this mass before and after impact, and Δt

is the time period during which the deceleration takes place. Assuming Δt to be the time the liquid stays in the solidified state, that is, the relaxation time (t_r), and dividing equation (1) by the cross sectional area of the solidified liquid slug, there results an expression for the pressure developed on impact.

$$P = \frac{F}{A} = \frac{M\ (V_2 - V_1)}{A\ tr} \qquad (2)$$

The mass of the liquid is given by:

$$M = \varrho_L\ A\ u \qquad (3)$$

Where ϱ_L is the liquid density, and u is the length of the solidified liquid slug along the direction it is moving. As a first approximation u can be taken to be:

$$u = C\ t_R \qquad (4)$$

Where C is the shock propogation velocity through the liquid. Consequently, Equation 2 becomes

$$P = \frac{\varrho_L A\ C\ t_r\ (V_2 - V_1)}{A\ t_R} = \varrho_L C\ (V_2 - V_1) \qquad (5)$$

Which is the classical water hammer pressure equation corrected for shock velocity. This simplistic analysis demonstrates the probability that even in hypervelocity impact where relaxation times and strain rates may be similar the resulting impact pressure is similar to that predicted by compressible flow theory. Nevertheless, the occurrence of induced glassiness in liquids during impact is an interesting phenomenon worthy of further investigation.

A.2 EXPERIMENTAL APPROACH

When a liquid is in the glassy state due to extremely high strain rates it behaves as a solid and can exhibit both elastic and brittle behavior. In order to demonstrate this behavior, Shalnev and Kozirev[2] have utilized high speed cinematography to study the impact between a vertical liquid stream and a projectile fired perpendicularly into the stream. In this situation, relaxation-dominated behavior is manifested by a failure of the liquid stream to flow around the impacting projectile during the first moments of impact. If the strain rate caused by the impacting projectile is sufficiently high, the liquid stream will deform, and brittle fracture of the stream will occur, as is in fact observed in their photographs. Following the time required for relaxation the liquid will again exhibit normal liquid flow patterns.

Figure A.1 is a series of prints provided by Shalnev and Kozirev from one of their experimental photographic sequences. Taken at a rate of 8×10^3 frames/second, this figure shows a spherical projectile with a velocity of 24 m/s impacting a vertical, low-velocity liquid stream. The liquid is a mixture of transformer oil and rosin, with a viscosity of 3×10^4 cp. Figure A.1 appears to show that the liquid stream responds to the impacting projectile by bending slightly then fracturing and disintegrating into a large number of fragments. This series of pictures clearly demonstrates induced glassiness in a liquid subjected to high strain rates; however, it is probable that this liquid is highly non-newtonian due to its composition and extremely high viscosity.

Consequently, the question of whether relaxation dominated behavior can occur in more normal liquids at similar strain rates is left unanswered by the available published work of Shalnev and Kozirev.

It was decided to conduct an investigation here in the University of Michigan Cavitation and Multiphase Flow Laboratory similar to that of Shalnev and Kozirev in order to investigate the behavior of common liquids at high strain rates. Figure A.2 is a photograph of the apparatus utilized in this investigation. The experiment was set up so that 0.22 caliber pellets fired from a J. C. Higgins pellet rifle travelled through a blast deflector and then impacted on a liquid stream flowing from an orifice in the fluid reservoir. The B & W Model 330 Camera, in conjunction with diffuse back light provided by the Cordin Model 450 light source, was used to photograph the event. A laser was directed across the path of the bullet in the area of impact, and triggering for the light source was provided by interruption of the laser beam by the pellet as detected by the photodiode sensor. The velocity of the impacting pellet could be varied by controlling the gas pressure to the pellet gun. The experiments were conducted at room temperature.

Table A.1 is a summary of the liquid-pellet impact photographic sequences taken in this study. Selected frames from these sequences are printed as Figures A.2 through A.6.

Table A.1. IMPACT PHOTOGRAPHIC SEQUENCES

IMPACTED LIQUID	LIQUID VISCOSITY	PELLET VELOCITY	FIGURE NUMBER
Water	1 cp	103 m/s	A.3
Water	1 cp	152 m/s	A.4
PEO*(.25%,WSR-301)-Water Solution	22 cp	67 m/s	A.5
PEO*(.25%,WSR-301)-Water Solution	22 cp	160 m/s	A.6
Mineral Oil	45 cp	161 m/s	A.7

*PEO = Polyethylene Oxide, Water Soluble Resin

Photographic sequences are also presented of pellet impacts on solids. Figure A.8 consists of frames selected from a photographic sequence taken of a pellet impacting on a taut rubber band, which illustrates elastic behavior upon impact. Figure A.9 consists of frames selected from a photographic sequence taken of a pellet impacting on the edge of a solid plexiglass block. This sequence illustrates liquid-like plastic flow in the lead pellet upon impact; also visible in Figure A.9 is the propogation of strain waves in the plexiglass block following pellet impact. These strain waves are visible due to the photoelastic behavior of plexiglass. In some of the photographic sequences a small piece of tape which is attached to the front of the pellet may be observed. This tape was part of the blast deflector in front of the muzzle of the pellet rifle and often became attached to the pellet as it passed through the blast deflector.

A.3 DISCUSSION OF RESULTS

It appears from a comparison of the results of Shalnev and Kozirev (Figure A.1) to the results of this study (Figures A.3 through A.7) that the brittle fracture phenomenon so obvious in Figure A.1 is absent in Figures A.3 through A.7.

It seems probable this difference in experimental results is best explained in terms of differences in the impacted liquids rather than in terms of differences in the strain rates imposed upon the liquids by the experimental designs. Due to the large number of molecules participating in the relaxation phenomena occurring in the impacted liquids, it is impossible to precisely characterize each liquid with a particular relaxation time, since the actual relaxation process occurring is characterized by a distribution of relaxation times. Nevertheless, the so-called Zimm relaxation time[1,3] gives an index of the relative magnitudes of relaxation times for water and PEO-water solution. Very approximately, the relaxation time for water is on the order of 10^{-10} to 10^{-12} seconds and the relaxation time for the 0.25% PEO solution is on the order of 10^{-5} to 10^{-6} seconds. Due to a complete lack of data other than viscosity on the transformer oil-rosin solution studied by Shalnev and Kozirev, it is impossible to estimate its relaxation time. However, due to the extremely high viscosity of this solution (3×10^4 cp) it seems probable that its relaxation time is many orders of magnitude longer than that calculated for the PEO-water solution (10^{-5} - 10^{-6} seconds). If this is the case, it is not particularly surprising that it demonstrates relaxation dominated flow behavior at the strain rates generated by an impacting projectile. However, the failure of this experiment to demonstrate any sort of induced glassy behavior in liquids normally associated with liquid-solid impact, coupled with the approximation developed for impact forces in Section A.1,

casts doubt on the hypothesis that relaxational processes play an important part in the mechanism by which liquid-solid impact damages materials in practical application.

PRINTS FROM SHALNEV AND KOZIREV

BULLET VELOCITY = 24 m/s
SOLUTION VISCOSITY = 30,000 cp
FRAMING RATE = 8000 f/s
EXPOSURE TIME = 60 μs

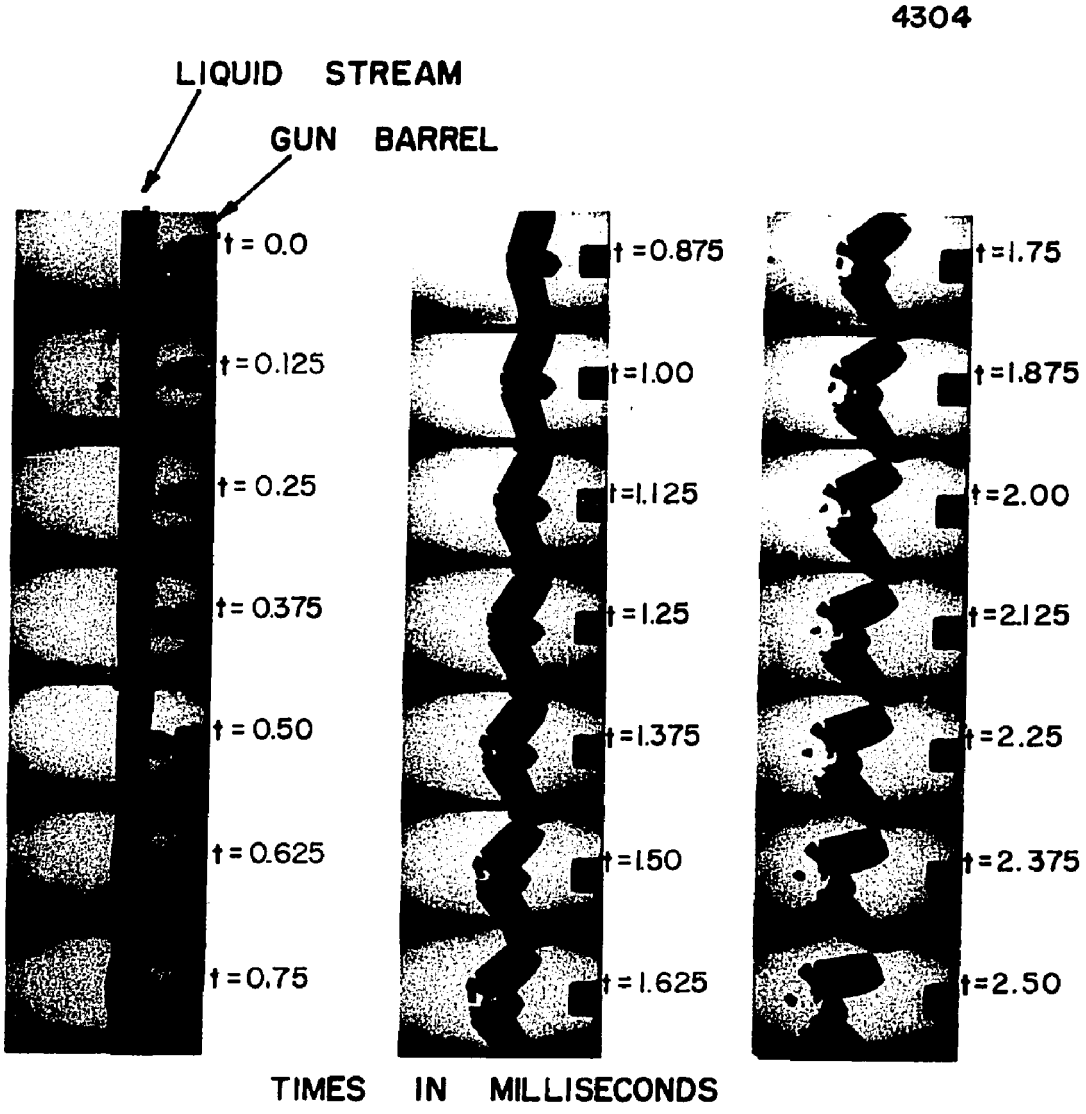


Figure A.1 Prints, Shalnev and Kozirev

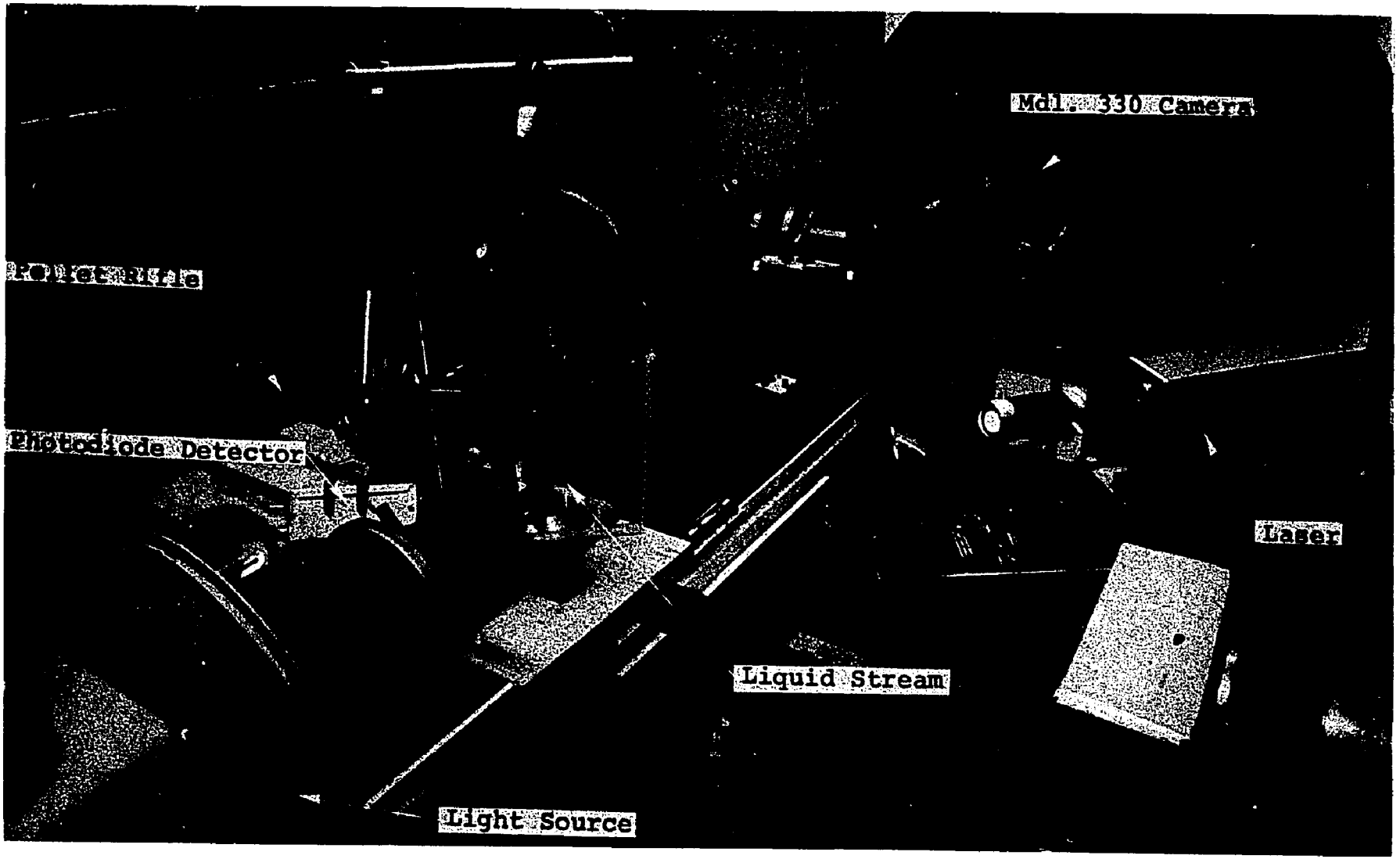


Figure A.2 Liquid Stream Impact Unit w/ Mdl. 330 Camera

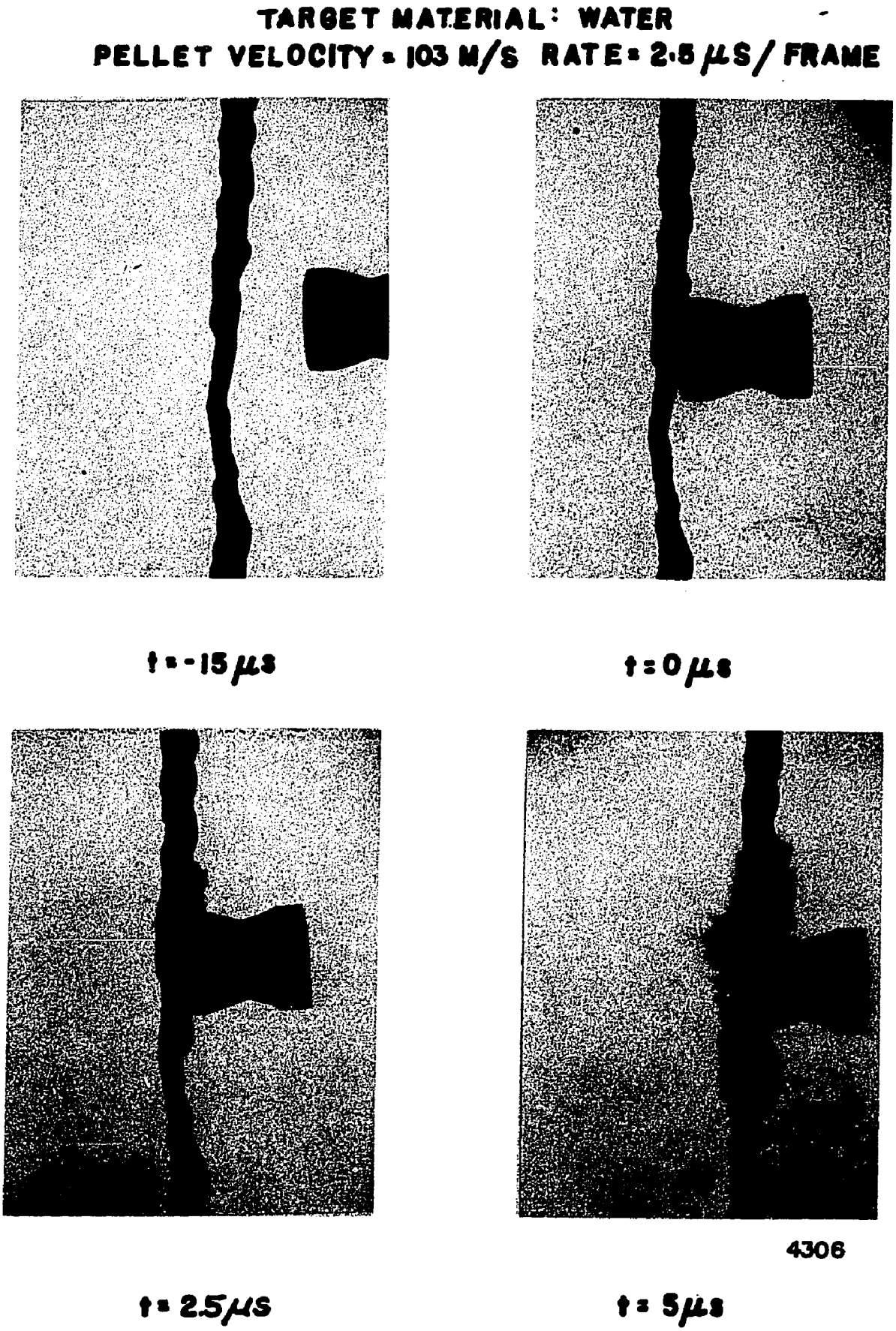


Figure A.3 Prints, Run 4192-BW-BF-2

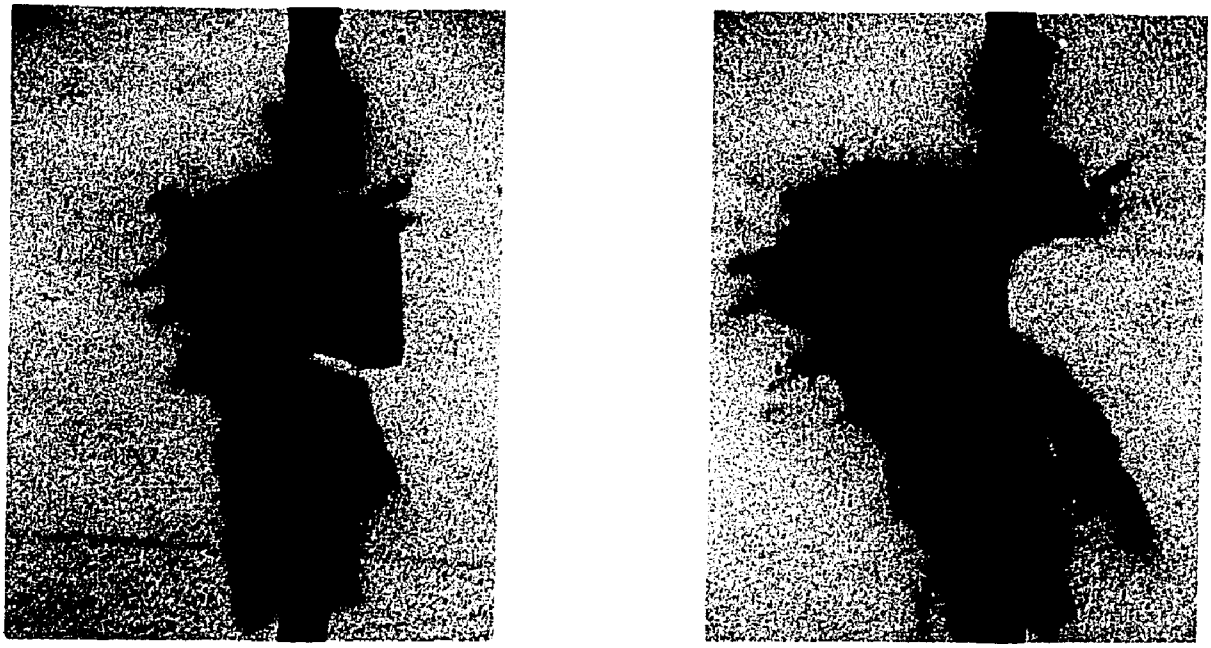


Figure A.3 Prints, Run 4192-BW-BF-2, p. 2

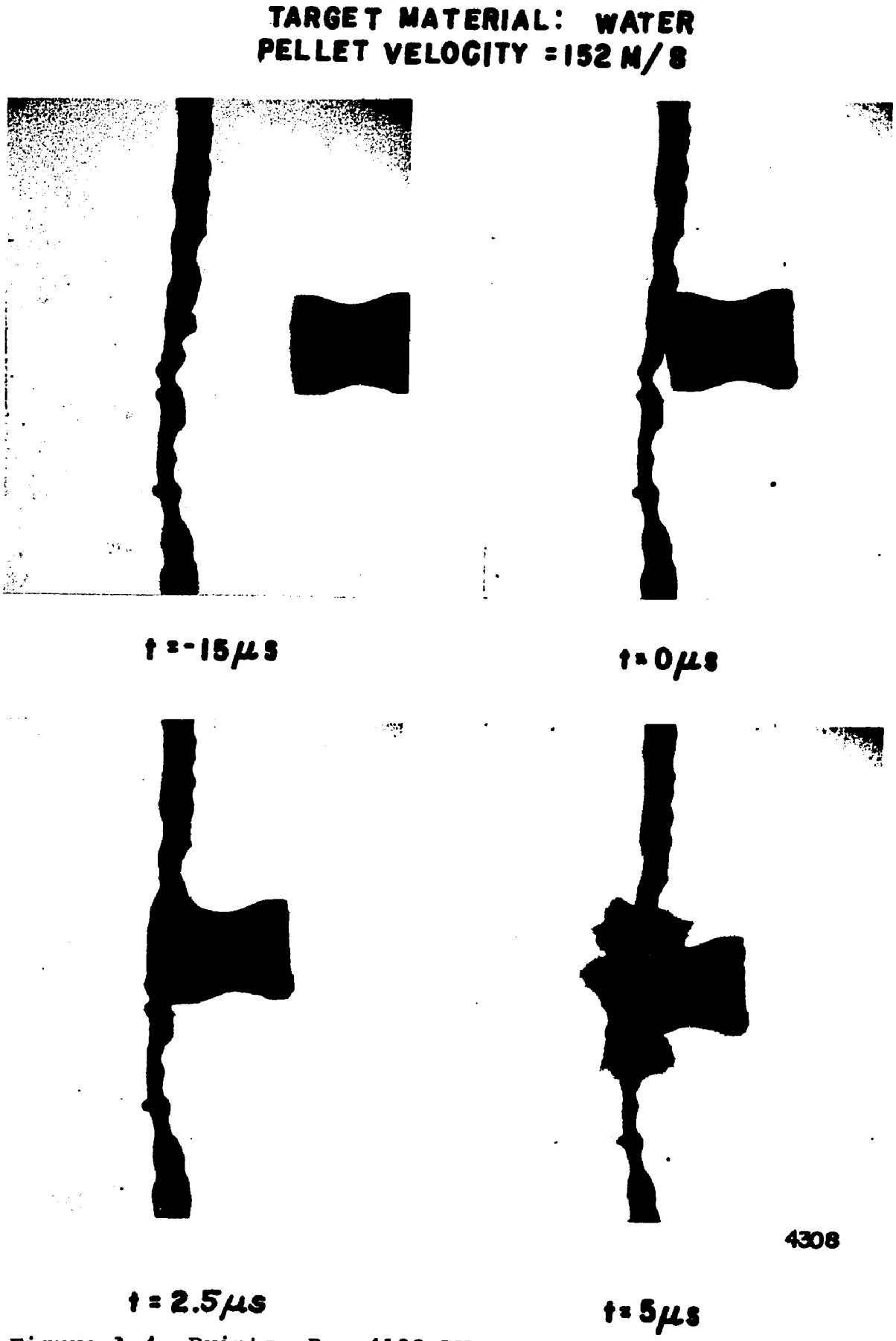
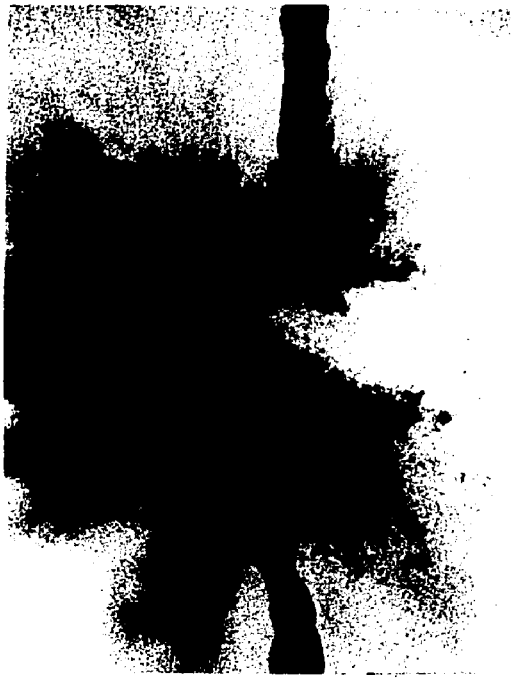


Figure A.4 Prints, Run 4192-BW-BF-1



t = 15 μs



t = 30 μs

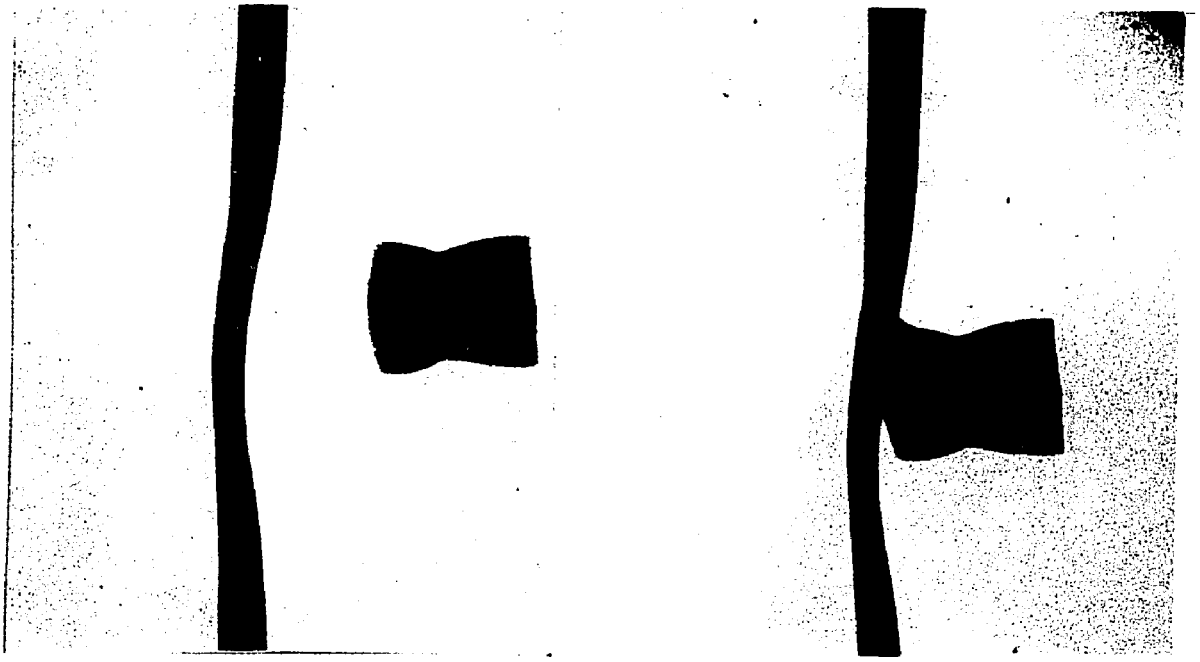


4309

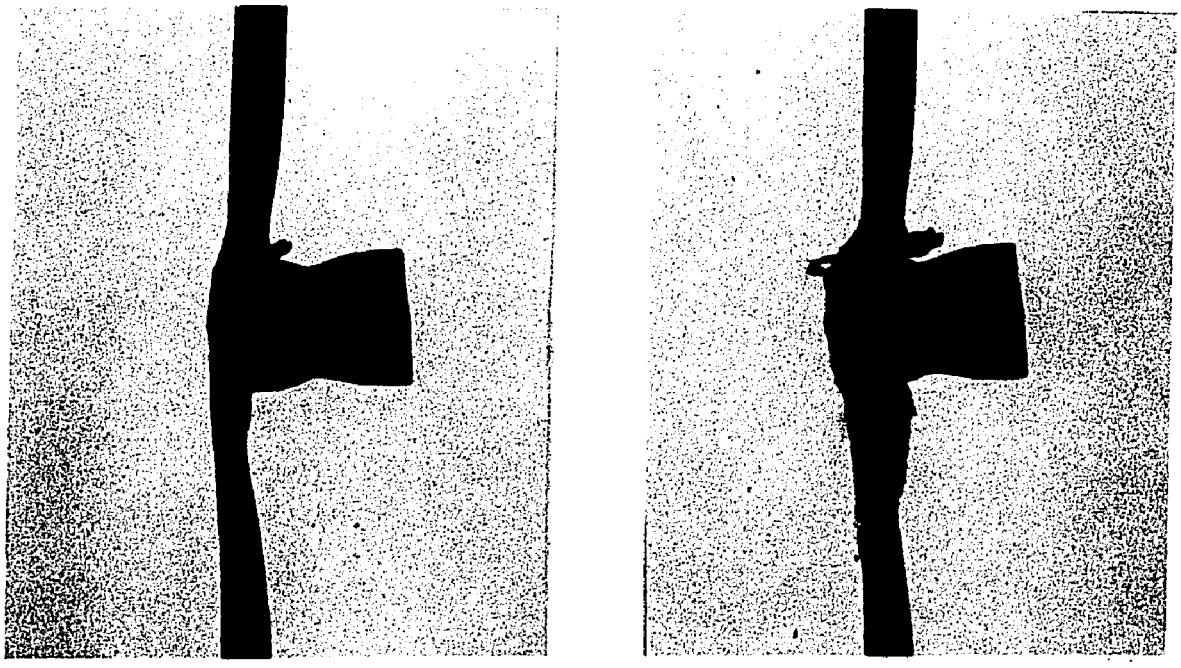
t = 45 μs

Figure A.4 Prints, Run 4192-BW-BF-1, p. 2

TARGET MATERIAL: POLETHYLENE OXIDE SOLUTION
PELLET VELOCITY = 67 M/S



t=-30μs t=0μs



t=5μs t=10μs

Figure A.5 Prints, Run 4202-BW-BF-2

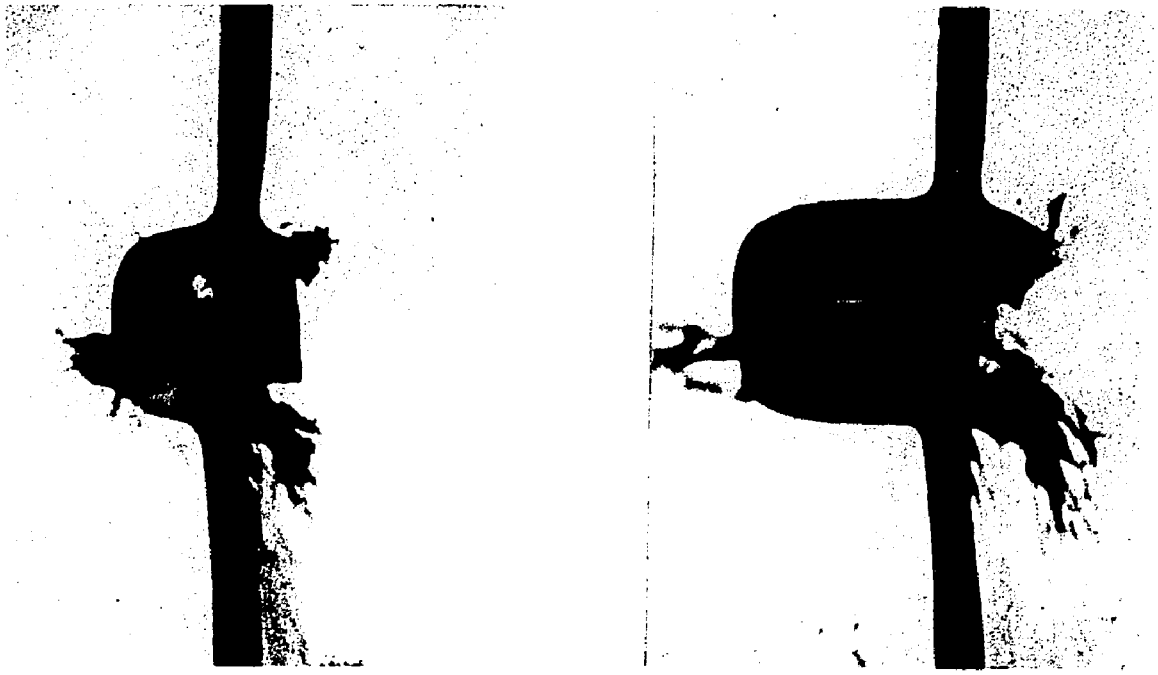


Figure A.5 Prints, Run 4202-BW-BF-2, p. 2

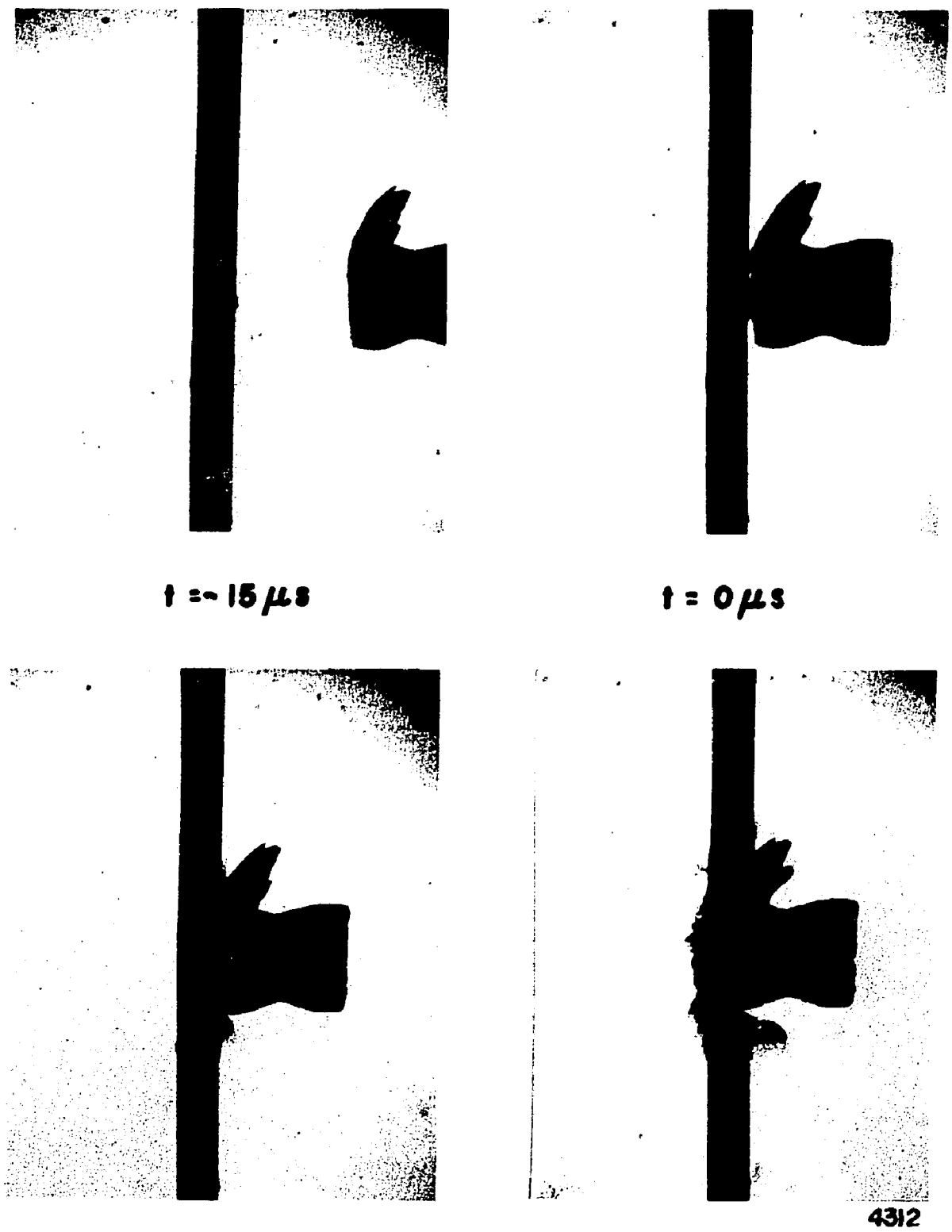
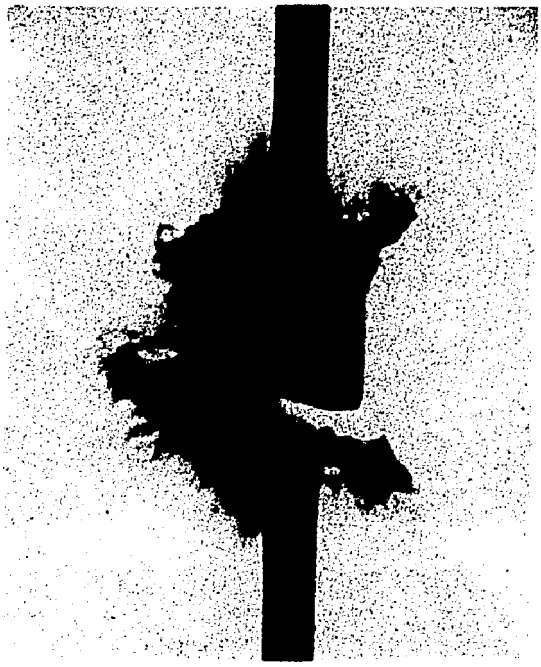
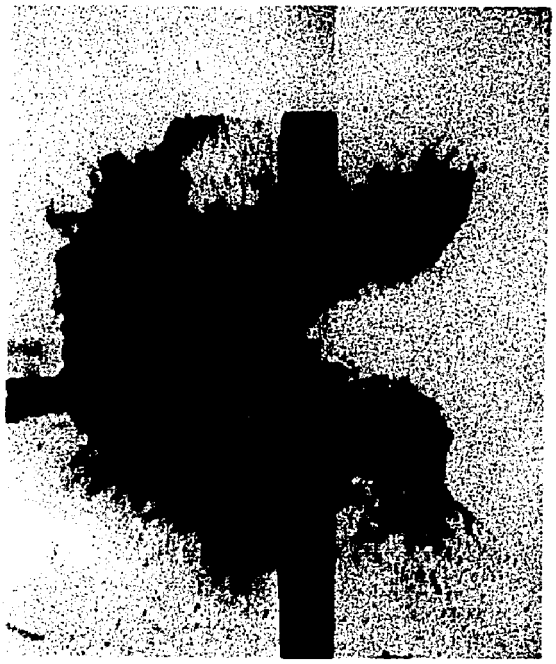


Figure A.6 Prints, Run 4192-BW-BF-3



t = 15 μs



t = 30 μs

4313

Figure A.6 Prints, Run 4192-BW-BF-3, p. 2

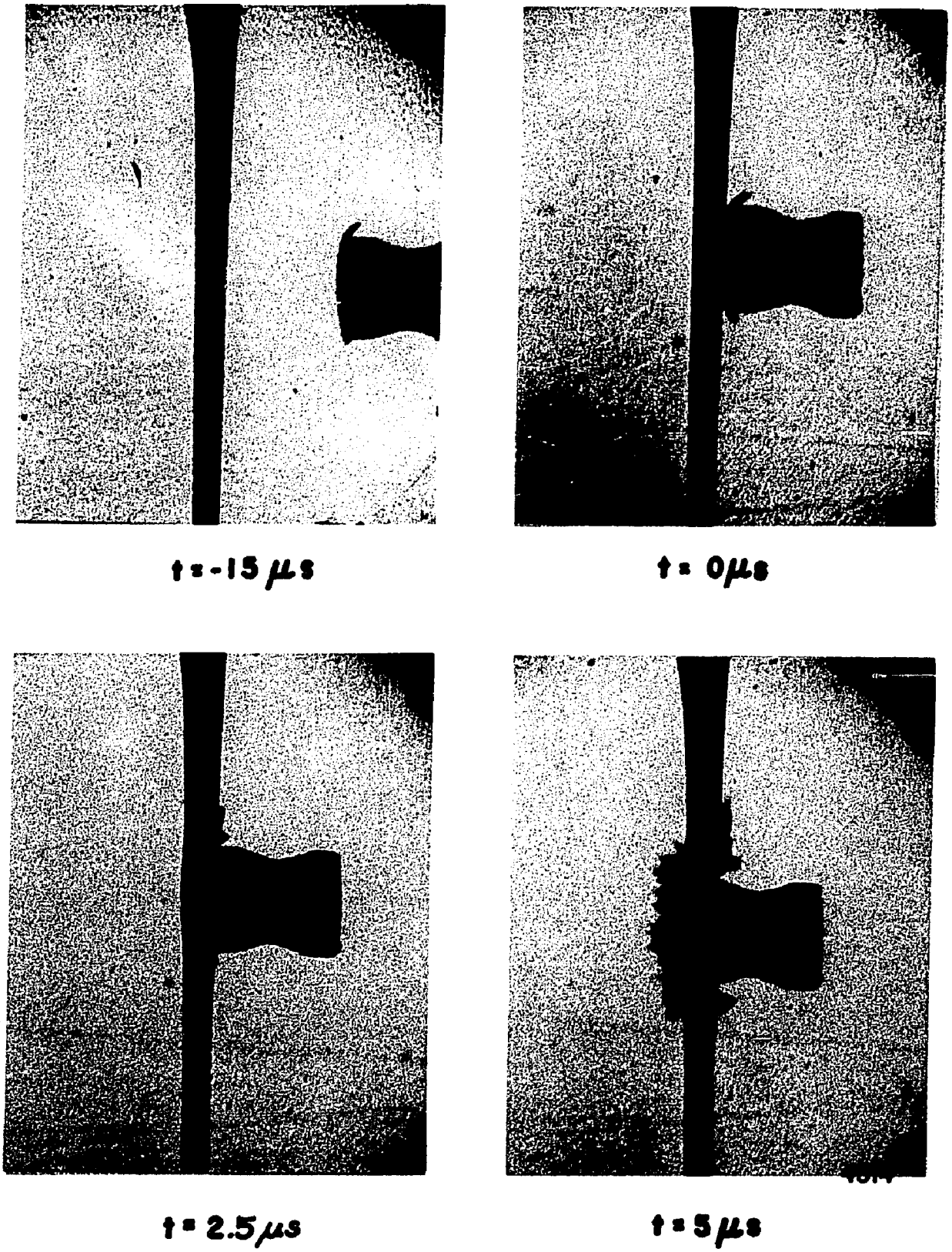


Figure A.7 Prints, Run 4192-BW-BF-4



Figure A.7 Prints, Run 4192-BW-BF-4, p. 2

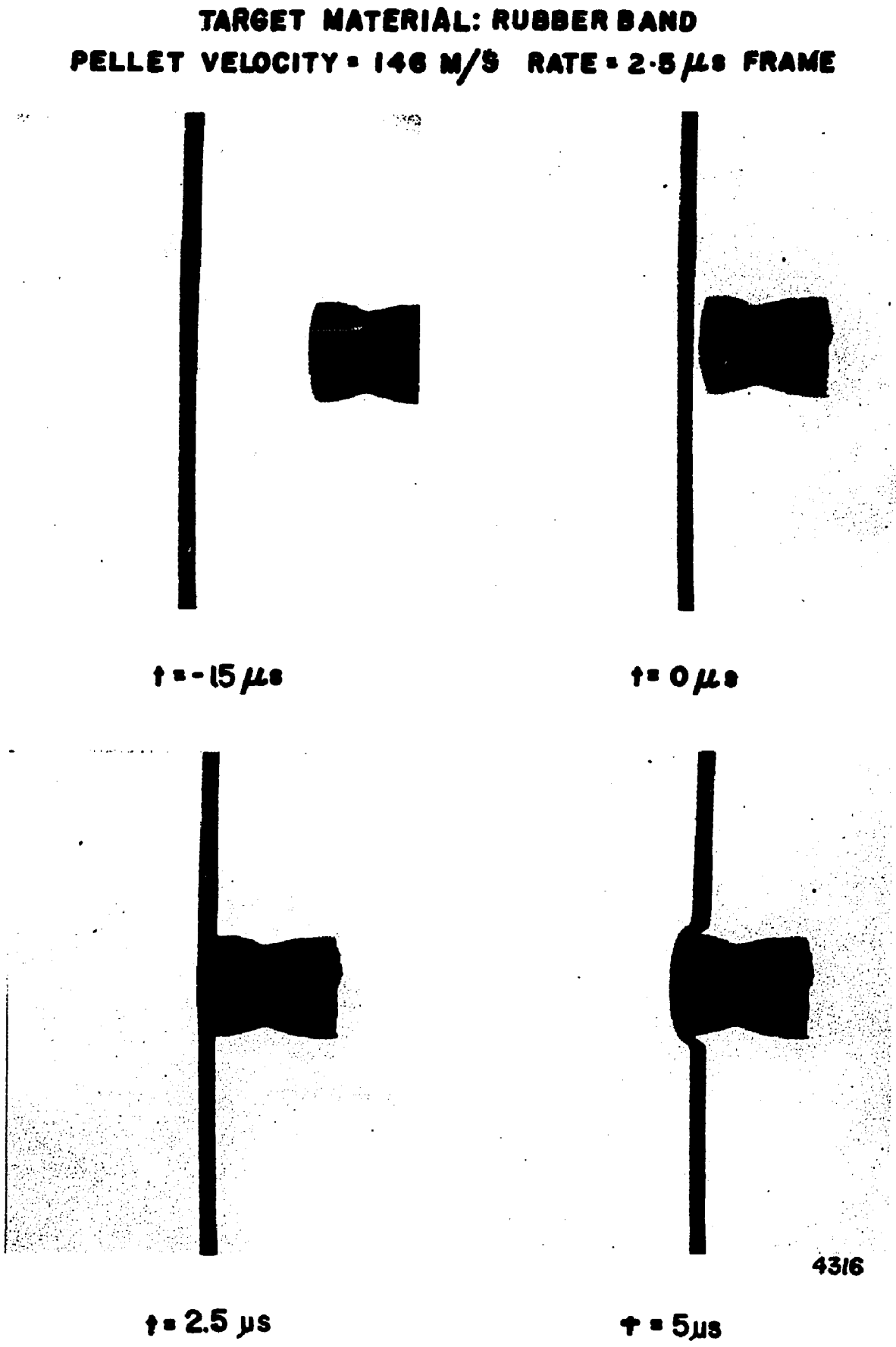


Figure A.8 Prints, Run 522-BW-BF-1

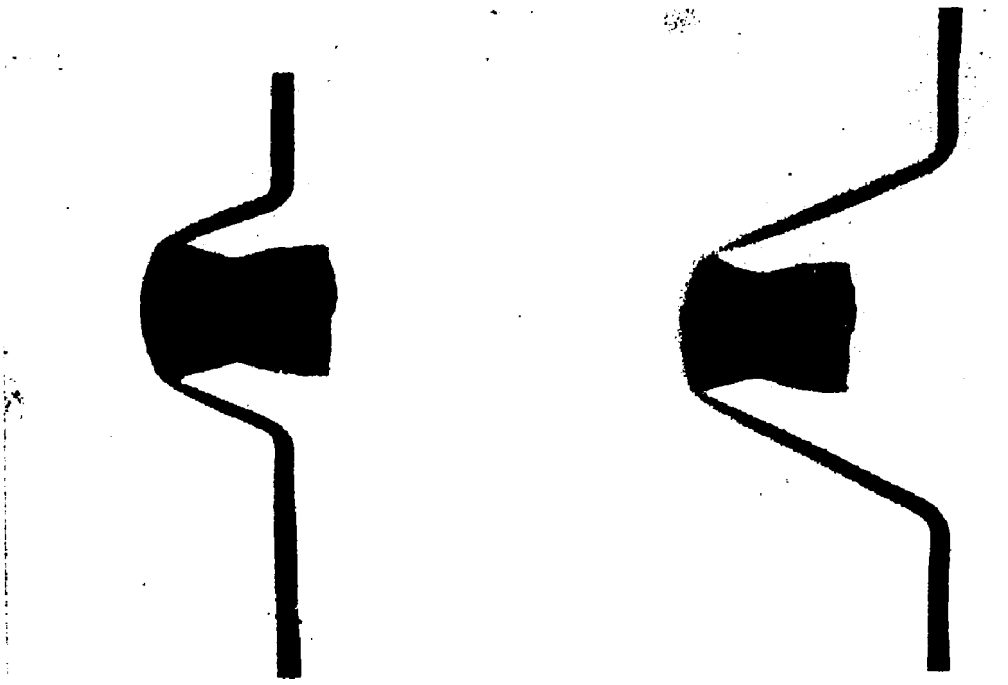


Figure A.8 Prints, Run 522-BW-BF-1, p. 2

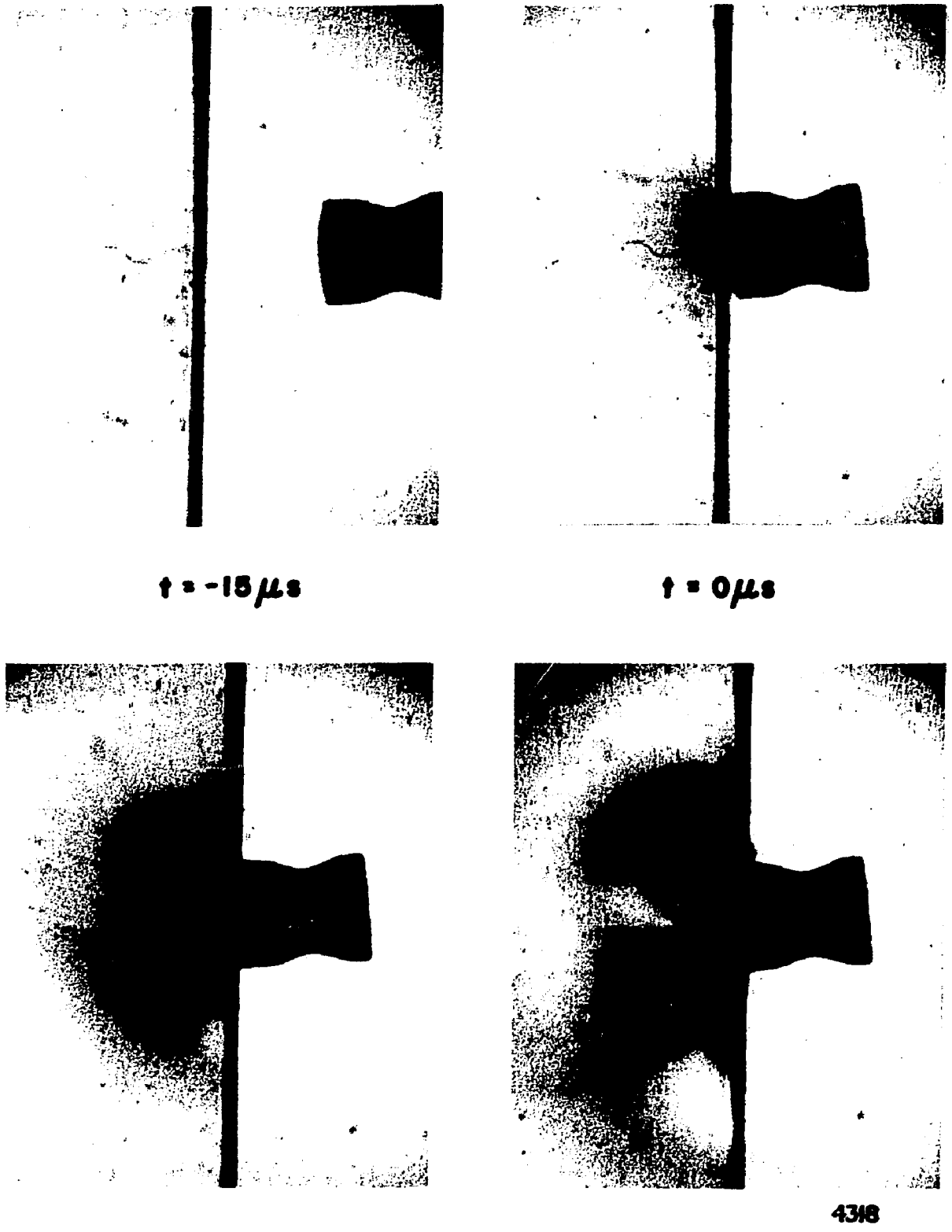
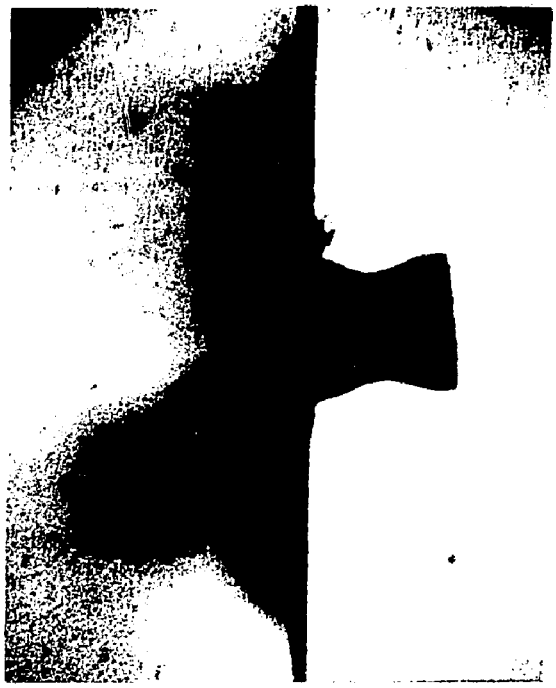
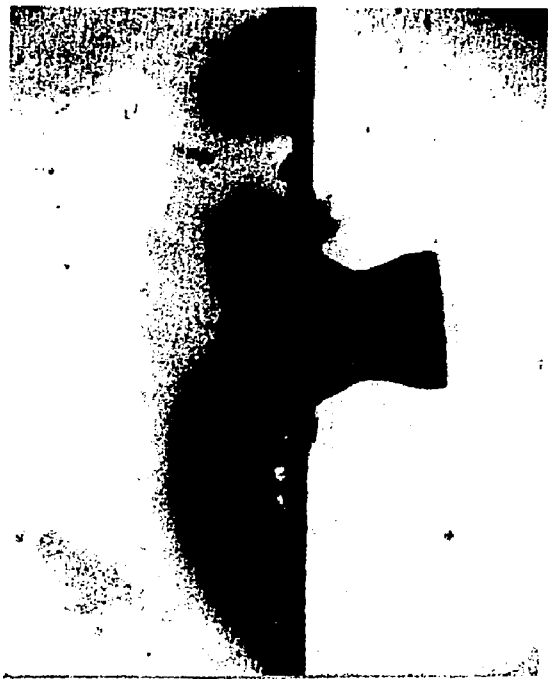


Figure A.9 Prints, Run 522-BW-BF-2



t = 7.5 μs



t = 10 μs



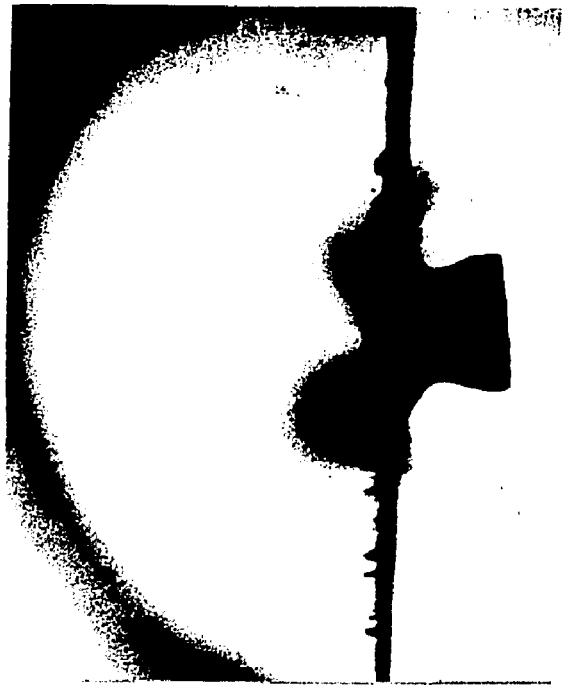
t = 12.5 μs



4319

t = 15 μs

Figure A.9 Prints, Run 522-BW-BF-2, p. 2



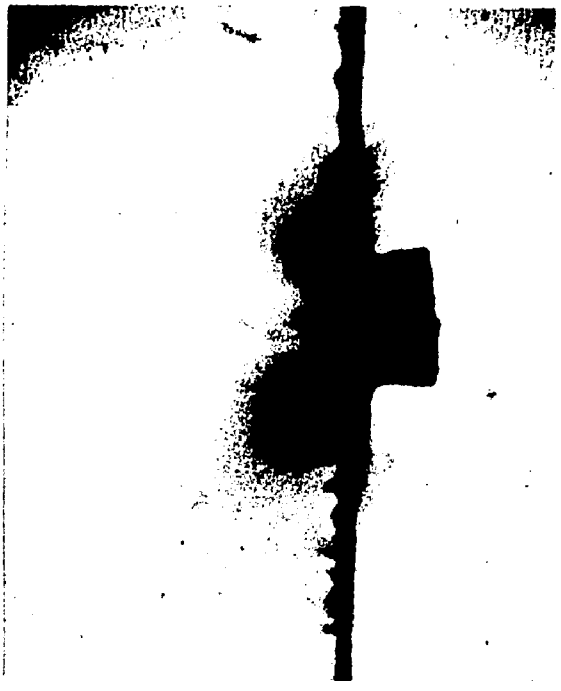
t = 17.5 μs



t = 20 μs



t = 22.5 μs



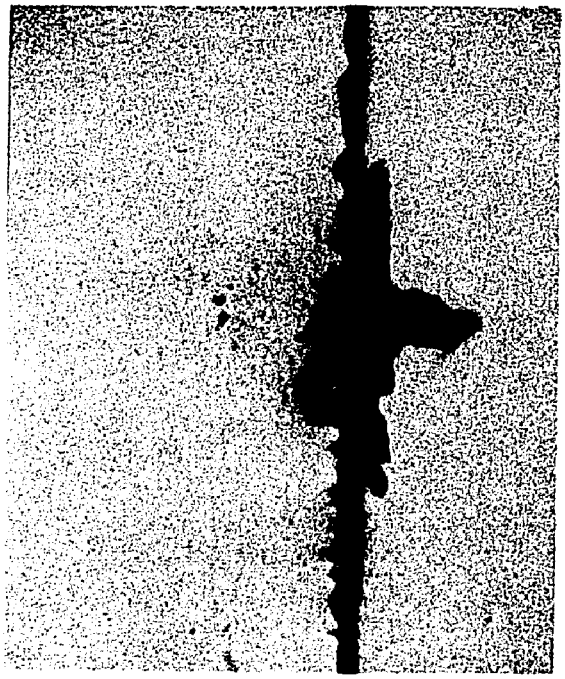
4320

t = 25 μs

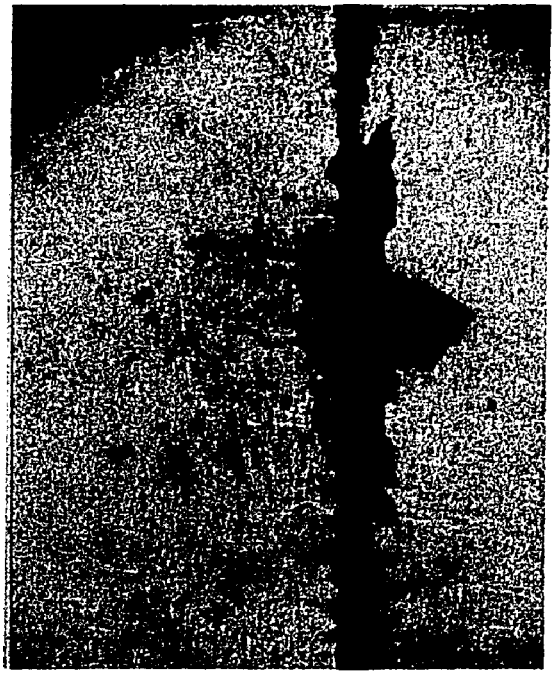
Figure A.9 Prints, Run 522-BW-BF-2, p. 3



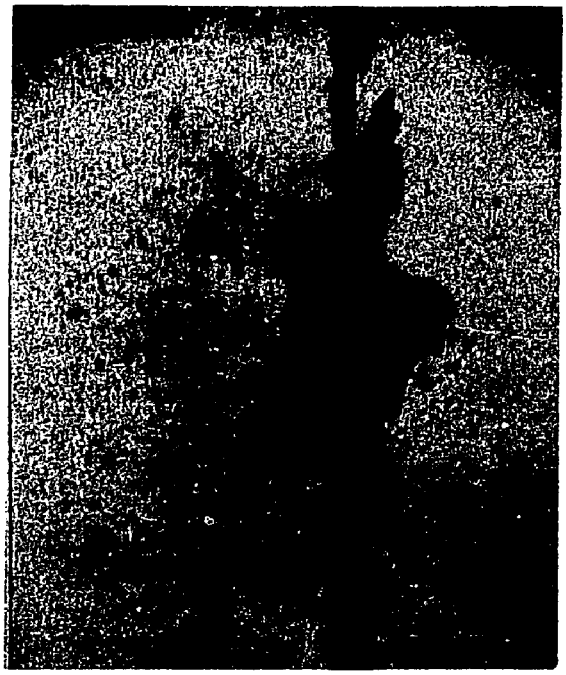
t = 37.5 μs



t = 50 μs



t = 75 μs



4321

t = 100 μs

Figure A.9 Prints, Run 522-BW-BF-2, p. 4

APPENDIX BIBLIOGRAPHY

1. Bond, A., Molecular Crystals, Liquids, and Glasses, Wiley and Sons, New York, (1968).

2. Shalnev, K. K., and Kozirev, S. P., "Significance of Relaxational Liquid Properties in Damaging Solids by Free Jet Impact and Cavitation," Inst. of Mechanical Problems, Soviet Academy of Sciences, Moscow, (1971).

3. Hand, J. H., Drag Reduction in Dilute Polymer Solutions, Ph.D. Thesis, Univ. of California, Berkley, (Dec., 1971).